ISSN 0915-633X

NATIONAL INSTITUTE FOR FUSION SCIENCE

NIFS Contributions to 19th IAEA Fusion Energy Conference
(Lyon, France, 14-19 October 2002)

(Received - Nov. 22, 2002)

NIFS-764 Nov. 2002

TOKI, JAPAN

NIFS Contributions to 19th IAEA Fusion Energy Conference (Lyon, France, 14-19 October 2002)

Abstract

NIFS has presented 21 papers at the 19th IAEA Fusion Energy Conference (Lyon, France, 14-19 October 2002). The contributed papers are collected in this report.

Keywords: NIFS, 19th IAEA Fusion Energy Conference, contributed papers

Recent Advance in LHD Experiment

O. Motojima, N. Ohyabu, A. Komori, O. Kaneko, H. Yamada, K. Kawahata, Y. Nakamura, K. Ida, T.Akiyama[1], N.Ashikawa, W.A. Cooper[17], A.Ejiri[5], M.Emoto, N.Ezumi[12], H.Funaba, A. Fukuyama[3], P.Goncharov[2], M.Goto, H.Idei, K.Ikeda, S.Inagaki, M.Isobe, S.Kado[10], H.Kawazome[3], K.Khlopenkov, T.Kobuchi, K.Kondo[3], A.Kostrioukov, S.Kubo, R.Kumazawa, Y.Liang, J.F. Lyon[16], A.Mase[11], S.Masuzaki, T.Minami, J.Miyazawa, T.Morisaki, S.Morita, S.Murakami, S.Muto, T.Mutoh, K.Nagaoka, Y.Nagayama, N.Nakajima, K.Nakamura[9], H.Nakanishi, K.Narihara, Y.Narushima, K.Nishimura, N.Nishino13, N.Noda, T.Notake[4], H.Nozato[5], S.Ohdachi, Y.Oka, H. Okada[3], S.Okamura, M.Osakabe, T.Ozaki, B.J.Peterson, A.Sagara, T.Saida[2], K.Saito, S.Sakakibara, M.Sakamoto[9], R.Sakamoto, M.Sasao, K.Sato, M.Sato, T.Seki, T.Shimozuma, M.Shoji, H.Suzuki, Y.Takeiri, N.Takeuchi[4], N.Tamura, K.Tanaka, M.Y.Tanaka, Y.Teramachi[14], K.Toi, T.Tokuzawa, Y.Tomota[15], Y.Torii[4] K.Tsumori, K.Y.Watanabe, T.Watari, Y.Xu, I.Yamada, S.Yamamoto[4], T.Yamamoto[4], M.Yokoyama, S.Yoshimura, Y.Yoshimura, M.Yoshinuma, N.Asakura[7], T.Fujita[7], T.Fukuda[7], T.Hatae[7], S.Higashijima[7], A.Isayama[7], Y.Kamada[7], H.Kubo[7], Y.Kusama[7], Y.Miura[7], T.Nakano[7], H.Ninomiya[7], T.Oikawa[7], N.Oyama[7], Y.Sakamoto[7], K.Shinohara[7], T.Suzuki[7], H.Takenaga[7], K.Ushigusa[7], T. Hino[6],M. Ichimura[8], Y. Takase[5], F. Sano[3], H. Zushi[9], T. Satow,S. Imagawa, T. Mito, I. Ohtake, T.Uda, K. Itoh, K. Ohkubo, S. Sudo, K. Yamazaki, K. Matsuoka, Y. Hamada, M. Fujiwara

National Institute for Fusion Science, Toki, Gifu, Japan
1 Research Laboratory for Nuclear Reactors, Tokyo Institute of Technology, Tokyo, Japan
2 Department of Fusion Science, School of Mathematical and Physical Science, Graduate University for Advanced Studies, Hayama, Japan
3 Graduate School of Energy Science, Kyoto University, Uji, Japan
4 Department of Energy Engineering and Science, Nagoya University, Japan
5 Graduate School of Frontier Sciences, The University of Tokyo, Japan
6 Faculty of Engineering, Hokkaido University, 7.Naka Fusion Research Institute, JAERI, Japan, 8.University of Tsukuba, Japan, 9.Research Institute for Applied Mechanics, Kyushu University 10. High Temperature Plasma Center, The Univ. of Tokyo, Tokyo
11. Advanced Science and Technology Center for Cooperative Research, Kyushu Univ.
12. Nagano National College of Technology. 13 Faculty of Engineering, Hiroshima Univ.
14. The Polytechnic University, Japan, 15 Department of Engineering, Ibaraki Univ. Japan
16. Ork Ridge National Laboratory, Tennessee, USA, 17. CRPP, EPFL, Lausanne, Switzerland

e-mail contact of main author: motojima@LHD.nifs.ac.jp

Abstract: In the first four years of LHD experiment, several encouraging results have emerged, the most significant of which is that MHD stability and good transport are compatible in the inward shifted axis configuration. The observed energy confinement at this optimal configuration is consistent with ISS95 scaling with an enhancement factor of 1.5. The confinement enhancement over the smaller heliotron devices is attributed to the high edge temperature. We find that plasma with an average beta of 3 % is stable in this configuration even though the theoretical stability conditions of Mercier modes and pressure driven low n modes are violated. In the low density discharges heated by NBI and ECR heatings, ITB(internal transport barrier) and an associated high central temperature (> 10 keV) are seen. The radial electric field measured in these discharges is positive (electron root) and expected to play a key role in the formation of the ITB. The positive electric field is also found to suppress the ion thermal diffusivity as predicted by neoclassical transport theory. The width of the externally imposed island (n/m=1/1) is found to decrease when the plasma is collisionless with finite beta and it increases when the plasma is collisional. The ICRF heating in LHD is successful and a high energy tail (up to 500keV) has been detected for minority ion heating, demonstrating good confinement of the high energy particles. The magnetic field line structure unique to the heliotron edge configuration is confirmed by measuring the plasma density and temperature profiles on the divertor plate. A long pulse (2minute) discharge with an ICRF power of 0.4 MW has been demonstrated and energy confinement characteristics are almost the same as those in short pulse discharges.

1.Introduction

In the first four years of the Large Helical Device (LHD) experiment, we have made the necessary progress in achieving high quality plasmas [1-10]. As indicated by the presently achieved plasma parameters listed in Table I, recently high central electron temperatures of 10 keV have been obtained by localizing the ECH power deposition (a total of 1.2 MW) within $\rho = 0.2$ [11,12]. One of the most important achievement in the CHS [13] and LHD experiments has been to resolve favorably the conflict between stability and confinement. The inward shifted configurations are ideal in terms of particle orbit and consequently the neoclassical loss [14] and volume of the confinement region. On the other hand they have been predicted to have poor MHD stability. The experiments demonstrate that LHD helical plasmas in the inward shifted configuration are stable despite of the unfavorable prediction by ideal linear MHD stability theory. Also it has been shown that the heat diffusivity of anomalous transport in this configuration is even lower than that in the outward shifted configuration having theoretically better MHD stability. Enhancement of the energy confinement is the key to advancing the LHD experiment. We have found that with central deposition of ECH power, an ITB (Internal Transport Barrier) appears in the low density, beam heated discharges, which provided significant impetus to the LHD experimental program. The LHD is a heliotron type device with an intrinsic divertor. It is the largest superconducting fusion device, with its specifications listed in Table II. The major goal of the LHD experiment is to demonstrate the high performance of helical plasmas in a reactor relevant plasma regime. The LHD experiment began in March 1998 after its intensive eight-year construction period. In the present LHD experiments, plasmas are heated by NBI, ICRH and ECH systems and the maximum powers absorbed by the plasma have been gradually increased. A list of available power is shown in Table II. Plasma generation is normally initiated by ECH power and then the main power is added to heat the plasma. With good wall conditions, however, plasma initiation or start-up is possible by simple injection of the NBI power [15]. With this start-up, we can operate low field discharges, independently of the ECH resonance conditions. Carbon divertor tiles are used to handle the heat flux from the core. Stainless protection plates cover the vacuum vessel. The wall conditioning is mainly done by glow discharges and vessel baking (100° C). In the following the recent results of the LHD experiment are summarized for several important research subjects, i.e., heat transport, stability and long pulse operation.

Table I Achieved plasma parameters

	T	n_e
High Electron Temperature	10 keV	0.6×10^{19} m^{-3}
High Ion Temperature	5.0 keV	0.7×10^{19} m^{-3}
High Confinement	1.3 keV	4.8×10^{19} m^{-3}
$\tau_E = 0.36$ s. $nT\tau_E = 2.2\times 10^{19}$ keV m^{-3} . $P_{abs} = 1.5$ MW.		
Maximum Stored Energy	Wp = 1.2 MJ	
Highest Beta	$\langle\beta\rangle = 3.2$ % at B = 0.5 T	
Maximum Density	1.5×10^{20} m^{-3}	

Table II LHD device parameters and heating power used in the experiment.

Major radius	3.9 m	B_o	2.9 T
Coil minor radius	0.975 m	$\iota(0) / \iota(a)$	0.4 / 1.3
Plasma radius	~0.6 m	HeatingPower(absorbed)	
l/m	2 / 10	NBI	9.0 MW
α (pitch modulation)	0.1	ECRH	1.7 MW
Helical ripple	0.2	ICRF	2.7 MW

2. Heat Transport of the LHD plasmas

2.1. Global Energy Confinement of LHD Plasma

The energy confinement times in the LHD inward shifted discharges (R_{ax} = 3.6 m) are consistent with the ISS95 scaling [16] with an enhancement factor of ~1.5 and are comparable to those in ELMy H-mode tokamaks discharges with q = 4.5 [17]. They are a factor of 2 higher than those of smaller heliotron devices such as CHS, Heliotron E, and ATF. This enhancement is attributed to high edge temperature, as described below [18,19]. Further enhancement of the energy confinement and hence suppression of the plasma turbulence are required for high performance of the LHD plasmas. The neoclassical transport loss (ripple loss) is also a concern for the LHD type devices. Numerical calculation shows that the inward shifted configuration (R_{ax} = 3. 5-3.6 m) has good particle orbit properties [15], i.e., deviation of the deeply trapped particle orbit from the magnetic surface is small and the deviation becomes larger with increasing R_{ax} ,reaching a fraction of the minor radius at R_{ax} = 3.75-3.9 m.

The dependence of the energy confinement on the position of the magnetic axis is studied [20].The enhancement factor over the ISS95 scaling is found to be sensitive to variation in the magnetic axis position (R_{ax}). It is optimum at R_{ax} = 3.55-3.6 m and decreases with increasing R_{ax}. For R_{ax} = 3.9 m, it is as small as 0.6. Furthermore, strong deterioration of the confinement occurs for R_{ax} = 3.75 and 3.9 m when the plasma becomes collisionless ($\nu^* < 1$). This is believed to be due to neoclassical transport (ripple loss). For inward shifted discharges with low neoclassical transport, the enhancement factor is independent of ν^* and hence the anomalous transport dominates over the neoclassical transport.

2.2. Electron Temperature Profile in LHD Discharges

The shape of the electron temperature profile does not vary much over a wide range of the density ($1.5\times10^{19}m^{-3} < n < 9\times10^{19}m^{-3}$) when the island size (n/m=1/1) is minimized by the correction coils in the discharges (P = 8 MW, B = 2.75T, R_{ax} = 3.6m). Fig. 1(a) shows electron temperature profiles at two different densities ($3.5\times10^{19}m^{-3}$, $7\times10^{19}m^{-3}$). The shapes of the

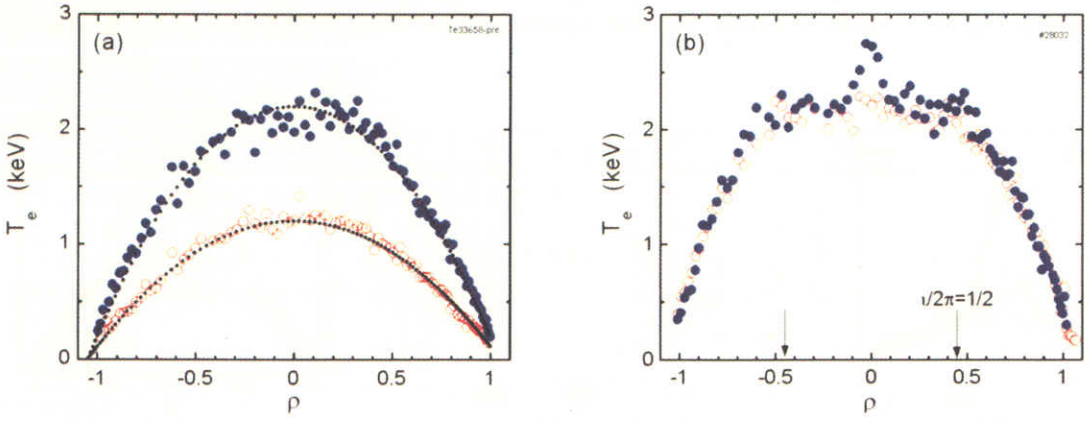

Fig. 1. (a). Shape of the electron temperature profile. The profile shapes for the discharges with two different densities (• $3.5\times10^{19}m^{-3}$, o $7\times10^{19}m^{-3}$) are nearly identical. The curves (……) are : $T_e = T_e(0)[1-(\rho/1.05)^2]$. B = 2.75 T, R_{ax} = 3.6m. (b). (o): flattening of the core electron temperature profile for low density, ctr-beam heated discharges. . (•): with modest ECRH power (300kW) in the core, a small ITB appears in the center. n =1.35×10^{19} m^{-3}

temperature profiles are similar and they are close to a parabolic profile if plotted in terms of ρ (the normalized radius). The parabolic profile is fairly broad and leads to better normalized global confinement compared with smaller heliotron devices with peaked profiles [18,19]. The broadness of the profile is found to be similar to those of a comparable H-mode tokamak such as ASDEX-U[21] [For ASDEX-U, T_e (0.4)/T_e (0.8) is ~1.8 and for LHD it is ~2.0].

In the low density ($n < 1.5\times10^{19}m^{-3}$) counter(ctr)-beam heated discharges (R_{ax} = 3.5, 3.6 m), however, core flattening of the profile occurs, deviating significantly from the parabolic profile as shown in Fig.1(b) [22]. Part of reason for the flattening is that a smaller fraction of power is deposited in the core region compared with the co-beam heated discharges which exhibit a peaked temperature profile even at such low density. But profile flattening persists even if the localized ECH power is deposited in the core and hence dominates NBI power in the core power balance. We find that flattening is localized within the $\iota/2\pi = 1/2$ surface. The effective electron thermal diffusivity χ_{eff} in the core is very high more than 50 m^2s^{-1}(here χ_{eff} is defined as $q = n\,\chi_{eff}\,\nabla T_e$). Ripple transport without radial electric field causes large χ at high temperature, but it is as small as 0.8 m^2s^{-1} for the temperature of the present case (T_e =2.2 keV). Thus it is difficult to explain this level of rapid transport without invoking some kind of structural confinement loss .

2.3. Internal Transport Barrier (ITB)

The temperature profile in the normal LHD discharge is close to parabolic. In the low density ($n < 1.5\times10^{19}m^{-3}$) counter(ctr)-beam heated discharges (R_{ax} = 3.53m), however, flattening of the profile occurs in the core region within the $\iota/2\pi = 1/2$ surface. With higher ECH power, a bump (a small ITB) appears in the center[Fig.1(b))]. Further higher ECH power leads to complete formation for the ITB [13]. There is a clear ECH power threshold for a complete formation of the ITB as shown in Fig. 2. At P_{ECH} = 180kW (R_{ax}= 3.5 m), there is a small bump in the flattened core and at P_{ECH} = 280kW, a complete formation of the ITB occurs. The power threshold increases with increasing density. The foot location of the ITB defined as the location of the jump in ∇T is typically around $\rho \approx 0.2$ and increases slightly with P/n.

Core heat transport in the low density co-beam heated discharges is quite different from that of the ctr-beam case [22]. Core flattening does not occur and its profile is even slightly peaked than the parabolic profile. With added ECH power, the central temperature increases and a much wider ITB forms, as shown in Fig. 3. The jump in ∇T is much smaller at the foot point compared with ctr-beam case, but the central temperature is comparable. The foot point

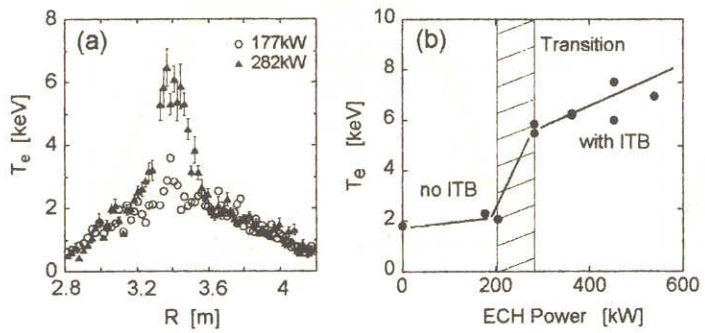

Fig.2. (a) A typical ITB electron temperature profile for the ctr-beam and ECRH heated discharges.

(b) A clear ECH power threshold for ITB formation for ctr-beam heated discharges.

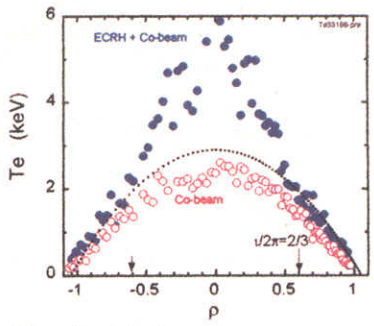

Fig. 3. (•) electron temperature profile during co-beam and ECH heatings. (o): the profile during co-beam heating. The dotted curve is T_e = 2.9 [1-(ρ/1.05)²]

is located around the $\rho \approx 0.5$ surface. Outside the footpoint, the profile is close to the parabolic profile. Unlike ctr-beam case, a clear ECH power threshold for the ITB does not seem to exist.

A natural question arises, as to why the temperature profile or ITB width differ between the co and ctr-beam heated discharges. A co-(ctr-) beam drives positive (negative) Ohkawa current of > 60 kA (sign convention of the current is that positive (negative) current increases (decreases) the rotational transform). The core ι-profile is sensitive to this current and hence influences the core transport. We find, however, that there exists strong beam effects on the core transport and the ITB formation. For example, the location of the ITB footpoint during co-beam plus ECH heating phase is around $\rho = 0.5$, being insensitive to current amplitude and direction. In the LHD Experiment, the co-beam phase with negative current is created by being preceded by a ctr-beam phase. The counter-beam is found to have unfavorable effects on ITB, i) existence of a power threshold for ITB formation, (ii) core flattening of the electron temperature profile below the threshold power, (iii) narrow ITB ($\rho < 0.2$), surrounded by a flattening region, (iv) with high ctr-beam power, core plasma tends to collapse like a sawtooth oscillation in tokamaks. On the other hand, co-beam has favorable effects (i) broader profile ($\rho < 0.5$), (ii) no power threshold, (iii) furthermore the externally imposed large island (n/m=1/2) tends to be suppressed. These observations support our working hypothesis that some kind of structural confinement loss appears in the ctr-beam heated low density discharges. We also observe that the amplitude of the magnetic fluctuations in the form of a burst is high during the ctr beam heated phase and is low during the co-beam phase. Thus the observed fluctuations may play a key role in the core transport mentioned above. Further study will be needed for deeper understanding of the observed transport.

2.4. Role of Radial Electric Field in the transport of the LHD Plasmas

The radial electric field (E_r) is required for confinement of collisionless helical plasmas. Its shear is believed to be the important parameter to suppress the plasma turbulence, which causes the anomalous heat loss

The transition from ion (negative radial electric field) root to electron (positive radial electric field) root is observed at the low density of 0.4 – 1.0 x $10^{19}m^{-3}$ in the beam heated LHD discharges. The E_r was negative at the electron density higher than 1.0 x $10^{19}m^{-3}$, while it became positive especially near the plasma edge at the low density below 1.0 x $10^{19}m^{-3}$. Fig. 4 shows the ion temperature and E_r profiles for ion root and electron root cases in the standard discharges (R_{ax}=3.75 m) [23]. In the LHD, the density profile is flat, slightly inverted for the low-density discharges. The ion temperature profile, particularly temperature gradients in the

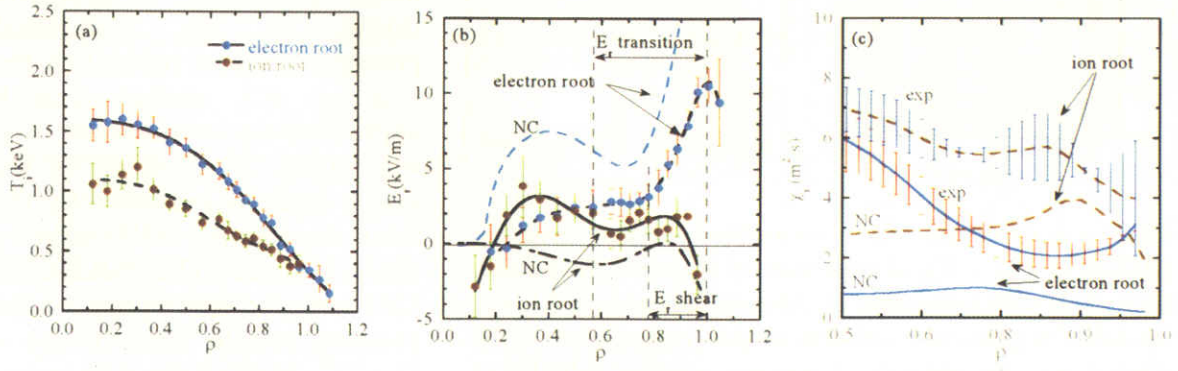

Fig. 4. Radial profiles of (a) ion temperature, (b) radial electric field, (c) ion thermal diffusivity are plotted for the electron root ($n=0.7\times10^{19}m^{-3}$)(blue circle) and ion root ($n=1.0\times10^{19}m^{-3}$) (black circles) plasmas.

edge are quite different (Fig. 4(a)). The electron temperatures are higher than ion temperatures and are nearly identical for two cases. From the profile data, the E_r can be estimated by neoclassical transport theory and the estimated values qualitatively agree with the measured values (Fig. 4(b)). The ion temperature gradient for the electron root (lower density) case is substantially higher than that of the ion root (higher density) case in the outer region ($\rho >$ 0.6)(Fig. 4 (a)) where high positive E_r (3-10 keV/m) is seen (Fig. 4(b)). Thus ion thermal diffusivity for the electron root is lower in the outer region (Fig .4(c)). High E_r in the electron root suppresses the neoclassical ion transport. Such suppression is not observed for the inward shifted configuration (R_{ax} = 3.6m), in which neoclassical transport is low and hence the anomalous transport easily dominates over the neoclassical transport.

With combined heating of NBI and ECH in the low density discharges, an ITB appears and the measured E_r is found to be positive in the entire region and its value is approximately a half of the neoclassical prediction. Even though the transition from ion to electron root in the core does not trigger the ITB formation, a positive feedback cycle is plausible, i.e., due to neoclassical effect, higher electron temperature gradient leads to higher E_r and hence higher shear of the E_r, which in turn suppresses the plasma turbulence and improve confinement, leading to higher temperature gradient [24]. The electron thermal diffusivity is observed to be reduced significantly when the ITB forms. But it is a factor of 10 higher than the neoclassical value which takes into account the measured E_r.

3. Stability of the LHD Plasmas

3.1. Stability of pressure driven MHD instabilities in the LHD

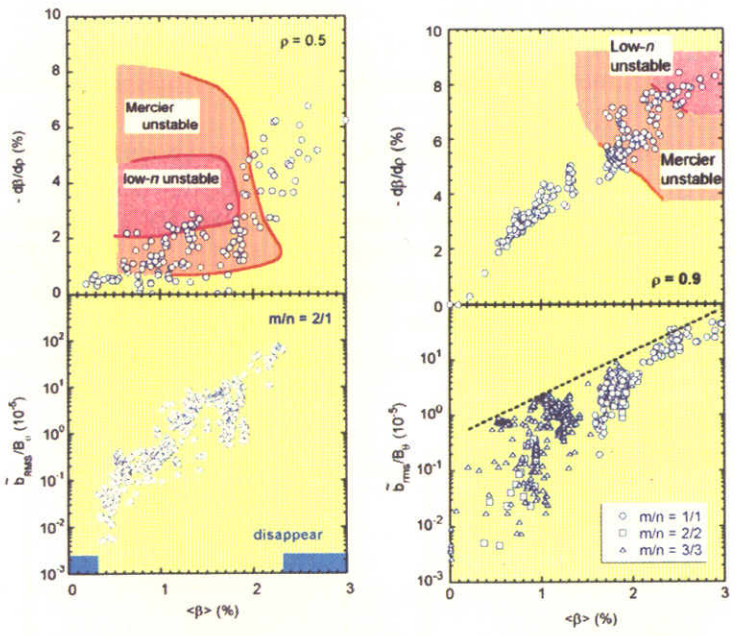

Fig. 5. (a) Evolution of the normalized pressure gradient ($d\beta/d\rho$) at ρ = 0.5 and amplitude of magnetic fluctuation (n/m=1/2) with increasing β. Mercier unstable and low n unstable regimes are illustrated for comparison. (b) Evolution of the normalized pressure gradient t($d\beta/d\rho$) at ρ = 0.9 and amplitude of magnetic fluctuation (n/m=1/1,2/2,3/3) with increasing β. Mercier unstable and low n unstable regimes are illustrated for comparison.

We have achieved averaged beta (<β>) of ~ 3 % at B = 0.5 T[25]. The <β> value was limited by the available heating power. It is achieved in the inward shifted configuration (R_{ax} ~ 3.60 m), in which the magnetic hill exists in the entire region. Fig. 5(a) shows Mercier and low n mode unstable regions and LHD data points in a parameter space ($d\beta/d\rho_{at\ \rho=0.5}$ and <β>). The mode (n/m=1/2) is primarily driven by the normalized pressure gradient ($d\beta/d\rho$) at the $\iota/2\pi$ = 0.5 surface (which approximately corresponds to ρ = 0.5)[20]. The stability of the low n mode is evaluated by the three-dimensional MHD stability analysis code TERPSICHORE [26] with the assumption of the pressure profile form, $P(\rho) = (1-\rho^M)^N$. Most of the data points below 2% of <β> are in the Mercier unstable region, but in the outside of the low n unstable region, indicating that the plasma

may naturally adjust its pressure gradient in such a way as to avoid a presumably violent low n mode. The n/m=1/2 mode appears when <β> exceeds about 0.3 % and its amplitude increases rapidly until <β> reaches 2.3 %. Beyond 2.3 % of <β>, it disappears, entering the second stability regime of the n/m=1/2 mode. Mode appearance and disappearance are consistent with the predictions of the linear ideal MHD theory.

Other critical modes reside around the $\iota/2\pi$ = 1 surface (ρ=0.9). Fig. 5(b) depicts the unstable regime in $d\beta/d\rho_{at\ \rho=0.9}$ and <β> space. When <β> is low (below 1.8 %), the mode is theoretically stable despite a hill geometry. High shear in the outer region stabilizes the mode. High beta plasma near 3 % of <β> is in a low n mode unstable regime theoretically. Magnetic fluctuations with mode numbers (n/m=1/1, 2/2, 3/3) have no threshold <β> value for their excitation and the fluctuation amplitudes are still increasing with <β> within the present operational range. The observed magnetic fluctuations do not lead to any serious MHD phenomena which degrades the global energy confinement time since the confinement time still follows the ISS95 scaling even when <β> ~ 3%. It is significant and very encouraging that the MHD stable plasma up to 3 % of <β> is maintained in the inward shifted configuration, which has good transport properties.

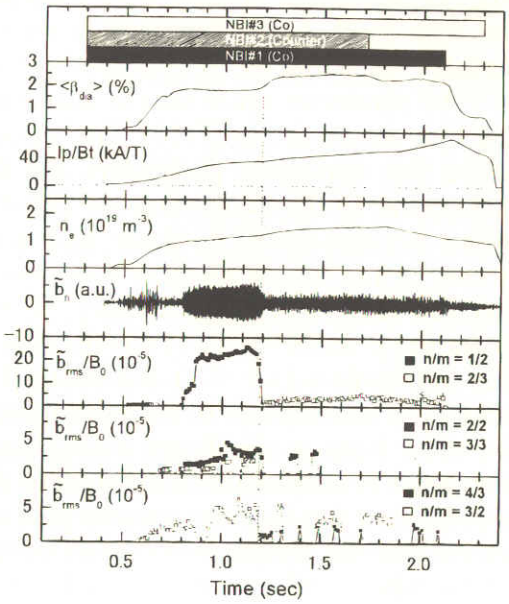

Fig. 6 With positive plasma current, MHD activities disappear at high beta.

Figure 6 shows an interesting observation that the MHD activities, monitored by the magnetic probes disappear at high beta [27]. In this discharge with R_{ax} = 3.5 m (strong hill geometry), the positive plasma current is driven by co-beam and bootstrap currents. With increasing current in time, the magnetic fluctuations suddenly disappear at t = 1.2 s ,which corresponds to the timing of the disappearance of the $\iota/2\pi$ = 1 surface from the plasma region. The fluctuation amplitude with n/m =1/2 drops to near zero, as expected. But at the same time the mode amplitude with n/m = 1/1resonant mode decreases significantly and the β-value increases from 1.9 to 2.4 %. This appears to cause an increase in the pressure gradient in the outer region and hence improvement of the global confinement. This phenomenon occurs when I_p/B > 25 kA/T. It is puzzling that higher pressure gradients, a source of the pressure driven MHD mode stabilize the MHD activities.

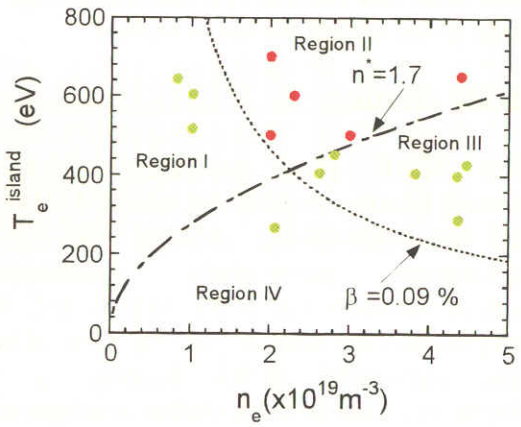

Fig. 7. Parameter space ($T_{e(island)}$, n) for island suppression for the case (w_{ex}= 0.085, B = 2.5-2.75T, R_{ax} = 3.6m). • no detectable island. • island with $w \geq w_{ex}$. Island suppression occurs in region II.

3.2 Dynamics of the externally imposed island(n/m=1/1)

In the toroidal systems, formation of an island is a major concern since it degrades the confinement and sometimes leads to a plasma disruption. We find that the width of the island (n/m=1/1) (w: island full width in terms of ρ) varies depending upon the plasmas [28-31]. In our experiment, the width of the vacuum island, i.e., that without plasma

(w_{ex}) is determined mainly from a perturbation field by the correction coils and partly from the error field. Local flattening is seen in the T_i, T_e ,E_r and n profiles around the $\iota/2\pi$ =1 surface. The width (w) is estimated by measuring that of the flattening.

The parameter space for the island suppression for a case (R_{ax} = 3.6 m, w_{ex} = 0.085, B = 2.8 T) is shown in Fig. 7 [29]. The temperature and density at the $\iota/2\pi$ = 1 surface are thought to be the important parameters for the island suppression mechanism. The points (•) correspond to the cases with no detectable island (which means that $w < 0.5\ w_{ex}$) and the points (•) correspond to those with a clear island with $w \geq w_{ex}$. Suppression of the island occurs in the higher electron temperature and lower density region (region II). Instead of electron temperature and density, it may be more appropriate to use the dimensionless quantities β and ν* [$=\nu_{ee}\ (2\pi/\iota)\ (R/v_e^{th})(Z_{eff}/\varepsilon^{3/2})$] at $\iota/2\pi$ = 1. Data obtained so far shows that the collisionless (ν* < 1) and finite β (> 0.1 %) plasma suppresses the island, hopefully leading to stabilization of the most unstable mode (n/m=1/1), which appears at high beta. On the other hand, a significant enlargement of the island ($w \geq 2w_{ex}$) occurs when the plasma parameter is located far to the right in the region III (i.e., collisional finite beta plasma). But we also find that this enlargement is avoided by making the vacuum island small ($w_{ex} < 0.04$) by the external simple perturbation coils. This is an important observation since the accuracy of the whole coil system required for fabrication and installation of the helical devices is substantially relaxed with a simple set of correction coils.

According to neoclassical tearing mode theory, positive bootstrap current modified by the island structure causes suppression of the island when $d\iota/d\rho > 0$ as in LHD. The bootstrap current flows significantly only when ν* < 1, consistent with the above experimental condition for the suppression. The main uncertainty is whether the bootstrap current flows in the positive direction at the $\iota/2\pi$ =1 surface even though we observe positive total bootstrap current. In the hill geometry, Pfirsh-Schluter current modified by the island structure tends to enlarge the island. The island enlargement occurs in the collisional plasmas in the inward shifted configurations. It is not seen in the configuration with a weaker hill geometry such as R_{ax} =3.75 m.

4. Towards Steady State Operation

Demonstration of steady-state plasma with high performance is one of the most challenging issues in developing a fusion reactor and is one of the major goals in the LHD programs. There are two key ingredients in our program of steady state operation, ICRF heating, which provides near steady state (~1h) heating power, and the divertor which handles the heat load and controls particle recycling. In this section, the research status of these areas and long pulse operation are reviewed.

4.1. ICRF Heating

The ICRF (Ion cyclotron range of frequency) heating experiment on the LHD was carried out successfully, proving that plasma characteristics particularly confinement properties between the ICRF heated and NBI heated plasmas are similar [32-34]. One of keys to the successful ICRF heating is the employment of the inward-shifted configuration with good particle orbit, i.e., R_{ax}=3.6m. High energy ions are produced by the ICRF electric field and its energy is transferred to the bulk plasma. The plasma is sustained by the ICRF heating power only. The optimum ICRF heating

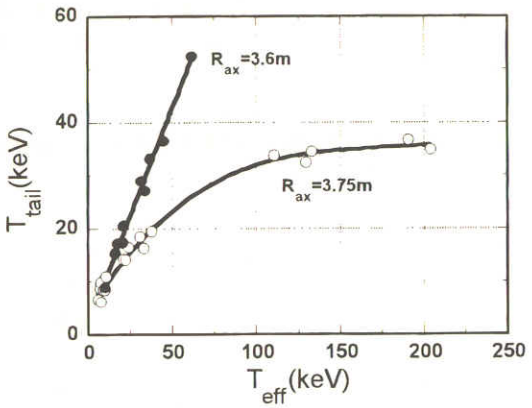

Fig.8. Relation between T_{tail} and T_{eff} at R_{ax}=3.6m and 3.75m.

is found at the normalized frequency of ω/ω_{ci0}=0.9, in terms of two physical parameters; one is the enhancement factor of the confinement time normalized by ISS95, τ_E/τ_E^{ISS95}. The other is the heating efficiency, which is defined as the ratio of the absorbed RF power to the radiated power from the loop antennas. Here the applied frequency is $f=\omega/2\pi$=38.47MHz and ω_{ci0} is the cyclotron frequency at the magnetic axis. For ω/ω_{ci0}=0.9 the cyclotron resonance is located on the saddle point of the mod-B surface. The value of τ_E/τ_E^{ISS95} was 1.5. The heating efficiency reached its maximum of 80~85% [33,35]. The maximum RF power of 2.7MW is injected to the plasma using five loop antennas and the discharge with the maximum plasma stored energy (240kJ) is obtained at the electron density of $n_e=1.4\times10^{19}m^{-3}$.

The confinement characteristics of high energy ions between the inward-shifted (R_{ax}= 3.6m) and the standard (R_{ax}=3.75m) configurations are examined. In Fig. 8, the measured tail temperature (T_{tail}) and the effective temperature (T_{eff}) are plotted where T_{eff} is the temperature calculated by Stix's formula, i.e., one without high energy particle loss. The ratio (T_{tail} / T_{eff}) is a good indication of the confinement of high energy ions, accelerated by an RF field. We proved experimentally the prediction of the orbit calculation, that the high energy ions are well confined in the inward-shifted configuration. On the other hand, the confinement in the R_{ax}=3.75m configuration is not satisfactory [36]. These experimental data give the transfer efficiency, which is defined as the ratio of the power transferred to the bulk plasma to the power absorbed by the high energy ions. These data are in good agreement with those of the Monte Carlo simulation [37,38]. These results indicate that ICRF heating of 10MW, planned in the near future is expected to be very effective in heating the plasma with the electron density higher than $4\times10^{19}m^{-3}$ for the case of 7% minority ion concentration.

4.2. Divertor

The LHD is equipped with an intrinsic built-in divertor structure [39]. Normally it is operated with an open divertor configuration. In 1999, the carbon tiles were installed as divertor plates, resulting in a significant reduction in metal impurity (Fe). Since the LHD divertor magnetic configuration has a three-dimensional structure, i.e., the divertor/ SOL structure is not a simple layer as in a tokamak. Numerical field line tracing predicts that split layers with a few cm gap strike the divertor plates at some locations. Our probe measurements clearly confirms such a structure clearly[40]. The divertor temperature ($T_{e\,div}$) and density (n_{div}) measured by probes on the divertor plates were typically 5-40 eV and 0.1 – 5.0 × $10^{18}m^{-3}$, respectively. In Fig. 9, they are shown together with the temperature and density in the vicinity of the LCFS (n_{LCFS}, $T_{e\,LCFS}$) as a function of the average density[41]. The electron densities (n_{LCFS}, n_{div}) are about a half of the average density (n) and 1/10-1/30 of n, respectively. These linear relations are insensitive to variation in input power. The electron temperatures at the LCFS and divertor ($T_{e\,LCFS}$, $T_{e\,div}$) decrease gradually with line average density (n). The ratio of $T_{e\,div}$ to $T_{e\,LCFS}$ is approximately 0.2 and almost independent of the density. We also find that the temperature ratio remains almost unchanged when the absolute value of the temperature is increased by higher power. As described above, the shape of the temperature profile is close to parabolic in the plasma-confining region and thus the Te profile stiffness approximately holds in the entire region from the center of the discharge to the divertor plates. The configuration with R_{ax} =3.6m is surrounded by a thinner ergodic layer with a thickness of ~10 cm near the X-pont. In this configuration, $T_{e\,LCFS}$ and $T_{e\,div}$ decreases gradually with n up to n = 9 × $10^{19}m^{-3}$ and at this timing, the radiative power suddenly increases and both temperatures drastically drop. There is no sign of a high recycling divertor plasma or stable detached divertor plasma, which is often observed in the tokamaks. On the other hand, a plasma somewhat similar to a detached plasma is seen near the plasma thermal collapse in the configuration of R_{ax} = 3.75 m, which has thicker ergodic layer of ~25cm near the X-point. Near the density limit, both the divertor density and temperature start to drop.

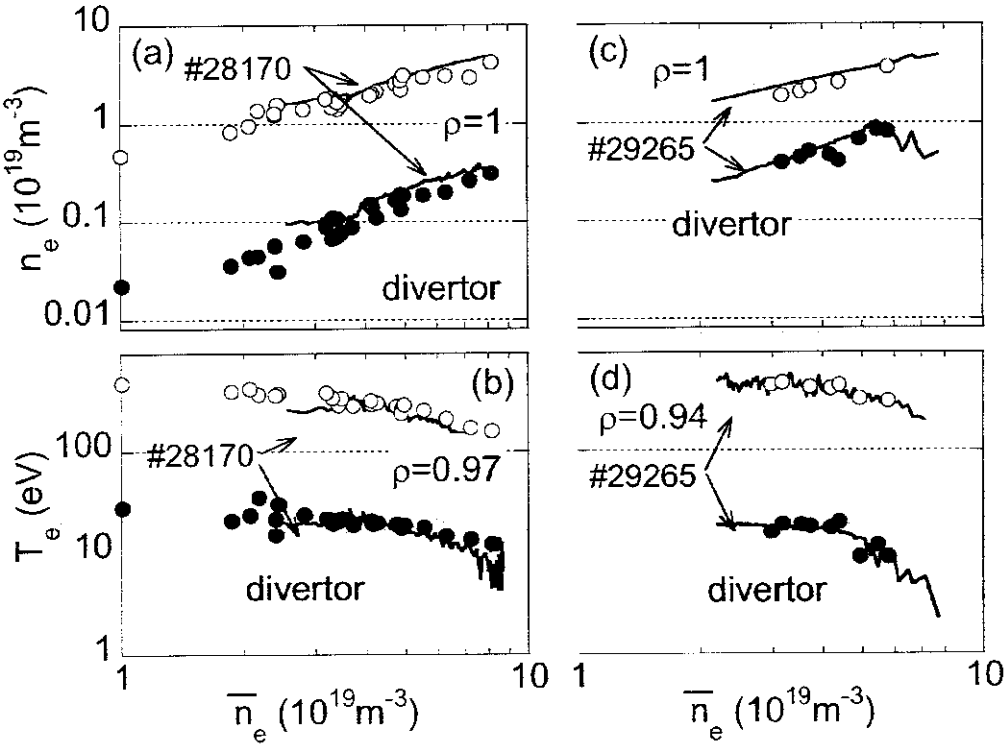

Fig.9. Electron densities (a)(c) and temperatures (b)(d) at the divertor and at LCFS are plotted as a function of the average density (n) for two types of discharges with H2 gas puffing (R_{ax}= 3.6m (narrow ergodic layer), R_{ax}=3.75 (thick ergodic layer)). Data points (• ,o) are those at the peak of the stored energy (W_p) in many discharges.

4.3 Long Pulse Discharges

Demonstration of steady-state plasma with high performance is one of the most challenging issues in developing a fusion reactor. Such an investigation is particularly appropriate for the superconducting Large Helical Device research program[42]. The NBI (0.5 MW) heated plasma is sustained up to 80 s and an ICRF (0.4 MW) heated plasma with the discharge duration of 2 minutes is achieved. In both discharges with helium gas puffing, the electron densities are maintained at around 1 x 10^{19}m^{-3} and the temperatures are more than 1 keV during the discharge. The radiation power is less than 25 % of the input power and there is no sign of impurity accumulation. As to the operational density limit in long pulse discharges, high-density plasma with 6.7 x 10^{19}m^{-3} is sustained for 10 s with an NBI power of 2 MW. The global energy confinement characteristics of long-duration plasmas are almost the same as those in short-pulse discharges. Impurity transport is also studied using long pulse discharges with constant density and ones with slow density ramping. We find that there is a certain range of density, at which the intrinsic impurity ions accumulates in the core with a long time constant of ~10 s. The radial electric field seems to be responsible for the change of the transport [43,44]. In the near future, we have a plan to operate one-hour discharges with an input power of 3 MW. High power handling will be demonstrated together with particle control and heat removal.

5. Summary

We have made significant progress in achieving the plasma parameters with high performance [W_p(stored plasma energy) = 1.2 MJ, $T_e(0)$ = 10 keV, $<\beta>$ ~ 3.2 %] during the first four years of the LHD experiment. The most important finding is that good MHD stability and favorable transport are compatible in the inward shifted configuration (R_{ax} = 3.6m). This configuration has a magnetic hill geometry and thus was predicted to be MHD unstable by ideal linear MHD stability theory. However, the plasma produced is stable at least up to $<\beta>$ = 3 %. This configuration has also good orbit properties and consequently low neoclassical transport. Furthermore the observed energy confinements is a factor of 1.5 higher than that predicted by the ISS95 scaling, which means that anomalous heat diffusivity is also low. This is attributed to a high edge temperature, which is comparable to those of H-mode tokamaks. The shape of the electron temperature profile (from plasma center to divertor) is rather insensitive to variations in density and input power. With the central deposition of ECH power, however, a very peaked temperature profile (ITB) appears, providing encouragement to confinement improvement efforts. The other important achievements and observations are (i) a long pulse discharge with a duration time of 2 minutes (80 seconds) has been achieved with 0.4 MW ICRH (0.5 MW NBI) power. (ii) The externally imposed island (n/m=1/1) has a tendency of being suppressed by collisionless finite beta plasmas. (iii) ICRF heating (minority ion heating) has been very successful and the heating efficiency is comparable to that of NBI heating. (iv) The transition from ion root to electron root is seen in the low density beam heated discharges. It is confirmed that the ion thermal diffusivity is reduced by the radial electric field. (v) The divertor is very effective in preventing impurity contamination. The divertor field line structure, unique to the heliotron type configuration, has been confirmed by measuring the divertor plasma by electrostatic probes. The obtained data from the recent LHD experiment are stimulating us to propose the next step of the experiment which aims at clarifying the properties of the currentless steady state toroidal plasmas.

Acknowledgements

The authors would like to gratefully acknowledge the continuous efforts of the engineering and technical staff at NIFS and the collaborative research with participants from domestic and foreign universities, institutes and laboratories.

References

[1] A. Iiyoshi, M. Fujiwara, O. Motojima, et al., Fusion Technol. 17 , (1990)169.
[2] A. Iiyoshi, A. Komori, A. Ejiri, et al., Nucl. Fusion, 39, (1999)1245.
[3] O. Motojima et al., Nucl. Fusion, 40 (2000) 599.
[4] O. Motojima, H. Yamada. A. Komori, et al., Phys. Plasma 6, (1999)1843
[5] M. Fujiwara, K. Kawahata, N. Ohyabu et al., Nucl. Fusion, 41, (2001)1355.
[6] N. Ohyabu, A. Fujisawa, N. Ashikawa et al., Phys. Plasmas 7, (2000)1802.
[7] K. Kawahata, N.Ohyabu O.Kaneko, et al., Plasma Phys. Control. Fusion 42, (2000)B51.
[8] A, Komori, N. Ohyabu, H. Yamada, et al., Phys. Plasmas 8, (2001)2002.
[9] H. Yamada et al., Nucl. Fusion 41, (2001) 901.
[10] O. Kaneko, A. Komori, H. Yamada, et al., Phys. Plasmas 9 (2002) 2020.
[11] S. Kubo, T. Shimozuma, H. Idei et al., Journal of Plasma and Fusion Research, 78 (2002) 99.
[12] T. Shimozuma, 12th Joint Workshop on ECE and ECRH, paper No. 056 (2002).
[13] S. Okamura et al., Nucl. Fusion, 35, 283 (1995).
[14] S. Murakami, A. Wakasa, H. Maassberg, et al., Nuclear Fusion 42 (2002) L19..
[15] O. Kaneko, Y. Takeiri, K. Tsumori, et al., Nucl. Fusion, 39, 1087 (1999).

[16] U. Stroth, M. Murakami, H. Yamada et al., Nucl. Fusion 36, 1063 (1996).
[17] H. Yamada et al.,. Plasma Phys. Control. Fusion 44 (2002) A245.
[18] N. Ohyabu, K. Narihara, H. Funaba et al., Phys. Rev. Let., 84, 103 (2000).
[19] H. Yamada, K. Y. Watanabe, S. Sakakibara, et al., Phys. Rev. Lett. 84, 1216 (2000).
[20] H. Yamada et al., Plasma Phys. Control. Fusion 43 (2001) A55
[21] F. Ryter, J. Stober, A. Stabler, et al., Nucl. Fusion 41 (2001) 537.
[22] N. Ohyabu et al., to be submitted to Phys. Rev. Lett. (2002).
[23] K. Ida, H. Funaba, S. Kado, et al., Phys Rev. Lett., 23, (2001)5297.
[24] A Fujisawa, H. Ichiguchi, T. Minami, et al., Phys. Rev. Lett. 82, (1999) 266.
[25] S.Sakakibara et al., Plasma Physics and Controlled Fusion. 44 (2002) A217.
[26] A. Cooper, Plasma Phys. Control. Fusion 34 (1992) 1011.
[27] S. Sakakibara, K.Y. Watanabe, H. Yamada et al., in the Proc. Internatinal Conf. Plasma Phys., Sydney (2002)
[28] K. Narihara et al., Phys. Rev. Lett. 87 (2001) 135002.
[29] N.Ohyabu et al., Phys. Rev. Lett. 88 (2002) 055005.
[30] K. Tanaka et al., Plasma Phys. Control. Fusion 44 (2002) A231.
[31] Ida et. al., Phys. Rev. Lett. 88 (2002) 015002.
[32] T. Watari, T. Mutoh, R. Kumazawa, et al., Nucl. Fusion 41, 325 (2001).
[33] R. Kumazawa et al., Physics of Plasmas, Vol. 8 , pp. 2139-2147 (2001).
[34] T. Mutoh et al., Phys. Rev. Let., 85, (2000) 4530.
[35] K. Saito et al., Plasma Phys. Contol. Fusion 44 (2002) 103.
[36] Kumazawa R. et al., Proc. 29th Eur. Conf. Montreux, P-5.(2002) 064,.
[37] M.Sasao, S.Murakami, M.Isobe, et.al., in Proc. 18th IAEA Fusion Energy Conf. (Sorento, 2000), IAEA-CN-77/EX9/1.
[38] S. Murakami et al., Nucl. Fusion **39** (1999) 1165.
[39] N. Ohyabu, T. Watanabe, H. Ji et al., Nucl. Fusion 34, (1994) 387.
[40] S. Masuzaki, T. Morisaki, N. Ohyabu, et al., Nucl. Fusion. 42 (2001)750.
[41] S. Masuzaki, et al., to be published in J. Nucl. Mater. (2003).
[42] N. Noda et al., Nucl. Fusion, 41, (2001) 779.
[43] Y. Nakamura et al., IAEA-CN-94/EX/C5-1, this conference.
[44] Y. Nakamura et al., Plasma Phys. and Control. Fusion. 44 (2002) 2121.

Increased Understanding of Neoclassical Internal Transport Barrier on CHS

T.Minami, A.Fujisawa, H.Iguchi, Y.Liang, K.Ida, S.Nishimura, M.Yokoyama, S.Murakami, Y.Yoshimura, M.Isobe, C.Suzuki, I.Nomura, K.Toi, M.Yoshinuma, A.Shimizu, C.Takahashi, K.Matsuoka, S.Okamura, CHS group

National Institute for Fusion Science, 322-6 Oroshi, Toki, 509-5292, Japan
E-mail: minami@nifs.ac.jp

Abstract.

We report the recent progress of the study on neoclassical internal transport barrier (N-ITB) on Compact Helical System experiment. N-ITB has been observed for EC heated NBI plasma. The improved confinement region for electrons is expanded compared to that of the previous N-ITB plasma heated by only ECH. Moreover, the ion temperature is found to be increased simultaneously by about two to three times ($T_i(0)$~400-500eV) with steep gradient region at ρ~0.6. From the measurement of the averaged peak energy intensity using the soft X-ray CCD camera it is confirmed that the impurity confinement is also improved with N-ITB. The radial electric field is observed to bifurcate into electron root (E_r~15kV/m) and rather large electric field shear (dE_r/dr~-300kV/m^2) is produced in the layer between ion and electron root.

1. Introduction

The internal transport barrier of the helical devices plays an important role on plasma confinement like tokamaks. The barrier of the helical device is formed due to the positive electric field and the electric field shear. The radial electric field is determined by the ambipolar diffusion of neoclassical particle fluxes, so that this internal transport barrier is called neoclassical internal transport barrier (N-ITB).

In the previous N-ITB experiment on Compact Helical System (CHS) with the electron cyclotron heating plasma (ECH), the electron temperature increased up to ~3keV in the plasma core and the large temperature gradient (dT_e/dr~43 keV/m) was observed at the barrier point (ρ~0.3). This plasma is characterized by the large electric field (E_r~7kV/m) and the electric field shear (dE_r/dr~-300 kV/m^2). The drop of the electron thermal diffusivity to the level of the neoclassical transport (χ_e~2-6 m^2/s) and the reduction of the density fluctuation (the reduction of the fluctuation power is 48%) were observed at the barrier location [1,2].

Recently N-ITB was also observed for EC heated NBI plasma [3]. The ion temperature increased as well as the electron temperature. In this paper, experimental observations of the new N-ITB plasma are reported and the transport properties are discussed.

2. Experimental Setup

CHS is a medium size heliotron/torsatron device with a poloidal mode number l=2 and a toroidal mode number m=8. The plasma major radius and averaged minor radii are 1.0 and 0.2m, respectively. The profiles of the electron and ion temperature are measured by the YAG Thomson scattering system and charge exchange spectroscopy (CXS). The YAG Thomson system has 24 spatial channels, spatial resolution is about 1-2 cm ,and repetition time of the measurement is 5-10 ms [4]. For low density plasma, we accumulate signals of several shots to obtain good S/N ratio (typical case 5-10). The CXS measurement using fully stripped carbon has 30 spatial points and the resolution is about 1 cm [5]. The charge exchange signal is accumulated for 20 ms and, for low density plasma, signal for 5-10 shots are summed up. Electron density profile and line averaged density are measured with the YAG Thomson system and the microwave interferometer. The radial electric field is measured by Heavy Ion Beam Probe (HIBP) of which the sample volume is a few cm. To investigate the impurity

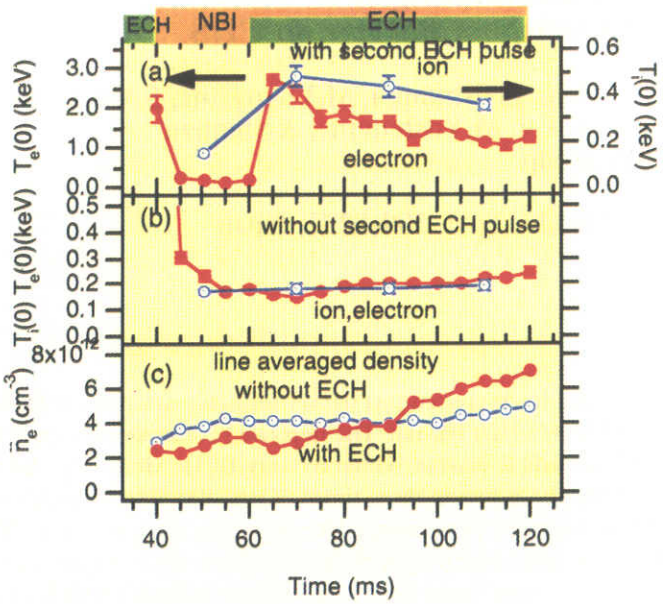

Figure 1. Time evolution of the typical EC heated NBI discharge with N-ITB (a) electron (red) and ion temperature (blue) with N-ITB (b) without second pulse of ECH (c) line averaged densities for two cases.

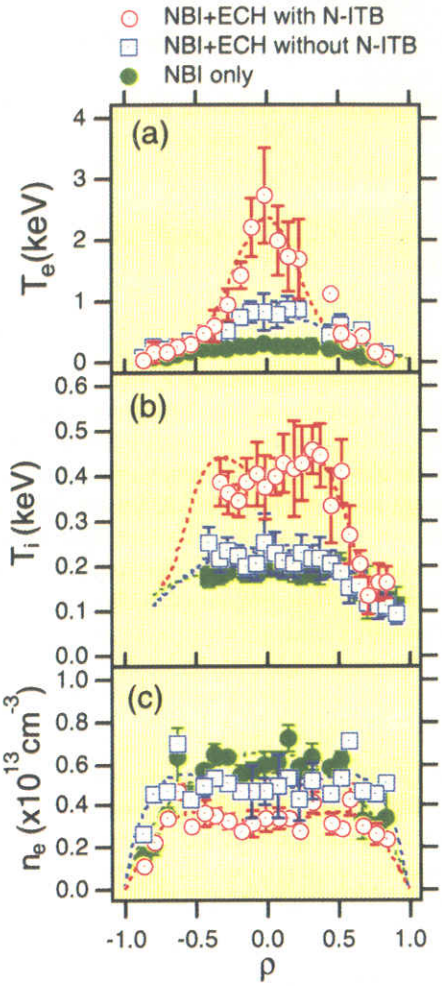

Figure 2. Radial profiles of the EC heated NBI plasma with N-ITB. (a) electron temperature (Te). (b) ion temperature (Ti.) (c) electron density (ne). The red circles denote with N-ITB. The blue squares denote without N-ITB. The green triangles denote without ECH.

transport the photon counting two-dimensional x-ray CCD camera [1024x512 pixels] is used [6].

3. Simultaneous Increase of Electron and Ion Temperature in N-ITB Discharge

Figure 1 shows the typical time evolution of the central electron and ion temperature and the line averaged density for the N-ITB discharge (and NBI discharge without second pulse ECH as a reference). The target plasma is produced by the first pulse of 53.2GHz 2nd harmonic ECH (P_{inj}~130-150kW, 20-40 ms), then heated and sustained by the NBI (P_{inj}~ 0.7MW). The NBI is tangentially injected into the plasma. The magnetic field is 0.88T and the magnetic axis of the plasma is 92.1 cm. When the second pulse of ECH is superposed to the NBI plasma (60-120 ms), with the condition that density is below the critical value, the electron temperature increases up to ~3 keV with a sharp temperature gradient (Fig. 1 (a)). As the electron density gradually increases (Fig. 1 (c), red curve), the central electron temperature decreases to ~1 keV, which is one-third of that with N-ITB ,and the sharp temperature gradient disappears. These characteristics are generally similar to the results of the previous N-ITB ECH experiment without NBI. However, the significant difference is in the electron temperature profile: the improved confinement region is expanded in the present experiment and the temperature profile has "bell" shape rather than "dome" shape which was observed in the previous experiment.

Figure 2 (a) shows the electron temperature profile of N-ITB plasma. It also shows profiles of EC heated NBI plasma without N-ITB (density is above threshold) and NBI plasma without ECH. For N-ITB plasma, the foot point of the enhanced region of the electron temperature is

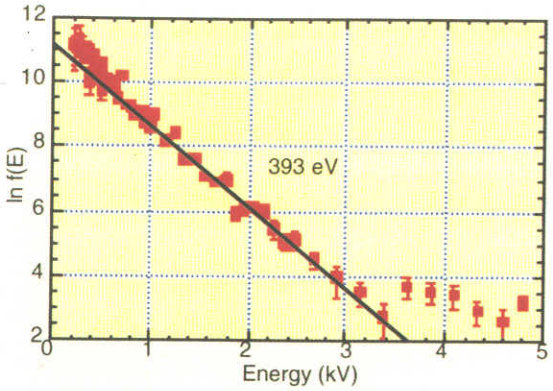

Figure 3. NPA spectrum in the EC heated NBI plasma with N-ITB. The fitting line show that the ion temperature is ~400 eV.

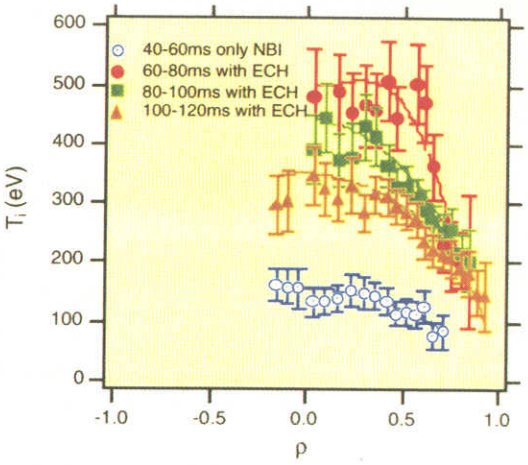

Figure 4. Time evolution of the ion temperature profile in the EC heated NBI plasma with N-ITB. The open circles and squares denote NBI phase in 40-60ms, and 100-120ms. The closed circles and squares denote ECH+NBI phase in 60-80, and 80-100 ms.

located at the outer location (ρ_f =0.4-0.5) compared to the previous ECH N-ITB experiment (ρ_f =0.3-0.4) [1,2,3]. The ion temperature simultaneously increases ($T_i(0)$~400-500 eV) by two to three times compared to the plasma without N-ITB. It is clearly different from the ion temperature (150-200 eV) of the NBI plasma without N-ITB. The sharp ion temperature gradient is also produced (8-12 keV/m) at the location ρ_g~0.4-0.7. The foot point for ion appears at outer position (ρ_f~0.7) than that for electrons. The neutral particle analyzer (NPA) is also used for ion temperature measurement. Figure 3 shows the spectrum of the NPA for the EC heated NBI plasma with N-ITB. The ion temperature is about 400 eV, which is in a good agreement with the result of CXS measurement.

Figure 1 (a) shows that the ion temperature slowly goes down as the density increase. Figure 4 shows the temporal evolution of the ion temperature profile. With second pulse of ECH, the ion temperature gradient grows up and the sharp shoulder of the temperature profile is produced. When the averaged density exceeds the threshold for N-ITB at 80 ms, the ion temperature gradient quickly decreases and the shoulder disappears. However decrease in the central ion temperature is relatively slow. After ECH is turned off, the ion temperature still remains around 400eV in spite of the density increase to 4-5x10^{12}cm^{-3}, which is above the threshold. In this period, the density profile is almost flat, thus the mechanism for the high ion temperature is not the same as the high T_i mode [7], because the High T_i mode is caused by the density peaking.

4. Critical Density for N-ITB Formation

The N-ITB formation strongly depends on the plasma density. Figure 5 (a) (b) shows the dependence of the central electron temperature and the temperature gradient at the N-ITB on the averaged density. When the averaged electron density is below the threshold density (n_e ~4x10^{12}cm^{-3}), the central electron temperature considerably increases. The electron temperature gradient also increases to 20-30 keV/m). The threshold density and other characteristics are very close to the ECH plasma N-ITB experiments [8].

The dependence of the ion temperature on the density is the same as the electron temperature. As shown in Figure 5 (c), the central ion temperature rapidly increases by the application of ECH when the density is lower than 4x10^{12}cm^{-3}. On the other hand, when the averaged density is above the threshold, the ion temperature of the EC heated NBI plasma is almost the

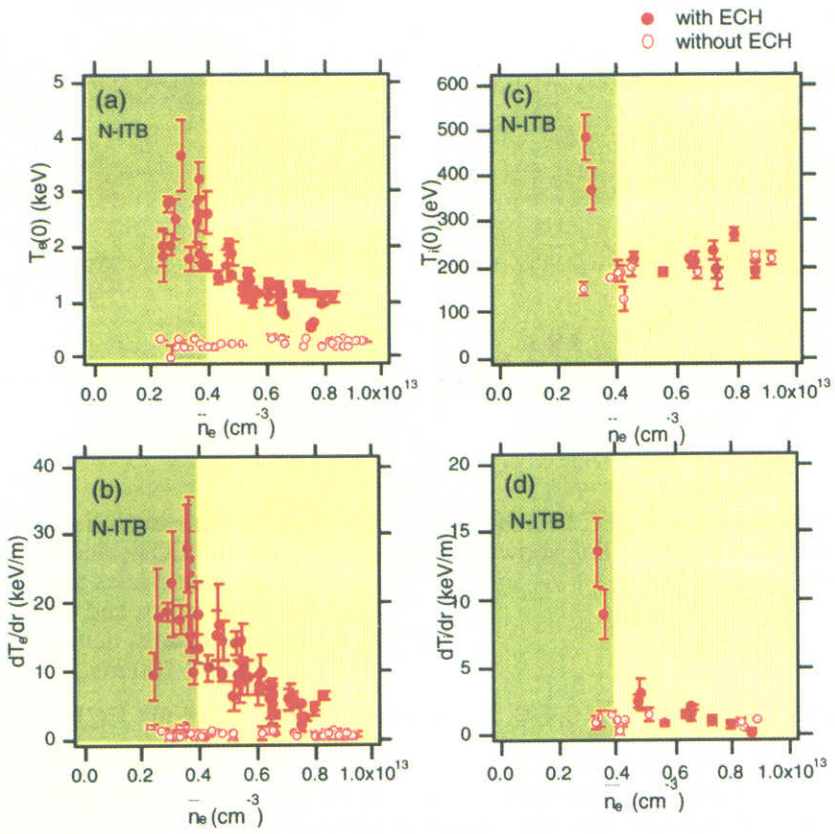

Figure 5. Central electron (a) and ion (c) temperature and electron temperature gradient (b) and ion temperature gradient (d) as a function of line averaged density. The close circles denote the plasam with ECH. The open circles denote the plasma without ECH.

same as the NBI plasma without ECH. The ion temperature gradient increases from 2-3 keV/m up to 8-12 keV/m in the case of N-ITB, while the gradient is comparable to that of the NBI plasma without ECH when the density is above the threshold.

5. Impurity Transport for N-ITB Plasma

It is important to study the particle transport in N-ITB plasma. As a part of such a study, the titanium impurity transport was measured with the soft X-ray CCD camera for the plasma with N-ITB. The CCD camera has an 900μm-thick Be filter and a pinhole of 0.3 mm-diameter. The energy resolution is 3.22±0.04 eV/electron (16.5±0.2eV/ADC count). Because the frame rate is slow (0.2Hz), all emission from the discharge in CHS (100-150 ms) is accumulated. The ionization level of the impurity ions are determined by the balance between the particle confinement and ionization. The energy level of T_i Kα lines depends on the charge state. Because the energy resolution of the soft X-ray camera is not enough to distinguish individual Kα lines for different charge states, we tried to measure the change of the charge states distribution from the shift of averaged energy of the Ti Kα lines.

Figure 6 (a) shows the energy spectra measured with X-ray CCD camera in EC heated NBI plasma experiments. For the plasma with N-ITB, the peak energy of the intensity of Ti Kα line at ρ=0.03 is 4.72-4.73 keV which is dominated by He-like ions. For the plasma without N-ITB, the peak energy is shifted to 4.68-4.69kV which is dominated by Be-like ions [6]. The averaged peak energy depends on the electron temperature and the diffusivity of the impurity. To evaluate the diffusion coefficients of impurity in the plasma, the numerical impurity code MIST and LINES are used.

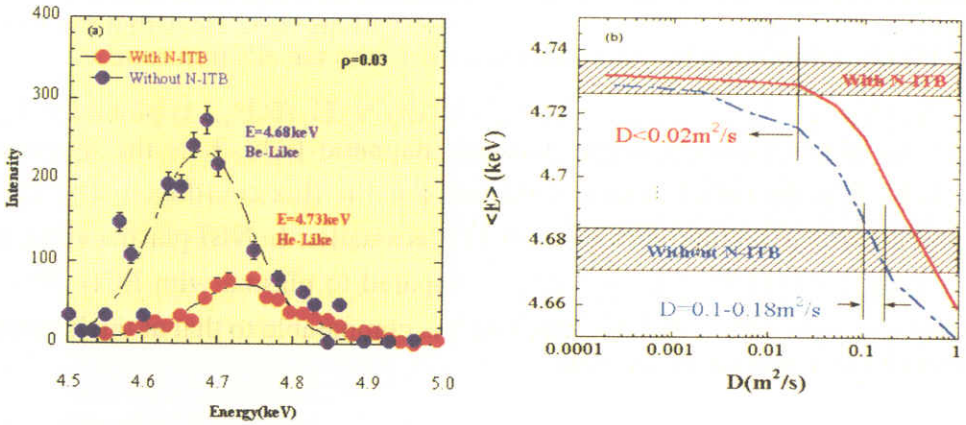

Figure 6. (a) Energy spectrum for the plasmas with and without N-ITB. (b) The calculated averaged energy of the Ti spectrums as a function of the diffusion coefficients for the plasma with N-ITB (solid line) and without N-ITB (dashed line).

The impurity flux is expressed as $\Gamma = -D(\partial n_z / \partial r) - n_z V$, where D and V are coefficients for the diffusive and convective term, respectively. Because the electron density profile is almost flat during ECH as shown in Figure 2 (c), we assume that convective velocity can be neglected (V=0). The results of the calculation are shown in Figure 6 (b). The average energy of the titanium K_α lines is plotted as a function of the impurity diffusion coefficients $D_{in.}$. The solid line denotes the dependence for the plasma with N-ITB, and the dashed line denotes that for the plasma without N-ITB. The core diffusion coefficient is reduced to <0.02 m^2/s in the plasma with N-ITB, while it is 0.1-0.18 m^2/s in the plasma without N-ITB. In the N-ITB discharge, because the transport time scale is comparable to the atomic process time (the ionization and the recombination), the averaged Ti Kα line energy is sufficiently sensitive to the impurity diffusion.

6. Radial Electric Field in EC Heated NBI Plasma with N-ITB

It is also confirmed with the HIBP measurement that this transport barrier is accompanied with the large positive radial electric field (E_r~15kV/m), as shown in Figure 7(a). On the other hand, the plasma without N-ITB has smaller E_r (Er<5kV/m) and the NBI plasma without ECH has negative E_r. Figure 7 (a) also shows profiles of the neoclassical estimation of radial

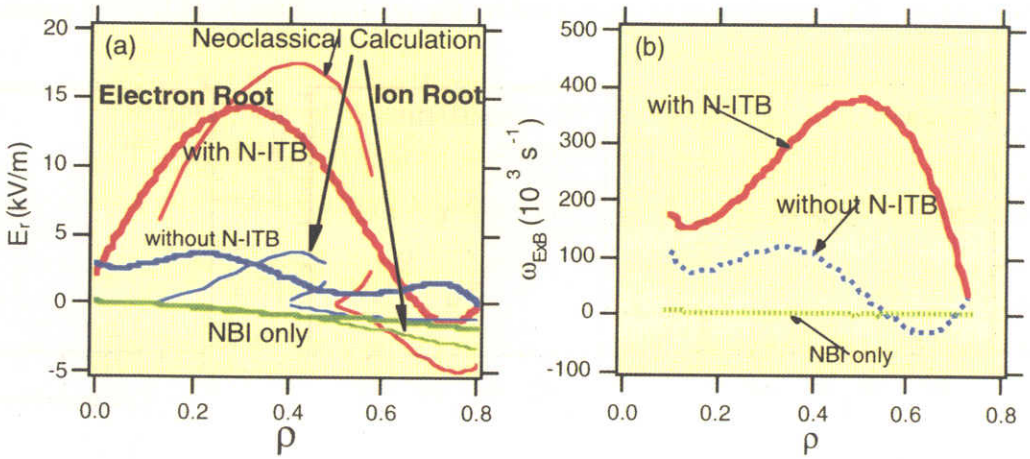

Figure 7. (a) Profiles of the radial electric field and (b) ExB shearing rate. The thick and the thin lines denote the experimental and the neoclassical estimation. The red and the blue lines denote the plasma with N-ITB and without N-ITB, respectively. The green line denotes the NBI plasma without ECH.

electric field that is derived from the ambipolar condition for those three cases. These theoretical curves qualitatively support the experimental observations. It is clear that the radial electric field of N-ITB is induced by the transition from the ion to the electron root.

The ExB shearing rate [9] ($\omega_{EXB} = RB_\theta{}^2/B(\partial/\partial y)E_r/RB_\theta$) is plotted in Figure 7 (b). Here, R is the major radius, B_θ is the poloidal magnetic field, B is the magnitude of the magnetic field, E_r is the radial electric field and ψ is the flux coordinate. The ExB shearing rate (ω_{ExB}~$1x10^5 s^{-1}$) in the plasma without N-ITB is smaller. In NBI plasma without ECH, the sharing rate (ω_{ExB}~$-0.4x10^3 s^{-1}$) is negligible compared to plasma with ECH. The maximum shearing rate (ω_{ExB}~$4x\ 10^5 s^{-1}$, dEr/dr~300kV/m^2) is comparable to that at the internal transport barrier observed in Tokamak experiment.

7. Estimation of Thermal Diffusivity for N-ITB Plasma and Discussions

In the previous N-ITB experiment with ECH, the improvement of the ion thermal transport was not identified. This is because the transferred energy to ions from electrons is small for low collision frequency in the high electron temperature. In EC heated NBI plasma, on the other hand, the more electron temperature increase, the larger contribution to the ion heating is given from NBI. We estimate NBI power deposition with MCNBI code, which is based on the Monte Carlo simulation [10]. According to the MCNBI code calculation, the fraction for the ion heating of the deposited NBI power is greater than ~50%, when the electron temperature is higher than ~1keV on CHS, as shown in Figure 8 (c). In this calculation, the acceleration voltage is 36kV, the beam current is ~40A, the port through NBI power is ~700kW, and the density is $3.5x10^{12}cm^{-3}$.

There is a problem whether the increase in the electron and ion temperature is due to the improvement of the confinement or due to the increase in the deposition power of NBI. To make sure of this, the calculation of the power deposition is carried out with MCNBI code for the N-ITB plasma (Fig. 8 (a)) and the plasma without N-ITB (Fig. 8 (b)). Total deposited power is 37 kW for Fig.8 (a) and 60kW for Fig.8 (b). The calculation uses the real geometry and orbit averaging is made. But the finite orbit effect during slowing down processes is not calculated and electric field is not included.

First, we consider difference of power deposition to electrons in the plasmas with N-ITB and without N-ITB. ECH power deposition rate is estimated larger than 90% for both cases (see below). The total deposited NBI power to electrons in the plasma with N-ITB is about 55% compared to the plasma without N-ITB. Consequently, electron heating power is smaller for N-ITB plasma and the large increase of the central temperature is not explained by the change of heating power. This conclusion is supported by the results of the N-ITB ECH experiments

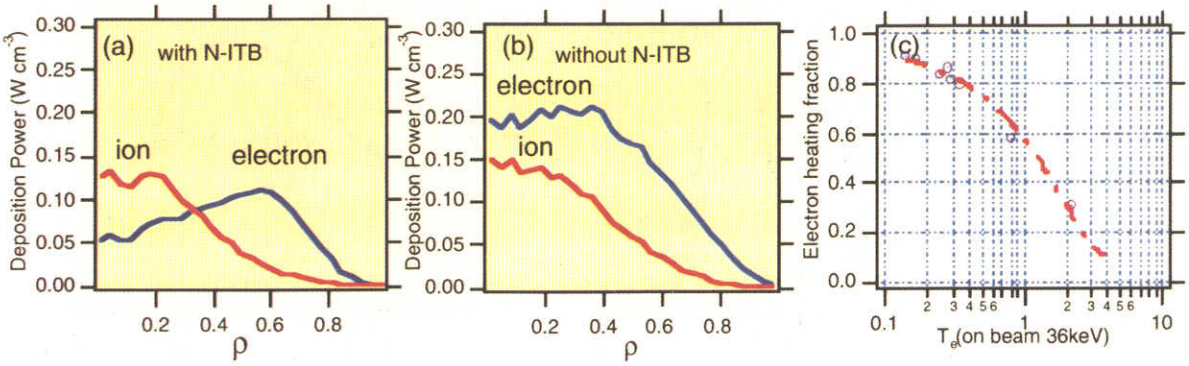

Figure 8. NBI power deposition profile to electrons and ions for the plasma with N-ITB (a) and without N-ITB (b).
(c) Electron heating fraction of NBI deposition as a function of the electron temperature.

which provide the similar results [1] . Secondly, for the power deposition to ions, Fig. 8 (a) and (b) give almost the same level heating power. Although the density of N-ITB plasma is slightly lower for N- ITB plasma, large increase of ion temperature (two to three times higher) is not explained by the difference of heating power.

In order to analyze confinement properties N-ITB plasma. We calculated thermal diffusivity using plasma profile data in Fig. 3 and power deposition profile in Fig. 8.

The transport analysis is carried out to clarify the characteristic of the N-ITB. In the steady state, the heat conductions $Q_{cond}^{electron}$, Q_{cond}^{ion} are expressed as follows.

$$Q_{cond}^{electron} = \frac{3}{2}\nabla(T_e\Gamma_e) - 3\frac{m_e}{m_p}\frac{n_e}{\tau_e}[Z](T_e - T_i) + Q_{ech} + Q_{NBI}^{electron} \quad (1)$$

$$Q_{cond}^{ion} = \frac{3}{2}\nabla(T_i\Gamma_i) - 3\frac{m_e}{m_p}\frac{n_e}{\tau_e}[Z](T_i - T_e) + Q_{NBI}^{ion} \quad (2)$$

Here Γ_e and Γ_i are the radial particle fluxes of the electron and ion ,respectively. m_p,m_e indicate electron and ion mass, respectively, τ_e is electron collision time. These values are estimated using the Proctr-MOD code [11]. Q_{ech} is for ECH. ECH absorbed power is derived by the formula using I. Fidone and G. Granata [12]. In the plasma with low density and high electron temperature plasma, all injected power (P_{inj}~ 130kW) reaches the resonance zone and over 90% power is absorbed when the electron temperature is above 1 keV. The χ_e and χ_i is defined as $\chi_e = Q_{cond}^{electron} / n_e\Delta T_e, \chi_i = Q_{cond}^{ion} / n_e\Delta T_i$.

Figure 9 shows electron ion diffusivity for two plasma discharges with N-ITB (in red) and without N-ITB (in blue). Error bar for the experimental diffusivity reflect error bars in the profile measurement. Figure 9 also shows neoclassical transport coefficients evaluated with the analytical formulae derived by Kovrizhnykh [13,14] . Due to the nonlinear dependence of the neoclassical particle fluxes on the radial electric fields (E_r), the E_r and the fluxes are determined by the ambipolar condition($\Gamma_e(E_r)$=$\Gamma_i(E_r)$) calculated from T_e,T_i and n_e.

For the electron thermal diffusivity, the N-ITB plasma gives reduced χ_e at ρ~0.3 compared to plasma with N-ITB. It is main reason for the electron temperature increase of core region. For ion diffusivity ,the present transport analysis shows the χ_i reduction at ρ~0.6 for N-ITB plasma which is the direct reflection of the steep ion temperature gradient at that position. Although further study is necessary to make final conclusion and more complete understanding,

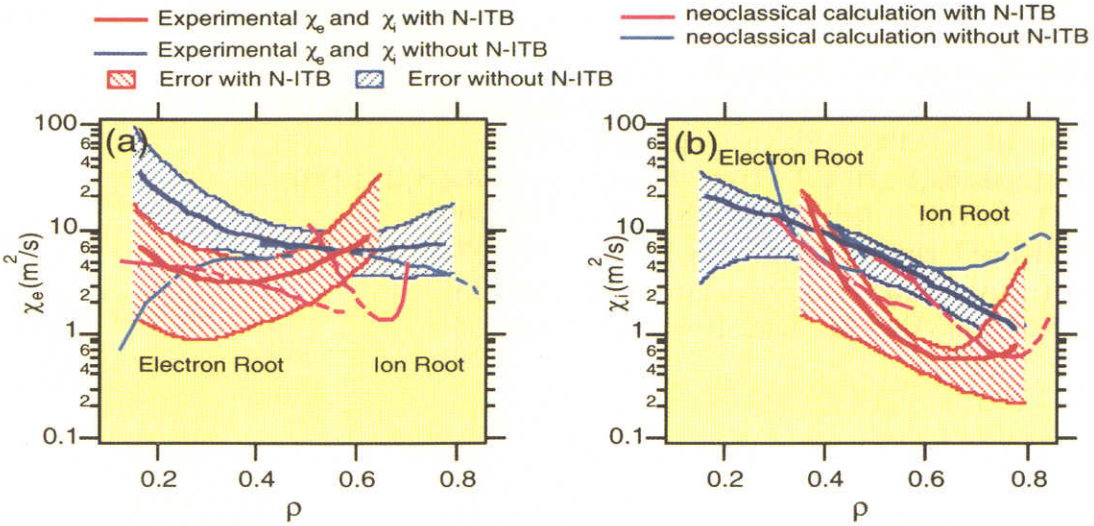

Figure 9. Comparison between experimental thermal diffusivity with N-ITB and without N-ITB for the electrons (a) and teh ions (b). The dashed lines denote the neoclassical estimation.

this results suggest the formation of the ion thermal transport barrier in the new N-ITB plasma.

8. Summary

(1) New N-ITB regimes are found with the improved confinement for both ions and electrons in EC heated NBI plasmas.

(2) The improved confinement region is expanded for electrons from ρ_t~0.3 to ρ_t~0.4 compared to previous N-ITB experiments.

(3) With N-ITB formation, the ion temperature increases by about two to three times. The ion temperature gradient also increases at ρ~0.6. The present transport analysis suggests the formation of ion thermal transport barrier.

(4) The decrease of the ion temperature is much slower than that of the electron temperature after the electron transport barrier disappears.

(5) The large E_r and E_r shear are observed.

(6) The impurity transport is decreased inside the barrier.

(7) Further investigation should be made to understand (a) whether the mechanism of the confinement improvement for electrons and ions are different or the same, (b) the difference of foot point locations for electrons and ions, (c) the relation between confinement improvement and the electric field structure.

Acknowledgement

We thank Prof. K. Itoh for useful discussions and director general M. Fujiwarafor his continuous support.

References

[1] Minami, T., et. al.,Plasma Phys. Control. Fusion **44** (2002) 197
[2] Fujisawa, A.,.et.al. Phys.Rev.Lett **82** (1999) 2669
[3] Minami, T., et. al., J.Plasma Fusion Res. SERIES, **4** (2001) 451
[4] Narihara, K., et.al., Rev.Sci.Instrum. **66** (9) (1995)
[5] Ida, K., et.al. Rev. Sci. Instrum. **60** (1989) 867
[6] Liang, Y., et.al. Phys. of Plasmas **9** (10) (2002) 4179
[7] Ida, K., et.al. Nucl. Fusion **39** (1999) 1649
[8] Minami, T., et. al., (proc. 26th EPS Conference Maastricht 1999) P3.109 p1357
[9] Burrell, K.H.Phys., Plasmas **4** (5) (1997) 1499
[10] Murakami,S., et.al.,J. Plasma Fusion Res. SERIES, **2** (1999) 255.
[11] Howe, H, C.,. Rep. ORNL/TM-11521, TN(1990)
[12] Fidone,I. and Granata,G., Nucl. Fusion **11** (1971) 133
[13] Yokoyama,M., et.al., Nucl.Fusion **42** (2002) 133
[14] Kovrizhnykh,L.M., Nucl. Fusion **24** (1984) 435

Response of Temperature and Density Profiles to Heat Deposition Profile and Its Impact on Global Scaling in LHD

H.Yamada 1), S.Murakami 1), K.Yamazaki 1), O.Kaneko 1), J.Miyazawa 1), R.Sakamoto 1), K.Y.Watanabe 1), K.Narihara 1), K.Tanaka 1), S.Sakakibara 1), M.Osakabe 1), B.J.Peterson 1), S.Morita 1), K.Ida 1), S.Inagaki 1), S.Masuzaki 1), T.Morisaki 1), G.Rewoldt 2), H.Sugama 1), N.Nakajima 1), W.A.Cooper 3), T.Akiyama 4), N.Ashikawa 1), M.Emoto 1), H.Funaba 1), P.Goncharov 5), M.Goto 1), H.Idei 1), K.Ikeda 1), M.Isobe 1), K.Kawahata 1), H.Kawazome 6), K.Khlopenkov 1), T.Kobuchi 1), A.Komori 1), A.Kostrioukov 1), S.Kubo 1), R.Kumazawa 1), Y.Liang 1), T.Minami 1), S.Muto 1), T.Mutoh 1), Y.Nagayama 1), Y.Nakamura 1), H.Nakanishi 1), Y.Narushima 1), K.Nishimura 1), N.Noda 1), T.Notake 7), H.Nozato 8), S.Ohdachi 1), N.Ohyabu 1), Y.Oka 1), T.Ozaki 1), A.Sagara 1), T.Saida 5), K.Saito 1), M.Sasao 1), K.Sato 1), M.Sato 1), T.Seki 1), T.Shimozuma 1), M.Shoji 1), H.Suzuki 1), Y.Takeiri 1), N.Takeuchi 7), N.Tamura 1), K.Toi 1), T.Tokuzawa 1), Y.Torii 7), K.Tsumori 1), T.Watanabe 1), T.Watari 1), Y.Xu 1), I.Yamada 1), S.Yamamoto 7), T.Yamamoto 7), M.Yokoyama 1), Y.Yoshimura 1), M.Yoshinuma 1), T.Mito 1), K.Itoh 1), K.Ohkubo 1), I.Ohtake 1), T.Satow 1), S.Sudo 1), T.Uda 1), K.Matsuoka 1), O.Motojima 1)

1) National Institute for Fusion Science, Toki, Gifu 509-5292, Japan
2) Princeton Plasma Physics Laboratory, Princeton, NJ 08544, USA
3) Centre de Recherches en Physique des Plasmas, Ecole Polytechnique Federale de Lausanne, PPB 1015, Lausanne, Switzerland
4) Research Laboratory for Nuclear Reactors, Tokyo Institute of Technology, Tokyo 152-8550, Japan
5) Department of Fusion Science, School of Mathematical and Physical Science, Graduate University for Advanced Studies, Hayama 240-0193, Japan
6) Graduate School of Energy Science, Kyoto University, Uji 611-0011, Japan
7) Department of Energy Engineering and Science, Nagoya University, Nagoya 464-8603, Japan
8) Graduate School of Frontier Sciences, The University of Tokyo, Tokyo 113-0033, Japan

e-mail contact of main author: hyamada@lhd.nifs.ac.jp

Abstract. Energy confinement and heat transport of net current-free NBI-heated plasmas in the Large Helical Device (LHD) are discussed with an emphasis on density dependence. Although the apparent density dependence of the energy confinement time has been demonstrated in a wide parameter range in LHD, the loss of this dependence has been observed in the high density regime under the specific condition. Broad heat deposition due to off-axis alignment and shallow penetration of neutral beams degrades the global energy confinement while the local heat transport maintains a clear temperature dependence lying between Bohm and gyro-Bohm characteristics. The central heat deposition inclines towards an intrinsic density dependence like $\tau_E \propto (\bar{n}_e / P)^{0.6}$ from the saturated state. The broadening of the temperature profile due to the broad heat deposition profile contrasts with the invariant property which has observed widely as profile consistency and stiffness in tokamak experiments.

1. Introduction

Studies on the energy confinement and heat transport of net current free plasmas have progressed due to the recent experiments in Large Helical Device (LHD) [1] with upgraded heating capability up to 9 MW of NBI. The NBI lines are arranged in the tangential direction and the energy of the NBI ranges between 120-150 keV in this study. The apparent density dependence of the energy confinement time as described in the ISS95 scaling [2] has been demonstrated [3,4] in the extended wide parameter regimes in LHD. This favorable density dependence observed in LHD is of importance from the prospect of net current-free plasmas

towards high confinement and high β by high density operation. When the plasma profiles are fixed, the density dependence of the energy confinement time, i.e., $\tau_E \propto (\bar{n}_e / P)^{0.6}$ or $\tau_E \propto (\bar{n}_e / P)^{0.5}$ can be interpreted by the gyro-Bohm local heat conduction as $\chi \propto T^{3/2}$ or the Bohm as $\chi \propto T$, respectively. Since the density dependence of the global confinement and the temperature dependence of the local heat transport are two sides of the same physical mechanism, it is also attracting interest to the physics issue of anomalous transport.

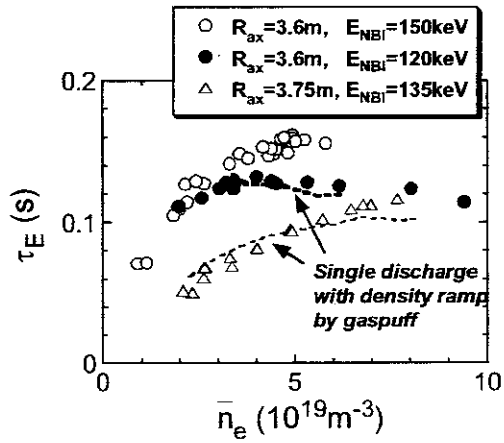

Fig.1 Dependence of energy confinement time on density. Closed circles: R_{ax}=3.6m, P_{NBI}=4.7MW. E_{NBI}=120keV. Open circles: R_{ax}=3.6m. P_{NBI}=4.3MW. E_{NBI}=150keV. Open triangles: R_{ax}=3.75m. P_{NBI}=4.1MW. E_{NBI}=135keV. Dotted lines:traces of the single discharges with density ramp-up.

Although the existence of this kind of density dependence has been verified in many toroidal experiments, its absence also has been reported [5]. Recent experiments employing a wide range of heating power in LHD have indicated that the favorable density dependence saturates at a certain density under specific conditions. This paper discusses the cause of this saturation and the related characteristics of anomalous transport. Through this study, the response of the temperature profile to the heat deposition profile is highlighted, which contrasts with the concept of stiffness or profile consistency observed in many tokamaks.

2. Experimental Results

Confinement improvement by shifting the magnetic axis inward already has been demonstrated in LHD [3]. Saturation of the energy confinement time with the increase in density has been observed in gas-fueled NBI-heated plasmas, particularly, in this inward shifted configuration with R_{ax}=3.6 m. Closed circles in Fig.1 shows the data in the density flat phase for a series of density scans with a fixed heating power of 4.7MW and the averaged beam energy E_{NBI} of 120 keV in the case with R_{ax}=3.6m and B = 2.8 T. The energy confinement time ceases to increase above 4×10^{19}m^{-3}. This density regime is one third of the empirical density limit [6]. Indeed this saturated state can be maintained in a quasi-steady state and extended close to 1×10^{20}m^{-3} by this heating power. The increase of the beam energy mitigates this saturation. The density scan with E_{NBI} of 150 keV raises this performance density

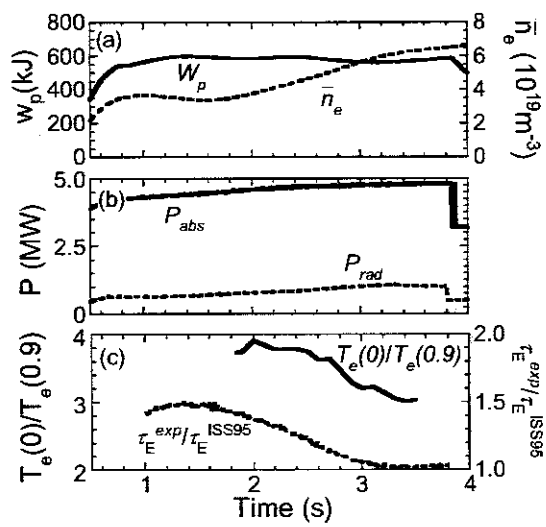

Fig.2 Waveforms of the discharge with density ramp-up in the case with R_{ax}=3.6m. P_{NBI}=4.7MW. E_{NBI}=120keV. (a) Stored energy and line averaged density. (b) Absorbed power of NBI and total radiation power. (c) Ratio of the central electron temperature to that at ρ=0.9 and improvement factor of energy confinement time on ISS95.

limit to 5×10^{19}m^{-3}(see open circles in Fig.1). Although the heating power in the scan with E_{NBI} of 150 keV is 10 % less than that with E_{NBI} of 120 keV, the deterioration of confinement in the case with E_{NBI} of 120 keV can not be attributed to simple power degradation. The other case with R_{ax}=3.75m and B = 2.64 T shows a contrasting result (see triangles in Fig.1). Although the absolute value of the energy confinement time is worse than in the case with R_{ax}=3.6m [3], the density dependence is maintained close to the operational density limit.

The saturation or degradation of confinement is highlighted in the density ramp-up phase by gas-puffing in a single discharge with R_{ax}=3.6 m. The discharge shown in Fig.2 corresponds to the thick dotted line in Fig.1. The line averaged density is doubled from t = 1.5 s to 4.0 s, however, the stored energy and the energy confinement time do not change. The improvement factor on ISS95 is degraded from 1.5 to 1. The ratio of the radiation power to the absorbed power increases from 16 % to 22 % which is well below the condition of radiation collapse. The radiation is also localized at the plasma edge. Therefore the radiation loss does not play an essential role in confinement saturation. Although temperatures decrease with the increase in density, the decrease of electron temperature is more distinguished in the center than in the edge. The degradation of confinement seems to coincide with a broadening of temperature profile.

The discharge in the case with R_{ax}=3.75m indicates a contrasting behavior to the case with R_{ax}=3.6m. The temporal behavior shown in Fig. 3 corresponds to the thin dotted line in Fig.1. The stored energy increases monotonically with the increase in density. The confinement degradation referred to ISS95 and broadening of temperature profile in the high density region is much mitigated compared to the case with R_{ax}=3.6m. A slight difference in the condition of the NBI does not explain this distinguished result.

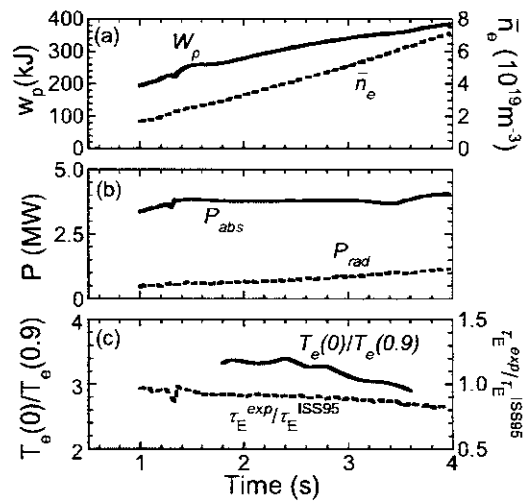

Fig.3 Waveforms of the discharge with density ramp-up in the case with R_{ax}=3.75m. P_{NBI}=4.1MW, E_{NBI}=135keV..(a) Stored energy and line averaged density. (b) Absorbed power of NBI and total radiation power. (c) Ratio of the central electron temperatures to that at ρ=0.9 and improvement factor of energy confinement time on ISS95.

The temporal changes of the density and temperature profiles, and the power balance are investigated for two discharges with R_{ax}=3.6m and R_{ax}=3.75m illustrated in Fig.2 and 3, respectively. Figure 4 shows the case with R_{ax}=3.6m. The density profile remains flat during the density ramp-up and the electron temperature becomes broad with the increase in density. The high density operation prevents the deep penetration of tangentially injected neutral beams and heat deposition moves from the core to the periphery (see Fig.4(c)). This tendency is emphasized with the inward-shifted magnetic axis due to the off-axis heating because of the tangency radius of 3.7 m of the NBI beam lines and the broad density profile due to gas-puffing particularly in the density ramp-up phase. Broadening of the temperature profile correlates with broadening of the power deposition profile. The local heat transport is investigated for time slices in the density ramp-up phase. Although the density dependence going as $\tau_E \propto \bar{n}_e^{0.6}$ is lost completely, the local heat conduction coefficient shows a temperature dependence with the

power between 1.1 and 1.6 at both radii of ρ=0.5 and 0.9 (see Fig.4(d)). The transport of NBI heated plasmas has no significant dependence on collisionality [4], which suggests that the thermal conductivity does not depend on density. The density dependence in the energy confinement time is derived from the replacement of the temperature dependence by the heating power and density. The clear dependence of the thermal conductivity on the temperature shown in Fig.4(d) supports this argument. The discussion of whether the transport is Bohm or gyro-Bohm requires clarification of the dependence on the magnetic field strength, however, the essential point is that the apparent contradiction between the global confinement and the local transport can be qualitatively explained by the change of the heat deposition profile.

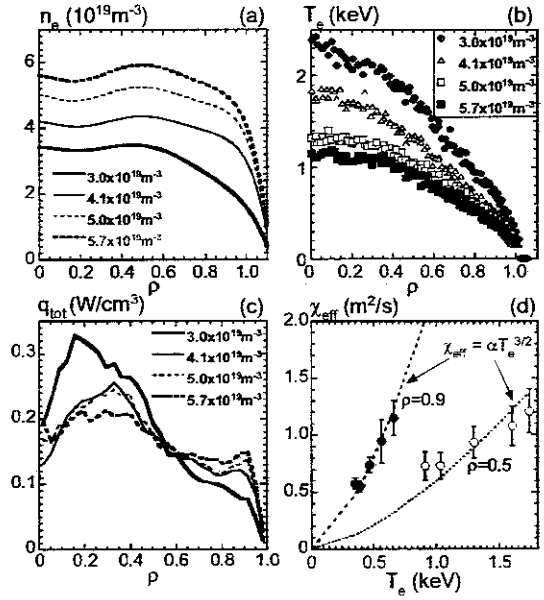

Fig.4 Plasma profiles at different times in the discharge (#28168) shown in Fig.2. (a) Density. (b) Temperature. (c) Power deposition. (d) Temperature dependence of thermal diffusivity at two radii of ρ=0.5 (open circles) and ρ=0.9 (solid circles) derived from the power balance analysis of 5 time slices.

In contrast to the case with R_{ax}=3.6m, the degradation of the energy confinement time due to the density ramp-up is mitigated in the case with R_{ax}=3.75m. Since the geometrical arrangement of tangential NBI's is optimized for the central heating in this configuration, the heat deposition profile is peaked and insensitive to the increase in density (see Fig.5(a)) in this case. The thermal diffusivity shows a clear temperature dependence as in the case with R_{ax}=3.6m, which is consistent with the behavior of the energy confinement time because of the unchanged heat deposition profile.

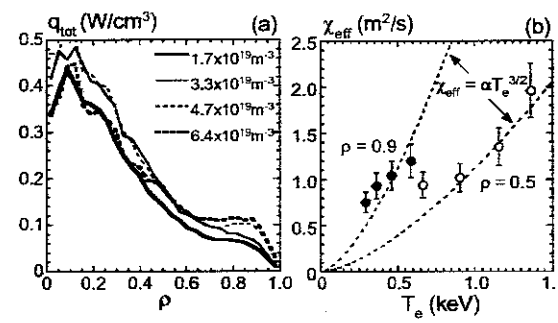

Fig.5 (a) Profile of power deposition from NBI in the discharges in the case with R_{ax}=3.75m. (b) Temperature dependence of thermal diffusivity at two radii of ρ=0.5 (open circles) and ρ=0.9 (solid circles) derived from the power balance.

The above discussion on the correlation between the power deposition profile and the global energy confinement time reminds a simple picture where the central heating is favorable for the global confinement. The advantage of the higher beam energy is related to this argument. Two data points with different beam energy in Fig.1 are compared in Fig.6. These two plasmas have almost the same heating and absorbed power, and line-averaged density but different beam energies. The energy confinement is 25 % better in the higher beam energy case than in the lower beam energy case, which cannot be explained by the heating power dependence. The case with E_{NBI} of 150 keV indicates the peaked power deposition profile due to deep penetration and higher central electron temperature in spite of 10 % less total power. Here the linkage between the central heating deposition and the global energy confinement

through no invariant in the electron temperature is observed.

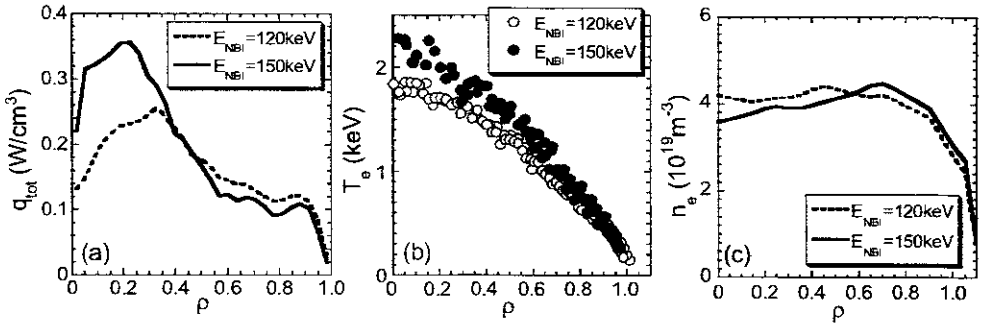

Fig.6 Plasma profiles in discharges with different NBI conditions. (a) Heat deposition. (b) Electron temperature. (c) Electron density. Dotted lines and open circles:P_{NBI}=4.7MW, E_{NBI}=120keV (#28168). Solid lines and closed circles: P_{NBI}=4.3MW, E_{NBI}=150keV (#28936).

3. Discussions and Conclusions

A major part of an apparent contradiction between the global energy confinement time and local thermal diffusivity, which has been observed in the case with R_{ax}=3.6m, can be explained by the broadening of heat deposition. These observations are linked with the fact that the temperature profile changes straight-forwardly according to the heat deposition profile of the net current free plasmas in LHD. The experimental results described in this paper are added to examples that net-current free plasmas do not have a clear invariant like concepts of stiffness and profile consistency in tokamaks [7]. The apparent discrepancy between the global and the local transport suggests that the central heating improves the saturated state and indeed this effect is demonstrated by the increased beam energy.

It should be noted that the difference in the power deposition profile alone does not explain the change of density dependence of the energy confinement time completely. It is probable that the response of the magnetic island [8] and some confinement improvement related to the central heating contribute to these phenomena.

The favorable density dependence can be extended towards much higher density by pellet fueling [9] in both cases of R_{ax}=3.6 m and 3.75 m. The peaked density profile realized by pellet fueling promotes the core heating and recovers the intrinsic density dependence when the density is moderate. However, the peripheral heat deposition becomes predominant even in the peaked density profile by pellet injection above 8×10^{19}m^{-3}, therefore, another mechanism related to confinement improvement is prerequisite to explain the advantage of pellet injection.

Acknowledgements

The authors acknowledge the continuous efforts of all members of the device engineering group to reliably operate LHD.

Reference

[1] MOTOJIMA, O., et al., OV/1-6 in this conference.
[2] STROTH, U., et al., Nucl. Fusion **36** (1996) 1063.
[3] YAMADA, H., et al., Nucl. Fusion **41** (2001) 901.
[4] YAMADA, H., et al., Plasma Phys. Control. Fusion **43** (2001) A55.
[5] STROTH, U., Plasma Phys. Control. Fusion **40** (1998) 9.
[6] SUDO, S., et al., Nucl. Fusion **30** (1990) 11.
[7] WAGNER, F., et al., Phys. Rev. Lett. **56** (1986) 2187.
[8] OHYABU, N., et al., Phys. Rev. Lett. **88** (2002) 055005-1.
[9] SAKAMOTO, R., et al., Nucl. Fusion **41** (2001) 381.

Transport Barrier Formation by Application of Localized ECH in the LHD

S. Kubo, T. Shimozuma, H. Idei, Y. Yoshimura, T. Notake[1], M. Sato, K. Ohkubo, T. Watari, K. Narihara, I. Yamada, S. Inagaki, Y. Nagayama, S. Murakami, S. Muto, Y. Takeiri, M. Yokoyama, N. Ohyabu, K. Ida, K. Kawahata, O. Kaneko, A. Komori, T. Mutoh, Y. Nakamura, H. Yamada, T. Akiyama[2], N. Ashikawa, M. Emoto, H. Funaba, P. Goncharov[3], M. Goto, K. Ikeda, M. Isobe, H. Kawazome[4], K. Khlopenkov, T. Kobuchi, A. Kostrioukov, R. Kumazawa, Y. Liang, S. Masuzaki, T. Minami, J. Miyazawa, T. Morisaki, S. Morita, H. Nakanishi, Y. Narushima, K. Nishimura, N. Noda, H. Nozato[5], S. Ohdachi, Y. Oka, M. Osakabe, T. Ozaki, B. J. Peterson, A. Sagara, T. Saida[3], K. Saito, S. Sakakibara, R. Sakamoto, M. Sasao, K. Sato, T. Seki, M. Shoji, H. Suzuki, N. Takeuchi[1], N. Tamura, K. Tanaka, K. Toi, T. Tokuzawa, Y. Torii[1], K. Tsumori, K.Y. Watanabe, Y. Xu, S. Yamamoto[1], T. Yamamoto[1], M. Yoshinuma, K. Itoh, T. Satow, S. Sudo, T. Uda, K. Yamazaki, K. Matsuoka, O. Motojima, Y. Hamada, and M. Fujiwara

National Institute for Fusion Science, Toki, Gifu 509-5292, Japan
[1] Department of Energy Engineering and Science, Nagoya University, 464-8603, Japan
[2] Research Laboratory for Nuclear Reactors, Tokyo Institute of Technology, Tokyo 152-8550, Japan
[3] Department of Fusion Science, School of Mathematical and Physical Science, Graduate University for Advanced Studies, Hayama, 240-0193, Japan
[4] Graduate School of Energy Science, Kyoto University, Uji 611-0011, Japan
[5] Graduate School of Frontier Sciences, The University of Tokyo 113-0033, Japan

e-mail contact of main author: kubo@LHD.nifs.ac.jp

Abstract. In the past three years, the LHD [1]has revealed confinement properties as good as those of tokamaks. And achieved beta value of 3.2 % has been attained, satisfying necessary condition to be a candidate for a reactor core [2]. However, a fundamental question remains; whether or not such high performance is maintained in a collisionless regime as the electron temperature gets higher. Indeed, the electron temperature remained below 4 keV for the past 3 years as if it were caught in the vicious dependence that the energy confinement time is proportional to $T_e^{-7/2}$ as predicted in the neoclassical theory without electric field. This paper reports that a plasma of 10 keV was achieved in the 5th campaign of the LHD, carried out in 2001, resolving such a concern and opening a new regime of extremely low collisionality. This regime of high T_e has the the features of the ITB and is obtained by achieving special experimental conditions.

1. Introduction

There was a working hypothesis that a regime of improved confinement is obtained as the heat flux exceeds a certain threshold value [3]. One of the proposed mechanisms of this improvement is the suppression of the turbulent transport by velocity or radial electric field shear. Attaining high electron temperature itself is the result of the improvement of the confinement but also open the way to investigate the improved confinement mechanism in the collisionless regime. Achievement of relatively high electron temperatures has been reported from CHS [4], W7-AS [5] and TJ-II [6], and various explanations have been given for the improved energy confinement. Since the LHD has a higher aspect ratio than the CHS, the LHD has a better orbit of trapped particles, and as the magnetic axis is shifted inward it approaches advanced helical systems in the properties of its drift orbits. Thus, the LHD plays a unique role in understanding the mechanism of the ITB in terms of space potential. The electric field, if it has a key role, would contribute to the reduction of the anomalous parts of χ_e rather than to that of the

neoclassical one. The resonance heating on axis became possible in LHD. Almost 1 MW electron cyclotron power is concentrated in the core region of LHD, resulting in the transition from normal to higher confinement in LHD. It is also observed that these transition occurs above a threshold power and this threshold changes as the density. These are similar observation of the ITB in tokamaks and helical systems. In this paper, the attainment of more than 10 keV plasma is reported. This high temperature is attained by triggering the transition by concentrating almost 1 MW power near the central part of the plasma.
In the next section, the plasma attained 10 keV is described with the specific features of the electron cyclotron heating system in LHD. One of the main interests from the view point of confinement barrier, it is of much interest that the presence of foot point of the transport barrier really exist or not. NBI target plasma is used because the foot point is more clear than pure ECH plasma. The ITB (internal transport barrier) observation on NBI target plasma is described in section 3. Temporal transition and its relation to the temperature gradient is described and implication from these observations are discussed also in section 3.

2. Attainment of T_{e0} = 10 keV

The central electron temperature of more than 10 keV is achieved in the experimental campaign in 2001. So far, it had not been possible to do efficient heating by ECH on LHD due to the lack of the resonance condition on the axis. The magnetic field at the magnetic axis is increased by shifting the axis inward (R=3.5 - 3.6) from the standard position(R = 3.75 m) to locate the cyclotron layer across the axis. In accordance with this shift in the magnetic axis the steering range of the ECH injection beam was modified [7].

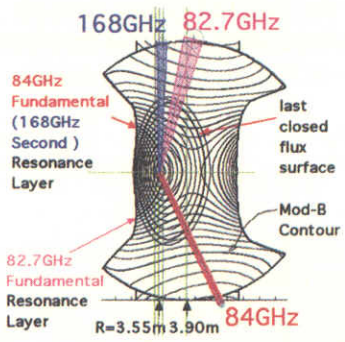

Fig. 1: *Flux surfaces and mod-B contours in LHD at vertically elongated cross section. Injected microwave beam from upper and lower antennas are shown with the beam waist size in scale.*

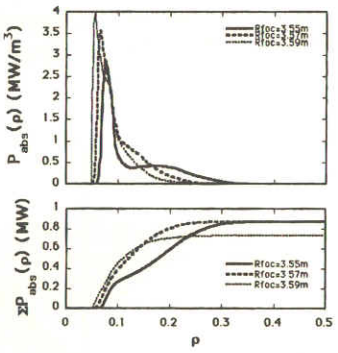

Fig. 2: *Expected power deposition profile calculated from ray tracing. Power from horizontal antenna is excluded in this calculation.*

As a result, ECH beams were concentrated on the shifted axis. For the on axis heating, strongly focussed Gaussian beams at the fundamental and second harmonic resonances are directed to the resonances near the magnetic axis. The microwave sources used are two 84 GHz collector potential depression (CPD)-type gyrotrons, two 82.7 GHz non-CPD gyrotrons, and three 168 GHz CPD gyrotrons. Each gyrotron delivers 100-400 kW microwave power into the LHD. Figure 1 shows the injection beams, Mod-B contours, and flux surfaces in the vertically elongated poloidal cross section. Two sets of upper beams, one lower beam from a vertical antenna, and two beams from horizontal antennas are used. The magnetic field strength and the configuration are selected to have a power deposition as nearly on axis as possible. The selected magnetic axis is 3.53 m and the toroidally averaged magnetic field strength on the axis is 2.951 T. The expected power deposition profile estimated by ray tracing, including the weakly relativistic effect, indicates that almost all of the injected power from the upper and lower antennas are concentrated within an averaged minor radius of $\rho \approx 0.2$ as shown in Fig.2, here, three cases of different injection

angle is plotted to see the allowances and errors in antenna setting. Lower traces are integrated absorption power. Almost 100% power absorption can be expected in the density, and temperature ranges discussed in this paper, provided that the beams crosses the resonance in the plasma confinement region. Fig.3 shows the evolution of plasma parameters and temperature profiles when the central electron T_{e0} exceeded 10 keV. The time evolution of the injected total power, the electron density, and the stored energy are shown here for the shot when the highest central electron temperature is recorded in the LHD. Almost 1.2 MW ECH power is concentrated inside $\rho \approx 0.2$. The electron density is slightly increasing but stays 0.5 to 0.6 $\times 10^{19}$m^{-3} in this case.

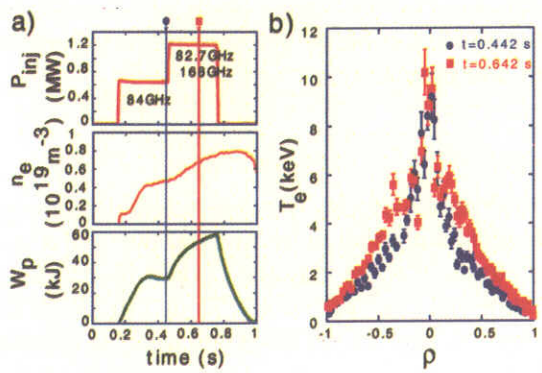

Fig. 3: *a)Time evolution of injected ECH power (upper), electron density (middle) and stored energy (bottom). b) T_e profile measured at each timing indicated by the arrow in a).*

The two 84 GHz gyrotrons injected 0.7 MW to produce and heat the plasma. After the density and the stored energy had attained a quasi- steady state, the 168 GHz and 82.7 GHz power are added simultaneously. Although no additional gas puff is supplied, the density keeps increasing slightly. A high power YAG-Thomson scattering system is used at the times indicated by the arrows in Fig.3 a). The profile is already sharp in the phase when only the 84 GHz power is injected. The 82.7 GHz power raises the central electron temperature to more than 10 keV. These high electron temperature modes appear only when the injected power exceeds a certain threshold level, and this threshold level increases with the electron density.

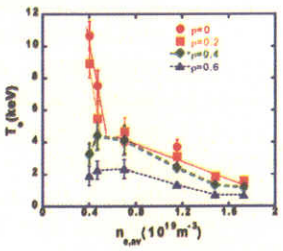

Fig. 4: *Dependence of T_e at ρ = 0, 0.2, 0.4, and 0.6 on the electron density.*

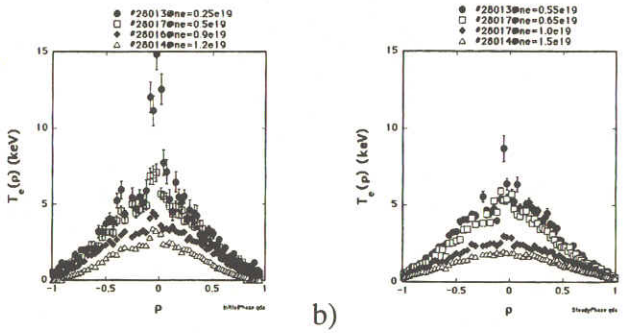

Fig. 5: *Electron temperature profiles measured by YAG-Laser Thomson scattering system for various density a) just after power increased and b) 200 ms after.*

Figure 4 shows the dependence of the temperatures at ρ = 0, 0.2, 0.4, and 0.6 on the averaged electron density under the same injection condition. Since the expected power deposition and the deposition profiles do not change significantly, the sharp increase in the electron temperatures at ρ = 0, 0.2 suggest the presence of some non-linear mechanism. Especially, in the comparison of the time evolution of the electron temperature profiles for the low and high density case as shown in Fig.5. The electron temperature profile shows ITB like feature even at the initial phase of applying high power with a relatively low temperature even at the density more than 1 $\times 10^{19}$m^{-3} as shown in Fig.5 a). The foot point of ITB point within here the sharp reduction of the transport appears and spreads outside as the target electron density decreases. In the

low density case, the ITB like structure may appear just after the power exceeds threshold but soon spreads over $\rho > 0.2$ where sharpness of the transition between high and low confinement region smeared out resulting in the disappearance of prominent ITB foot point.

3. ITB formation on NBI target plasma by ECH

The feet of the ITB are more prominent when the ECH is applied on NBI target plasma. The electron temperature profiles for two different injection powers, one above the threshold (282 kW) and one below it (205 kW), are shown in Fig. 6 a). A high electron temperature gradient is formed with the power above the threshold. The χ_e decreases to 0.7 m^2/s from 2.0 m^2/s at the steepest gradient position as the threshold power is exceeded. The dependences of the central electron temperature on the injection power are shown for averaged electron densities of 0.3 and 0.5×10^{19} m^{-3} in Fig. 6 b). It is clear that the threshold power depends on the electron density. Other observations with respect to the ITB are: 1) The power deposition profile plays an important role in the formation of the ITB. The total deposited power inside $\rho < 0.2$ seems the key factor. 2) Reduction of the ion and impurity transport is in the ITB are suggested from impurity observations. formation indicates the presence of a positive electric field. 3) The location of the feet of the ITB depends on the direction of the NBI, which may be related to the position of the rational surface $\iota/2\pi = 0.5$. 4) The density and electron temperature region of electron root predicted from neoclassical theory coincides with the region where the ITB appears. These facts support the proposed anomalous transport reduction mechanism which the radial electric field shear reduces the fluctuation level and the shear itself is formed by the radial interface between electron and ion root [4]. The $\iota/2\pi = 0.5$ surface plays an important role in expanding this interface outside. This might be the reason why the width of the ITB foot is rather insensitive to the power, density as shown in Fig. 6 b). The transition between ITB and normal confinement occurred during the turning off and on phase. In Fig. 7 a) and b) shows the response of the electron temperature to the ECH on and off power modulation. These temperatures are measured by multi-channel ECE radiometer. Each line is labelled by measuring position in averaged minor radius. Modulated part of ECH is turned off at $t = 0.96$ s and on at $t = 1.06$. Another ECH power is applied in the case of Fig. 7 b) to keep the base electron temperature high and to assist the ITB formation. It is clearly seen that the temperature decay in time is much longer in the high temperature case especially in the core region. The changes in the electron density and its profile were negligible. Fast change in the electron temperature just after the turning on and off of the modulated part of ECH reflects the power deposition profile of the modulated power. The power deposition profiles analyzed using just before and after 1.5 ms data at the turn on and off shows in good agreement with that expected from ray tracing calculation [8]. The deduced power deposition profiles are similar in each turn on or off

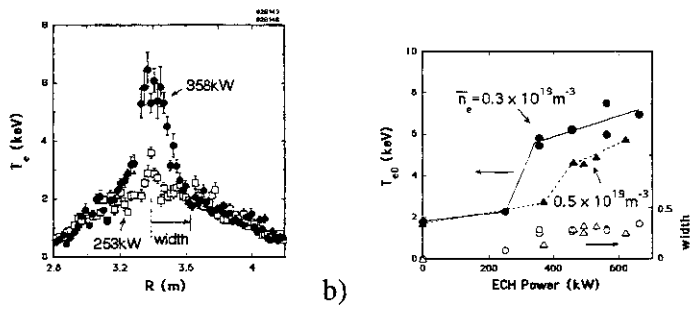

a) b)

Fig. 6: *Typical electron temperature profile during the ITB formation. a) T_e profile with (triangles) and without (open circles) the ITB for the injection powers of 282 kW and 205 kW, respectively. b) Averaged T_{e0} as a function of injection power for the averaged electron densities of 0.3 and 0.5 × 10^{19} m^{-3}. The dependence of the ITB width as defined in a) is also plotted.*

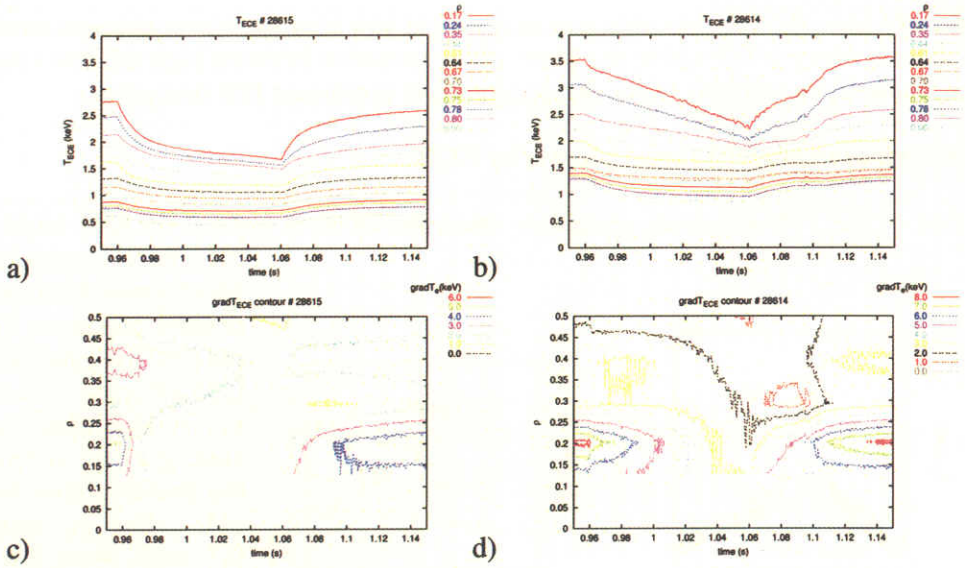

Fig. 7: *Time behavior of T_e measured by ECE. a) without and b) with base ECH on NBI target plasma. c) , d) Contour plot of ∇T_e estimated from a) and b), respectively*

phase for both high and low T_e cases. Power deposition profile itself is not much affected by the change in the plasma parameters discussed here. Fig. 7 c) and d) show ∇T_e contours deduced from difference between adjacent ECE channels shown in Fig. 7 a) and b), respectively. The high normalized gradient $\frac{\partial T_e}{\partial \rho} > 6$ keV region exists in the high temperature cases and such high gradient states is kept almost 60 ms after the stepwise decrease of the injection power as shown in Fig. 7 d). The high gradient state appears suddenly at 38 ms after the stepwise increase. It is necessary to analyze more in the other plasma parameters and also direct measurement of the radial electric field to draw a conclusion, but these responses support the dynamic model that the suppression of the anomalous transport by the shear in the the radial electric field results in high ∇T_e and this high ∇T_e lower the threshold level of transition then further expand the transition region [9].

References

[1] A. Iiyoshi, M. Fujiwara, O. Motojima et al. Fusion Technol. 17 (1990)169.

[2] O. Motojima, H. Yamada, A. Komori et al. Phys. Plasmas 6 (1999) 1843.

[3] K. Itoh, S. -I. Itho, and A. Fukuyama, *in Transport and Structual Formation in Plasmas*, edited by P. Scott and H. Wilhelmesson (Institute of Physics Publishing, Bristol, 1999).

[4] A. Fujisawa, H. Iguchi, T. Minami, et al. Phys. Plasmas 7 (2000) 4152.

[5] H. Maassberg, C. D. Beidler, U. Gasparino, et al. Phys. Plasmas 7 (2000) 575.

[6] C. Alejaldre, L. Almoguera, J. Alonso, et al. Nucl. Fusion 41 (2001) 1449.

[7] S. Kubo, T. Shimozuma, H. Idei, Y. Yoshimura, et al. J. Plasma Fusion Res. 78 (2002) 99.

[8] S. Kubo, H. Idei, T. Notake, et al. to be published J. Plasma Fusion Res.

[9] M. Yokoyama, K. Ida, H. Sanuki, et al. Nucl. Fusion 42 (2002) 143.

Plasma Performance and Impurity Behavior in Long Pulse Discharges on LHD

Y.Nakamura, Y.Takeiri, R.Kumazawa, M.Osakabe, T.Seki, B.J.Peterson, K.Ida, H.Funaba, M.Yokoyama, N.Tamura, A.Komori, S.Morita, K.Sato, K.Narihara, S.Inagaki, T.Tokuzawa, S.Masuzaki, J.Miyazawa, N.Noda, T.Mutoh, T.Shimozuma, K.Kawahata, Y.Oka, H.Suzuki, N.Ohyabu, T.Akiyama[1], N.Ashikawa, M.Emoto, P.Goncharov[2], M.Goto, H.Idei, K.Ikeda, S.Imagawa, M.Isobe, O.Kaneko, H.Kawazome[3], K.Khlopenkov, T.Kobuchi, A.Kostrioukov, S.Kubo, Y.Liang, T.Minami, T.Morisaki, S.Murakami, S.Muto, K.Nagaoka, Y.Nagayama, H.Nakanishi, Y.Narushima, K.Nishimura, T.Notake[4], H.Nozato[5], S.Ohdachi, S.Okamura, T.Ozaki, A.Sagara, T.Saida[2], K.Saito, S.Sakakibara, R.Sakamoto, M.Sasao, M.Sato, M.Shoji, N.Takeuchi[4], K.Tanaka, M.Y.Tanaka, K.Toi, Y.Torii[4] K.Tsumori, K.Y.Watanabe, T.Watari, Y.Xu, H.Yamada, I.Yamada, S.Yamamoto[4], T.Yamamoto[4], S.Yoshimura, Y.Yoshimura, M.Yoshinuma, K.Itoh, T.Mito, K.Ohkubo, I.Ohtake, T.Satow, S.Sudo, T.Uda, K.Yamazaki, K.Matsuoka, O.Motojima, Y.Hamada, M.Fujiwara

National Institute for Fusion Science, 322-6 Oroshi-cho, Toki 509-5292, Japan
1) Research Laboratory for Nuclear Reactors, Tokyo Institute of Technology, Tokyo, Japan
2) Department of Fusion Science, School of Mathematical and Physical Science, Graduate University for Advanced Studies, Hayama, 240-0193, Japan
3) Graduate School of Energy Science, Kyoto University, Uji 611-0011, Japan
4) Department of Energy Engineering and Science, Nagoya University, 464-8603, Japan
5) Graduate School of Frontier Sciences, The University of Tokyo 113-0033, Japan

e-mail contact of main author: ynakamu@lhd.nifs.ac.jp

Abstract. The superconducting machine LHD has conducted long pulse experiments for four years to achieve long-duration plasmas with high performance. The operational regime was largely extended in discharge duration and plasma density. In this paper, the plasma characteristics, in particular, plasma performance and impurity behavior in long pulse discharges are described. Confinement studies show that global energy confinement times are comparable to those in short-pulse discharges. Long sustainment of high performance plasma, which is equivalent to the previous achievement in other devices, was demonstrated. Long pulse discharges enabled us to investigate impurity behavior in a long time-scale. Intrinsic metallic impurity accumulation was observed in a narrow density window ($2 \sim 3 \times 10^{19} m^{-3}$) only for hydrogen discharges. Impurity transport study by using active impurity pellet injection shows a long impurity confinement time and an inward convection in the impurity accumulation window, which is consistent with the intrinsic impurity behavior. The pulsed neon gas injection experiment shows that the neon penetration into the plasma core is caused by the inward convection due to radial electric field. Finally, impurity accumulation control with an externally induced magnetic island at the plasma edge was demonstrated.

1. Introduction

Demonstration of high confinement, long-duration discharges is one of the most challenging issues for magnetic fusion research. The achievement of this goal requires the development of heating scenarios (also current drive scenario for tokamaks) as well as solving particle and heat flux problems in steady state. Such investigations are particularly suited for the superconducting Large Helical Device (LHD) (major radius R = 3.6 – 3.9 m, minor radius a = 0.6 m, toroidal field on axis B = 2.9 T) research program which is aimed at the study of long-duration and high-performance plasmas [1]. LHD has a fully superconducting coil system [2], which generates a heliotron magnetic configuration (l/m = 2/10) in steady state for plasma confinement. Helical plasmas require no plasma current drive and can be sustained only by injecting the power for plasma heating. Therefore LHD could provide a new platform for fusion research on steady state operation with net current free plasmas. This device has an intrinsic helical divertor configuration and plasma experiments so far have been performed with an open divertor configuration [3]. The divertor target plates and the plasma vessel were designed and constructed so as to remove a steady state heat load of 3 MW [4, 5]. The heating systems (ECH, NBI and ICH) have been also developed to achieve an injection of 3MW total heating power in steady state [4]. The near future target is to demonstrate a steady state one-hour discharge with 3 MW heating. This paper summarizes the recent results of long pulse operation and its plasma characteristics obtained on LHD. Long pulse experiments have been carried out extending the pulse duration of heating power (ECH, NBI and ICH) since LHD came into operation in 1998, and big progress has been made in discharge duration and operational density regime. The NBI heated plasma was sustained up to 110 s and a steady-state ICRF heated plasma with the discharge duration of 2 minutes was achieved. The next section reports on the progress towards steady state operation in LHD. Confinement properties of long-duration plasmas are discussed in Sec. 3. The global energy confinement was completely similar to that in short-pulse discharges and plasma with improved confinement in the inward shifted configuration was sustained over a long period of time for both NBI and ICRF discharges. Impurity behavior, which is of great importance in steady state operation, was also investigated for NBI heated long pulse discharges. Impurity accumulation was observed in a specific range of plasma density with a long time-scale as described in Sec. 4. Impurity pellet and gas injection experiments were carried out and the results

were consistent with the intrinsic impurity behavior. Finally, impurity accumulation control with a magnetic island (n/m = 1/1) in long pulse discharges is described in Sec. 5.

2. Progress towards steady-state operation

Our efforts towards steady-state operation mainly have been devoted to the extension of the discharge duration using both NBI and ICRF heating systems. The discharges obtained during the 1998-1999 experimental campaign are described in detail in Refs. [4 - 6], including the historical description and the development of heating systems. Before the 1999 campaign, all the strike points at the divertor legs were covered with graphite tiles, and it enabled us to enlarge the operational range of density and duration to a great extent. The divertor plates and the plasma vessel were cooled by water for the capability of steady-state operation with an injection power of 3 MW. However, the available power of the heating systems (NBI, ICRF) was restricted for long pulse operation as shown in Fig. 1, where the discharge duration and the operational density are plotted in terms of the injection power. In the NBI heating system, the limitation on the injection power was caused by the loss of stable operation of ion sources due to the temperature increase of the plasma electrodes and the heating-up of the molybdenum protection plates at the injection port, which were not directly cooled by water. For NBI discharges, it was easy to raise the plasma density and a high-density discharge with a maximum density of 6.7 x $10^{19}m^{-3}$ was sustained for 10 s with the power of 2 MW. The maximum density may be related to the density limit in helical devices [7]. ICRF long-pulse experiments with H-minority heating in helium plasmas have made smooth progress in extending the discharge duration [8]. Once the coupling of ICRF with the plasma was optimized by scanning the magnetic field and the minority ion concentration, it was very easy to extend the discharge duration if there was no trouble in the RF power source. In fact, a two minute long-duration discharge in the 2001 campaign was achieved after only several long-pulse shots [9]. For ICH discharges, the injected radio frequency (rf) power from a pair of loop antennas was restricted by the electric break down and heat-up of the rf amplifiers. The plasma density achieved with ICH remained at 1.15 x $10^{19}m^{-3}$ even for high power operation (1.1 MW, 5 s). The maximum density is very low compared to that (5.9 x $10^{19}m^{-3}$) obtained with the corresponding NBI power. This density limit may be due to some

reason different from the usual density limit in the case of NBI, which is one of major concerns of the ICH experiments in the coming experimental campaign.

Figure 2 shows the longest duration discharge with ICH (P_{ICH} ~ 0.35 MW) alone. The helium plasma with minority hydrogen ions was sustained for 120 s with a density of around 0.8 x $10^{19}m^{-3}$ and an electron temperature of 1.3 keV from ECE signals. The ion temperature was around 1.3 keV, which was measured from Doppler broadening of TiXXI (0.261 nm) using an x-ray crystal spectrometer. In this discharge, the amount of gas puffing was manually controlled by an operator watching the density signal from a far-infrared (FIR) interferometer. Radiation with a hollow profile [10] as well as the impurity line emissions (CIII, OV) were kept almost constant during the discharge. Spectroscopic and soft x-ray measurements show that there was no impurity accumulation of metal. The NBI heated plasma was also sustained for 110 s with a very low injection power of 0.11 MW. In spite of the low power level, a plasma with a density of 1.0 x $10^{19}m^{-3}$ and an electron temperature of 0.35 keV was obtained by exceeding the radiation barrier. Demonstration of long-duration discharges with high performance is illustrated by Fig. 3 which shows plasma performance (through the usual criterion $n\tau_E T_{i0}$) versus pulse duration, and where the present results stand with respect to ITER objectives. The large tokamaks can produce a reactor-grade high performance plasma and a steady state plasma of more than 3 h in duration was demonstrated in the small superconducting tokamak TRIAM [11, 12]. However, these results are not sufficient for the database for long sustainment of high performance plasma required in ITER. In LHD, since the helical plasma requires no plasma current drive, various heating methods (ECH, NBI, ICH) can be applied for sustaining the plasma with each heating source alone. First of all, an ECH plasma was sustained for 2 min with an input power of 50 kW [13]. The long pulse operation of high performance ECH plasma would require the development of a steady-state high power gyrotron and transmission line. The NBI heated plasma was very stably sustained with high performance as in short-pulse discharges. The plasma performance in the 80 s discharge is superior to the previous achievement in Tore Supra [14]. One more neutral beam line, which is available for long pulse operation, has been installed and tested in the last experimental campaign. Further extension to a higher performance regime can be expected for NBI long pulse discharges. For the ICH system, a new steady-state RF generator is now under preparation for the next experimental campaign and the first goal is steady state operation with 1 MW for more than 30 min.

3. Plasma confinement characteristics of long pulse discharges

The energy confinement characteristics in LHD have been mainly investigated using short-pulse discharges with $\tau_d < 3$ s [15]. Here we summarize the results in brief. The LHD experiments in the standard configuration (R = 3.75 m) showed that the global energy confinement time τ_E could be expressed by the international stellarator scaling 95 (ISS95), which was derived from the experiments in medium-sized helical devices. Moreover, the experiments in the inward shifted configuration (R = 3.6 m) indicated an improvement by a factor of 1.5 in τ_E without confinement degradation due to MHD instabilities, which are predicted in an ideal MHD analysis.

It is of great concern whether the improved LHD plasmas could be maintained over a long period of time. Figure 4 shows a typical long pulse discharge with high performance. The target plasma was produced by ECH and NBI power of around 1.5 MW was injected into the plasma for 10 s. The plasma density was controlled by hydrogen gas puffing, the amount of which was preprogrammed until 1 s and then controlled with a feedback loop so as to keep the density constant. As seen in Fig. 4, although a large amount of gas puffing was required to bring up the density, the gas puff rate was reduced with time. This suggests that wall pumping is strong in the density build-up phase and wall recycling increases with time as indicated by the recycling coefficient R [16]. The plasma temperature and density were kept constant and the profiles remained unchanged until the end of the discharge. The energy confinement time reaches 0.3 s and the enhancement factor in ISS95 scaling remains at around 1.4 during the discharge. There was no sign of confinement degradation in this discharge. It was evident that the high performance plasma obtained in short-pulse discharges can be sustained over a long period of time. However, the density scan revealed a new feature of long-duration plasma. Figure 5 shows the dependence of normalized plasma stored energy on the line averaged electron density. The open circles represent the plasmas in the initial stage of the discharge (t = 2 ~ 3 s) and the solid ones the plasmas at the end of the discharge (t = 8 ~ 10 s). A scaling of the normalized stored energy can be derived from the ISS95 scaling: $W_p / P_{dep}^{0.41} = 0.11\ \bar{n}_e^{051}$ where P_{dep} is the NBI deposition power calculated by using the shine-through power, which was measured with calorimeter arrays embedded in beam facing armor plates [17]. The plasmas at the initial stage showed the ISS95 scaling with an enhancement factor of 1.4. On the other hand, a

significant decrease of the stored energy was observed after about 10 s in the density range of 2 ~ 4 x $10^{19}m^{-3}$. When the density was kept constant in this region, the plasma performance was remarkably degraded with time and the stored energy decreased up to 68 % at the end of the discharge (t = 10 s). This degradation of plasma performance may be related to the energy loss caused by the radiation due to metallic impurity accumulation, which will be described in Sec. 4. Figure 6 shows the relationship between the enhancement factor in τ_E and the radiation emissivity at the plasma center in the density ramp-up discharge (shot 17093). When the density increased with time, the central radiated power increased remarkably with increasing density, thereby leading to the reduction of the enhancement factor. In the high-density region, the central radiated power decreased and the plasma performance recovered rapidly with the decrease of the radiation. Since the radiated power density corresponds to about 32 % of the deposited power density in the core region, the power balance of the core plasma may be largely affected by strong core radiation. On the contrary, long-pulse operation for more than 10 s has been carried out with helium gas puffing and there was no sign of impurity accumulation. Therefore, plasma confinement degradation has not been seen in all operational regimes. Both NBI and ICRF heated long-duration plasmas in the inward shifted configuration (R = 3.6 m) indicated an enhancement factor of around 1.5 relative to the ISS95 scaling as well as in short-pulse discharges.

4. Impurity behavior in long pulse discharges

4.1 Long time-scale impurity accumulation

In a variety of long pulse discharges, we found that metallic impurity accumulation was observed only in NBI heated hydrogen discharges in a narrow density window of 2 ~ 3 x 10^{19} m^{-3} [18]. Figure 7 shows a typical long pulse discharge with impurity accumulation. The plasma was initiated by ECH and heated with a neutral beam line with an injection power of 1.1 MW. The plasma density was controlled by hydrogen gas puffing with a feedback loop and kept at 2.9 x 10^{19} m^{-3} until 28 s. A remarkable increase of central radiation (ρ = 0) is observed with a long time-scale until 12 s and then the radiation decreases very slowly with time. On the other hand, the radiation at the peripheral region (ρ = 0.84) decreases gradually until 10 s and then remains almost constant. Clear evidence of impurity accumulation is observed in the profiles of radiated

power density as shown in Fig. 8(a). Strong core radiation is observed at 12 s and then the radiation profile is maintained until the end of the discharge. This increase of central radiation causes a significant decrease of central electron temperature as shown in Fig. 8(c). However, there is no radiation collapse in these discharges. The core density profile is flat in the initial stage and it becomes slightly peaked with impurity accumulation (Fig. 8(b)). The low-Z impurity emission (OV) originating from the edge plasma is kept constant during the discharge (Fig. 7(d)). On the other hand, the time evolution of the heavy metallic impurity emission (FeXVI), which reflects the impurity behavior in the core region, is similar to that of the central radiation. Spectroscopic and soft x-ray measurements indicated that the main metallic impurity was iron, which is an element of the plasma wall material.

A density scan during a long-duration discharge revealed a dramatic change of impurity behavior. In the density ramp-up discharge, the central radiation increases with density and then turns down in the high-density region. Such a remarkable change of impurity behavior was also observed in constant density discharges. Figure 9 shows the time evolution of central radiated power density and the most prominent metallic emission (FeXXIII), which originates from the core plasma (T_{e0} > 1 keV), for the discharges with different plasma densities. Remarkable temporal increases of the central radiation and the iron line emission were found only for the discharge with the density of 2.7 x $10^{19}m^{-3}$. This implies that there is an impurity accumulation window in the operational regime. Figure 10 shows the classification of long-duration plasmas on n-T space from the point view of impurity behavior. The discharges with impurity accumulation (crosses) were distinguished from those without accumulation and with pump-out (open squares and solid circles). The solid line represents the transition between the plateau regime and the Pfirsch-Schlüter regime for iron impurity. The broken line represents the transition between the electron root and the ion root for background plasma in a nonaxisymmetric torus. This indicates a critical point of the specific space where the plasma has multiple solutions for the ambipolar electric field [19]. In the region of high-temperature and low-density (low collisionality), metallic impurities do not accumulate in the plasma core due to the positive radial electric field in electron root. Radial electric field measurements show that the transition from a positive electric field to a negative one occurs when the plasma has a density 1 x $10^{19}m^{-3}$ and an ion temperature of 2 keV. In fact, small positive electric fields were observed even in the density range of ion root near the transition to electron root [20]. In the

region of low-temperature and high-density (high collisionality), there is no sign of impurity accumulation, which may be caused by the dominant contribution of the temperature gradient in the PS regime ("temperature screening effect") on account of the flat density profile in the plasma core. In the intermediate region, which corresponds to the plateau regime for impurity ions, impurity accumulation is always observed with a long time constant (~10 s). In our helical device, it is found that there is a narrow window for impurity accumulation in plasma parameter space (collisionality space). On the whole, the qualitative features are consistent with neoclassical impurity transport. However, the negative impurity flux (accumulation) is not found in a simple analysis with neoclassical theory, which includes the expression for axisymmetric torus plasmas [18].

4.2 Transport study by impurity pellet injection

Impurity transport was also investigated by using impurity injection with a tracer-encapsulated solid pellet (TESPEL) [21], which has been developed as a new type of pellet for impurity transport study [22]. The flexible choice of the tracer particle is a unique feature of this method and the TESPEL with a titanium (Ti) tracer was used in this case. Figure 11 shows the time evolutions of the Ti Kα emission in the case of pellet injection, together with those of Fe Kα emission, which were measured by a soft x-ray pulse height analyzer viewing a central plasma chord. The same TESPEL was injected into the NBI heated hydrogen plasmas with the constant densities of 1.9 x $10^{19}m^{-3}$ (T_{e0} = 3 keV) and 3.7 x $10^{19}m^{-3}$ (T_{e0} = 2 keV) at 1.2 s. The plasma density and temperature remain almost unchanged by the pellet injection, thereby not influencing the transport. In the low-density case, there is a rapid increase in the Ti Kα emission signal, followed by a more gradual decay back down to the pre-injection level. The Fe Kα emission originating from the intrinsic metallic impurity saturates in the course of the discharge. This indicates that for this type of discharge the titanium leaves the plasma and there is no accumulation. Impurity transport analysis with a one-dimensional impurity transport code (MIST) indicates that the time evolution of the Ti Kα emission can be explained only by the diffusion component. On the other hand, in the high-density case, the Ti Kα emission intensity increases very slowly and reaches a maximum point after about 1 s. Then the emission intensity decreases with a long decay time (τ_{decay} = 4.1 s) up to 3 s when the NBI heating turns off. The decay time is closely

connected with the impurity confinement time. In the Fe Kα emission signal, there is no saturation and the intensity continues to increase during the NBI heating. This implies that the impurity confinement time is very large and the impurities accumulate in the core plasma if the impurity influx is larger than the loss of impurities. Furthermore, significant inward convection must be taken into account for understanding the temporal behavior of the Ti Kα emission in the transport analysis. In order to compare the plasma parameters with impurity accumulation with those in the impurity accumulation window described above, the decay time of Ti Kα emission is plotted as a function of normalized collision frequency for impurity ions as shown in Fig. 12, where the central iron density in a long pulse discharge with density ramp-up is also plotted. The iron density is calculated from measured radiated power density by coupling the MIST with measured plasma density and temperature profiles. As described before, the metallic impurities accumulate in a specific region of the collisionality and diffuse out in the high-density region for the density ramp-up discharge. The impurity accumulation window is represented by the increasing phase of the central iron density as indicated by the dashed lines. The decay time increases gradually with increasing density (the collisionality) and then increases abruptly in the impurity accumulation window. Moreover, the intrinsic impurity accumulation is also observed in the Fe Kα emission signal for the discharges with a decay time of more than 3 s, which are in the impurity accumulation window. The experimental results of the impurity pellet injection are in good agreement with the impurity behavior observed in long pulse discharges.

4.3 Role of radial electric field

Another important experiment into the relationship between impurity behavior and radial electric field in the plasma was carried out by neon gas injection with a short pulse (100 ms). In particular, it is of great importance to clarify the influence of radial electric field on impurity transport in the low collisionality ($1/\nu$) regime, where helically trapped particles play an important role in the transport for a nonaxisymmetric device such as LHD. Figure 13 shows the profiles of the radial electric field and the fully ionized neon density for the discharges with various electron densities. The radial electric field (E_r) was derived from the poloidal rotation velocity measured with charge exchange spectroscopy (CXS) [23] at the midplane in the LHD plasma by using a charge exchange reaction between fully ionized neon impurity and atomic hydrogen

from the neutral beam (NB), which was employed as the main plasma heating source. The neon density was estimated from the NeX line intensity in CXS by using the beam density profile, which was determined from measured NB port-through power by using a Monte Carlo calculation [17]. The neon gas was injected into the NBI heated plasmas at 1.5 s and the neon density profile was measured at intervals of 2 s by integrating the NeX line emission for about 2 s. In Fig. 13, the measured profiles at the same time (t = 3 s) when the line intensity has a maximum value are indicated. The radial electric field is positive (electron root) in the low-density region and negative (ion root) in the high-density region, in particular, near the plasma edge [20]. The transition from electron root to ion root is observed at the density of around $1.0 \times 10^{19} m^{-3}$ and the radial electric field is nearly zero at all radii. The impurity collisionality at the critical density is nearly equal to that at the left hand side of the impurity accumulation window in Fig. 12. The penetration of neon impurity into the plasma core increases as the electron density is increased as shown in Fig. 13(b). The MIST code shows that the neon density in the plasma core depends on the diffusion coefficient and the convection velocity for impurities. The result from neon penetration indicates that the convection component decreases with increasing density because the neon impurity is in the plateau regime and the diffusion coefficient is almost constant in this operational regime. The radial electric field decreases monotonically from a positive value to a negative one as the density is increased. The neoclassical impurity transport theory for a nonaxisymmetric torus predicts a large contribution of the convective component proportional to E_r in the $1/\nu$ regime, in particular, for high Z impurities. Therefore, the qualitative behavior of neon penetration into the plasma core can be explained by the convection due to the radial electric field. However, as described in Sec. 4.1, the neoclassical analysis using a simple analytic expression for radial impurity flux in each transport regime (classical, Pfirsch-Schlüter, banana-plateau and $1/\nu$ regime) shows that the convective component due to radial electric field does not produce the inward impurity flux because the diffusion coefficient in the $1/\nu$ regime decreases with ν^{-1} and the convective component is greatly reduced near the transition to the PS regime [18]. Further investigation is required for understanding the physical mechanism underlying the impurity behavior in long pulse discharges.

5. Impurity accumulation control

In order to realize steady state operation with a high performance plasma, it is of great importance to reduce the impurity concentration or prevent impurities from penetrating into the core plasma. In previous LHD experiments [24], the influence of magnetic islands on impurity behavior was observed by using external perturbation coils, which produce an n/m = 1/1 magnetic island near the plasma edge. Therefore, impurity control by magnetic island formation was attempted in long pulse discharges with impurity accumulation as described in Sec. 4.1. The structure of the n/m = 1/1 magnetic island without plasma (vacuum island) in the poloidal plane is shown in Fig. 14, where the electron temperature profile at the midplane of the plasma with the same toroidal angle is also indicated. In this case, the perturbation coil current is 1800 A and the electron temperature profile shows a flattening in the region where the O point of the magnetic island is located [25]. It has been confirmed that in addition to the electron profiles the ion temperature profile and the radial electric field also show a clear flattening (zero E_r) inside the magnetic island [26]. The long pulse discharge with the perturbation field is shown in Fig. 15, where both discharges with and without the perturbation field are indicated. The perturbation field is applied at 10 s and increased linearly until 28 s. A drastic change of impurity behavior was observed 3 s after the application of the perturbation field. The central radiation decreases on a large scale and a significant increase of the central electron temperature is observed. At that time, magnetic islands with the width of around 7 cm appear clearly in both O point regions as seen in the temperature profile (Fig. 16(c)). The peaked radiation profile returns to a hollow one and the peaked density profile to flat one by applying the perturbation field (Fig. 16(a) and 16(b)). The impurities in the core plasma may diffuse out by the reduction of the impurity influx due to the formation of a magnetic island. However, further experimental and theoretical investigation would be required for understanding the physical mechanism for the impurity pump-out. Another important feature in this discharge is the change of particle transport caused by the application of the perturbation field. As seen in Fig. 15(b), a large difference in the gas puffing rate with and without the perturbation field is observed and the gas fueling rate is very low for the discharge with impurity pump-out by means of magnetic island formation. The particle transport seems to be closely connected with the impurity transport.

As described above, impurity control using the perturbation field has been clearly

demonstrated during long pulse discharges, in which the intrinsic impurity accumulation is observed. This method of controlling impurity accumulation with perturbation fields could be applied to long pulse operation in the future.

6. Conclusions

Significant progress towards long pulse operation has been made in the LHD experiments over four years time. Long pulse operation with a high plasma performance has been demonstrated with both NBI and ICRF heating. In particular, the achievement of a two minutes discharge with ICH alone enabled us to enter a new regime of high confinement and long-duration discharges. Confinement characteristics of long-duration plasmas were completely similar to those in short-pulse discharges. The improved confinement plasmas in the inward shifted configuration were sustained over a long period of time for both NBI and ICRF discharges. Long pulse experiments showed impurity accumulation over a long time-scale (~10 s) only for NBI heated hydrogen discharges. The intrinsic metallic impurities (mainly iron) were accumulated in a specific range of operational plasma density (2 ~ 3 x $10^{19}m^{-3}$), that is, a narrow collisionality regime of the core plasma. Impurity pellet injection experiments show that the impurity transport characteristics are consistent with the intrinsic impurity behavior. Radial electric field plays an important role in drawing the impurities into the plasma core. The successful control of impurity accumulation in long pulse discharges was demonstrated with a magnetic island (n/m = 1/1) near the plasma edge.

Acknowledgments

The authors thank all members of device engineering group for their operational support of LHD.

References

[1] IIYOSHI, A., et al., Nucl. Fusion **39** (1999)1245.
[2] MOTOJIMA, O., et al., Nucl. Fusion **40** (2000)599.
[3] FUJIWARA, M., et al., Nucl. Fusion **41** (2001) 1355.
[4] FUJIWARA, M., et al., Nucl. Fusion **40** (2000) 1157.
[5] NODA, N., et al., Nucl. Fusion **41** (2001) 779.

[6] TAKEIRI, Y., et al., Plasma Phys. Control. Fusion **42** (2000) 147.

[7] SUDO, S., et al., Nucl. Fusion **30** (1990) 11.

[8] KUMAZAWA, R., et al., Phys. Plasmas **8** (2001) 2139.

[9] SEKI, T., et al., Proc. of 14th Topical Conf. on Radio Frequency Power in Plasmas, Oxnard, California, May 2001, CP595, p. 67.

[10] PETERSON, B. J., et al., J. Nucl. Mater. **290-293** (2001) 930.

[11] ITOH, S., et al., Nucl. Fusion **39** (1999) 1257.

[12] SAKAMOTO, M., et al., IAEA-CN-94/EX/P4-07, this conference.

[13] SHIMOZUMA, T., et al., Fusion Eng. Des. **53** (2001) 525.

[14] EQUIPE TORE SUPRA (presented by B. Saoutic), Fusion Energy 1996 (Proc. 16th Int. Conf. Montreal, Canada 1996), IAEA, Vol. 1, Vienna (1997) 141.

[15] YAMADA, H., et al., Nucl. Fusion **41** (2001) 901.

[16] NAKAMURA, Y., et al., J. Nucl. Mater. **290-293** (2001) 1040.

[17] OSAKABE, M., et al., Rev. Sci. Instrum. **72** (2001) 590.

[18] NAKAMURA, Y., et al., Plasma Phys. Control. Fusion **44** (2002) 2121.

[19] YOKOYAMA, M., et al., Nucl. Fusion **42** (2002) 143.

[20] IDA, K., et al., Phys. Rev. Lett. **86** (2001) 5297.

[21] TAMURA, N., et al., Proc. of 29th EPS Conf. on Plasma Phys. And Contr. Fusion, Montreux, June 2002, ECA Vol. 28B, P-1.126.

[22] SUDO, S., et al., Plasma Phys. Control. Fusion **44** (2002) 129.

[23] IDA. K., et al., Rev. Sci. Instrum. **71** (2000) 2360.

[24] KOMORI, A., et al., Phys. Plasmas **8** (2001) 2002.

[25] NARIHARA, K., et al., Phys. Rev. Lett. **87** (2001) 135002.

[26] IDA, K., et al., Phys. Rev. Lett. **88** (2002) 015002.

Figure captions

Fig. 1. Operational regime for long pulse discharges with (a) ICRF and (b) NBI heating. The solid and open circles indicate the discharge duration and the electron density, respectively.

Fig. 2. Two minutes discharge with ICRF heating alone. An RF power of around 0.35 MW is radiated from one loop antenna in this case.

Fig. 3. Plasma performance versus pulse duration. The solid symbols indicate the achieved parameters in LHD.

Fig. 4. A typical long pulse discharge with high performance. The enhancement factor (τ_E/τ_E^{ISS95}) is maintained at around 1.4 until the end of the discharge. The recycling coefficient (R) increases with time and reaches to 0.9 at 10 s,

Fig. 5. Dependence of normalized stored energy on line-averaged electron density. The stored energy from diamagnetic measurements is normalized by the deposition power with the ISS95 scaling. The open and solid circles indicate the stored energy at the initial stage and at the end of the discharge, respectively. The ISS95 scaling is also indicated by the dotted line and the solid line represents the scaling with an enhancement factor of 1.4.

Fig. 6. Correlation between central radiation and enhancement factor in τ_E. Each line indicates the time trace during the discharge of shot 17093. The degradation of plasma performance is closely connected with the increase of central radiation.

Fig. 7. A typical NBI hydrogen discharge with long time-scale impurity accumulation. The constant injection power is 1.1 MW. The plasma density is kept constant by a gas puff system with a feedback loop. Intrinsic metallic impurity accumulation is observed.

Fig. 8. Temporal variation of (a) radiation, (b) electron density and (c) electron temperature profiles. The radiation profile is strongly peaked and the temperature profile becomes flat in the core region at 12 s. The density also becomes peaked with impurity accumulation.

Fig. 9. Time evolution of (a) central radiation and (b) FeXXIII emission for discharges with constant densities. Remarkable increases are observed only for the discharge with $2.7 \times 10^{19} m^{-3}$.

Fig. 10. A n-T diagram for impurity behavior in long pulse discharges. The crosses indicate the plasmas with impurity accumulation and the open squares indicate the plasmas without accumulation. The solid circles indicate the plasmas with the decrease of impurities or without accumulation.

Fig. 11. Time evolution of Ti Kα and Fe Kα emissions for the discharges with impurity pellet injection. The tracer-encapsulated solid pellet (TESPEL) with a titanium (Ti) tracer is injected at 1.2 s. A clear difference in the temporal behavior between the discharges with low and high densities is observed.

Fig. 12. Decay time of Ti Kα emission as a function of normalized collision frequency for impurity ions. The central iron density (solid circles) in a density ramp-up discharge is also indicated to compare the collisionality with that in the impurity accumulation window.

Fig. 13. Radial profiles of (a) radial electric field and (b) fully ionized neon density for the discharges with a pulsed neon gas injection. The radial electric field changes from positive to negative with increasing electron density. The neon density increases monotonically as the density is increased.

Fig .14. (a) The structure of the n/m = 1/1 magnetic island without plasma in the poloidal plane and (b) the electron temperature profile at the midplane of the plasma with the same toroidal angle. The perturbation coil current is 1800 A. Temperature flattening is observed in the region where the O point of the magnetic island is located. The width of the islands (W_a, W_b) is about 15 cm.

Fig. 15. Impurity accumulation control by the application of a perturbation field. A magnetic island is produced by the perturbation coil current (I_{PF}). The solid and broken lines indicate the discharges with and without a perturbation field, respectively.

Fig. 16. Temporal variation of (a) radiation, (b) electron density and (c) electron temperature profiles for the discharge with a perturbation field. The strong core radiation disappears with the application of the perturbation field, thereby leading to the increase of the electron temperature in the core region. The density profile becomes flat.

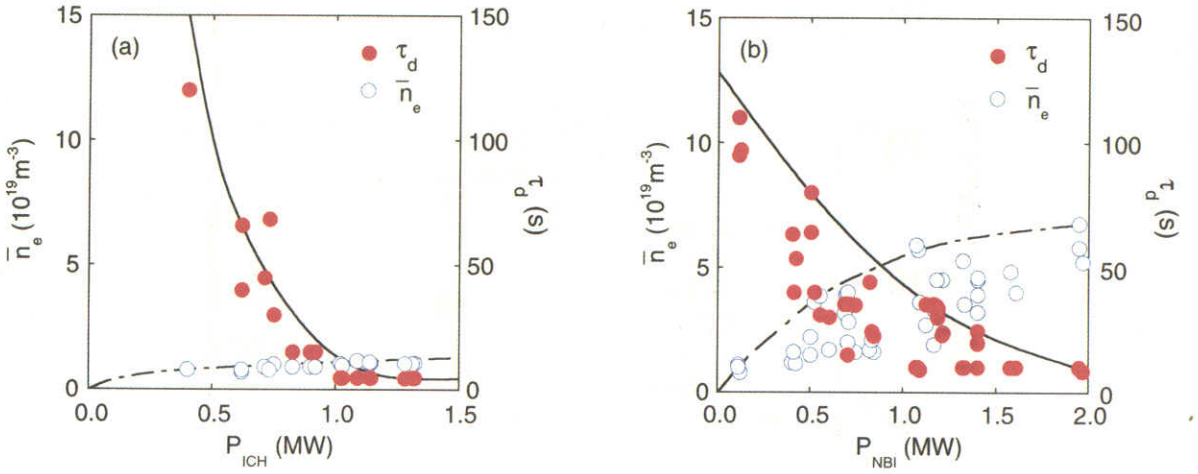
(a)
(b)
τ_d
$\bar{n}_e$
$\bar{n}_e$ (10^{19}m^{-3})
τ_d (s)
P_{ICH} (MW)
P_{NBI} (MW)

Fig. 1

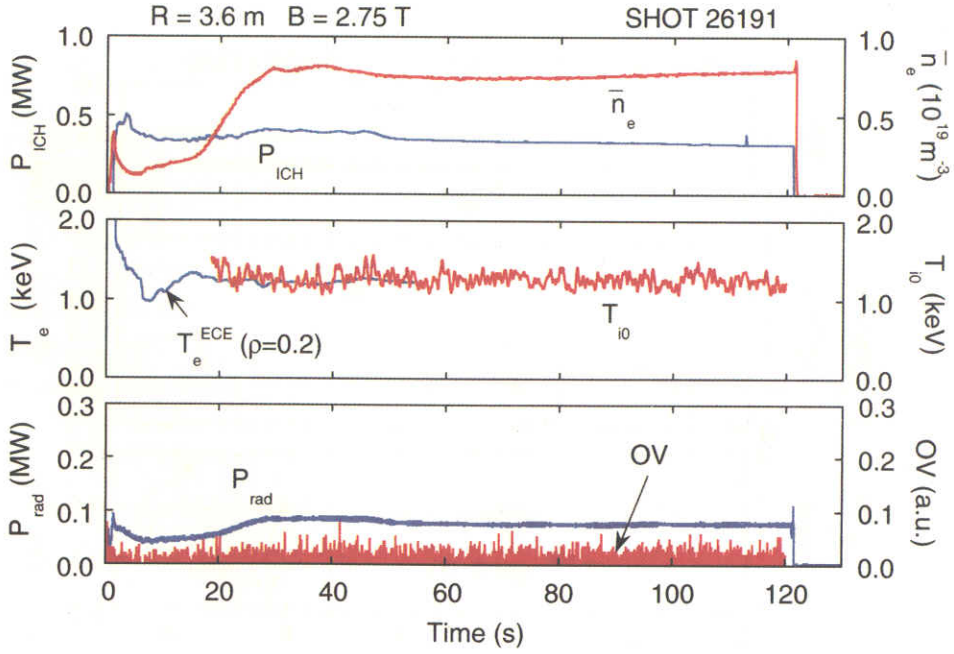
R = 3.6 m B = 2.75 T
SHOT 26191
P_{ICH} (MW)
$\bar{n}_e$
P_{ICH}
$\bar{n}_e$ (10^{19} m^{-3})
T_e (keV)
T_e^{ECE} (ρ=0.2)
T_{i0}
T_{i0} (keV)
P_{rad} (MW)
P_{rad}
OV
OV (a.u.)
Time (s)

Fig. 2

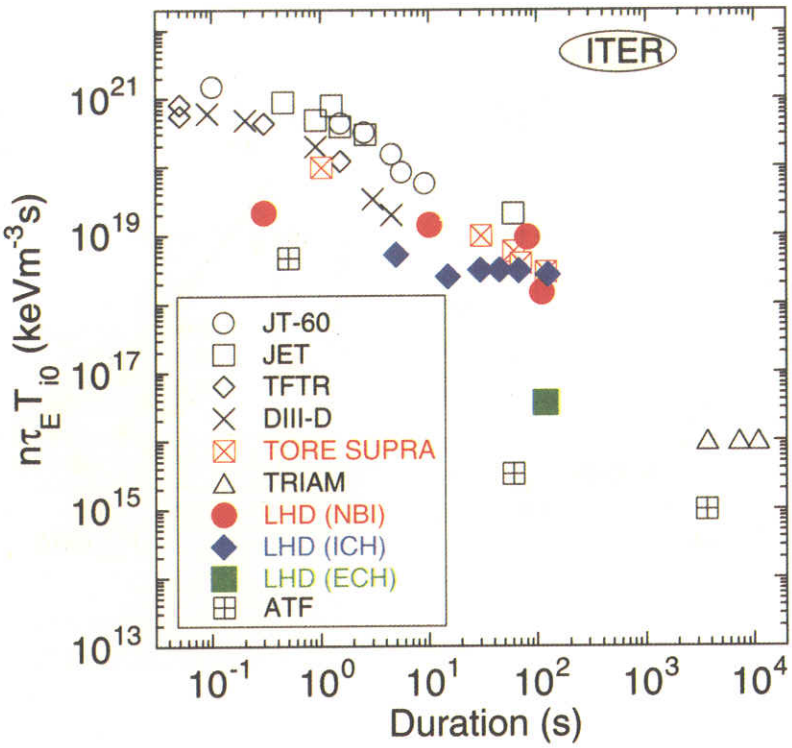
ITER
10^{21}
10^{19}
10^{17}
10^{15}
10^{13}
$n\tau_E T_{i0}$ (keVm^{-3}s)
JT-60
JET
TFTR
DIII-D
TORE SUPRA
TRIAM
LHD (NBI)
LHD (ICH)
LHD (ECH)
ATF
10^{-1} 10^{0} 10^{1} 10^{2} 10^{3} 10^{4}
Duration (s)

Fig. 3

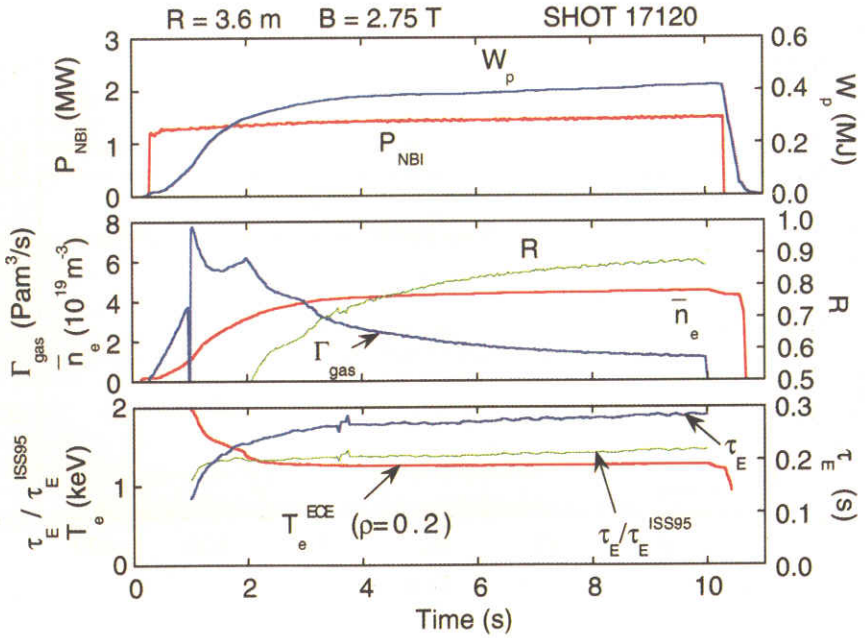
R = 3.6 m B = 2.75 T SHOT 17120
W_p
P_{NBI}
P_{NBI} (MW)
W_p (MJ)
R
$\bar{n}_e$
Γ_{gas}
Γ_{gas} (Pam^3/s)
$\bar{n}_e$ (10^{19} m^{-3})
R
τ_E
T_e^{ECE} (ρ=0.2)
τ_E/τ_E^{ISS95}
τ_E / τ_E^{ISS95}
T_e (keV)
τ_E (s)
Time (s)

Fig. 4

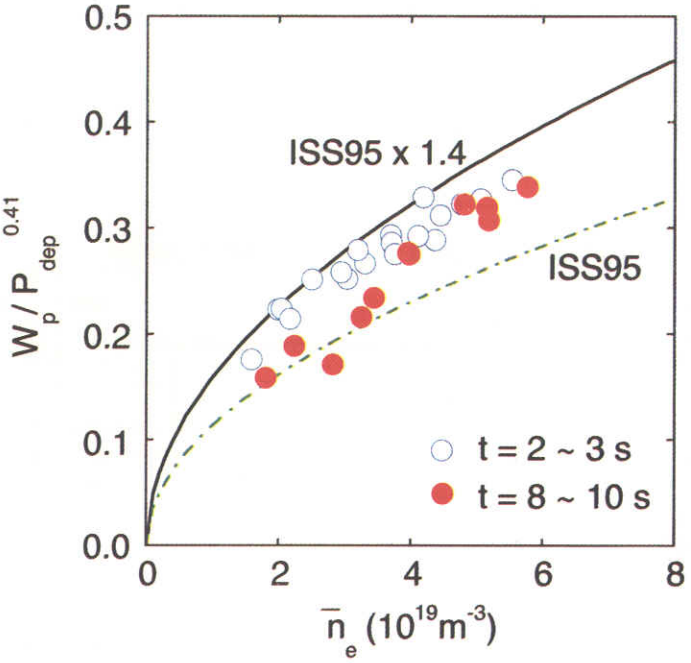
0.5
0.4
0.3
0.2
0.1
0.0
0
2
4
6
8
ISS95 x 1.4
ISS95
t = 2 ~ 3 s
t = 8 ~ 10 s
$W_p / P_{dep}^{0.41}$
$\bar{n}_e$ (10^{19}m^{-3})

Fig. 5

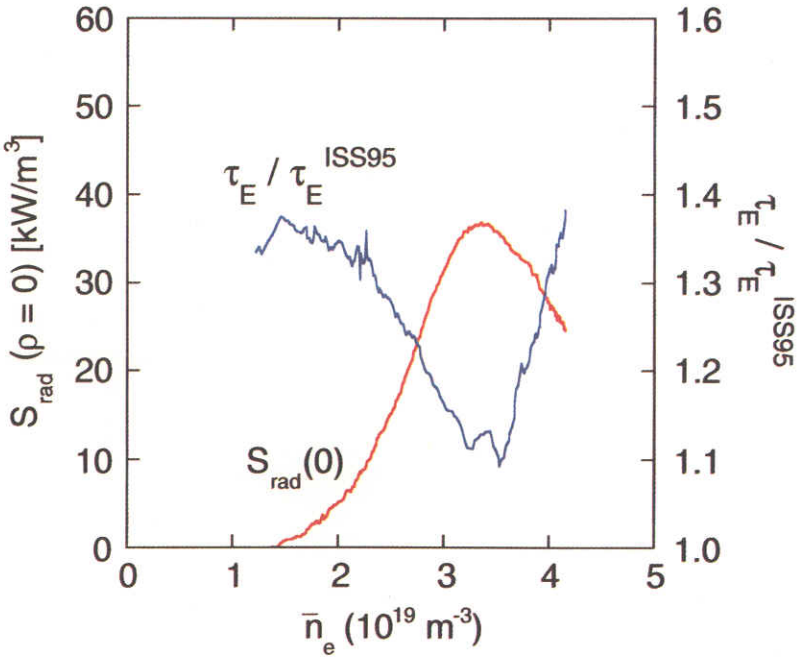
60
50
40
30
20
10
0
1.6
1.5
1.4
1.3
1.2
1.1
1.0
0
1
2
3
4
5
τ_E / τ_E^{ISS95}
$S_{rad}(0)$
S_{rad} (ρ = 0) [kW/m^3]
τ_E / τ_{ISS95}
$\bar{n}_e$ (10^{19} m^{-3})

Fig. 6

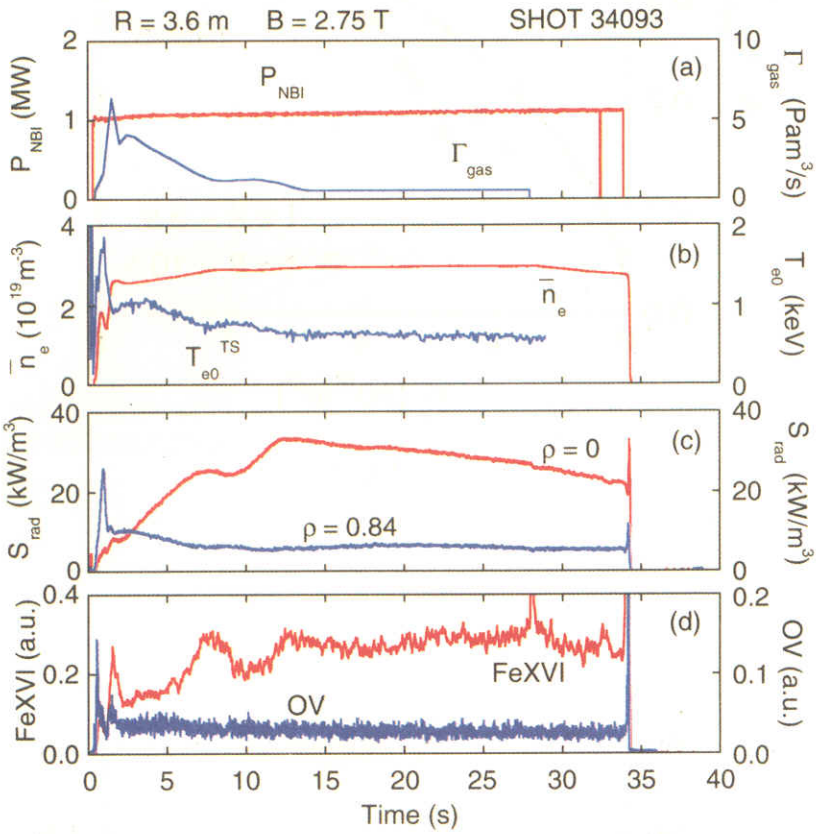
R = 3.6 m
B = 2.75 T
SHOT 34093
(a)
P_NBI
Γ_gas
P_NBI (MW)
Γ_gas (Pam³/s)
(b)
n̄_e
T_e0^TS
n̄_e (10¹⁹m⁻³)
T_e0 (keV)
(c)
ρ = 0
ρ = 0.84
S_rad (kW/m³)
(d)
FeXVI
OV
FeXVI (a.u.)
OV (a.u.)
Time (s)

Fig. 7

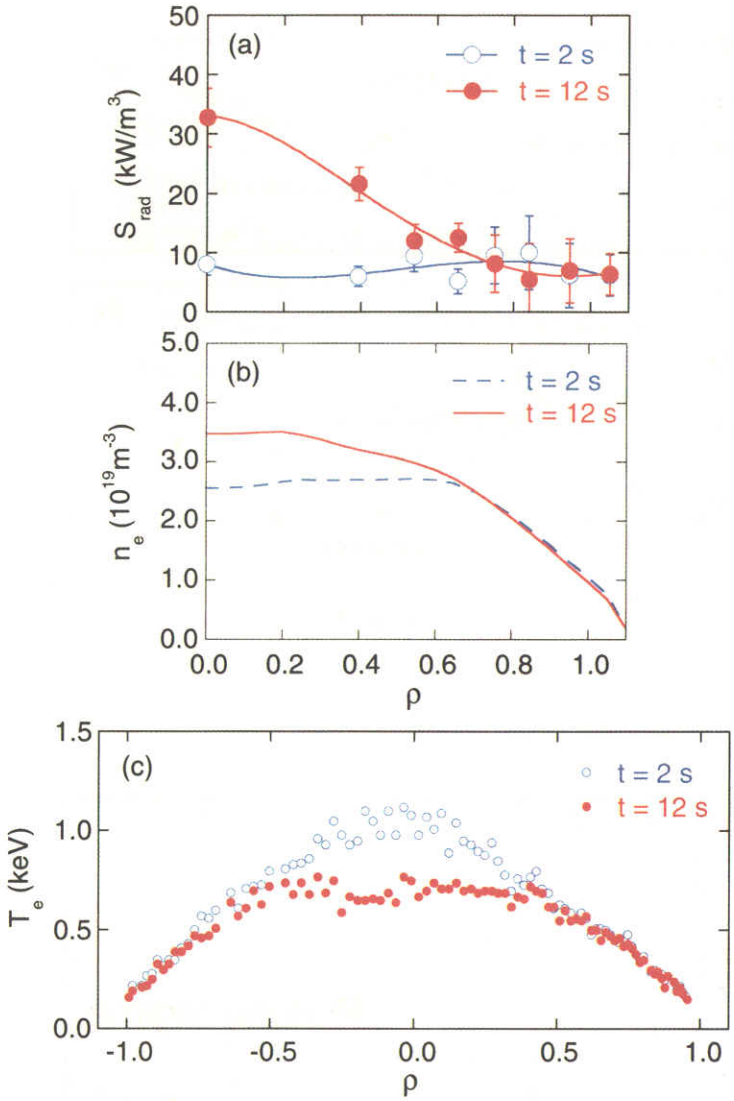

Fig. 8

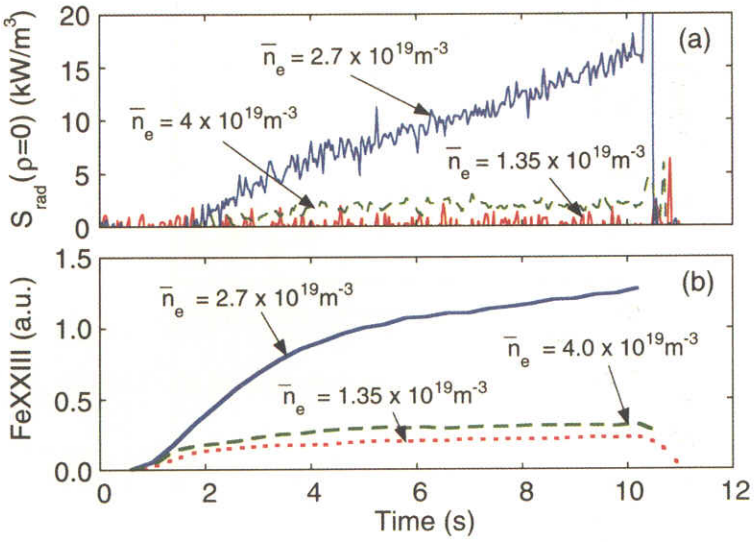
(a)
$\bar{n}_e$ = 2.7 x 10^{19}m^{-3}
$\bar{n}_e$ = 4 x 10^{19}m^{-3}
$\bar{n}_e$ = 1.35 x 10^{19}m^{-3}
S_{rad}(ρ=0) (kW/m^3)
(b)
$\bar{n}_e$ = 2.7 x 10^{19}m^{-3}
$\bar{n}_e$ = 4.0 x 10^{19}m^{-3}
$\bar{n}_e$ = 1.35 x 10^{19}m^{-3}
FeXXIII (a.u.)
Time (s)

Fig. 9

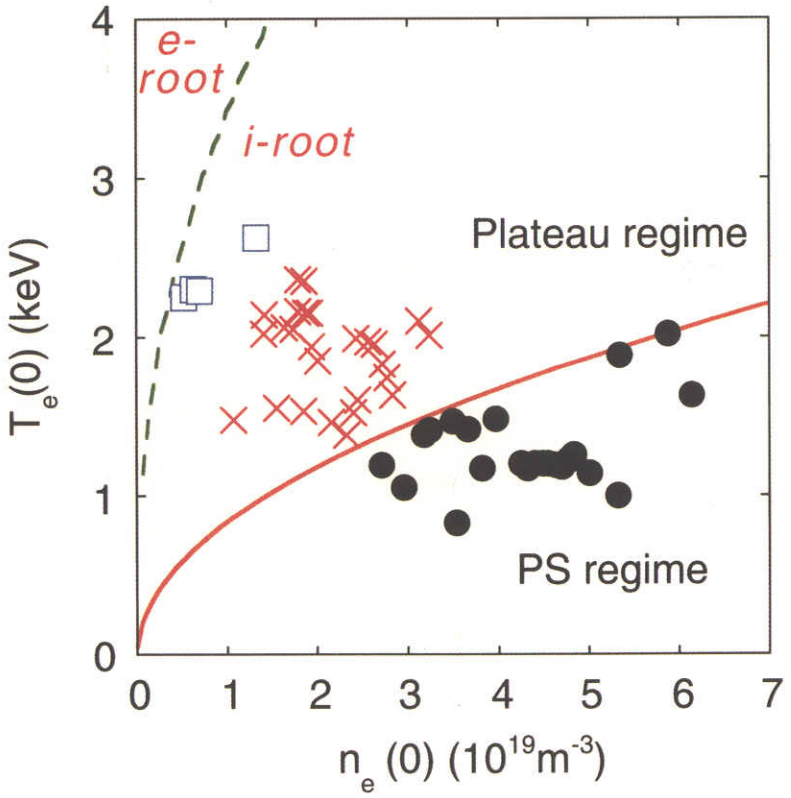
e-root
i-root
Plateau regime
PS regime
T_e(0) (keV)
n_e (0) (10^{19}m^{-3})

Fig. 10

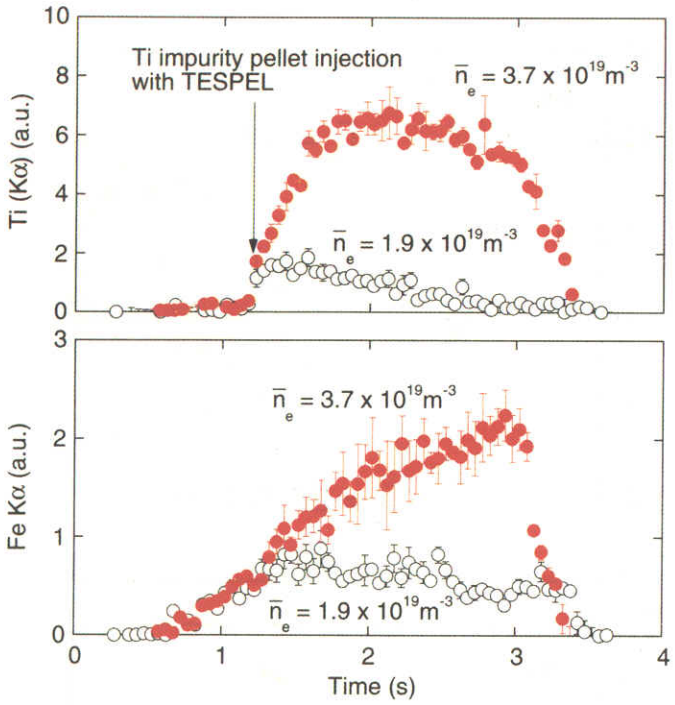
Ti impurity pellet injection
with TESPEL
$\bar{n}_e$ = 3.7 x 10^{19}m^{-3}
$\bar{n}_e$ = 1.9 x 10^{19}m^{-3}
Ti (Kα) (a.u.)
Fe Kα (a.u.)
Time (s)

Fig. 11

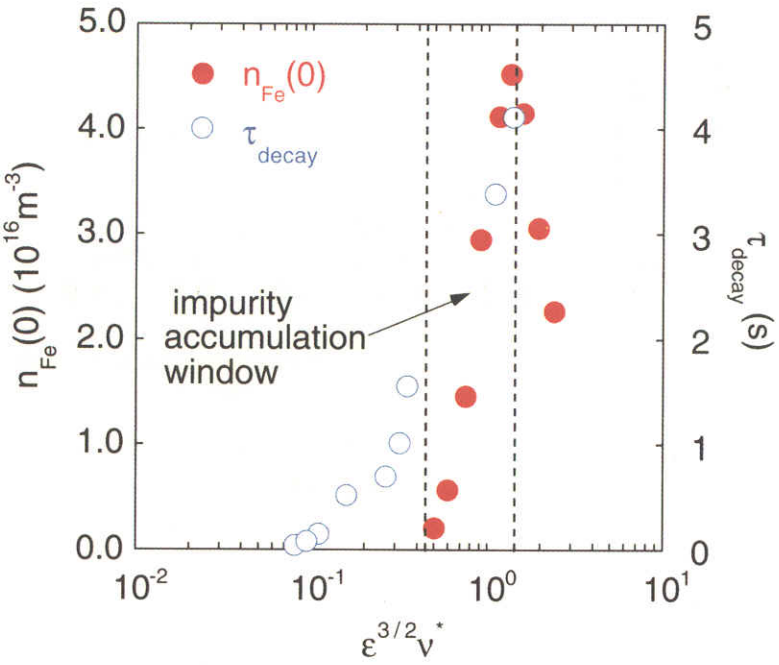
$n_{Fe}(0)$
τ_{decay}
impurity
accumulation
window
$n_{Fe}(0)$ (10^{16}m^{-3})
τ_{decay} (s)
$\varepsilon^{3/2}\nu^*$

Fig. 12

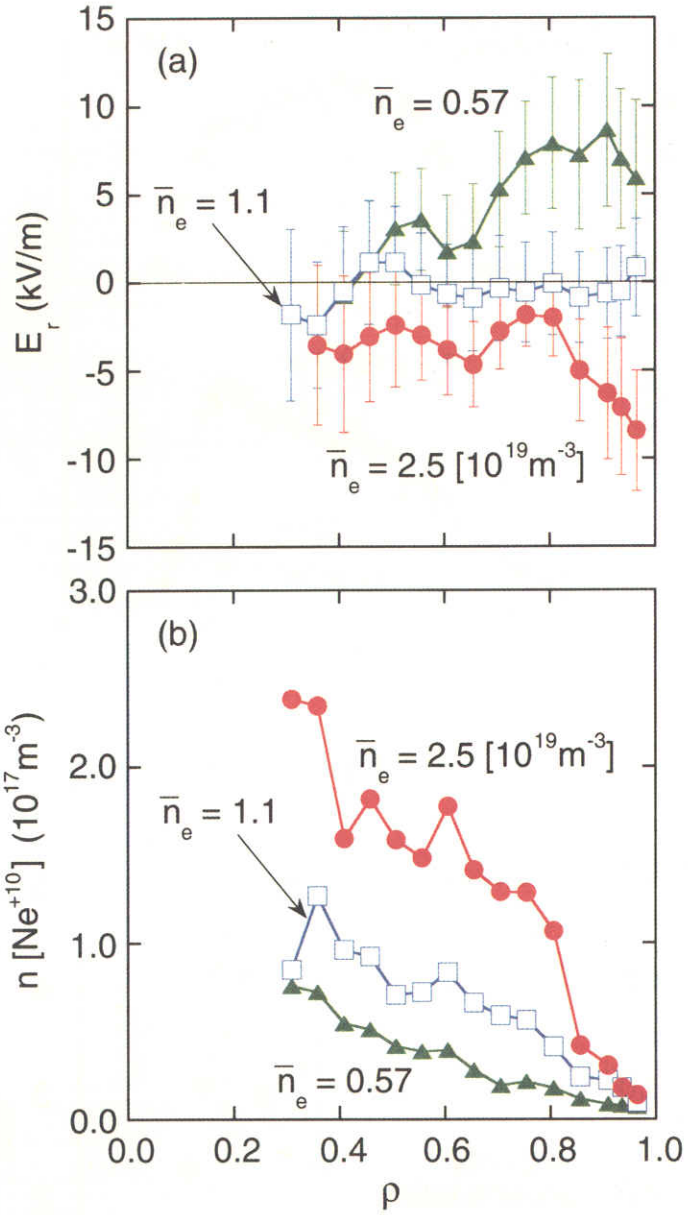
(a)
$\bar{n}_e$ = 0.57
$\bar{n}_e$ = 1.1
$\bar{n}_e$ = 2.5 [$10^{19}$$m^{-3}$]
E_r (kV/m)
15
10
5
0
-5
-10
-15
(b)
$\bar{n}_e$ = 2.5 [$10^{19}$$m^{-3}$]
$\bar{n}_e$ = 1.1
$\bar{n}_e$ = 0.57
n [Ne^{+10}] ($10^{17}$$m^{-3}$)
3.0
2.0
1.0
0.0
0.0
0.2
0.4
0.6
0.8
1.0
ρ

Fig. 13

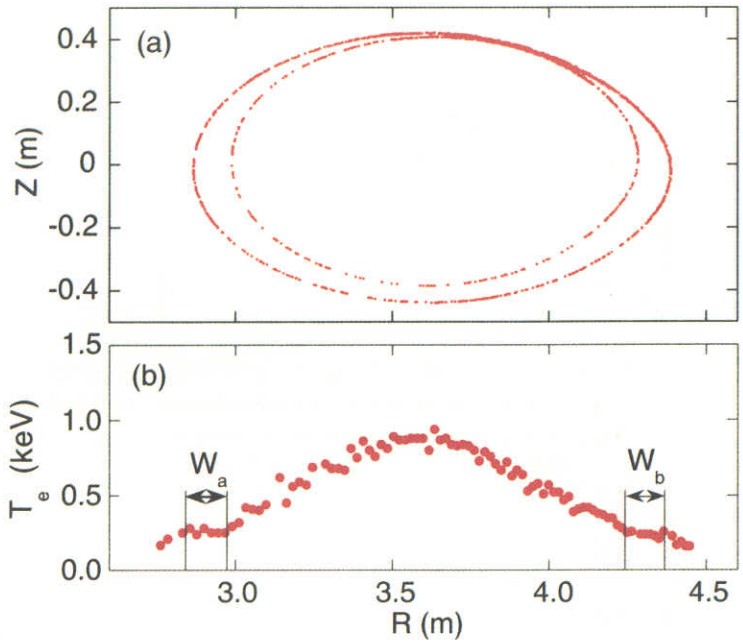
(a)
Z (m)
0.4
0.2
0
-0.2
-0.4
(b)
T_e (keV)
1.5
1.0
0.5
0.0
W_a
W_b
3.0
3.5
4.0
4.5
R (m)

Fig. 14

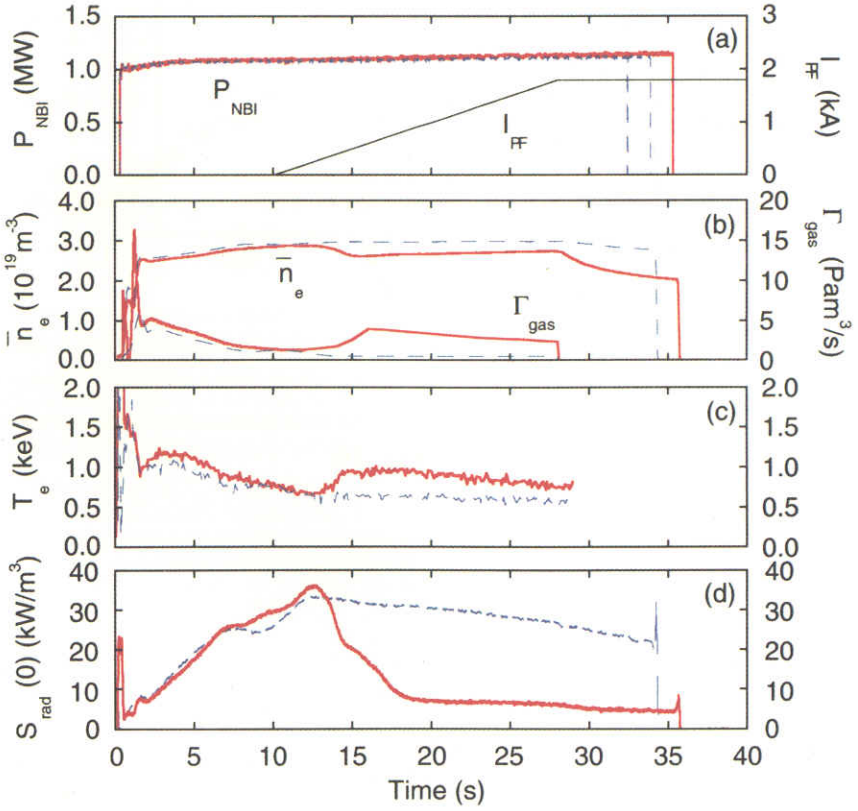
(a)
P_NBI (MW)
I_PF (kA)
P_NBI
I_PF
(b)
n̄_e (10^19 m^-3)
Γ_gas (Pam^3/s)
n̄_e
Γ_gas
(c)
T_e (keV)
(d)
S_rad (0) (kW/m^3)
0
5
10
15
20
25
30
35
40
Time (s)

Fig.15

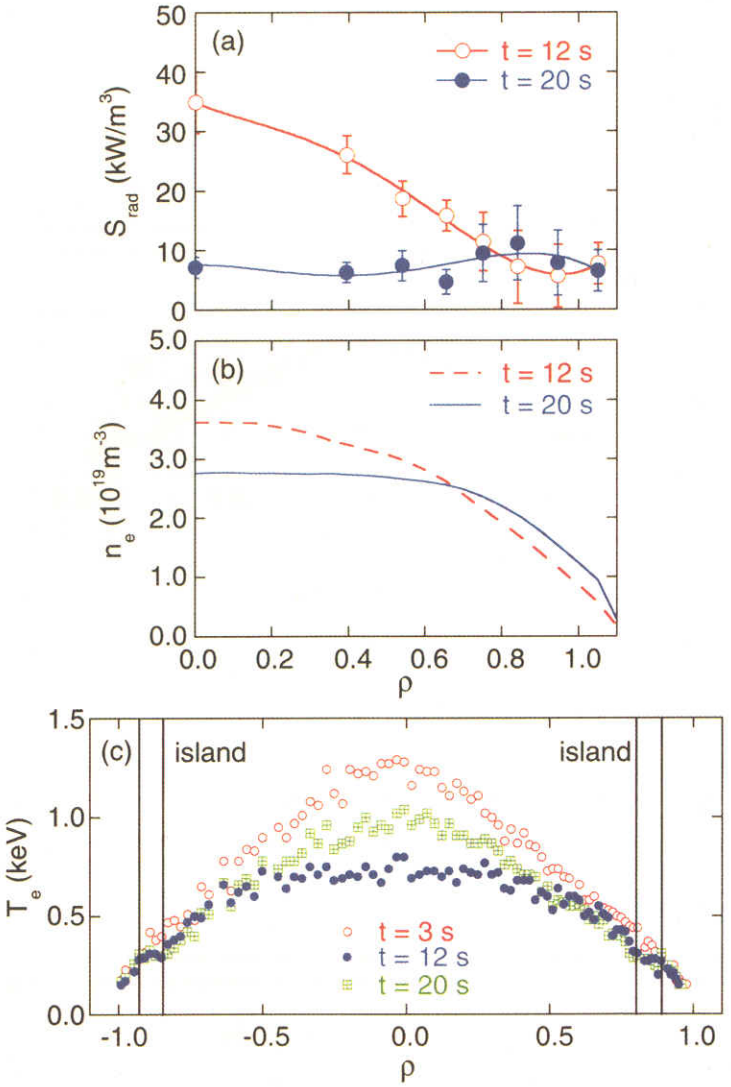
(a)
t = 12 s
t = 20 s
S_{rad} (kW/m^3)
(b)
t = 12 s
t = 20 s
n_e (10^{19}m^{-3})
ρ
(c)
island
island
t = 3 s
t = 12 s
t = 20 s
T_e (keV)
ρ

Fig. 16

A Demonstration of Magnetic Field Optimization in LHD

S. Murakami 1), H. Yamada 1), A. Wakasa 2), M. Sasao 1), M. Isobe 1), T. Ozaki 1), P. Goncharov 3), T. Saida 3), J. F. Lyon 4), M. Osakabe 1), K. Narihara 1), K. Tanaka 1), H. Inagaki 1), S. Morita 1), K. Ida 1), J. Miyazawa 1), H. Idei 1), K. Ikeda 1), S. Kubo 1), R. Kumazawa 1), T. Mutoh 1), Y. Oka 1), K. Saito 1), T. Seki 1), Y. Takeiri 1), Y. Torii 5), K. Tumori 1), T. Watari 1), K. Y. Watanabe 1), H. Funaba 1), M. Yokoyama 1), H. Maassberg 6), C. D. Beidler 6), K. Itoh 1), O. Kaneko 1), A. Komori 1), T. Akiyamal 7), N. Ashikawa 1), M. Emoto 1), M. Goto 1), K. Kawahata 1), H. Kawazome 8), K. Khlopenkov 1), T. Kobuchi 1), A. Kostrioukov 1), Y. Liang 1), S. Masuzaki 1), T. Minami 1), T. Morisaki 1), S. Muto 1), Y. Nagayama 1), Y. Nakamura 1), H. Nakanishi 1), Y. Narushima 1), K. Nishimura 1), N. Noda 1), T. Notake 1), H. Nozato 9), S. Ohdachi 1), N. Ohyabu 1), B. J. Peterson 1), A. Sagara 1), S. Sakakibara 1), R. Sakamoto 1), K. Sato 1), M. Sato 1), T. Shimozuma 1), M. Shoji 1), H. Suzuki 1), N. Takeuchi 5), N. Tamura 1), K. Toi 1), T. Tokuzawa 1), Y. Xu 1), I. Yamada 1), S. Yamamoto 5), T. Yamamoto 5), Y. Yoshimura 1), M. Yoshinuma 1), M.Y. Tanaka 1), S. Okamura 1), S. Yoshimura 1), K. Nagaoka 1), T. Satow 1), S. Imagawa 1), T. Mito 1), I. Ohtake 1), T. Uda 1), K. Ohkubo 1), S. Sudo 1), K. Yamazaki 1), K. Matsuoka 1), O. Motojima 1), Y. Hamada 1), M. Fujiwara 1)

1) National Institute for Fusion Science, Toki, Gifu 509-5292, Japan
2) Graduate School of Engineering, Hokkaido University, Sapporo 060-8628, Japan
3) Department of Fusion Science, School of Mathematical and Physical Science, Graduate University for Advanced Studies, Hayama, 240-0193, Japan
4) Oak Ridge National Laboratory, Oak Ridge, TN 37831-8072, USA
5) Department of Energy Engineering and Science, Nagoya University, 464-8603, Japan
6) Max-Planck-Institut fuer Plasmaphysik, EURATOM Ass., D-17491 Greifswald, Germany
7) Research Laboratory for Nuclear Reactors, Tokyo Institute of Technology, Tokyo 152-8550, Japan
8) Graduate School of Energy Science, Kyoto University, Uji 611-0011, Japan
9) Graduate School of Frontier Sciences, The University of Tokyo 113-0033, Japan

e-mail contact of main author: murakami@nifs.ac.jp

Abstract. An optimized configuration of the neoclassical transport and the energetic particle confinement to a level typical of so-called "advanced stellarators" is found by shifting the magnetic axis position in LHD. Electron heat transport and NBI beam ion distribution are investigated in low-collisionality LHD plasma in order to study the magnetic field optimization effect on the thermal plasma transport and the energetic particle confinement. A higher electron temperature is obtained in the optimized configuration, and the transport analysis suggests a considerable effect of neoclassical transport on the electron heat transport assuming the *ion-root* level of radial electric field. Also a higher energetic ion distribution of NBI beam ions is observed showing the improvement of the energetic particle confinement. These obtained results support a future reactor design by magnetic field optimization in a non-axisymmetric configuration.

1. Introduction

Improvement of the energetic particle confinement and the reduction of the neoclassical transport are key issues in the development of a reactor based on the helical system. Recently, efforts have been undertaken to find configurations having both significantly reduced neoclassical transport and good MHD stability, so-called ``advanced stellarators''. However, the effects of magnetic optimization on the thermal transport and the energetic particle confinement have not been experimentally verified satisfactorily. The experimental

demonstration of the magnetic field optimization (``advanced stellarators'' level) is required for the prospect of a reactor design based on the magnetic field optimization.

On the other hand, the Large Helical Device (LHD)[1] has been constructed as a standard heliotron type device, where a configuration called the ``standard'' configuration, with the magnetic axis at a major radius of R_{ax}=3.75m, has been proposed. This configuration satisfies the requirements for good plasma performance, i.e. good particle confinement, high plasma beta, and the presence of a divertor. However, a relatively large effective helical ripple exists and the existence of strong positive radial electric field (*electron-root*) is indispensable for the reactor design in this configuration. To exclude this condition, further optimization of neoclassical transport is possible[2,3] if we exclude the ideal MHD stability condition[4].

LHD experiments started in 1998 and have shown good plasma[5-7]. The experiments have been performed not only in the standard configuration (R_{ax}=3.75m) but also in the ``inward shifted'' configuration (R_{ax}=3.6m), in which the ideal MHD stability analysis predicts instability. Interestingly, however, no degradation of the plasma confinement has been observed in the experimental plasma of the R_{ax}=3.6m configuration and, furthermore, the energy confinement is found to be better than that of the R_{ax}=3.75m case[8]. The similar improvement of plasma confinement in the inward shifted configuration was also observed in the CHS[9]. These facts suggest that the MHD stability problem is not a severe one for plasma confinement in heliotron and makes it reasonable to consider shifting the magnetic axis further inwards where further improvement of the neoclassical transport can be expected in LHD. Actually, LHD can be operated in the configuration shifting the magnetic axis from 3.45m to 4.05m.

In this paper, we show an optimized configuration in LHD to a level typical of so-called "advanced stellarators", and demonstrate experimentally the effect of magnetic field optimization on the thermal plasma transport and the energetic particle confinement.

2. Magnetic field optimization in LHD

The shift of the magnetic axis alters the magnetic field configuration in flux coordinates. In the R_{ax}=3.75m (``standard'' configuration) case there are two dominant magnetic field components, the main helical curvature term, $B_{2,10}$, and the toroidal curvature term, $B_{1,0}$, and an additional small component $B_{1,10}$. Shifting the magnetic axis inwards to R_{ax}=3.6m, two side bands of the main helical curvature term, $B_{1,10}$ and $B_{3,10}$, increase and their amplitudes become comparable to that of $B_{1,0}$. Then the R_{ax}=3.6m configuration conforms to a ``σ-optimized'' field[10], where the neoclassical transport would be significantly improved relative to a standard heliotron configuration. A further inward shift of the magnetic axis increases the toroidal mirror term, $B_{0,10}$, in addition to the two side band terms.

We evaluate a mono-energetic local transport coefficient using DCOM (Diffusion COefficien calculator by Monte-Carlo method)[11,12] in which test particle orbits are followed solving the equations of motion in Boozer coordinates and the transport coefficient is evaluated statistically from the mean square displacement of the particles. Thus, DCOM can be applicable to the local neoclassical transport analysis and the global simulation code, e.g. GNET[13], should be applied in the case where the large orbit size of trapped particle plays an important role.

The diffusion coefficients are evaluated for configurations with different magnetic axis

positions, R_{ax}, at three different normalized plasma radii; r/a =0.25, 0.5, and 0.75. In this study we assume electrons as test particles with an energy of 3keV. The magnetic field is set to 3T at the magnetic axis. We select two typical collision frequencies, ν; one is ν=3.16 x 10^3 sec^{-1}, at which a 3keV electron is in the 1/ ν regime and the other is ν=3.16 x 10^5 sec^{-1}, at which the electron is in the plateau regime. Figure 1 shows the normalized mono-energetic transport coefficients, $D^*(=D/D_p)$, in the 1/ ν and the plateau regimes. The transport coefficients are normalized by the plateau value of the equivalent circular tokamak, $D_p=(\pi/16)(v^3/\iota R\omega_c^2)$, where v, R, ι and ω_c are the electron velocity, the major radius, the rotational transform, and the cyclotron frequency, respectively.

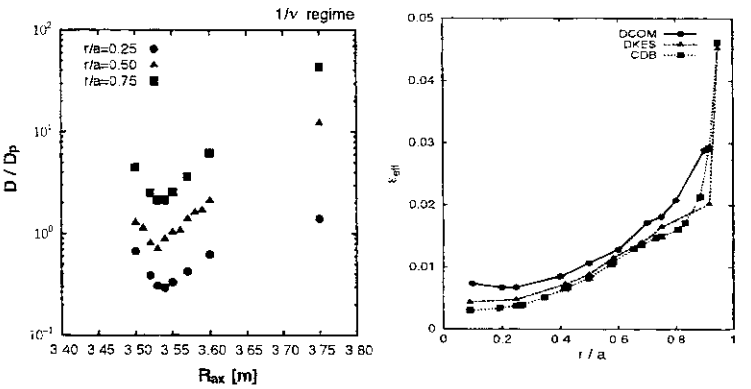

FIG. 1. Plots of the normalized neoclassical transport coefficients evaluated by DCOM in the 1/ν regime (left) and the radial profiles of the effective helical ripple in the R_{ax}=3.53m configuration evaluated by DCOM, DKES, and an analytic formula (right).

We can see a strong reduction of the diffusion coefficient by shifting the magnetic axis inwards from R_{ax}=3.75m and an optimum point is found around R_{ax}=3.53m in the 1/ν regime in Fig. 1 (top). Interestingly, the radial dependence of the optimum axis position is weak and the optimum positions are at R_{ax}=3.53m in the r/a=0.5 and 0.75 cases, and at R_{ax}=3.54m in the r/a=0.25 case. Thus, although a bit arbitrary, we shall define the R_{ax}=3.53m configuration as the neoclassical-transport-optimized configuration of the LHD.

In the plateau regime the diffusion coefficient decreases monotonically by shifting the magnetic axis inwards. This is due to the reduction of $B_{1,0}$, and also the coupling of the toroidal and helical contributions by $B_{1,10}$[11]. A similar coupling of the toroidal and helical contributions in the plateau regime is also found in helias configuration[14].

In order to compare the neoclassical transport level with that of other devices, the effective helical ripple for 1/ν transport, ε_{eff}, is evaluated by the relation between the transport coefficients and collision frequency in the 1/ν regime. Figure 1(rihght) shows the radial profile of ε_{eff} in the R_{ax}=3.53m configuration evaluated by DCOM, DKES[15,16] and a recently developed analytic formula by C.D. Beidler, et. al[17]. All three results show a very small value of ε_{eff} with the values obtained less than 1% up to r/a=0.5 and less than 2% up to r/a=0.8. Beyond r/a=0.8, ε_{eff} increases rapidly up to 5 %.

Next we study the energetic ion confinements in strongly inward shifted configurations of LHD. Collisionless α–particle confinements are investigated assuming reactor sized devices (α–particle; 3.4MeV, Plasma volume; 1000 m^3, and Magnetic field; 5 T)[18] based on three typical configurations of LHD with different magnetic axis positions in the major radius; R_{ax}=3.75m, 3.6m, 3.53m.

Figure 2 shows typical orbits of helically trapped α–particles in the three configurations of reactor sized LHD; R_{ax}=3.75m (left) and 3.53m (right). We plot the toroidal projection of the

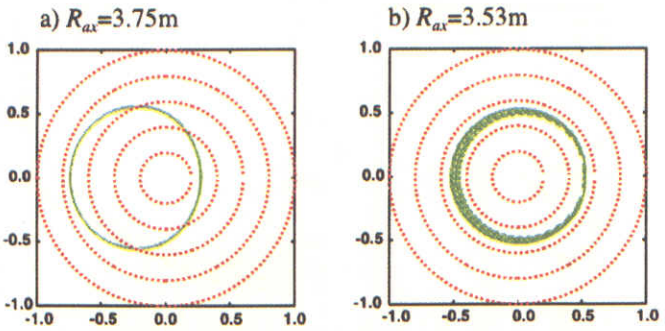

FIG. 2. Typical orbit of a helically trapped particle (pitch angle: 0.47π) in the three configurations of reactor sized LHD based on the R_{ax}=3.75m (left) and 3.53m d (right) configurations.

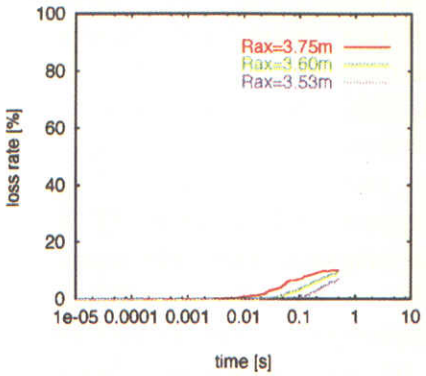

FIG. 3. Time development of alpha-particle loss rates in the three configurations of reactor sized LHD.

orbits in the Boozer coordinates. The co-centric circles correspond to magnetic surfaces. We can see the deviation of the trapped particle orbit from the magnetic surfaces reduced by shifting the magnetic axis position inwardly. The deviation almost disappears in the R_{ax}=3.53m case.

We evaluate the loss rate of α–particles as a function of time in Fig. 3. It is found that there is no loss before 0.01 s but the loss rate increases after 0.01s in the R_{ax}=3.75m case. However the loss of α–particle starts after the energy slowing down time (~0.1s) in the R_{ax}=3.53m case. Thus a sufficient confinement of α–particle is obtained in the R_{ax}=3.53m configuration for a helical reactor.

Consequently, the neoclassical transport analysis shows the optimum configuration with respect to 1/ν transport. Also the deviation of trapped particle orbit from magnetic surfaces is very small and good confinement of α–particle is obtained for a time longer than the energy slowing-down time in the reactor scaled device. These facts indicate flexibility of LHD configuration from the standard helical to an optimized configuration with a level typical of so-called``advanced stellarators'' (a small effective helical ripple < 2% and a good energetic particle confinement during the energy slowing-down time).

3. Optimization effect on thermal plasma transport

The electron heat transport in the long-mean-free-path regime (1/ν regime) is investigated to clarify the magnetic field optimization effect on the thermal plasma transport in the LHD. The electron heat transport coefficients are estimated by shifting the magnetic axis position, R_{ax}. We considered three typical configurations; R_{ax}=3.45m, 3.53m and 3.6m. In order to compare the electron heat transport we set the magnetic field strength so that the heating deposition profile is similar in the three configurations. Because we cannot set the ECH resonance point to the magnetic axis in the R_{ax}= 3.6m case, the heating deposition is adjusted to distribute inside of $r/a < 0.2$.

Figure 4 shows a comparison of electron temperatures obtained by the Thomson scattering system (center) in the three configurations (R_{ax}= 3.45m [#32347, t=0.42s], 3.53 m [#32303, t=0.52s] and 3.6 m [#32123, t=0.52s]) with nearly the same density profile (left). The fitted curves of the electron temperatures are also shown in the Fig. 3 (right). We cannot see a clear difference in the electron temperature in the region $r/a > 0.7$, though a higher electron

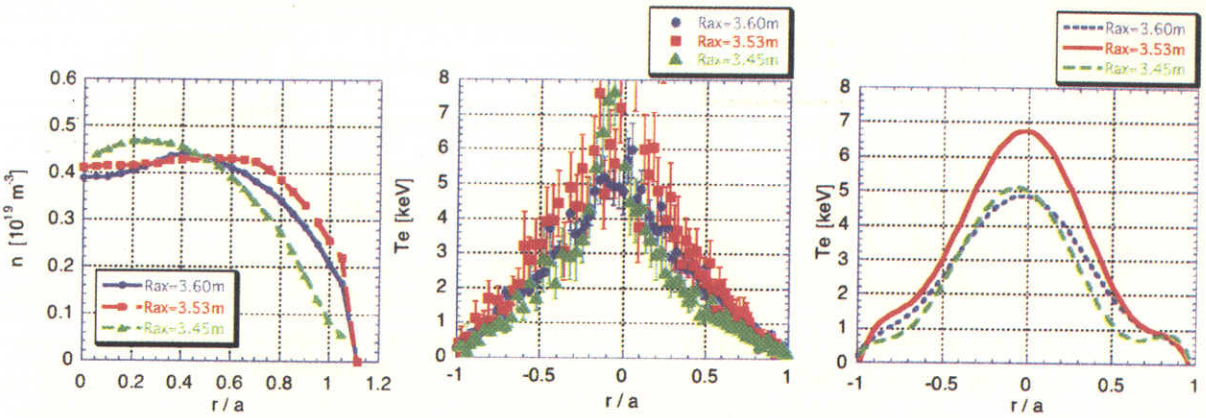

FIG. 4. Comparisons of the radial profiles of the density (left), the electron temperature (center), and the fitted curves of the electron temperatures (right) in the three configurations (R_{ax} = 3.45m [#32347, t=0.42s], 3.53 m [#32303, t=0.52s] and 3.6 m [#32123, t=0.52s]).

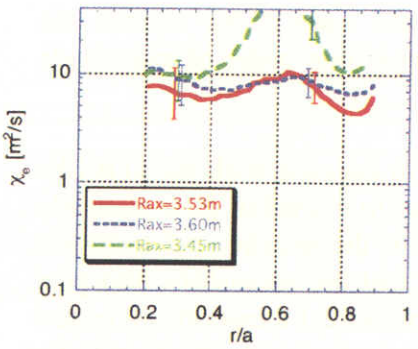

FIG. 5. The estimated effective electron heat transport coefficients in the three configurations.

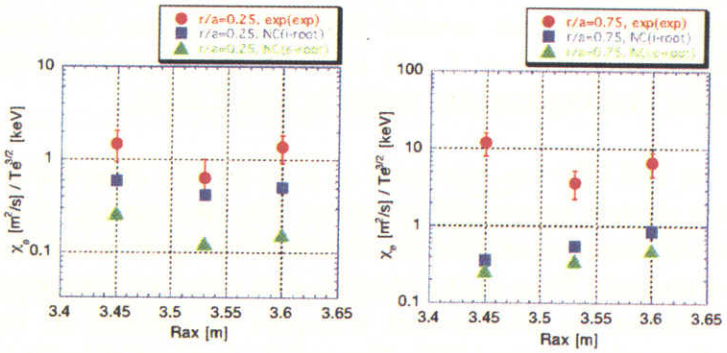

FIG. 6. Comparisons of the neoclassical transport and the experimentally observed electron heat transport at r/a=0.25 (left) and 0.75 (right).

temperature is observed in the central region ($r/a < 0.4$) in the R_{ax} = 3.53 m configuration case. Near the magnetic axis the electron temperature rapidly increases in the R_{ax} = 3.45 m case. This would be due to the rather peaked ECH deposition profile compared with other two configurations.

The estimated effective electron heat transport coefficients, χ_e, are plotted in Fig. 5. The obtained χ_e shows nearly the same value around 10m^2/s from r/a=0.2 to 0.4 even though the different electron temperatures in three configuration cases. Considering a strong electron temperature dependency of χ_e, this indicates an improvement of χ_e in the central region ($r/a <$ 0.4) in the R_{ax}= 3.53m case, where the highest electron temperature is observed. We can see the increase of χ_e near r/a=0.6 in the R_{ax}= 3.45m case is due to the temperature flattening from r/a=0.5 to 0.7.

We analyze the neoclassical transport using the DCOM code to show the role of neoclassical transport. In this experiment there is no measurement of the radial electric field, E_r, and ion temperature profile. So as a first step we evaluated the neoclassical transport coefficient assuming E_r values of the *ion-root* (~1kV) and *electron-root* (~6kV) levels. Figure 6 shows the comparisons of the neoclassical transport and the experimentally observed electron heat

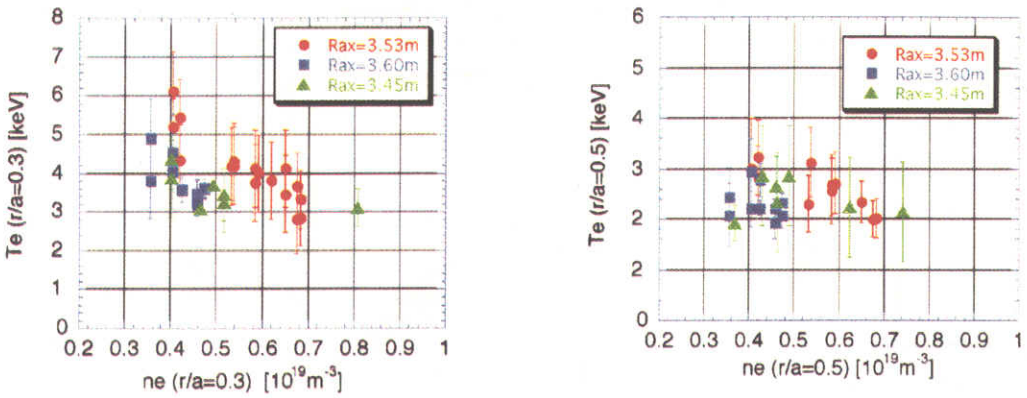

FIG. 7. Comparisons of the density dependencies of the electron temperature in the three configurations at r/a=0.3 and 0.5.

transport at r/a=0.25 (left) and 0.75 (right). We can see the considerable effect of neoclassical transport if we assume the *ion-root* level of E_r at r/a=0.25, while the neoclassical transport coefficient becomes several times smaller than the experimental ones if we assume the *electron-root* level of E_r. At r/a=0.75 the neoclassical transport is one order of magnitude smaller than experimental values in both E_r cases.

In the LHD the *ion-root* level of E_r is usually observed except in the case with the ITB-like steep electron temperature gradient. Thus we consider that the *ion-root* level of E_r is plausible and the improvement of electron heat transport would be due to the neoclassical transport optimization. Even in the *electron-root* case, we can emphasize that the anomalous transport in addition to neoclassical transport is reduced in the neoclassical-transport-optimized configuration of the LHD. The radial electric field will be measured and its effects will be clarified in the near future.

Figure 7 shows the comparison of the density dependence of the electron temperature in the three configurations at r/a=0.3 and 0.5. We found that the achieved electron temperature at r/a =0.3 is higher in the R_{ax} = 3.53m case compared with two other configurations and this difference shrinks as the density increases. At r/a =0.5 the difference becomes smaller and no clear difference can be seen among the three configurations.

4. Optimization effect on energetic particle confinement

The NBI beam ion distribution is investigated to clarify the magnetic field optimization effect on the energetic particle confinement in the LHD. The count rates of the neutral particle analyzers are compared during NBI heating by shifting the magnetic axis position, R_{ax}. We considered three typical configurations with R_a values near optimized point (3.53m, 3.6m and 3.75m). Figure 8 shows the energy loss rate by orbit loss evaluated by GNET[13] as a function of R_{ax}. In the LHD the tangential injection NBI heating is applied and the fraction of energy loss by orbit loss is normally small. So, this predicts a significant improvement of trapped energetic particle confinement in inward shifted configuration.

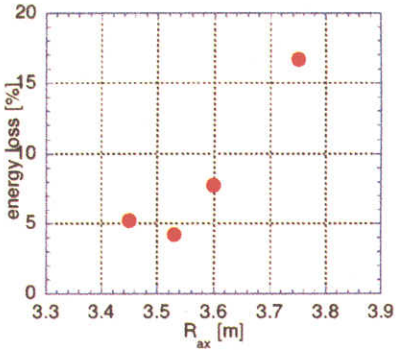

FIG.8. R_{ax} dependency of NBI heating energy loss rate by orbit loss evaluated by GNET

We study the NBI beam ion distribution by silicon detector-based neutral particle analyzer (SDNPA). A compact quasilinear horizontal array of six ion-implanted silicon detectors is used and a vertically movable collimating aperture provide two-dimensional scan of the non-axisymmetric LHD plasma column. The angle between the sight lines in the horizontal direction is 4.6 degrees. The angular sector observable due to the vertical scan is 14 degrees. The geometry of experiments is shown in Fig. 9. We evaluate the neutral particle count in the pitch angle region of trapped and partially trapped particles and compared the results changing the magnetic axis position with nearly same density (~$0.7\times10^{19}m^{-3}$) and heating power

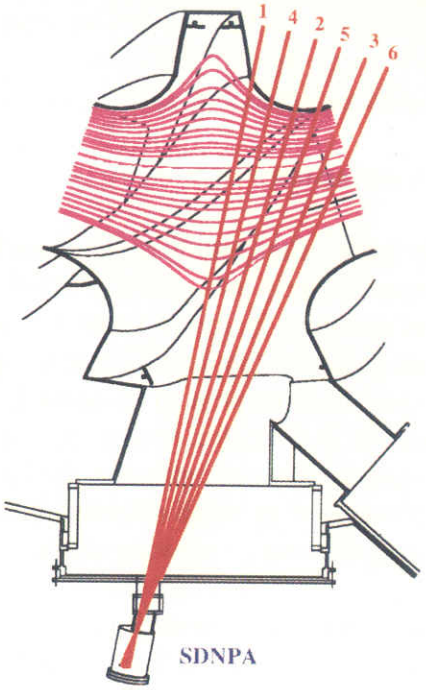

FIG. 9. SDNPA viewing chords

Figure 10 shows the comparisons of the normalized count rate of the three configurations for the chord #6 (left) and #2 (right). SDNPA chord #6 measures the pitch angle of 40 to 50 degrees and #2 is from 55 to 65 degrees. The initial pitch angles of NBI beam ions are less than 45 degrees. Because the thermal plasma confinement depends on R_{ax} in LHD, the obtained electron temperature is higher in the inward shifted case. So we normalized the count rate by the count rate at the slightly lower energy of the beam injection (140keV) so that we can directly compare the slowing-down process excluding the count rate difference due to the difference of the slowing-down time.

We can see the difference of the slope from injection energy to the thermal energy in the chord #6 (Fig. 10, left). In the R_{ax}=3.53m case larger increase of the normalized count number can be seen compare with others. The count rate is decreased until around 100keV in the R_{ax}=3.75m case. In this energy region the energy slow-down by electron plays dominant role in beam ion collisions with thermal plasma and this difference due to the radial diffusion of transition particle. We also can see the higher count rate in the R_{ax}=3.53m case in the chord #2 (Fig. 10, right).

To see more clearly the difference of count rate in the chord #6. We plot the ratio of the count rate between at the energy of 140keV and 100keV as a function of slowing down time in the

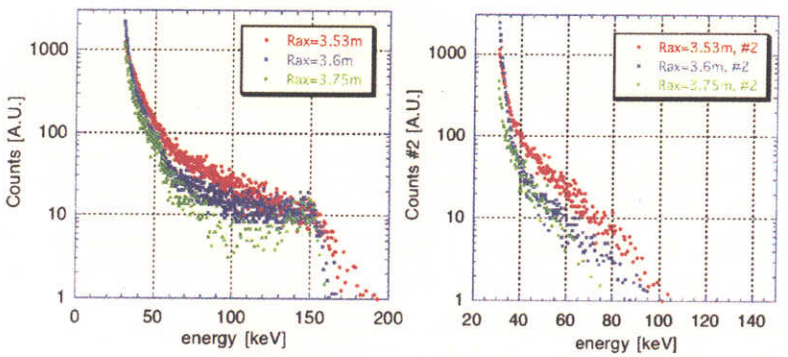

FIG. 10. Comparisons of normalized counts rate by SDNPA with the similar density in the three configuration of LHD.

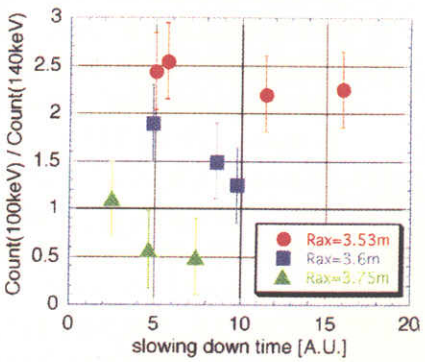

FIG. 11. Plot the ratio of the count rate between at the energy of 140keV and 100keV as a function of slowing down time.

three configurations. A clear difference can be seen in the three configurations. We can see the higher ratio in the R_{ax}=3.53m case compared with other two cases. In these cases the ratio goes up as the slowing-down time become short, because the effect of radial diffusion get smaller in the shorter slowing-down time case.

5. Conclusion

We have, first, studied the neoclassical transport for LHD configurations in which the magnetic axis has been shifted radially. With respect to 1/ν transport, the optimum configuration is found when the magnetic axis has a major radius of 3.53m. Also, in this configuration, the deviation of trapped particle orbit from magnetic surfaced is very small and a good confinement of α–particle is obtained for a time longer than the energy slow-down time in the reactor scaled device. These facts indicate that a strong inward shift of the magnetic axis can optimize the LHD configuration to a level typical of so-called``advanced stella-rators'' (a small effective helical ripple < 2% and a good energetic particle confinement during the energy slowing-down time).

Then, we experimentally demonstrate the effect of magnetic optimization on the thermal plasma transport and the energetic particle confinement in LHD. The experimental results in low collisionality plasmas show a higher electron temperature and a higher trapped ion distribution in the optimized configuration. These obtained results show further possibility of a heliotron type configuration and support a future reactor design by magnetic field optimization in a non-axisymmetric configuration.

References

[1] IIYOSHI, A., et al., Nucl. Fusion **39** (1999) 1245.
[2] TODOROKI, J., J. Phys. Soc. Jpn. **59** (1990) 2758.
[3] MURAKAMI, S., Nucl. Fusion **39** (1999) 1165.
[4] ICHIGUCHI, K., et al., Nucl. Fusion **33** (1993) 481.
[5] FUJIWARA, M., et al., Nucl. Fusion **39** (1999) 1659.
[6] MOTOJIMA, O, et al.,Phys. Plasmas **6** (1999) 1843.
[7] FUJIWARA, M, et al., Nucl. Fusion **40** (2000) 1157
[8] YAMADA, H., et al., Plasma Phys. Control. Fusion, **43**, A55(2001).
[9] OKAMURA, S., et al., Nucl. Fusion **39**, 1337(1999).
[10] MYNICK, H.E., CHU, T.K., and BOOZER, A.H., Phys. Rev. Lett. **48** (1982) 322.
[11] WAKASA, A., et al., J. Plasma Fusion Res. SERIES, Vol. **4**, 408(2001).
[12] MURAKAMI, S., et al., Nucl. Fusion **42** (2002) L19.
[13] MURAKAMI, S., et al., Nucl. Fusion **40** (2000) 693.
[14] BEIDLER, C.D. and MAASSBERG, H., in Theory of Fusion Plasmas (Proc. Joint Varenna-Lausanne International Workshop, Varenna, 1996), Editrice Compositori, Bologna (1996) 375.
[15] HIRSHMAN, S.P., et al., Phys. Fluids **29** (1986) 2951.
[16] MAASSBERG, H., et al., Phys. Fluids B **5** (1933) 3627.
[17] BEIDLER, C.D. and MAASSBERG, H., Plasma Phys. Control. Fusion **43** (2001) 1131.
[18] MURAKAMI, S., et al., J. Plasma Fusion Res. SERIES, Vol. 5 (in press).
[19] LYON, J.F., SPONG, D.A, J. Plasma Fusion Res. SERIES, 1, 358 (1998)
[20] GONCHAROV, P.R., et al. J. Plasma Fusion Res. SERIES, 5 (in press)
[21] LYON, J.F., et al. Proc. 14th High-Temp. Plasma Diagn. Conf., Rev. Sci. Instr. (to be published).

Radial Electric Field and Transport near the Rational Surface and the Magnetic Island in LHD

K.Ida, S.Inagaki, N.Tamura, T.Morisaki, N.Ohyabu, K.Khlopenkov, S.Sudo, K.Watanabe, M.Yokoyama, T.Shimozuma, Y.Takeiri, K.Itoh, M.Yoshinuma, Y.Liang, K.Narihara, K.Tanaka, Y.Nagayama, T.Tokuzawa, K.Kawahata, H.Suzuki, A.Komori, T.Akiyama[1], N.Ashikawa, M.Emoto, H.Funaba, P.Goncharov[2], M.Goto, H.Idei, K.Ikeda, M.Isobe, O.Kaneko, H.Kawazome[3], T.Kobuchi, A.Kostrioukov, S.Kubo, R.Kumazawa, S.Masuzaki, T.Minami, J.Miyazawa, S.Morita, S.Murakami, S.Muto, T.Mutoh, Y.Nakamura, H.Nakanishi, Y.Narushima, K.Nishimura, N.Noda, T.Notake[4], H.Nozato[5], S.Ohdachi, Y.Oka, M.Osakabe, T.Ozaki, B.J.Peterson, A.Sagara, T.Saida[2], K.Saito, S.Sakakibara, R.Sakamoto, M.Sasao, K.Sato, M.Sato, T.Seki, M.Shoji, N.Takeuchi[4], K.Toi, Y.Torii[4] K.Tsumori, T.Watari, Y.Xu, H.Yamada, I.Yamada, S.Yamamoto[4], T.Yamamoto[4], Y.Yoshimura, I.Ohtake, K.Ohkubo, T.Mito, T.Satow, T.Uda, K.Yamazaki, K.Matsuoka, O.Motojima, M.Fujiwara

National Institute for Fusion Science, Toki, Gifu 509-5292, Japan
1 Research Laboratory for Nuclear Reactors, Tokyo Institute of Technology, Tokyo 152-8550, Japan
2 Department of Fusion Science, School of Mathematical and Physical Science, Graduate University for Advanced Studies, Hayama, 240-0193, Japan
3 Graduate School of Energy Science, Kyoto University, Uji 611-0011, Japan
4 Department of Energy Engineering and Science, Nagoya University, 464-8603, Japan
5 Graduate School of Frontier Sciences, The University of Tokyo 113-0033, Japan

e-mail contact of main author: ida@nifs.ac.jp

Abstract.

The structure of the radial electric field and heat transport at the magnetic island in the Large Helical Device is investigated by measuring the radial profile of poloidal flow with charge exchange spectroscopy. The convective poloidal flow inside the island is observed when the n/m=1/1 external perturbation field becomes large enough to increase the magnetic island width above a critical value (15-20% of minor radius) in LHD. This convective poloidal flow results in a non-flat space potential inside the magnetic island. The sign of the curvature of the space potential depends on the radial electric field at the boundary of the magnetic island. The heat transport inside the magnetic island is studied with a cold pulse propagation technique. The experimental results show the existence of the radial electric field shear at the boundary of the magnetic island and a reduction of heat transport inside the magnetic island

1. Introduction

The structure of the magnetic island is observed in various plasma parameters. The electron temperature profiles measured with Thomson scattering or ECE signals shows flattening inside the magnetic island. [1,2]. On the other hand, density profile peaking inside the magnetic island is observed in TEXTOR and JET[3-5]. The density peaking is more significant when particles are fueled into the magnetic island by a pellet , which is observed in soft-X ray signals as a " snake" modulation in JET. If the space potential is not flat inside the magnetic island, both the radial electric field and the poloidal flow should be finite inside the magnetic island. Because of the conservation of particle flux inside the magnetic island, the poloidal flow should be convective, if it exists inside the magnetic island. When the poloidal flow is convective, the sign of the radial electric field should be reversed across the center of the magnetic island and radial electric field shear should appear inside the magnetic island. Although the structure of radial electric field and radial electric field shear are crucial

parameters to understand the good confinement (low diffusivity) inside the magnetic island, there have been no clear measurements of poloidal flow or radial electric field inside the magnetic island except at the plasma edge[6].

The Large Helical Device (LHD) [7] is a Heliotron device (poloidal period number L = 2, and toroidal period number M = 10) with a major radius of R_{ax} =3.5 – 4.1 m, an average minor radius of 0.6 m, magnetic field up to 3 T. The radial electric field (E_r) is derived from the poloidal and toroidal rotation velocity and pressure gradient of Neon impurity measured with charge exchange spectroscopy[8] at the mid plane in LHD (vertically elongated cross section) using a radial force balance. The radial force balance equation can be expressed as $E_r = (en_IZ_I)^{-1} (\partial p_I/\partial r) - (v_\theta B_\phi - v_\phi B_\theta)$, where B_ϕ and B_θ are toroidal and poloidal magnetic field and Z_I, n_I, p_I are the ion charge, density and pressure of the measured impurity, respectively.

2. Magnetic island produced by the n/m=1/1 perturbation coil

The Large Helical Device (LHD) has n/m=1/1 external perturbation coils. The size of magnetic island can be controlled up to 10cm by changing the current of the perturbation coils. The spatial resolution of the measurements of the radial electric field using the charge exchange spectroscopy is determined by the length of integration of the signal along the line of sight within the beam width of the neutral beam. The spatial resolution becomes poor near the plasma center and relatively good near the plasma edge and it is +/– 1.5cm at the R=4.05m.

Figure 1(a) shows the poloidal cross section of the last closed magnetic flux surface and magnetic island calculated (with zero beta) for the discharge with the n/m=1/1 external perturbation coil current of -1200A and electron temperature and density profiles. The magnetic island is located near the plasma edge at $\rho = 0.85$. As shown in Fig.1(b) and (c), the flattening of electron density and temperature and ion temperature are observed for the plasmas with an island and convective poloidal flow ($I_{n/m=1/1}$ = 1200A, $\langle n_e \rangle = 2.1\times10^{19}m^{-3}$) and without ($I_{n/m=1/1}$ = 390A, $\langle n_e \rangle = 2.2\times10^{19}m^{-3}$) an island as a reference. The magnetic field B is 2.83T with a vacuum magnetic axis of 3.5m. The flattening width of the electron temperature is considered to represent the width of the magnetic island in the plasma, which would not be identical to the width of the vacuum magnetic island due to the healing effect[2]. Since there is no pressure gradient inside the magnetic island, one can expect a flat space potential and zero radial electric field inside the magnetic island.

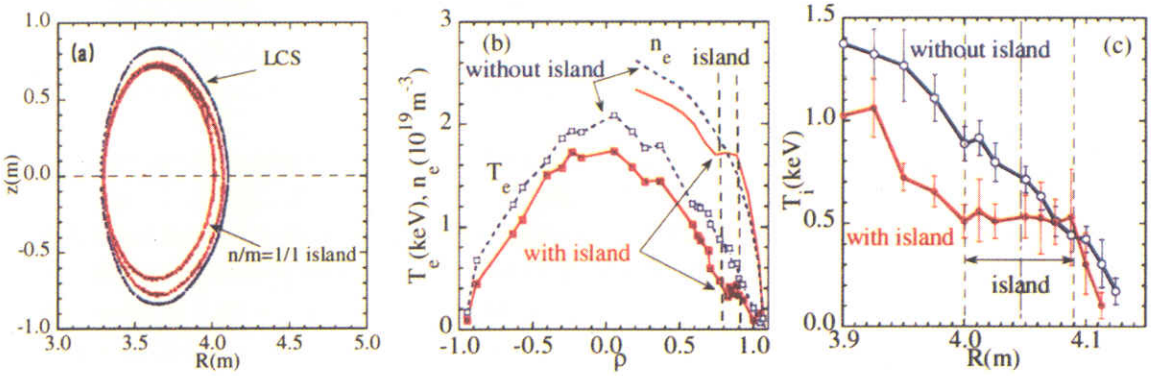

Fig.1 (a) Magnetic flux surface with 1/1 magnetic island and radial profiles of (a) electron density and temperature and (c) ion temperature profiles with and without 1/1 magnetic island.

The current of n/m=1/1 external perturbation coils is varied in a wide range from 260A to 1200A for the plasma with the magnetic field of 1.5T and vacuum magnetic axis of 3.5m and the averaged density of $\langle n_e \rangle = 1.2 \times 10^{19} m^{-3}$. When the current of n/m=1/1 external perturbation coils is small (see 260A case in Fig.2), no island structure appears in the profile of the radial electric field. As the perturbation coil current increases, the clear structure of the magnetic island appears in the radial electric field[9]. As the perturbation coil current increases, the width of the magnetic island estimated from the radial profiles of radial electric field also increases up to 9 cm, which corresponds to 17 % of the averaged minor radius. The large shear of the radial electric field is observed at the boundary of the magnetic island (R=4.00m and R=4.09m).

The bifurcation phenomena of plasma flow inside the magnetic island is observed. When the current of n/m=1/1 external perturbation coils, $I_{n/m=1/1}$, becomes large enough (see 1200A in Fig.2), the finite radial electric field appears inside the magnetic island. The radial electric field is zero at the center of the magnetic island and the sign of the radial electric field is reversed across the center of the island. The plasma flow inside the magnetic island is due to the imbalance of the viscous force between the two boundaries at the O-point of the magnetic island and the direction of the flow is determined by the sign of the radial electric field shear at the X-point of the magnetic island. The plasma flow velocity inside the magnetic island should be proportional to the square of the island width, W, as $v = (W^2/4\delta)(dV_\theta/dr)$, where δ is the shear width at the boundary of the magnetic island, if the viscous force at the boundary of the magnetic island is linearly proportional to the flow shear. Non-linearity of the viscous force [10] is required to cause the sudden appearance of plasma flow inside the magnetic island.

The flattening of space potential as well as ion temperature and electron temperature is observed inside the magnetic island, when the perturbation field is small

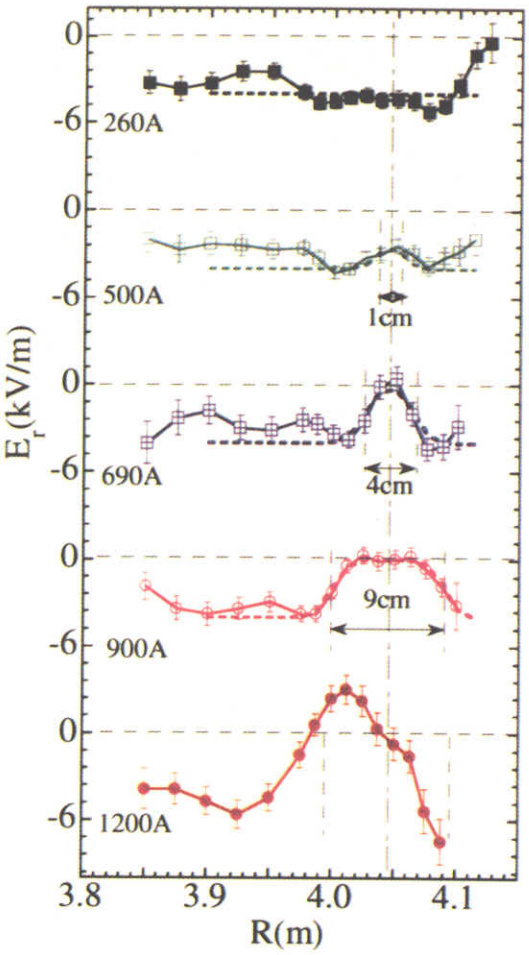

Fig.2 Radial profiles of radial electric field for various current of n/m=1/1 perturbation coil

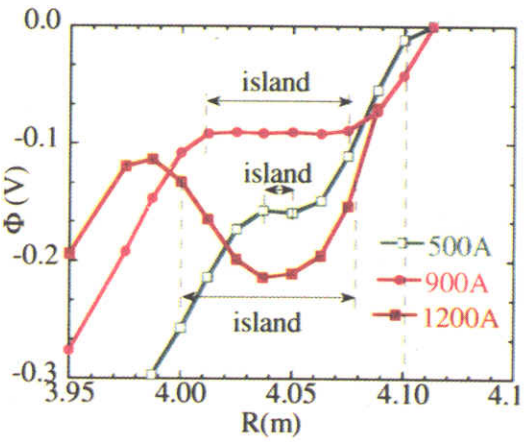

Fig.3 Radial profiles of space potential for various current of n/m=1/1 perturbation coil

as seen in Fig.3. However the convective poloidal flow inside the island is observed when the magnetic island width exceeds a critical value (15-20 %) of the minor radius. This convective poloidal flow results in a non-flat space potential ($d^2\Phi/dr^2 > 0$) inside the magnetic island, while keeping the same values of space potential at the both sides of the boundary of the magnetic island. The sign of the curvature of the space potential is determined such as to decrease the shear of poloidal flow at the boundary of the magnetic island.

3. Cold pulse propagation inside the magnetic island.

Since the radial profiles of electron temperature show a flattening inside the magnetic island, the transport analysis based on the temperature gradient and radial heat flux in the steady state is invalid. The localized flattening of the electron temperature profile is due to a modification of the magnetic topology resulting from the magnetic island produced by the perturbation field and not due to the increase of energy transport. Significant reduction of energy transport is expected inside the magnetic island, because there is no pressure driven turbulence. When there is no local heating inside the magnetic island, the electron temperature profile shows flattening even though the magnitude of the thermal diffusivity is small inside the magnetic island. In order to evaluate the transport inside the magnetic island, the response of the electron temperature to the cold pulse produced by a tracer-encapsulated solid pellet (TESPEL)[11] is investigated inside or at the boundary of the magnetic island[12].

As seen in Fig.4, the electron temperature profile measured with a ECE radiometer for the plasma with a magnetic axis of 3.5m and the magnetic field of 2.88T and with the n/m=1/1 external perturbation coil current of -1800A and the averaged density of $\langle n_e \rangle = 1.7 \times 10^{19} m^{-3}$. There is a clear flattening of the electron temperature observed at the O-point of the magnetic island, while there is no flattening observed at the X-point of the magnetic island. The ECE radiometer is located at the inboard side and TESPEL is injected from the outboard side of LHD 72 degrees apart in toroidal direction. Therefore when the measurement of the ECE radiometer is located at the X-point of the magnetic island, TESPEL is injected into the O-point and the cold pulse starts from the magnetic island. The cold pulse propagates inward (R > 2.905m) and outward (R < 2.905m) from the X-point of the magnetic island. On the other hand, when the measurement of the ECE radiometer is located at the O-point of the magnetic island, TESPEL is injected into the X-point and the cold pulse starts from the boundary of the magnetic island (R = 2.95m). Then the cold pulse propagates both inside (R < 2.95m) and outside (R > 2.95m) the magnetic island. The drop of the electron temperature due to the cold pulse is less than 10% of the electron temperature.

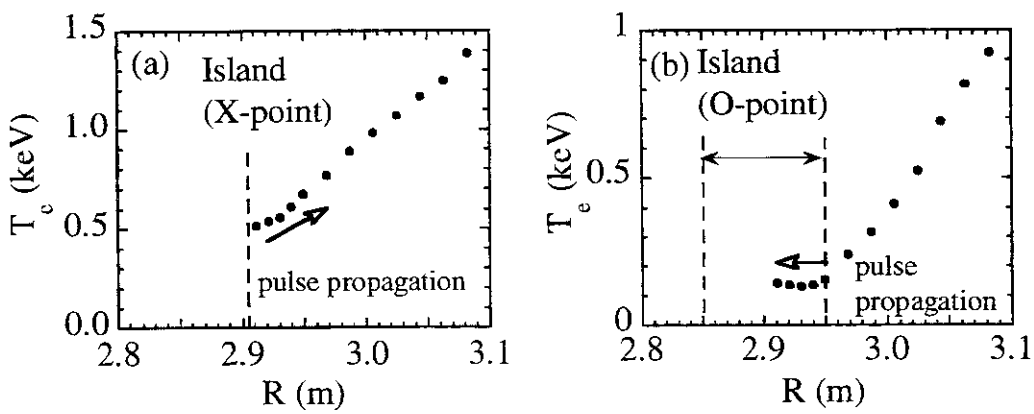

Fig.4 Radial profiles of electron temperature at the (a) X-point and (b) O-point of the magnetic island measured with ECE just before the TESPEL is injected.

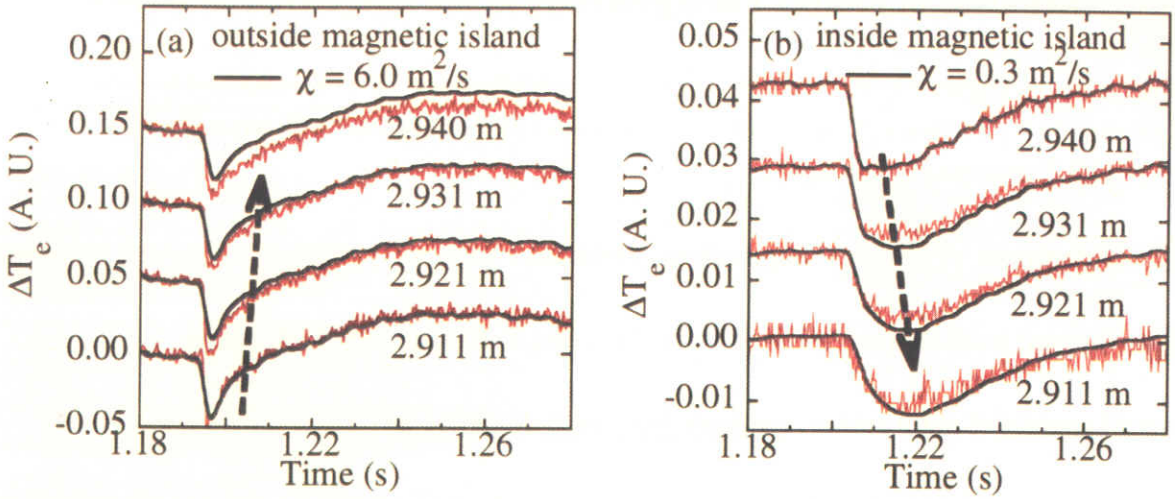

Fig.5 The time evolution of electron temperature measured with ECE (a) outside and (b) inside the magnetic island for the plasma where the TESPEL is injected.

As shown in Fig.5, the response time of the cold pulse inside the magnetic island is much longer than that observed outside of the magnetic island. The amplitude of the cold pulse is also smaller inside the magnetic island than outside of the island. The time delay and amplitude of the electron temperature of the cold pulse inside the magnetic island is reproduced by simulation of the cold pulse propagation in a slab mode with a low thermal diffusivity of $0.3m^2/s$, which is smaller than that ($6m^2/s$) outside the magnetic island by more than one order of magnitude. Because the structure of the magnetic island (the effect of poloidal asymmetry) is not included in the analysis, the estimate of the absolute value of the thermal diffusivity is rather crude. However, the differences in pulse propagation inside and outside the magnetic island clearly demonstrate the reduction of energy transport inside the magnetic island.

In conclusion, the structure of the radial electric field and heat transport at the magnetic island in LHD is investigated. The experimental results show 1) the existence of radial electric field shear at the boundary of the magnetic island, 2) plasma flow inside the magnetic island when the width of the magnetic island is large enough and 3) reduction of heat transport inside the magnetic island.

References

[1] N.J.Lopes Cardozo, et al., Phys. Rev. Lett. **73** (1994) 256.
[2] K.Narihara et al., Phys. Rev. Lett. **87** (2001) 135002.
[3] P.C.de Vries, et al., Nuclear Fusion **37** (1997) 1641
[4] A.Weller, A.D.Cheetham, A.W.Edwards, R.D.Gill, A.Gondhalekar, R.S.Granetz, J.Snipes, J.A.Wesson, Phys. Rev. Lett. **59** (1987) 2303.
[5] R.D.Gill, A.W.Edwards, D.Pasini, A.Weller, Nucl. Fusion **32** (1992) 723.
[6] C.Hidalgo et al., Plasma Phys. Control. Fusion **42** (2000) A153
[7] M.Fujiwara et al., Nucl. Fusion **40** (2000) 1157.
[8] K.Ida, S. Kado, Y. Liang, Rev. Sci. Instrum. **71** (2000) 2360.
[9] K.Ida, et. al., Phys. Rev. Lett. **88** (2002) 015002
[10] K.C.Shaing, Phys. Plasmas **9** (2002) 3470.
[11] S. Sudo et al., Plasma Phys. Control. Fusion **44** (2002) 129.
[12] S.Inagaki, et al., "Observation of Reduction of Heat Transport inside the Magnetic Island in the Large Helical Device" to be submitted to Phys. Rev. Lett.

Behavior of Plasma Facing Surface in the Large Helical Device

T.Hino 1), A.Sagara 2), Y.Nobuta 1), N.Inoue 2), Y.Hirohata 1), Y.Yamauchi 1), S.Masuzaki 2), N.Noda 2), H.Suzuki 2), A.Komori 2), N.Ohyabu 2), O.Motojima 2) and LHD Experimental Group 2)

1) Department of Nuclear Engineering, Hokkaido University, Kita-ku, Sapporo, 060-8628 Japan
2) National Institute for Fusion Science, Toki-shi, Gifu-ken, 509-5202 Japan

e-mail contact of main author: tomhino@qe.eng.hokudai.ac.jp

Abstract. Material probes have been installed at the inner walls along poloidal direction in LHD from the first experimental campaign. After each the campaign, the impurity deposition and the gas retention have been examined to clarify the plasma surface interaction and the degree of wall cleaning. In the 2nd campaign, the entire wall was considerably cleaned by helium glow discharge conditionings. For the 3rd and 4th campaigns, graphite tiles were installed at entire divertor strike region, and then the wall condition significantly changed compared to the case of stainless steel wall. The erosion of graphite took place during the main discharges and the eroded carbon deposited on the entire wall. In particular, the deposition thickness was large at the wall far from the plasma. Since the entire wall was well carbonized, amount of retained discharge gas such as H and He became large. In particular, the helium retention was large at the position close to the anodes used for helium glow discharge cleanings. One characteristics of the LHD wall is a large retention of helium gas since the wall temperature is limited below 368 K. In order to reduce the recycling of discharge gas, the wall heating before the experimental campaign and the surface heating between the main discharge shots are planned.

1. Introduction

It is quite important to know the wall conditions of fusion experimental devices and their changes arising from the progress of plasma experiments, by using plasma surface interaction (PSI) techniques. For this purpose, wall-condition data were systematically accumulated as a database and analyzed for the wall characteristics through four experimental campaigns, conducted in the Large Helical Device (LHD) since 1998, whose baking temperature is limited below 368 K. This paper presents the results obtained in all of these campaigns.

He ECR discharge cleaning was employed in the first campaign for the initial ECH plasma production, and glow discharge cleanings from the 2nd campaign for the production of NBI heated plasmas [1-5]. From the 3rd campaign for ICRF heated plasmas and high-power plasma production, graphite tiles have been installed in the divertor leg region to reduce impurities in the plasma [6,7]. Improved plasma performance was investigated in the 4th campaign, relevant mainly to the magnetic axis position. FIG. 1 shows the stored energies as a function of shot number, representing the progress of LHD plasma performance. The highest values of plasma parameters achieved in these four campaigns are summarized as follows:
(1) T_e of 1.3 keV and n_e of 1.3×10^{19} m^{-3} in the first campaign,
(2) T_e of 2.3 keV, T_i of 2.0 keV, n_e of 7×10^{19} m^{-3} and averaged beta $<\beta>$ of 1% in the 2nd

campaign,
(3) T_e of 4.4 keV, T_i of 3.5 keV, n_e of 1.1×10^{20} m^{-3} and $<\beta>$ of 2.4% in the 3rd campaign and
(4) n_e of 1.5×10^{19} m^{-3} and $<\beta>$ of 3% in the 4th campaign.

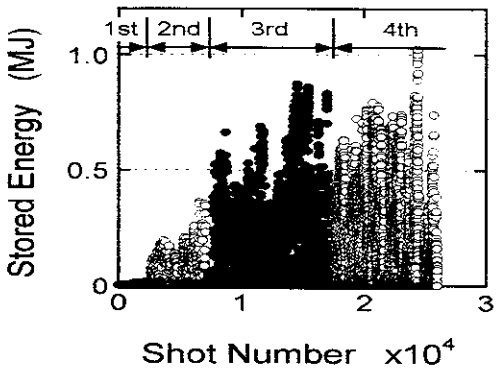

FIG.1. Increase of the plasma stored energy with shot numbers.

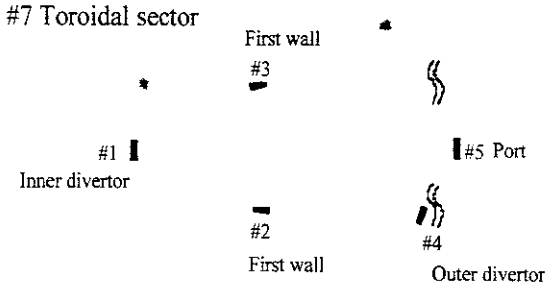

FIG.2. Position of material probes at inner wall of #7 toroidal sector.

From the first campaign to the 4th campaign, material probes of SS and graphite were placed at several inner wall positions of the same poloidal cross-section (FIG. 2). It is worthwhile for studying the wall characteristics, to fix the probe positions through the four campaigns. In the 4th campaign, material probes were placed along to the toroidal direction in order to clarify the effect of glow discharge cleaning. In addition, material probes were placed at the port, and the probe samples exposed to only main discharges and to only glow discharges were prepared. After each the campaign, impurity deposition, change of surface morphology and retention properties of discharge gas and impurity gas were examined, using AES, SEM and TDS, in order to clarify the PSI and degree of wall cleaning.

2. Impurity Deposition and Gas Retention

After the first campaign, on the entire wall surface there were deposited many sub-micron particles, which were identified as Fe-O particle. Oxygen concentration and the deposition thickness were large, 60 at.% and 200 nm, respectively. The amount of retained gas was large at the wall far from the plasma. The temperature rise during the discharge was very small in the entire wall. Thus these results suggest that the ECR discharge cleaning was effective for the wall near the plasma but not for the wall far from the plasma.

After the 2nd campaign, the deposition of Fe-O sub-micron particles disappeared at the wall except the inner divertor leg region. In addition, both the oxygen concentration and deposition thickness became low, 40 at.% and 20 nm, respectively. The total gas retention also decreased by 30 %, in particular, the decrease was largest at the wall far from the plasma. The retention of He, the gas species used for main discharges and glow discharges, was observed at the entire wall. The retained amount is not ignored, compared with that of hydrogen. These results suggest that both the glow discharge cleaning and the large increase of main discharge shot were quite effective for the wall conditioning.

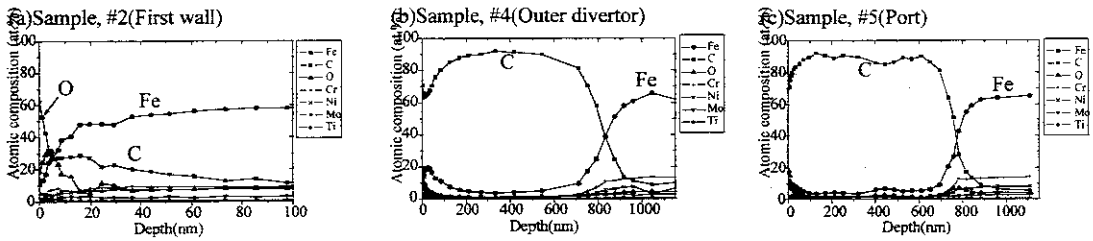

FIG.3. Depth profiles of atomic composition at the first wall (a), near the outer divertor (b) and the port (c).

From the 3rd campaign, the wall surface largely changed by the installation of graphite tiles at the divertor leg region. FIG. 3 shows the depth profiles of atomic composition in the samples at the first wall (a), near the outer divertor leg regions (b) and at the port (c). The entire wall was significantly covered by carbon, and hence, a large reduction of Fe impurities in the plasma was observed. FIG. 4 shows amounts of gas retained in samples after 3rd campaign. The amount of retained gas increased twice compared to the case of the 2nd campaign. The increase of the gas retention is due to the deposition of carbon. In particular, the retained amount at the wall far from the main plasma largely increased due to the thick deposition of carbon. FIG. 5 shows retained amount of helium for the positions shown in FIG.2. The helium gas was employed for a half of main discharge shots and helium glow discharge cleanings. The helium retention was clearly observed at the entire wall in this campaign The helium retention was large at the wall close to the plasma. It is presumed that the helium retention took place due to implantation of charge exchanged helium during the main discharge and helium ions during the helium glow discharge.

The toroidal sector of the sample shown in FIG. 5 is #7, which is far from the anode used for the helium glow discharge. In the 4th campaign, material probes were installed along the toroidal direction. The sample close to the anode retained very large amount of helium, one order larger than the amount shown in FIG. 5. This large retention is due to the ion implantation during the helium glow discharge. It was also observed that the deposition of impurities such as Fe was dominant in the vicinity of the anode. It is presumed that the emitted impurities during the glow discharge were ionized in the high density plasma near the anode and deposited to the cathode, the wall close to the anode.

The sample exposed to only main discharge shots or glow discharge cleaning was prepared using a rotating shutter, in addition to the samples along the poloidal and toroidal directions. FIG. 6 shows depth profiles of atomic composition for SS sample exposed to only main discharges (a) and graphite sample exposed to only helium glow discharges (b). In the SS sample exposed to only main discharges, carbon deposition was dominant mainly due to erosion of the divertor tiles. On the other hand, in the graphite sample exposed to only the glow discharges, dominant Fe deposition was observed. These results clearly show that major PSIs take place at the graphite divertor in the main discharge and at the first wall in the glow discharge. FIG.7 shows the desorption spectra of retained helium from SS samples exposed to only glow discharges and to only main discharges. The helium retained in the glow discharge

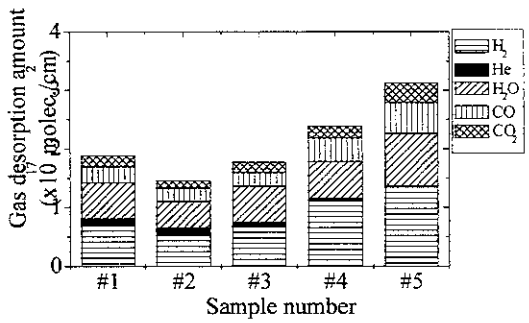

FIG.4. Retained amounts of gas retained in the samples after 3rd campaign.

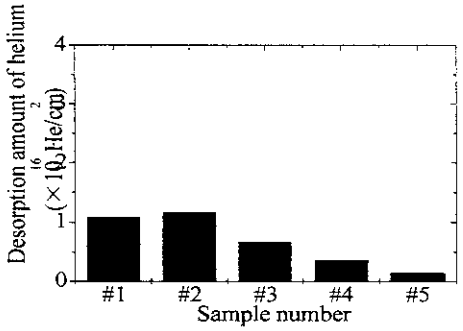

FIG.5. Retained amount of helium in the samples installed along poloidal direction at toroidal sector of #7.5 after the 3rd experimental campaign.

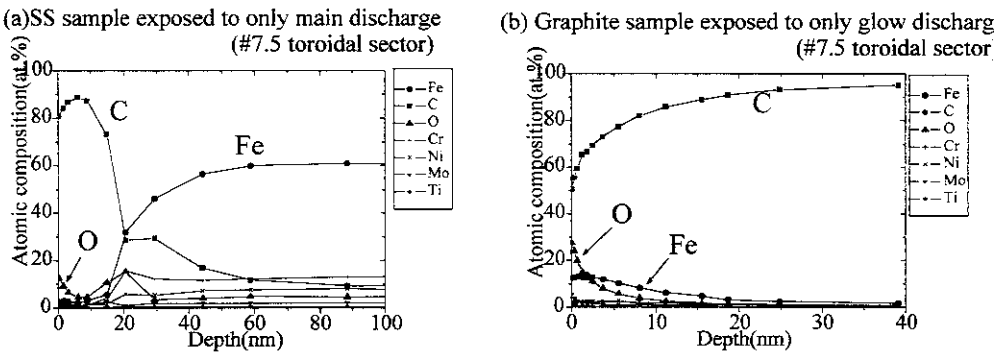

FIG.6. Depth profiles of atomic composition for SS sample exposed to only main discharges and graphite sample exposed to only helium glow discharges.

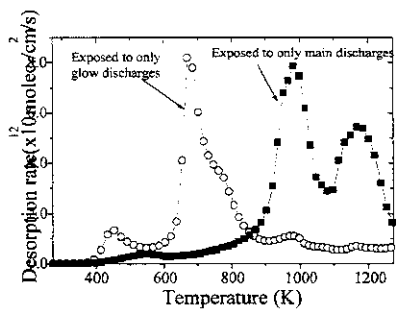

FIG.7 Desorption spectra of helium in the SS samples exposed to only glow discharges and main discharges.

and the main discharges desorbed in the temperature ranges below and higher than approximately 800 K, respectively. A large amount of helium was implanted during the He glow discharges. In particular, in the sample close to the anode, the retained amount was one order of magnitude larger than that of FIG.7. In order to reduce the helium recycling, baking with temperature higher than 800 K is required.

One of major characteristics of the LHD wall is a large retention of discharge gas such as

helium and impurity gas. In order to reduce the oxygen concentration in the plasma, boronization was conducted in the 5th campaign, and the oxygen concentration was reduced to approximately a half on the 4th campaign. For reduction of helium or hydrogen recycling, baking for the wall before the 6th campaign will be conducted. In addition, surface heating between the main discharge shots is planned. Thus, it is expected for the plasma confinement to be more improved.

3. Summary and Conclusion

The wall behavior in LHD was characterized, corresponding to the progress of plasma performance with the increase of heating power and the installation of graphite tiles for the divertor. It was found that the He glow discharge and charge exchange particles during the main shots largely contributed to the wall cleaning in the first and 2nd campaigns. In the 3rd and 4th campaigns, the graphite tiles were installed at the entire region of divertor trace, and then wall condition largely changed compared to the case of previous SS walls. The entire wall was well carbonized and then a large reduction of Fe impurity level in the plasma was observed. However, the gas retention increased by the deposition of carbon.

The retention of the discharge gas such as helium was observed to be large, and this is one of the characteristics of the LHD wall. One method of reducing the gas retention is baking the wall before the cooling down of superconductor coils. This plan will be conducted in the 6th campaign. The surface heating using a scanning laser flash between the main discharge shots is also useful. For reduction of oxygen impurities, boronization was observed to be effective in the 5th campaign. In the 6th experimental campaign, the boronization will be conducted. Both the wall heating and the boronization will enhance further improvement of the LHD plasma.

References

[1] FUJIWARA, M. et al, Nucl. Fusion, **41**(2001)1355.
[2] SAGARA, A. et al, J. Plasma and Fusion Res., **75**(1999)263.
[3] INOUE, N. et al, J. Plasma and Fusion Res., Series Vol. **3**(2000)324.
[4] HINO, T. et al, J. Nucl. Mater., **290-293**(2001)1176.
[5] MASUZAKI, S. et al, J. Nucl. Mater., **290-293**(2001)12.
[6] HINO, T. et al, To appear in J. Nucl. Mater., (2002).
[7] SAGARA, A. et al, To appear in J. Nucl. Mater., (2002)

Study on Ion Temperature Behaviors in Electron and Ion Heating Regimes of ECH, ICRF and NBI Discharges in LHD

S.Morita, M.Goto, Y.Takeiri, J.Miyazawa, S.Murakami, K.Narihara, M.Osakabe, T.Akiyama[1], N.Ashikawa, M.Emoto, M.Fujiwara, H.Funaba, P.Goncharov[2], Y.Hamada, K.Ida, H.Idei, T.Ido, K.Ikeda, S.Inagaki, M.Isobe, K.Itoh, O.Kaneko, K.Kawahata, H.Kawazome[3], K.Khlopenkov, T.Kobuchi, A.Komori, A.Kostrioukov, S.Kubo, R.Kumazawa, Y.Liang, S.Masuzaki, K.Matsuoka, T.Minami, T.Morisaki, O.Motojima, S.Muto, T.Mutoh, Y.Nagayama, Y.Nakamura, H.Nakanishi, Y.Narushima, K.Nishimura, A.Nishizawa, N.Noda, T.Notake[4], H.Nozato[5], S.Ohdachi, K.Ohkubo, N.Ohyabu, Y.Oka, T.Ozaki, B.J.Peterson, A.Sagara, T.Saida[2], K.Saito, S.Sakakibara, R.Sakamoto, M.Sasao, K.Sato, M.Sato, T.Satow, T.Seki, T.Shimozuma, M.Shoji, S.Sudo, H.Suzuki, N.Takeuchi[4], N.Tamura, K.Tanaka, K.Toi, T.Tokuzawa, Y.Torii[4] K.Tsumori, T.Uda, K.Y.Watanabe, T.Watari, Y.Xu, H.Yamada, I.Yamada, S.Yamamoto[4], T.Yamamoto[4], K.Yamazaki, M.Yokoyama, Y.Yoshimura, M.Yoshinuma

E-mail: morita@nifs.ac.jp

National Institute for Fusion Science, Toki, Gifu 509-5292, Japan
[1)] Research Laboratory for Nuclear Reactors, Tokyo Institute of Technology, Tokyo 152-8550, Japan
[2)] Department of Fusion Science, School of Mathematical and Physical Science, Graduate University for Advanced Studies, Hayama, 240-0193, Japan
[3)] Graduate School of Energy Science, Kyoto University, Uji 611-0011, Japan
[4)] Department of Energy Engineering and Science, Nagoya University, 464-8603, Japan
[5)] Graduate School of Frontier Sciences, The University of Tokyo 113-0033, Japan

Abstract

Ion heating experiments have been carried out in LHD using ECH (82.5, 84.0, 168GHz, ≤1MW), ICRF (38.5MHz, ≤2.7MW) and NBI (H° beam: 160keV, ≤9MW). The central ion temperature has been obtained from Doppler broadening of TiXXI (2.61Å) and ArXVII (3.95Å) x-ray lines measured with a newly installed crystal spectrometer. In ECH discharges on-axis heating was recently done with appearance of high $T_e(0)$ of 6-10keV and high ion temperature of 2.2keV was observed at n_e=0.6x10^{13}cm^{-3}. When the ECH pulse was added to the NBI discharge, a clear increment of T_i (ΔT_i~0.5keV) was observed with enhancement of the energy flow from electron to ion. These results demonstrate the feasibility toward ECH ignition. In ICRF discharges the increase of T_i (ΔT_i~0.8keV) was also observed at low density ranges of 0.4-0.6x10^{13}cm^{-3} with appearance of a new operational range of $T_i(0)$=2.8keV>$T_e(0)$=1.9keV. In the ICRF heating with P_{ICRF}=1MW, the fraction of bulk ion heating is estimated to be 60% to the total ICRF input power, which means P_i>P_e. Higher $T_i(0)$ up to 3.5keV was obtained for a combined heating of NBI (<4MW) and ICRF (1MW) at density ranges of 0.5-1.5x10^{13}cm^{-3}. The highest $T_i(0)$ of 5keV was recorded in Ne NBI discharges at n_e<1x10^{13}cm^{-3} with achievement of T_i>T_e, whereas the $T_i(0)$ remained at relatively low values of 2keV in H_2 or He NBI discharges. The main reasons for the high T_i achievement in the Ne discharges are; 1) 30% increment of deposition power, 2) increase in P_i/n_i (5 times, P_i/n_i>>P_e/n_e, P_i<P_e) and 3) increase in τ_{ei} (3 times). The obtained $T_i(0)$ data were plotted against P_i/n_i. The result strongly indicated that $T_i(0)$ smoothly increased with increasing P_i/n_i.

1. Introduction

Experiments in helical devices have been limited so far to only the electron heating regime ($P_i<P_e$) [1]. The ISS-95 sterallator scaling [2] was obtained from such ECH and NBI discharges. If the experiments in the ion heating regime ($P_i \geq P_e$) are realized, an increment of T_i and improvement of τ_E are expected, since the ion confinement is generally better than the electron confinement. The heating experiments have been extensively carried out in LHD in order to obtain higher T_i and understand the heating mechanism. In this paper the results are reported, especially on the ion temperature behavior [3]. Ion temperature at the plasma center has been measured from Doppler broadening of ArXVII and TiXXI x-ray lines using a newly installed crystal spectrometer with a CCD [4]. The difference in ion temperature between the measured impurity ions (Ar^{16+}, Ti^{20+}) and bulk ions (ECH and NBI: H^+, He^{2+}, ICRF: He^{2+}, neon discharge: Ne^{10+}) is estimated to be smaller than 50eV at n_e=0.5x10^{13}cm^{-3}.

2. H_2 and He discharges

2.1 ECH; Results from off-axis ECH heating (82.7, 84 and 168GHz) are plotted in Fig.1(a). The $T_e(0)$ is obtained from the YAG Thomson scattering measurement. The $T_i(0)$ is much lower than $T_e(0)$ in the low-density range and becomes equal at n_e~1x10^{13}cm^{-3}. The electron-ion heat exchange time, τ_{ei}, becomes equal to the energy confinement time, τ_e, (~150ms) at n_e~1.1x10^{13}cm^{-3}. The power flow from electrons to ions at the plasma center ranges in 3-6kWm^{-3} at n_e>0.5x10^{13}cm^{-3} and 0.4-2kWm^{-3} at n_e<0.5x10^{13}cm^{-3}. If the ion confinement time of (3-5)*τ_e is taken into account, the $T_i(0)$ can be roughly explained by the

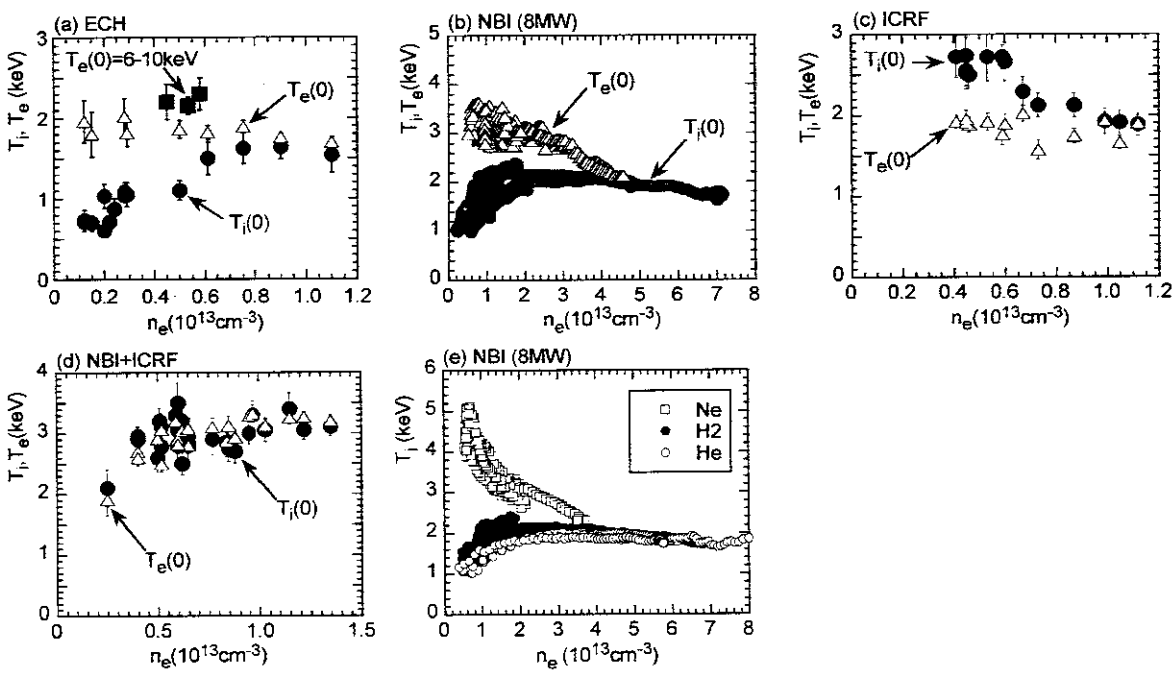

Fig.1 Comparison between $T_i(0)$ and $T_e(0)$ as a function of line-averaged density n_e in (a) ECH (0.4-0.6MW), (b)H_2 NBI (<8MW), (c) ICRF (1MW), (d) He NBI+ICRF (<4MW+1MW) and (e) high-power NBI discharges (≤8MW). Open squares in (e) indicate $T_i(0)$ from Ne discharges.

power input from electrons. Recently, on-axis ECH heating was carried out, and high $T_i(0)$ of 2.2keV has been observed with the appearance of high $T_e(0)$ such as 6-10keV [5,6]. The power flow from electrons to ions increased 2-3 times (see also Fig.1(a)). Furthermore, the ECH pulse was added to the NBI discharge. A clear increment of $T_i(0)$ was also observed as shown in Fig.2. These results strongly suggest the feasibility toward ECH ignition in future high-power and high-density ECH discharges. The global increase of T_e was important for the T_i increment, not related to the sharp peak near plasma center.

2.2 NBI; NBI heating in LHD is carried out at high beam energy of 160keV [7,8]. The beam shine-through power becomes considerably high (50% at $1x10^{13}cm^{-3}$) and an input power greater than 70% is absorbed by electrons ($P_i<P_e$, $P_i/n_i<P_e/n_e$). The ion heating in NBI discharges is entirely inefficient. As a result (see Fig.1(b)) the electron temperature becomes higher than the ion temperature in the low density region. Here, the fraction deposited to bulk ions (P_i/P_{NBI}) was 28% at T_e=3keV and 19% at T_e=2keV. The total P_i becomes 1.2MW at $n_e=1x10^{13}cm^{-3}$ and 0.8MW at $n_e=0.5x10^{13}cm^{-3}$ in the case of P_{NBI}=8MW, if the charge exchange loss can be neglected.

2.3 ICRF; Successful results [9-11] from ICRF (38.5MHz, H: minority, He: majority, P_{ICRF}=1MW) discharges are shown in Fig.1(c). An increment of $T_i(0)$ was clearly observed in a range of $0.4\le n_e\le 0.6x10^{13}cm^{-3}$. The bulk ions are heated through high-energy H^+ ions accelerated up to 200keV ($T_{tail}(H^+)$~25keV). The deposition profiles are calculated with a 5-D code by Murakami [12]. The results showed a broad ion deposition profile with a certain central deposition of $7kWm^{-3}$ at ρ=0 and $18kWm^{-3}$ at ρ=0.5, whereas the bulk electron heat deposition profile was located in a range of $0.4\le\rho\le 0.8$. The fraction of bulk ion heating, P_i/P_{ICRF}, was roughly 60%. Thus, a new operational range of $T_i>T_e$ was established with a successfully performed ion heating regime ($P_i>P_e$, $P_i/n_i>P_e/n_e$).

2.4 ICRF+NBI; The ICRF pulse was added to the NBI discharge (≤4MW). The result is shown in Fig.1(d). Since the ICRF heating, at present, is not effective at $n_e>2x10^{13}cm^{-3}$, the

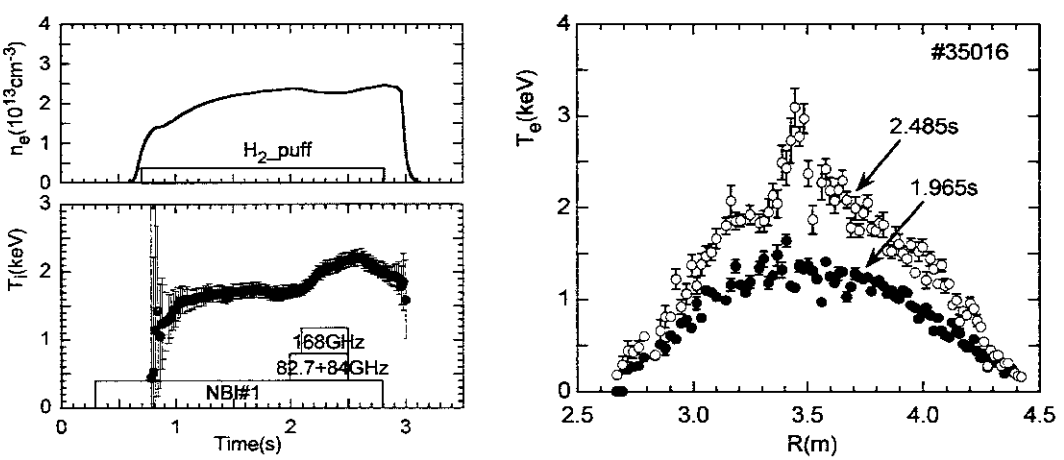

Fig.2 Ion heating during additional ECH pulse in H_2 NBI discharge (left) and electron temperature profiles before (1.965s) and during (2.485s) the ECH pulse (right).

data are plotted in lower density range. We understand that the ion temperature can be also raised up by the combination with NBI because of the further increase in P_i.

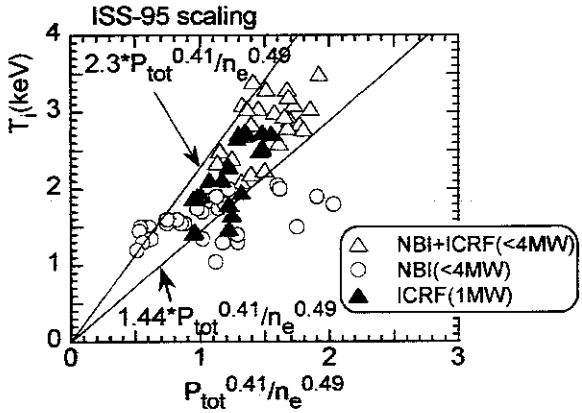

Fig.3 $T_i(0)$ plot by ISS-95 scaling.

The obtained T_i was compared with ISS-95 scaling under the assumption of $T_i=T_e$ (Fig.3). The value expected from the scaling is traced with the lower solid line of $1.44*P_{tot}^{0.41}/n_e^{0.49}$. In NBI discharges the $T_i(0)$ is a weak function of P_{tot}/n_e. On the contrary, most of the data from the ICRF and NBI+ICRF discharges exceed the scaling value, and those suggest an improvement of the heating efficiency of 60% at the maximum indicated by the upper solid line of $2.3*P_{tot}^{0.41}/n_e^{0.49}$. This increment of $T_i(0)$ originates in the presence of ICRF pulse.

3. Neon discharge

Neon discharges [13,14] were tried using NBI to obtain a higher T_i. A nearly pure Ne discharge (Z_{eff}~8.5) was successfully obtained because the main part of the neon radiation could be excluded from the core plasma and emitted in the ergodic layer outside $\rho=1$, which characterizes LHD. The highest ion temperature of 5keV was obtained with achievement of $T_i>T_e$ in the Ne discharges (Fig.1(d)). The global energy confinement was the same as the H_2 and He discharges. The main reasons why the high-T_i range was extended are; 1) increase in the NBI deposition at lower density ranges (+30%) (Fig.4(a)), 2) increase in the bulk ion heating fraction following the T_e increase (Fig.4(b)), 3) increase in P_i/n_i (5 times, $P_i/n_i>>P_e/n_e$, $P_i<P_e$) and 4) increase in τ_{ei} (3 times) (Fig.4(c)). Here, the $q_i(0)$ becomes ~200kWm^{-3} at $n_e=0.6\times10^{13}$cm^{-3} for P_{NBI}=8MW. The Ne ion density is mainly calculated from density rise after Ne gas puffing. Contribution of H^+ and He^{2+} ions to the n_i is

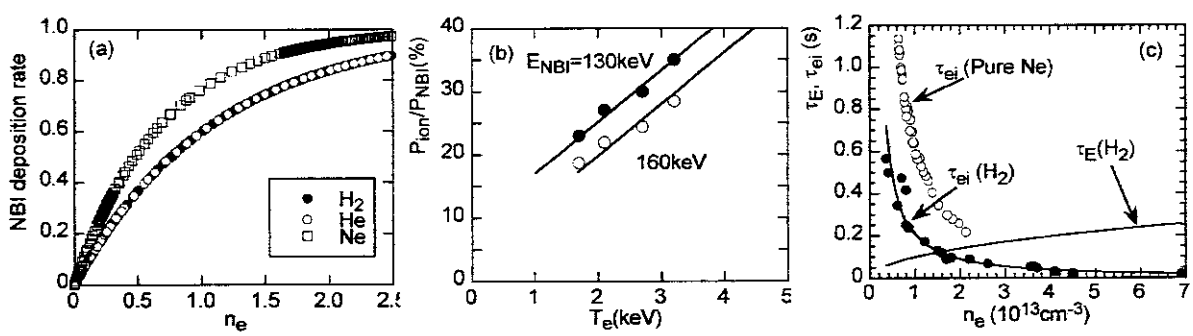

Fig.4 (a) NBI deposition rate of H_2, He and Ne, (b) ratio of bulk ion heating to total NBI input power and (c) τ_E for H_2 discharge and τ_{ei} for H_2 and Ne discharges.

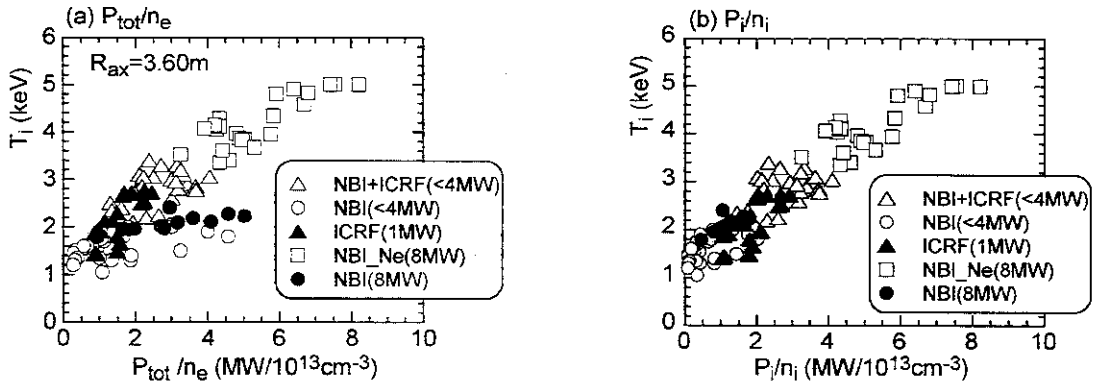

Fig.5 $T_i(0)$ as a function of (a) P_{tot}/n_e and (b) P_i/n_i (P_{tot}: total input power, P_i: input power to bulk ions, n_i: bulk ion density, NBI_Ne: neon discharge).

estimated from Z_{eff} values and visible and VUV spectroscopy, especially using recombination emissions at the end of discharges.

The obtained ion temperatures are plotted against P_{tot}/n_e (Fig.5(a)). The difference between the Ne and H_2 discharges is notable. The same data set as in Fig.5(a) was also replotted as a function of P_i/n_i (Fig,5(b)). It is seen that the $T_i(0)$ smoothly increases with increasing P_i/n_i. However, it should be noticed that the values of n_i is sensitive to the presence of H^+ and He^{2+} ions in the Ne discharges. Direct measurement of the ion density is necessary to increase the accuracy. Nevertheless, the two figures strongly suggest the importance of the direct power input to bulk ions in order to realize higher ion temperature.

In conclusions, a new parameter range of $T_i > T_e$ was found in LHD for ICRF and Ne-seeded NBI plasmas with achievement of the highest ion temperature of 5keV. The T_i increase in on-axis ECH heating also revealed feasibility toward ECH ignition.

References

[1] H.Yamada et al., Phys.Rev.Lett. **84** (2000) 1216.
[2] U.Stroth et al., Nucl.Fusion **36** (1996) 1063.
[3] S.Morita et al., Nucl.Fusion **42** (2002) 1179.
[4] S.Morita and M.Goto, submitted to Rev.Sci.Instrum.
[5] S.Kubo et al., Rapid communication, J.Plasma Fusion Res. **78** (2002) 99.
[6] T.Shimozuma et al., Proc. of EC-12, 2002, Aix-en-Provence, P-056.
[7] Y.Takeiri et al., Rev.Sci.Instrum. **70** (1999) 4260.
[8] O.Kaneko et al., Nucl.Fusion **39** (1999) 1087.
[9] T.Mutoh et al., Phys.Rev.Lett. **85** (2000) 4530.
[10] T.Watari et al., Nucl.Fusion **41** (2001) 325.
[11] R.Kumazawa et al., Phys.Plasmas **8** (2001) 2139.
[12] S.Murakami et al., Nucl.Fusion **42** (2002) L19.
[13] Y.Takeiri et al., Proc. of 29th EPS Conf., 2002, Montreux, P1-076.
[14] J.Miyazawa et al., Proc. of 29th EPS Conf., 2002, Montreux, P1-073.

ICRF Heating and High Energy Particle Production in the Large Helical Device

T.Mutoh, R.Kumazawa, T.Seki, K.Saito, T.Watari, Y.Torii[1], N.Takeuchi[1], T.Yamamoto[1], M.Osakabe, M.Sasao, S.Murakami, T.Ozaki, T.Saida[2], Y.P.Zhao[3], H.Okada[4], Y.Takase[5], A.Fukuyama[4], N.Ashikawa, M.Emoto, H.Funaba, P.Goncharov[2], M.Goto, K.Ida, H.Idei, K.Ikeda, S.Inagaki, M.Isobe, O.Kaneko, K.Kawahata, K.Khlopenkov, T.Kobuchi, A.Komori, A.Kostrioukov, S.Kubo, Y.Liang, S.Masuzaki, T.Minami, T.Mito, J.Miyazawa, T.Morisaki, S.Morita, S.Muto, Y.Nagayama, Y.Nakamura, H.Nakanishi, K.Narihara, Y.Narushima, K.Nishimura, N.Noda, T.Notake[1], S.Ohdachi, I.Ohtake, N.Ohyabu, Y.Oka, B.J.Peterson, A.Sagara, S.Sakakibara, R.Sakamoto, M.Sasao, K.Sato, M.Sato, T.Shimozuma, M.Shoji, H.Suzuki, Y.Takeiri, N.Tamura, K.Tanaka, K.Toi, T.Tokuzawa, K.Tsumori, K.Y.Watanabe, Y.Xu, H.Yamada, I.Yamada, S.Yamamoto[1], M.Yokoyama, Y.Yoshimura, M.Yoshinuma, K.Itoh, K.Ohkubo, T.Satow, S.Sudo, T.Uda, K.Yamazaki, K.Matsuoka, O.Motojima, Y.Hamada, M.Fujiwara

National Institute for Fusion Science, Toki, 509-5292, Japan
1) Department of Energy Engineering and Science, Nagoya University, 464-8603, Japan
2) Graduate University for Advanced Studies, Hayama, 240-0193, Japan
3) Institute of Plasma Physics, Academia Scinica, Hefei, Anhui, China
4) Kyoto University, Kyoto, Japan
5) Graduate School of Frontier Sciences, The University of Tokyo 113-0033, Japan

e-mail contact of main author: mutoh@nifs.ac.jp

Abstract. Significant progress has been made with Ion-Cyclotron Range-of-Frequencies (ICRF) heating in the Large Helical Device (LHD). This is mainly due to better confinement of the helically trapped particles, and less accumulation of impurities in the region of the plasma core. During the past two years, ICRF heating power has been increased from 1.35 MW to 2.7 MW. Various wave-mode tests were carried out using minority-ion heating, second-harmonic heating, slow-wave heating, and high-density fast-wave heating at the fundamental cyclotron frequency. This fundamental heating mode extended the plasma-density range of effective ICRF heating to a value of $1 \times 10^{20} m^{-3}$. This was the first successful result of this heating mode in large fusion devices. Using the minority-ion mode gave the best performance, and the stored energy reached 240 kJ using ICRF alone. This was obtained for the inward-shifted magnetic axis configuration. The improvement associated with the axis shift was common to both bulk plasma and highly accelerated particles. For the minority-ion mode, high-energy ions up to 500 keV were observed by concentrating the heating power near the plasma axis. The confinement properties of high-energy particles were studied for different magnetic axis configurations using the power-modulation technique. It confirmed that the confinement of high-energy particles with the inward-shifted configuration was better than that with the normal configuration. The impurity problem was not serious when the plasma boundary was sufficiently far from the chamber wall. By reducing the impurity problem, it was possible to sustain the plasma for more than two minutes using ICRF alone.

1. Introduction

The performance of Ion-Cyclotron Range-of-Frequencies (ICRF) heating has progressed steadily in the Large Helical Device (LHD) [1-9]. This is mainly due to better confinement of the helically-trapped particles, which was improved by the use of the inward-shifted configuration of the magnetic-confinement field [1],[2]. From the start of the LHD experiment, confinement of the helically-trapped particles was a major problem that needed to be solved for successful ICRF heating, and the success of the helical-fusion program. During the past two years, the ICRF

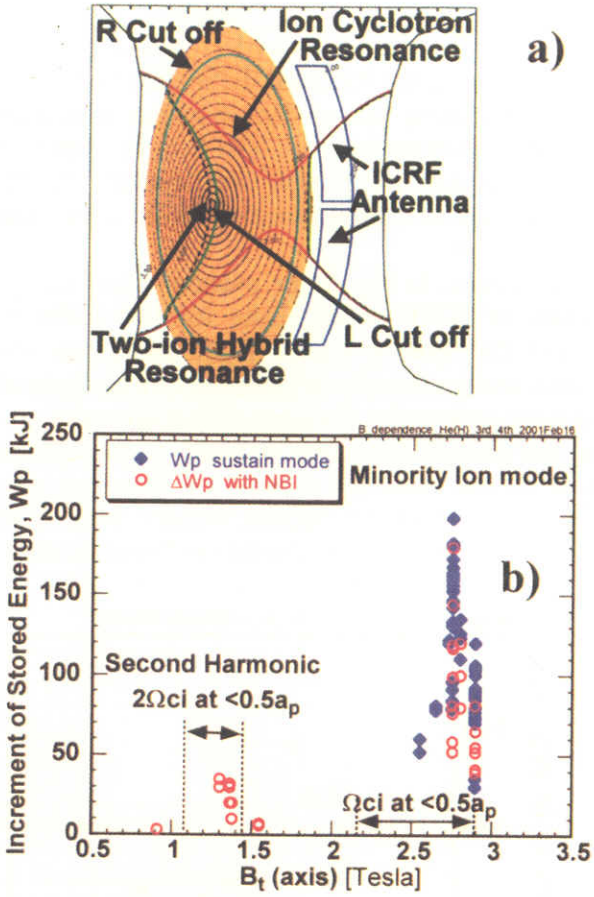

Fig.1 a) Resonance and Cut-off surfaces in LHD cross section in minority ion mode (B_0=2.75T, 38.5MHz, He(H:30%)plasma)
b) Plasma stored energy vs. magnetic field strength.Diamonds are ICRF sustained mode and circles are additional heating to NBI plasma.

magnetic field strength. For fields near 1.3 T, second-harmonic heating was also tested as a means of providing additional heating for the NBI plasma [10].

Those data were obtained for the inward-shifted magnetic axis configuration. The improvement associated with the axis-shift appeared to be common to both bulk plasma and highly-accelerated particles. Until now, there has been no direct indication of improved confinement of high-energy particles. In this paper, comparisons between inward-shifted and normal configurations using the power-modulation technique are shown.

heating power was increased from 1.35 MW to 2.7 MW to better resolve this problem.

Various wave-modes were tested, and the properties of accelerated-particle confinement examined. Tests were carried out using minority-ion heating, second-harmonic heating, slow-wave heating, and high-density fast-wave heating at the fundamental cyclotron-frequency. In Fig.1(a), the resonance and cut-off surfaces for the minority-ion mode are shown in a poloidal cross-sectional view of the LHD. ICRF antennas are located on the outer side of the toroid, and the mod-B contour had a saddle-point. The heating performance depended on the magnetic field-strength as shown in Fig.1(b). The increment of the stored plasma energy due to ICRF pulse is plotted versus magnetic field-strength at the axis. The frequency was fixed at 38.5 MHz. Good results were obtained mainly for the minority-ion heating mode at a magnetic field of 2.75 T, and the stored energy reached 240 kJ using ICRF alone. As shown in Fig.1(a), at the optimum magnetic-field strength, the resonance was located near the saddle point of the mod-B contours, and not at the magnetic axis. Under this condition, the area of cyclotron-resonance acceleration was greatest due to the small gradient of the

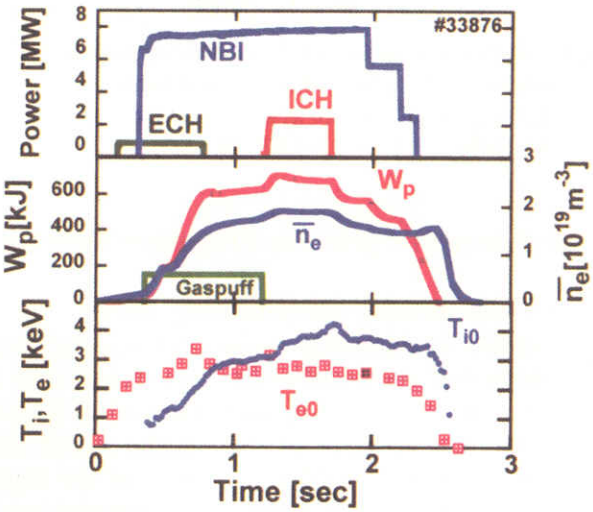

Fig.2 Temporal evolution of ICRF additional heating to NBI sustained plasma. (B_0=2.8T, R_{ax}=3.53m)

2. ICRF Heating Performances

After the last IAEA conference [6], the experimental program included the installation of six loop-antennas that raised the input power to 2.7 MW. By using this system, plasmas with high stored energy and high ion-temperatures were achieved in conjunction with NBI heating. Figure 2 shows time traces of the plasma parameters. ICRF power of 2 MW was applied to the NBI-sustained plasma, and clear increases were observed in stored plasma energy (W_p) and central ion temperature (T_{io}) measured from Ar*XVII* spectrum.

A sustained plasma using ICRF alone was also achieved. In Fig. 3, the plasma stored-energy achieved using ICRF alone is plotted as a function of ICRF power. Data for two different magnetic configuration parameters are shown: γ=1.254 and γ=1.259. Both cases are the minority-heating mode with a majority of helium ions and a minority of protons. For the case of the larger γ parameter, the distance from the plasma boundary to the chamber wall is around 1 cm. The radiation power was quite large and sustaining the plasma was quite difficult. In the case of the smaller γ parameter, the clearance was almost double, and the plasma performance was greatly improved as shown in Fig. 3. The stored energy and the plasma density were both increased by raising the ICRF power. Results of slow-wave mode (Ion Cyclotron Wave heating) with low plasma density are also shown.

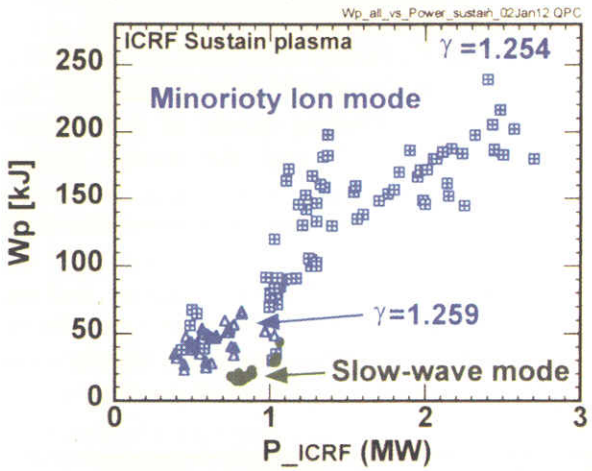

Fig.3 Stored energy of ICRF sustained plasma versus ICRF power. Minority Ion mode (He:majority,H:minority), Slow-wave (H:100%), B=2.75-2.9T, 38.5MHz,

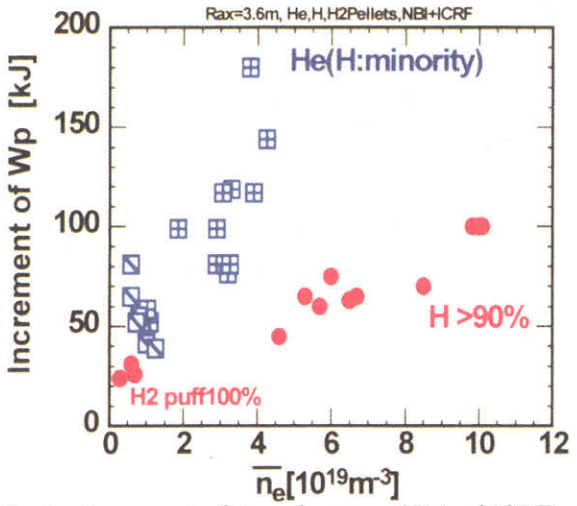

Fig.4 Increment of stored energy (Wp) of ICRF heating on NBI plasma. (Squares: minority ion heating,
Closed circles:fundamental cyclotron frequency heating,38.5MHz, 2.75-2.8T)

3. Fundamental-Cyclotron-Frequency Heating in High-Density Plasma

Of the several wave-heating modes, the most interesting result was achieved using high-density fundamental-cyclotron-frequency heating, which is thought to be a fast-wave mode. This mode had previously been abandoned due to its very small wave-damping rate. However, for LHD, effective heating was observed in high-density plasmas up to a density of 1 x 10^{20} m^{-3}. In Fig.4, the increment of the plasma-stored energy was plotted for a wide range of plasma densities, from 0.3 to 10 x 10^{19} m^{-3}. In the high-density region, only the fast-wave mode can propagate and heat the plasma. The plasma was built-up by injecting hydrogen gas, hydrogen pellets and injected proton beams. Therefore, almost 100% of the ions were protons.

From the observation of electron-cyclotron emission (ECE) at the power turn-off time, it was clear that the majority of the wave power was transferred to the ions by ion-cyclotron

damping. The substantial damping rate was considered to be due to the presence of NBI-beam particles and/or a large magnetic-field ripple. The efficiency was about half that of the minority-ion heating mode, as shown in Fig. 4. However, this fast-wave of the fundamental cyclotron frequency is still effective for the heating of high-density plasma and these data are the first successful results in large fusion devices.

4. High-Energy-Particle Production and Confinement

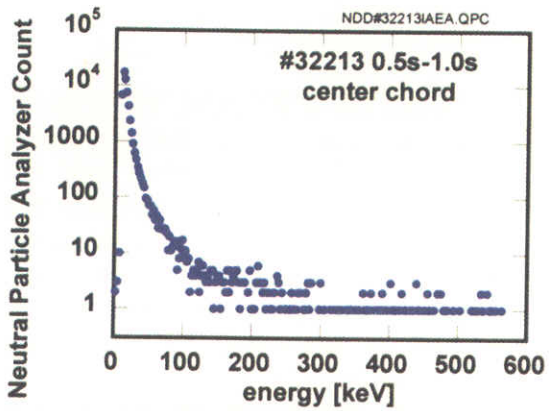

Fig.5 Energy distribution of minority protons for the axis resonant condition in ICRF sustained plasma. (B0=2.5T, Rax=3.6m)

In the minority-ion-heating mode, a high-energy tail component is produced in velocity space. This non-thermal tail extends up to an energy of 500 keV, as shown in Fig. 5. In this case, the cyclotron resonance is located on the magnetic axis. Under this condition, the heating-volume is small, and the power-density is high compared to the saddle-point resonance (see Fig.1(a)). Consequently, in this condition, the tail component grew more rapidly. The smooth distribution in velocity space implies that there is no apparent high-energy particle-loss channel such as suspected to be a serious problem in the helical systems.

However, the confinement properties for high-energy particles are still important subjects in LHD. The bulk plasma confinement with a magnetic axis radius (R_{ax}) of 3.6m was better than that of R_{ax}=3.75m. Therefore the properties of high-energy-tail confinement are also compared for NBI plasmas having different magnetic axes using the ICRF modulation technique [10][11]. Target plasma parameters were almost kept identical. Figure 6 shows the time dependence of the fast particle flux (by Silicon-diode detector, Si-FNA) and its associated phase delays from the modulated power phase. The ICRF power has a sinusoidal envelope of 4 Hz. As long as the confinement of accelerated high-energy particles was

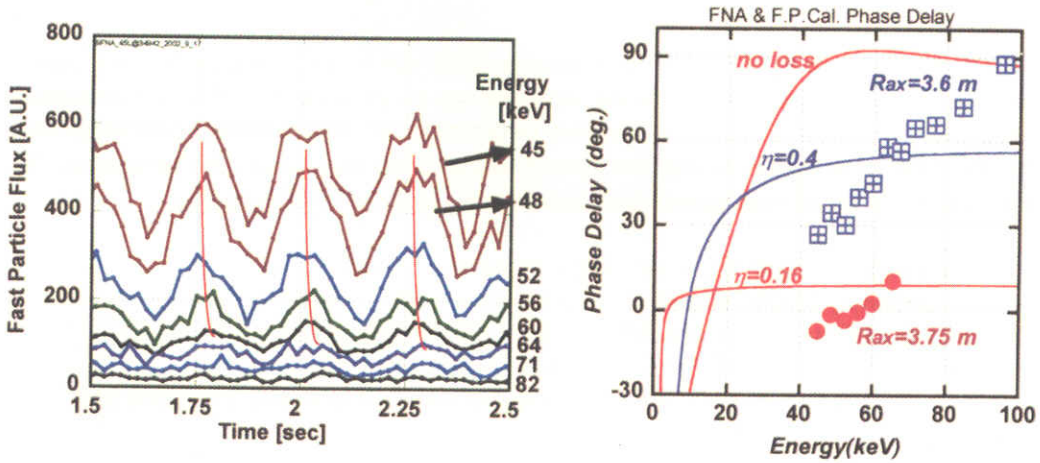

Fig.6 Time traces of Si-FNA flux for different particle energy with ICRF power modulation. (Left) Phase delay of Si-FNA flux from modulated ICRF power phase. Solid lines are Fokker-Planck Calculation in three cases, no loss and with a particle loss channel of transfer efficiency from fast particles to bulk plasma of 0.4 and 0.16. (Right)

shorter than the relaxation process time, the phase delay of the particle flux should be small. The phase delay of the flux for the inward-shifted configuration (Rax=3.6m) was larger than that of the normal configuration (Rax=3.75m) as shown in Fig. 6. The solid curves are the calculated phase delay by the time dependent Fokker-Planck equations, which includes artificial particle loss effects [10]. The particle confinement for Rax=3.75 m was clearly worse than that for Rax=3.6m. These results are the first direct observation of an improvement in high-energy particle-confinement for the inward-shifted configuration.

5. Long-Pulse Experiment

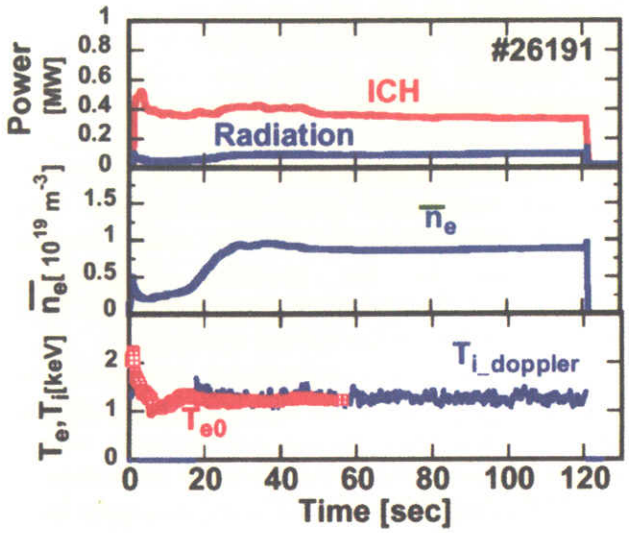

Fig.7 Long pulse plasma sustainment by ICRF for 2 minutes.
(B0=2.75T, Rax=3.6m, He gas, one antenna loop)

During the ICRF pulse, the impurity effect was sensitive to the separation between the plasma boundary and the chamber wall. At the correct distance (the same as γ=1.254 in Fig.3), the impurity effect can be suppressed to a small level, resulting in a longer pulse operation. An operation of two-minute duration was successfully performed at an ICRF power of 0.5 MW, an electron density of 0.9 x 10^{19} m^{-3}, and with an electron and ion temperature of 1.3 keV. (See Fig. 7) The radiation power stayed at a low level of around 25% of the input ICRF power. The achievement of long pulse-operation in the minority-ion mode is an indirect indication of the good confinement of helically-trapped particles and no impurity-ion accumulation in the LHD.

6. Summary

High-power ICRF heating up to 2.7 MW was successfully achieved. Various heating modes were tested, and the minority-ion-heating mode was shown to provide the best performance. Fast-wave heating at the fundamental cyclotron-frequency in high-density plasmas was demonstrated for the first time. When using the power-modulation technique, the inward-shifted configuration was shown to be advantageous for high-energy particle confinement.

[1] O. Motojima, H. Yamada. A. Komori, *et al.*, Phys. Plasma **6**, (1999) 1843
[2] M. Fujiwara, K. Kawahata, N. Ohyabu *et al.*, Nucl. Fusion, **41**, (2001) 1355.
[3] T.Mutoh, et al., Physical Review Letters, **85**, No. **21**, (2000) 4530-4533
[4] T.Mutoh, et al., Plasma Phys. Controlled Fusion **42**, (2000) 265-274
[5] R.Kumazawa, et al., Journal of Plasma and Fusion Research SERIES, Vol.**3**, (2000) 352.
[6] T.Watari, et al., Nuclear Fusion, **41**(2001) 325-332
[7] K.Saito, et al., Nuclear Fusion, **41**(2001) 1021-1035
[8] R.Kumazawa, et al., Physics of Plasmas, **8** (2001) 2139-2147
[9] T.Seki, et al., Journal of Plasma and Fusion Research SERIES Vol.**3** (2000) 359-362
[10] K.Saito, et al., Plasma Phys. Control. Fusion **44** (2002) 103-119
[11] Y. Torii, et al., Plasma Phys. Control. Fusion 43 (2001) 1191-1210

MHD Instabilities and Their Effects on Plasma Confinement in the Large Helical Device Plasmas

K. Toi, S. Ohdachi, S. Yamamoto[a], N. Nakajima, S. Sakakibara, K.Y. Watanabe, S. Inagaki, Y. Nagayama, Y. Narushima, H. Yamada, K. Narihara, S. Morita, T. Akiyama[b], N. Ashikawa, X. Ding[c], M. Emoto, H. Funaba, M. Goto, K. Ida, H. Idei, T. Ido, K. Ikeda, S. Imagawa, M. Isobe, K. Itoh, O. Kaneko, K. Kawahata, T. Kobuchi, A. Komori, S. Kubo, R. Kumazawa, J. Li[d], Y. Liang, S. Masuzaki, T. Mito, J. Miyazawa, T. Morisaki, S. Murakami, S. Muto, T. Mutoh, K. Nagaoka, Y. Nakamura, H. Nakanishi, K. Nishimura, A. Nishizawa, N. Noda, T. Notake[a], K. Ohkubo, I. Ohtake, N. Ohyabu, Y. Oka, S. Okamura, T. Ozaki, B.J. Peterson, A. Sagara, T. Saida[e], K. Saito, R. Sakamoto, M. Sasao, K. Sato, M. Sato, T. Satow, T. Seki, T. Shimozuma, M. Shoji, S. Sudo, M.Y. Tanaka, N. Tamura[e], K. Tanaka, K. Tsumori, T. Uda, T. Watari, A. Weller[f], Y. Xu, I. Yamada, M. Yokoyama, S. Yoshimura, Y. Yoshimura, K. Yamazaki, K. Matsuoka, O. Motojima, Y. Hamada, M. Fujiwara

National Institute for Fusion Science, Oroshi-cho 322-6, Toki, 509-5292,Japan
[a] Department of Energy Engineering and Science, Nagoya University, Nagoya, Japan
[b] Research Lab. for Nucl. Reactors, Tokyo Inst. Tech., Tokyo 152-8550, Japan
[c] Southwestern Institute of Physics, Chengdu, China
[d] Institute of Plasma Physics, Akademia Sinica, Hefei, China
[e] Department of Fusion Science, Graduate University for Advanced Studies, Hayama, Japan
[f] Max-Planck-Institut für Plasmaphysik, Garching, Germany

E-mail: toi@nifs.ac.jp

Abstract Characteristics of MHD instabilities and their impacts on plasma confinement are studied in current free plasmas of the Large Helical Device(LHD). Spontaneous L-H transition is often observed in high beta plasmas in the range of 2% averaged beta at low toroidal field ($B_t \leq 0.6$T). The stored energy rapidly rises with the transition, but quickly saturates due to the growth of m=2/n=3 and m=2/n=2 modes (m and n: poloidal and toroidal mode numbers) excited in the plasma edge region. Even in low beta plasmas, ELM like activities are sometimes induced in high performance plasmas with a steep edge pressure gradient, and transiently reduce the stored energy by about 10%. Energetic ion driven MHD modes such as Alfven eigenmodes are studied in the very wide range of characteristic parameters: the averaged beta of energetic ions $<\beta_{b//}>$ up to 5% and the ratio of energetic ion velocity to the Alfven velocity $V_{b//}/V_A$ up to 2.5. In addition to the observation of toroidicity induced Alfven eigenmodes (TAEs), coherent magnetic fluctuations of helicity induced Alfven eigenmodes (HAEs) have been observed for the first time in NBI heated plasmas. The transition of the TAE to the global Alfven eigenmode(GAE) is also observed in a discharge with temporal evolution of the rotational transform profile, having a similarity to the phenomenon in a reversed shear tokamak. At low magnetic field, bursting TAEs transiently induce a significant loss of energetic ions, but lead to the transient improvement of bulk plasma confinement in the plasma central region.

1. Introduction

In the Large Helical Device (LHD), high performance plasmas were obtained in the so-called "inward-shifted configuration" (the magnetic axis position of the vacuum field: $R_{ax} \leq 3.6$m) where energetic particles are expected to be well confined[1]. However, the inward-shifted configuration is unfavorable for MHD stability against pressure driven modes because of the presence of a magnetic hill region. The unfavorable behavior can be mitigated by the Shafranov shift, which tends to generate a magnetic well in the plasma core region. The edge region, however, is always in a magnetic hill. The rotational transform of the configuration in the vacuum field is in the range of $\iota(0)$~0.4 at the center and $\iota(1)$~1.3 at the last closed flux surface(LCFS), respectively. When the averaged toroidal beta $<\beta_t>$ increases, $\iota(0)$ increases and $\iota(1)$ decreases appreciably due to a large Shafranov shift. It is crucial for an LHD plasma to clarify the impacts of MHD instabilities on the confinement of bulk plasma and energetic ions, although serious deterioration of the confinement by MHD modes was not recognized in the past experimental campaigns with up to 4 MW absorbed NBI power (P_{abs}) and toroidal beta ($<\beta_t>$) less than 2%[2]. After that, experiments to investigate achievable $<\beta_t>$ were attempted with up to 6MW absorbed power. MHD stability of the inward-shifted plasmas was intensively studied over a wide parameter range. The main MHD instabilities observed in LHD are as follows: (1) low n MHD modes destabilized by the pressure gradient in the plasma edge as well as the core region, and (2) energetic ion driven MHD modes such as Alfven eigenmodes (AEs) . In this paper, we discuss characteristics of these MHD modes and their impacts on plasma confinement.

2. Pressure driven modes and their effects on plasma confinement

Most dangerous MHD modes in the plasma core region of LHD are low n pressure driven modes such as m=2/n=1 mode(m:poloidal mode number, n: toroidal mode number). When the plasma beta is increased in the inward-shifted configuration ($R_{ax} \leq 3.6$m), the rotational transform near the center tends to increase and approaches 0.5. Then, the m=2/n=1 mode becomes more unstable and affects the bulk plasma confinement [2]. A typical example that the averaged toroidal beta $<\beta_t>$ obtained with diamagnetic measurement saturates due to excitation of the m=2/n=1 mode is shown in Fig.1, where NBI absorbed power is relatively low (~3MW). In this shot, the plasma beta is increased rapidly by ice pellet injection and the m=2/n=1 mode is suddenly destabilized when $<\beta_t>$ exceeds about 2.2%. The m=2/n=2 MHD mode is simultaneously destabilized in the plasma edge, together with the m=2/n=1 mode. If the rational surface of ι=0.5 is removed by the effects of raising the plasma beta and small amount of net plasma current flowing in the co-direction, the m=2/n=1 mode is suppressed and the bulk confinement recovers [2]. When the pressure gradient in the core region is transiently increased by ice

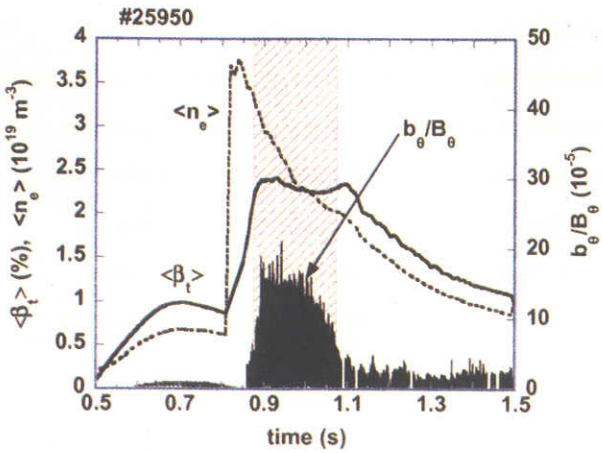

Fig.1 Time evolution of a high beta plasma affected by the m=2/n=1 MHD mode(b_θ), where B_t=0.6T and R_{ax}=3.6m. An ice pellet is injected at t=0.85s. B_θ stands for the averaged poloidal field at the magnetic probe position.

pellet injection, sawtooth oscillations or internal collapses are sometimes induced, accompanying m=2/n=1 pressure driven modes even in a fairly low beta plasma (~1%) [3]. In the previous experimental campaigns, the pressure profile becomes broad with the increase in the averaged plasma beta [4]. This may be favorable for increasing the beta value if the pressure profile has several local flat zones around the low order rational surfaces [5]. The broadening of the pressure profile in high beta plasmas would be due to anomalous transport and broader heating deposition rather than MHD stability, because no large amplitude MHD modes are observed in the plasma core region. It is crucial to increase $<\beta_t>$ further whether the edge stability is ensured in a plasma with steep pressure gradient near the edge. The broadening of the pressure profile tends to steepen the edge pressure gradient with the increase in the heating power. When higher NBI power is applied to a high density plasma, the plasma beta rapidly passes through ~2%, and the m=2/n=1 mode will not be excited. However, MHD modes such as the m=2/n=2 mode related to the ι=1 rational surface just inside the LCFS would be destabilized. In high beta plasmas with more than ~2% at fairly low toroidal field Bt=0.5-0.6T, L-H transition is often induced. So far, this transition only takes place in hydrogen plasmas in the configuration of R_{ax}=3.6m for more than P_{abs} ~3 MW. The L-H transition provides an excellent opportunity to test the edge stability of LHD plasmas. A typical high beta discharge with an L-H transition is shown in Fig.2 (a), where P_{abs} ~6MW at B_t=0.5T. The L-H transition takes place at t=1.40 s, exhibiting a density rise predominantly in the edge region, and an H-L back transition at t=1.86 s. The averaged beta suddenly increases with the transition, but saturates at about $<\beta_t>$ ~2.7 %. At the transition the m=2/n=3 and m=2/n=2 modes are suddenly enhanced and the former mode persists during H-phase, as shown in Fig.2 (b). The relevant rational surface of the m=2/n=3 mode will be in the ergodic layer just outside the LCFS. Only small ELMs are recognized during the H-phase. It is concluded that the observed beta saturation is caused by the destabilization of these low n MHD modes in the plasma edge region which is in the magnetic hill. In this high beta plasma the plasma boundary seems to expand slightly more than the boundary in the vacuum configuration. This may be due to the shrinkage of the edgodic layer by a healing effect [6].

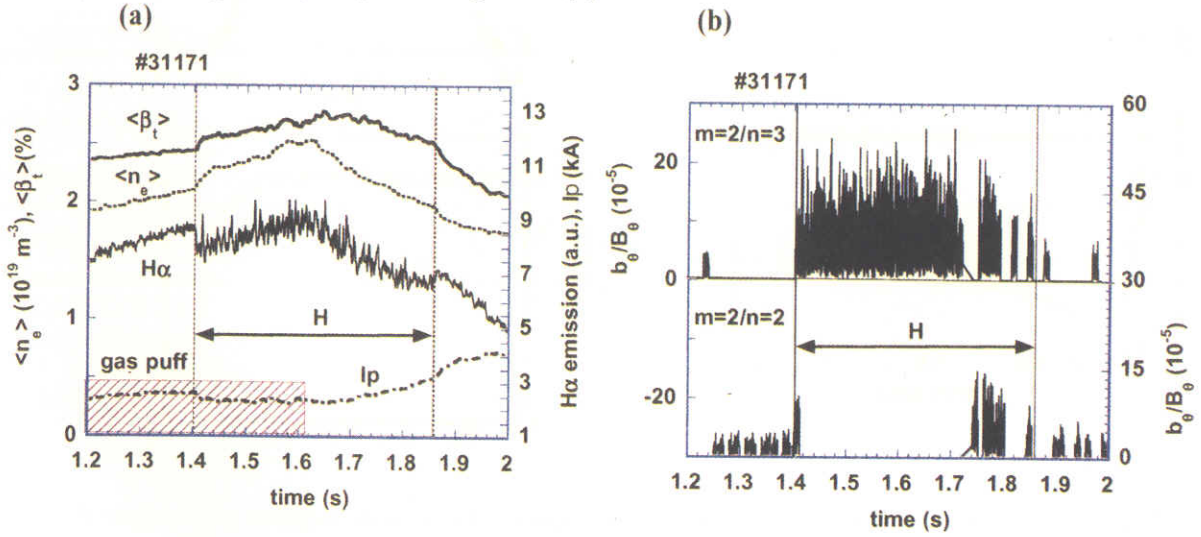

Fig.2(a) Time evolution of the averaged plasma beta obtained with diamagnetic measurement $<\beta_t>$, line averaged electron density of the center chord $<n_e>$, net plasma current Ip and Hα-emission in a high beta plasma with L-H transition at B_t=0.5T and R_{ax}=3.6m. The absorbed NBI power is P_{abs}~ 6 MW. (b) Time evolution of dominant magnetic fluctuations, that is, m=2/n=3 and m=2/n=2 modes.

If the edge pressure gradient is appreciably elevated having a high pressure pedestal, the above-mentioned edge MHD modes are also destabilized even in a fairly low plasma beta of $<\beta_t> \leq 1\%$ at high Bt ≥ 2.7 T. These modes are typically m=2/n=3 and m=3/n=4, and usually have multiple satellites. The modes are dubbed Edge Harmonic Modes (EHMs) [7]. When the plasma pressure gradient in the edge region exceeds a certain threshold, the EHMs seem to be bursting, as shown in Fig.3(a), where P_{abs} ~5MW and Bt=2.75T. The fundamental mode of this EHM is the m=3/n=4 mode and the rational surface is at the LCFS or in the ergodic layer. In this shot the net plasma current in the co-direction reaches up to 30 kA, but does not play an essential role in converting to bursting modes. The stored energy is reduced by up to 10% by each burst. This EHM burst dominantly reduces electron density near the edge rather than the electron temperature there(Figs.3(b) and (c)). Although the m=3/n=4 mode should be in the very edge region, the electron density up to ρ~0.7 is reduced by the burst. The Hα-emission exhibits very similar features to ELMs in a tokamak H-mode. Note that L-H transition does not take place in this shot. During the bursting phase of EHMs, the electron temperature profile has an island structure around the ι=1 rational surface (Fig.3(b)). The bursting EHMs with an m=3/n=4 mode structure have an obvious effect on global plasma confinement. The bursting character in EHMs is suppressed by the application of a resonant helical field perturbation in order to diminish the m=1/n=1 stationary magnetic island [7].

In LHD, careful tailoring of pressure and rotational transform profiles and radial electric field effects will be required to improve edge MHD stability and further increase the plasma beta [5,8,9].

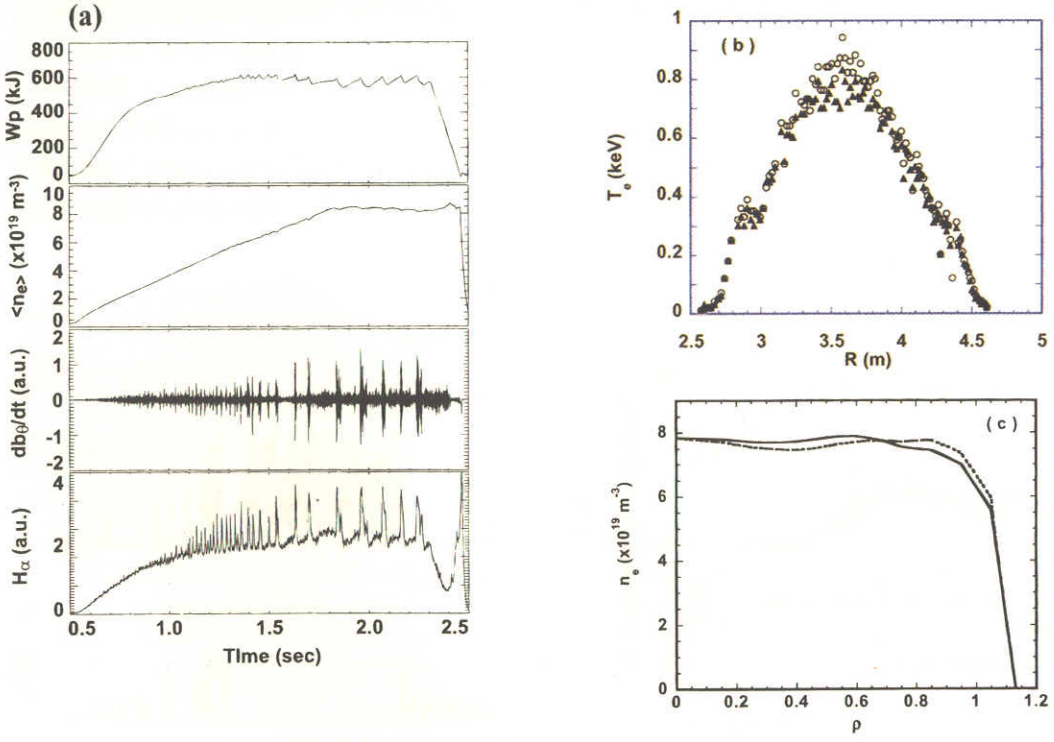

Fig.3(a) Time evolution of the stored energy, line averaged electron density, magnetic probe signal and Hα-emission in an NBI heated high density plasma with EHM bursts, where B_t=2.75 T, R_{ax}=3.6m and P_{abs}=5 MW. (b) Electron temperature profiles just before and after EHM burst as a function of major radius, where open circles and solid triangles stand for Te-profiles just before and after the EHM burst, respectively. (c) Electron density profiles just before(dotted curve) and after (solid curve) the EHM burst.

3. MHD instabilities destabilized by energetic ions and their effects on plasma confinement

The other important MHD instabilities are energetic ion driven Alfven eigenmodes such as toroidicity induced Alfven eigenmode(TAE). These MHD modes play a crucial role in realizing a fusion reactor. In major tokamaks, characteristics of AEs and their impacts on energetic ion confinement are intensively being studied, because it is thought that AEs might be destabilized by alpha particles generated by the deuterium-tritium fusion reaction and would degrade the confinement and damage the first wall. This study is also important for helical systems and has continued in LHD for several years [10-12]. Excitation of AEs depends on two characteristic parameters: the averaged beta of energetic ions $<\beta_{b//}>$ and the ratio of energetic ion velocity parallel to the magnetic field $V_{b//}$ to the Alfven velocity V_A. In LHD, these two parameters are scanned over a very wide range that includes those predicted for ITER[13], without suffering current disruption. Since LHD is a three dimensional magnetic configuration with l=2/N=10 (l: field polarity, N: field period number), various Alfven spectral gaps are generated through toroidal mode coupling as well as poloidal mode coupling. The related gap frequency is expressed as, $f^{\mu,\nu} = |Nvq^* - \mu| V_A/(4\pi R q^*)$ where $q^*=(2m+\mu)/(2n+\nu N)$ is the safety factor at the relevant spectral gap, and ν and μ are integers. The TAE corresponds to the case of μ=1,ν=0. The gap with μ=2,ν=1 is generated by the helical field component of $\cos(2\theta - N\varphi)$. Helicity induced Alfven eigenmode(HAE) can be excited in the gap. As seen from the above expression, the HAE gap frequency is higher than that of a TAE by a factor of $|Nvq^* - \mu|$. It is very high for LHD having N=10. It should be noted that the HAE frequency becomes comparable to the TAE gap frequency in optimized stellarators with low N[14]. Therefore, the study of the characteristics of HAEs is important for the development of new helical configurations. In LHD experiments, HAEs have been detected, in addition to the observations of energetic ion driven TAEs, global Alfven eigenmodes (GAEs) and energetic particle modes(EPMs) or resonant TAEs (R-TAEs). We summarize excitation conditions of TAEs and R-TAEs in Fig.4. TAEs are excited via sideband excitation ($V_{b//}/V_A$>1/3) as well as funadamental excitation($V_{b//}/V_A$~1). The threshold for $<\beta_{b//}>$ is ~0.02% for TAEs and ~0.1% for R-TAEs, where the beam beta value is estimated on the assumption of classical slowing down.

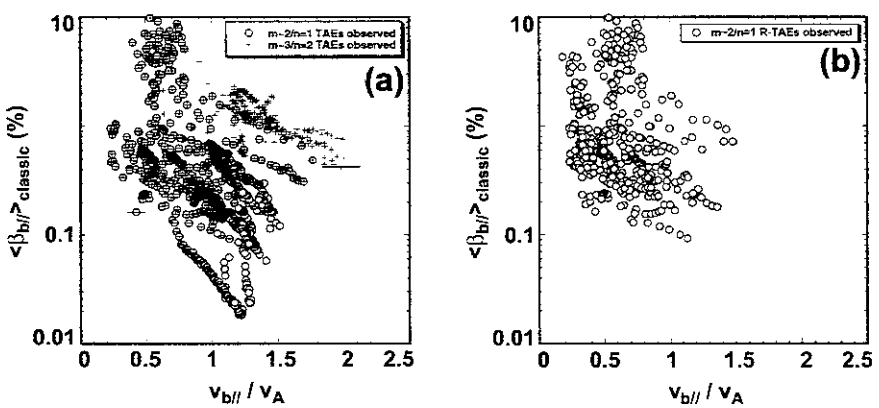

Fig.4 Parameter space for the excitation of TAEs (a) and R-TAEs (or EPMs) (b). In Fig.(a),open circles stand for m~2/n=1 TAE and pluses for m~3/n=2 TAE. In Fig.(b), m~2/n=1 R-TAEs are shown.

Recently, eigenmode transition from TAE to GAE has been observed in a particular shot, where counter (ctr.)-NBI was turned off and the net plasma current was increased in the co-direction[12], as shown in Fig.5. This transition is induced by the temporal evolution of the rotational transform near the plasma center, that is, the n=1 TAE gap generated with m=2 and m=3 mode coupling is diminished by the increase of ι(0) more than 0.4. Then TAE is converted to two n=1 GAEs with high and low frequency. The low frequency GAE will suffer from large continuum damping near the edge. As seen from Fig 5(a), the low frequency GAE quickly decays. Similar phenomena are also observed in negative shear tokamaks [15].

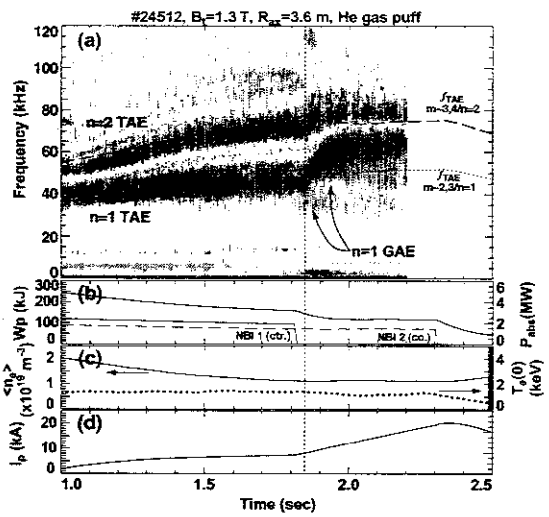

Fig.5(a) Time evolution of coherent magnetic fluctuations with n=1 and n=2 in a particular shot that eigenmode transition from TAE to GAE takes place at t=1.83s. The solid and broken curves indicate the calculated TAE frequencies for m~2+3/n=1 and m~3+4/n=2 mode. The stored energy, co and counter NBI absorbed power (b), the line averaged electron density, central electron temperature(c), and net plasma current (c) are also shown as a function of time.

As mentioned above, the gap frequency of the HAE is higher than the TAE gap frequency by about a factor of N/ι, where N is the field period of the helical field and N=10 for LHD. Coherent magnetic fluctuations which may be related to HAE have been detected in high beta plasmas at low toroidal field $B_t \leq 0.7$T (Fig.6(a))[16]. The frequency is by a factor of eight higher than the TAE gap frequency. Since toroidal mode coupling is essential to create the HAE gap, we calculate shear Alfven spectra including 919 Fourier modes as shown in Fig.6(b)). The observed frequency resides just inside the HAE gap in the edge region. The HAE is expected to have a peak near the plasma edge. In this discharge, an n=2 TAE related to m=2 and m=3 mode coupling is strongly excited, the gap of which is around ρ~0.85. This suggests that the energetic ion pressure profile would be broad, having an appreciable gradient near the edge region. The HAE fluctuations are interrupted by this n=2 TAE burst. The TAE burst would enhance radial transport energetic ions near the edge, and reduce the free energy to excite HAE there. So far, this mode has no obvious effect on energetic ion confinement, because the amplitude is fairly low and frequency is high. As seen in Fig.6(a), several spectral peaks are seen between TAE and the above-mentioned high frequency mode, that is, HAE. They are thought to be induced by higher order non-uniformity of the magnetic field strength. The observation of HAE will contribute to opening new AE-physics in a toroidal plasma.

Moreover, TAEs are strongly destabilized at the low Bt plasma and become bursting. Each TAE burst has an obvious impact on the signal of the stored (bulk) energy Wp measured by a diamagnetic

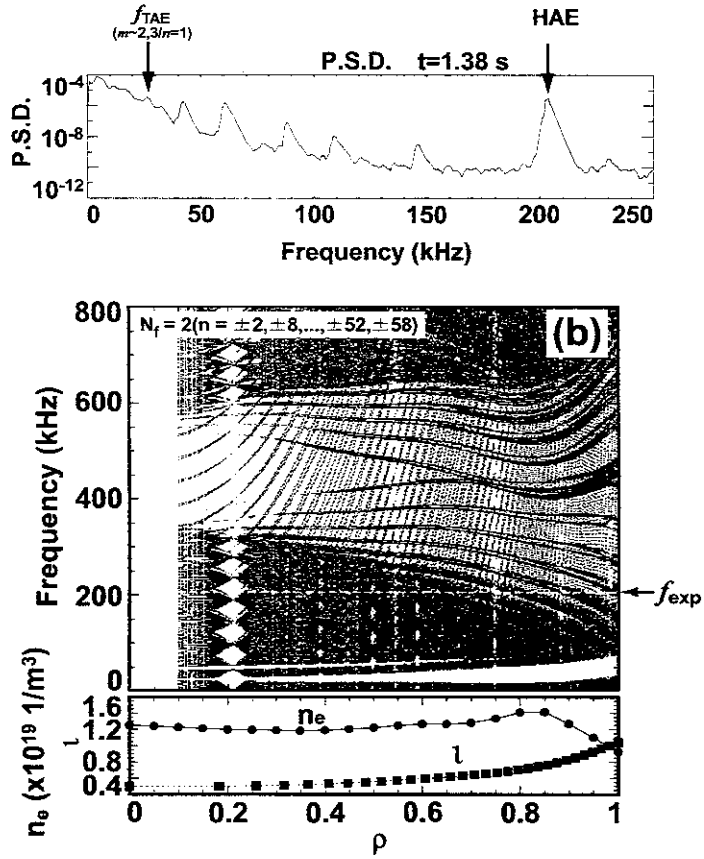

Fig.6(a) Power spectrum of magnetic probe signal. The peak at f~200kHz is thought to be HAE, where TAE gap frequency is about 25 kHz. (b) n=2 shear Alfven spectra calculated taking account of the toroidal mode

loop. By each burst, the stored energy Wp is transiently decreased by each burst as shown in Fig.7(a), where Wp is increased by ice pellet injection at t=0.8s. The characteristic decay time of Wp expresses the effective loss time of energetic beam ions τ_L, and is estimated to be about 3 ms. The transient loss fraction of energetic ions is estimated to be$[1-\exp(-\delta t/\tau_L)] \sim 40$-50%, where δt is an effective duration of the TAE burst. In this shot, an interesting event has been recognized. The stored energy quickly recovers just after the burst, having an appreciable positive value in dWp/dt (Fig.7(b)). This can be explained by the improvement of global confinement by a factor of 1.6. The soft X-ray emissions predominantly rise in the central region, associating with each TAE burst. The line integrated electron density also increases slightly but clearly in the central chord. These results suggest a possibility that transient loss of energetic ions trigger the transient formation of an internal transport barrier. A similar event induced by the fishbone instability is reported from ASDEX-U [17]. This event may be related to the sheared flow generation induced through rapid radial transport of energetic ions. In this shot, the repetition frequency of bursts will not be high enough to overcome the damping rate of bulk plasma flow.

4. Summary

Net current free plasmas in LHD exhibit a lot of interesting features related to MHD instabilities and the impacts on plasma confinement. In the high beta plasma, spontaneous L-H transition has been

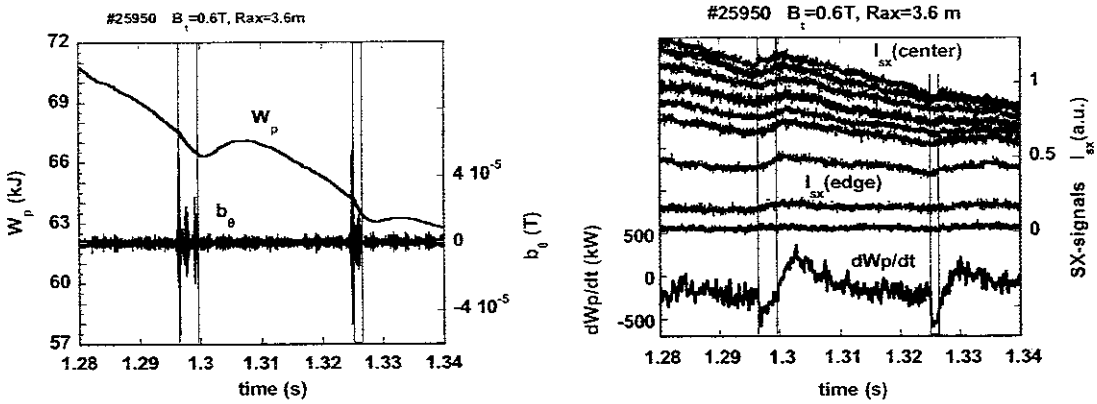

Fig.7(a) Time evolution of the stored energy in a shot with TAE bursts. (b) Time behaviors of dWp/dt and soft X-ray emissions in various radial locations from ρ=0.05 to 1.1.

observed and provides a possibility to study MHD stability in the edge region. So far, the plasma beta and global confinement are limited by the enhancement of edge MHD instabilities such as m=2/n=3, although the averaged beta value exceeds 2.5%. Edge MHD stability is crucial for further increasing the beta and achieving improvement of plasma confinement in LHD. It is also important to increase the pressure gradient in the core region with the help of transport barrier formation in the plasma core region where the magnetic well is created in the high beta regime. In LHD, HAEs have been observed for the first time, and this observation will contribute to design studies of optimized stellarators as well as to Alfven eigenmode physics itself. In LHD, bursting TAEs transiently enhance energetic ion loss in the high beta plasma, but also trigger the transient formation of an internal transport barrier.

Acknowledgements

This work was supported in part by a Grant-in-Aid for Scientific Research from Japan Society for the Promotion of Science.

References

[1] FUJIWARA, M. et al., Nucl. Fusion **41** (2001) 1355.
[2] SAKAKIBARA, S. et al., Nucl. Fusion **41** (2001) 1177.
[3] OHDACHI, S. et al., Proc. 13th Stellarator workshop, 2002, Canberra.
[4] SAKAKIBARA, S. et al., Plasma Phys. Control. Fusion **44** (2002) A217.
[5]ICHIGUCHI, K. et al., Nucl. Fusion **41**(2001) 181.
[6] NARIHARA, K., et al., Phys. Rev. Lett. **87** (2001) 135002-1.
[7] TOI, K. et al. ., 28th EPS on Contr. Fusion and Plasma Phys. Funchal, 2001, No.P4-050.
[8] WATANABE, K. et al., Nucl. Fusion **32** (1992) 1647.
[9] SUGAMA, H. and WAKATANI, M., Phys. Fluids B **3** (1991) 1110.
[10] TOI, K. et al., Nucl. Fusion **40** (2000) 1349.
[11] TOI, K. et al., to be published in J. Plasma Fusion Res. SERIES, Vol.4(2002).
[12] YAMAMOTO, S. et al., submitted to Nucl. Fusion.
[13] ITER Physics Expert Groups, Nucl. Fusion **39** (1999) 2137.
[14] OKAMAURA, S. et al., Nucl Fusion **41** (2001) 1865.
[15] TAKECHI, M. et al., submitted to Phys. Rev. Lett.
[16] YAMAMOTO, S. et al., to be submitted to Phys. Rev. Lett.
[17] GUENTER, S. et al., 28th EPS on Contr. Fusion and Plasma Phys. Funchal, 2001, No.P1-006.

Nonlinear MHD Analysis for LHD Plasmas

K. Ichiguchi 1), N.Nakajima 1), M. Wakatani 2), B.A. Carreras 3)

1) National Institute for Fusion Science, Oroshi-cho 322-6, Toki, 509-5292, Japan
2) Graduate School of Energy Science, Kyoto University, Gokasho, Uji, 611-0011, Japan
3) Oak Ridge National Laboratory, Oak Ridge, Tennessee 37831, USA

e-mail contact of main author: ichiguch@nifs.ac.jp

Abstract. The nonlinear behavior of the interchange modes with multi-helicity in the Large Helical Device is analyzed based on the reduced MHD equations. In the equilibrium at sufficiently low beta value, the saturation of a single mode and the following excitation of other single mode whose resonant surface is close to that of the saturated mode are slowly repeated. This sequence leads to the local deformation of the pressure profile. Increasing the beta value with the pressure profile fixed, a bursting phenomenon due to the overlap of multiple modes is observed in the kinetic energy, which results in the global reduction of the pressure profile. Increasing the beta value using the pressure profile saturated at the lower beta value suppresses the bursting behavior. This result indicates the possibility that the pressure profile is self-organized so that the LHD plasma should attain the high beta regime through a stable path.

1. Introduction

In the recent experiments in the Large Helical Device (LHD), high performance discharges have been successfully carried out in the configuration with the inward shift of the vacuum magnetic axis. Particularly, in the high beta discharges, the average beta value of 3.2% was achieved in the configuration with the vacuum magnetic axis located at $R_{ax} = 3.6$m[1]. On the other hand, the linear MHD stability of the plasmas was studied with the RESORM code[2] which is based on the reduced MHD equations for stellarator configurations. The initial stability studies[3] were done using smooth pressure profiles. The results of these studies showed that low-n ideal interchange modes are unstable for beta values lower than the experimental ones. Here, n denotes the toroidal mode number.

To explain the discrepancy between theory and experiment it is necessary to invoke the existence of a stabilizing mechanism. Because the ideal interchange modes are driven by the pressure gradient, one possible stabilizing mechanism is the local flattening of the pressure profile at the low order resonant surfaces[4,5]. It was shown by iterating the equilibrium and the linear stability calculations that staircase-like profile of the pressure can effectively stabilize the multiple modes with different n simultaneously. However, it was not clarified whether such locally flat profile can be actually achieved in the toroidal geometry. Besides, the overlap of the modes whose resonant surfaces are radially close to each other possibly becomes a critical issue. In order to study these problems, nonlinear analysis is inevitable. Thus, in this paper, we discuss the nonlinear behavior of the MHD fluctuation in the LHD plasmas, especially in the point of the the pressure profile variation.

2. Basic Equations and Numerical Scheme

We have developed a nonlinear MHD calculation code extending the RESORM code, which solves the reduced MHD equations based on the modified stellarator ordering including the

higher order toroidal effect[6]. The equations are Ohm's law, vorticity equation, and the equation of state. These equations can be written in terms of the poloidal magnetic flux, Ψ, the velocity stream function, Φ, and the plasma pressure, P. These equations are:

$$\frac{\partial \Psi}{\partial t} = -\left(\frac{R}{R_0}\right)^2 \mathbf{B}\cdot\nabla\Phi + \frac{1}{S}J_\zeta, \tag{1}$$

$$\frac{dU}{dt} = \left(\frac{R}{R_0}\right)^2 \left(-\mathbf{B}\cdot\nabla J_\zeta + \frac{\beta_0}{2\varepsilon^2}\nabla\Omega\times\nabla P\cdot\nabla\zeta\right) + \nu\hat{\nabla}_\perp^2 U, \tag{2}$$

and

$$\frac{dP}{dt} = \kappa_\perp \Delta_* P + \varepsilon^2 \kappa_\parallel \left(\frac{R}{R_0}\right)^2 \mathbf{B}\cdot\nabla(\mathbf{B}\cdot\nabla P). \tag{3}$$

Here, ζ denotes the toroidal angle and $\nabla_\perp$ is defined as $\nabla_\perp = \nabla - \nabla\zeta(\partial/\partial\zeta)$. The magnetic differential operator and the convective time derivative are given by

$$\mathbf{B}\cdot\nabla = g\left(\frac{R_0}{R}\right)^2 \frac{\partial}{\partial\zeta} - \nabla\Psi\times\nabla\zeta\cdot\nabla \tag{4}$$

and

$$\frac{d}{dt} = \frac{\partial}{\partial t} + \mathbf{v}_\perp\cdot\nabla, \quad \mathbf{v}_\perp = \left(\frac{R}{R_0}\right)^2 \nabla\Phi\times\nabla\zeta, \tag{5}$$

respectively. The factor g implies the diamagnetic effect in the toroidal field. The term of $\nabla\Omega$ means the averaged magnetic curvature driving the interchange mode and Ω is given by

$$\Omega = \frac{1}{2\pi}\int_0^{2\pi} d\zeta \left(\frac{R}{R_0}\right)^2 \left(1 + \frac{|\mathbf{B}_{eq} - \overline{\mathbf{B}_{eq}}|^2}{B_0^2}\right), \tag{6}$$

where the subscript 'eq' means the equilibrium quantity and the overline denotes the toroidally averaged value. The vorticity U and the toroidal current density J_ζ are expressed by

$$U = \hat{\nabla}_\perp^2\Phi = \left(\frac{R}{R_0}\right)^2 \nabla\cdot\nabla_\perp\Phi, \quad \text{and} \quad J_\zeta = \Delta_*\Psi = \left(\frac{R}{R_0}\right)^2 \nabla\cdot\left(\frac{R_0}{R}\right)^2 \nabla_\perp\Psi, \tag{7}$$

respectively. The magnetic field is normalized to its value at the magnetic axis, B_0, and β_0 denotes the beta value at the axis. The lengths in the ζ and the perpendicular directions are normalized by the major radius R_0 and the average minor radius a of the plasma, respectively, and ε is given by a/R_0. The time is normalized by the poloidal Alfvén time τ_A defined by $R_0\sqrt{\mu_0\rho_m}/B_0$, where ρ_m and μ_0 are the mass density and the vacuum permeability, respectively. The magnetic Reynolds number S is defined by $S = \tau_R/\tau_A$, where $\tau_R = \mu_0 a^2/\eta$ is the resistive diffusion time and η denotes the resistivity. The resistivity is assumed to be constant in the present work. We introduce the viscosity for the perpendicular flow in the vorticity equation. The coefficient ν is normalized by $a^2\rho_m/\tau_A$. The perpendicular and parallel heat conductivity terms are also introduced in the equation of state with the coefficients of $\kappa_\perp$ and $\kappa_\parallel$, respectively, which are normalized by a^2/τ_A. In the resistivity and the heat conductivity terms , only the perturbed parts of J_ζ and P are included, respectively.

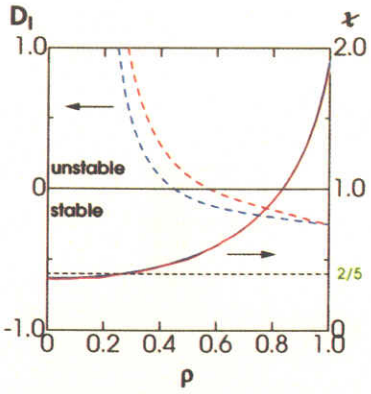

FIG.1. Profiles of Mercier quantity normalized so that the shear term should be -1/4 (dashed lines) and rotational transform (solid lines) for the pressure profile of eq.(8) at $\beta_0 = 0.5\%$ (blue) and 1.0% (red). Rational surface with $\iota = 2/5$ is indicated.

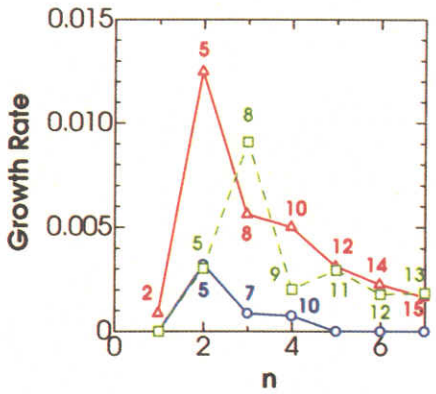

FIG.2. Linear growth rates versus toroidal mode number n. Circles and triangles show the growth rates for the pressure of eq.(8) at $\beta_0 = 0.5\%$ and 1.0%, respectively. Squares show the growth rates at $\beta_0 = 1.0\%$ for the pressure profile saturated nonlinearly at $\beta_0 = 0.5\%$. Numbers indicate the dominant poloidal mode number of each n mode.

The flux coordinates (ρ, θ, ζ) are employed to simplify the magnetic differential operator. Here ρ and θ are the square root of the normalized toroidal flux and the poloidal angle, respectively. The finite difference is employed for the radial discretization. The radial grid number used here is 192. The dependence of the poloidal and the toroidal angles are expressed by the Fourier series. The multi-helicity components of the perturbations are treated. The mode coupling is calculated through the direct convolution of the Fourier coefficients. For the time evolution, the two-step explicit algorithm[7] is employed, while only the linear dissipation operators are treated implicitly in each step. This code examines three-dimensional static equilibrium which is calculated by using the VMEC code[8]. The toroidally averaged geometry is used in the construction of the flux coordinates. Therefore, the toroidal effects are included automatically. The equilibrium toroidal current density is calculated by using the averaged equilibrium equation with the averaged curvature given by eq.(6).

2. Equilibrium and Linear Stability

First, we consider zero current equilibria for the shifted-in LHD configuration ($R_{ax} = 3.6$m) using the pressure profile of the form

$$P = P_0(1-\rho^2)(1-\rho^8). \tag{8}$$

In the equilibrium calculation, the free boundary condition is employed with the constraint that the separatrix plays a role of a virtual limiter at $R = 4.63$m[9]. The pressure profile of eq.(8) is close to the one observed in the experiments for $\langle\beta\rangle < 1\%$[10], where $\langle\beta\rangle$ denotes the volume average beta. Here we focus on the equilibria at $\beta_0 = 0.5\%$ and 1.0%, which correspond to $\langle\beta\rangle = 0.21\%$ and 0.43%, respectively. Figure 1 shows the profiles of the rotational transform and the Mercier quantity D_I[11]. The difference in the rotational transform between the equilibria is quite small. The equilibrium is Mercier unstable in the regions of $\rho < 0.44$ and $\rho < 0.57$ at $\beta_0 = 0.5\%$ and 1.0%, respectively, because of the low shear and high magnetic hill. For the

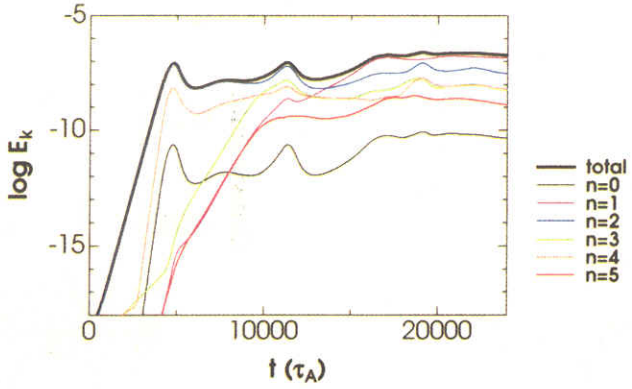

FIG.3. Time evolution of the kinetic energy of the perturbation for the $\beta_0 = 0.5\%$ equilibrium. Thick line shows the total energy and thin lines show the $n = 0$, 1, 2, 3, 4 and 5 components.

nonlinear analysis, we use the dissipation parameters of $S = 10^6$, $\nu = 10^{-4}$, $\kappa_\perp = 10^{-6}$ and $\varepsilon^2\kappa_\parallel = 10^{-2}$ ($\varepsilon = 0.16$). The linear growth rates with these parameters at $\beta_0 = 0.5\%$ and 1.0% are shown in Fig.2 as the function of the toroidal mode number n. All unstable modes have typical interchange mode structure. Only the modes with $n = 2$, 3 and 4 are linearly unstable at $\beta_0 = 0.5\%$, while all of the modes for $1 \leq n \leq 7$ are unstable at $\beta_0 = 1.0\%$ and the growth rates are much larger than those at 0.5%. In each equilibrium, the $n = 2$ mode has the largest growth rate and the $m = 5$ is the dominant component in this mode.

3. Mild Saturation with Local Pressure Flattening

For the nonlinear calculation with $\beta_0 = 0.5\%$, we use the following range of Fourier components: $0 \leq n \leq 5$ and $0 \leq m \leq 16$, where m denotes the poloidal mode number. Figure 3 shows time evolution of the kinetic energy of the perturbation which is defined by $E_k = \sum_n E_k^n$, $E_k^n = \frac{1}{2}\int |\nabla_\perp \sum_m \Phi_{mn} \sin(m\theta - n\zeta)|^2 dV$.

The linear phase is dominated by the $(m,n) = (5,2)$ mode, which is nonlinearly saturated at $t = 4800\tau_A$. In the nonlinear phase, the variation of the kinetic energy is small and slow. Figure 4 shows the flow pattern and the pressure contour at $t = 4800\tau_A$. The convective flow forms the vortices around the resonant surface with $\iota = 2/5$. The number of the vortices is two times of the poloidal mode number. These vortices interchange the high and the low pressure regions alternatively in the poloidal direction. Therefore, the structure like a mushroom is generated. As a result, the average pressure, $\langle P \rangle = \tilde{P}_{m=0,n=0} + P_{eq}$, is locally flattened around the rational surface as shown in Fig. 5, where the tilde means the perturbed quantity. On the other hand, it is obtained that the compression of the magnetic surface due to the vortices causes the driven reconnection of the field line. Because the island is located at the vortex position, the number is also two times of the poloidal mode number like the case in Ref.[12].

The local pressure flattening makes the pressure gradient steep at the both sides of the flat region. Then, the mode resonant at the region with the steepened pressure gradient can be destabilized. In the saturation of the $(m,n) = (5,2)$ mode, the pressure gradient at the surface with $\iota = 3/7$ is steepened, which is located just outside the $\iota = 2/5$ surface. Then, the $(m,n) = (7,3)$ mode grows, and saturates at $t = 11325\tau_A$, as shown in Fig.3. As shown in Fig.5, two flat pressure

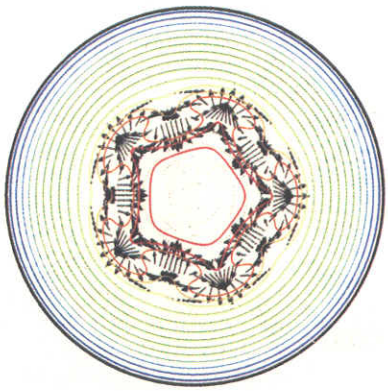

FIG.4. Flow pattern (black arrows) and pressure contour on the (ρ,θ) plane at $\zeta = 0$ cross section at $t = 4800\tau_A$ for the $\beta_0 = 0.5\%$ equilibrium, plotted only in the region of $\rho \leq 0.6$. Color of the pressure contour varies red to blue as the value decreases. The longest arrow corresponds to the largest velocity in this plane.

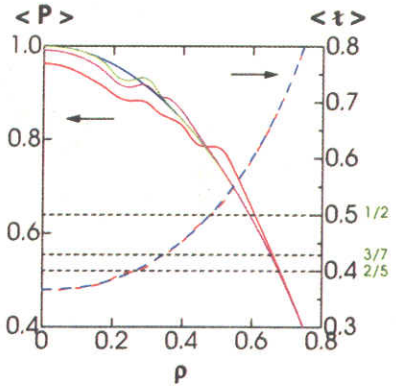

FIG.5. Profiles of average pressure $\langle P\rangle$ (solid lines) at $t = 0$(blue), $4800\tau_A$(green), $11325\tau_A$(purple) and $24000\tau_A$(red) and average rotational transform $\langle\iota\rangle$ (dashed lines) at $t = 0$(blue) and $24000\tau_A$(red) in the region of $\rho \leq 0.8$ for the $\beta_0 = 0.5\%$ equilibrium. Average pressure is normalized so that $\langle P\rangle(\rho = 0, t = 0)$ should be unity. Rational surfaces with $\iota = 2/5$, 3/7 and 1/2 are indicated.

regions coexist at this time. The saturation of the $(m,n) = (7,3)$ mode makes the gradient at $\iota = 1/2$ surface steep in turn, and excites the $(m,n) = (2,1)$ mode. All modes are saturated completely at $t = 24000\tau_A$. The average pressure profile is deformed so as to be the staircase-like shape with multiple flat regions, as shown in Fig.5. The average rotational transform defined by $\langle\iota\rangle = \frac{1}{\rho}\frac{\partial\tilde{\Psi}_{m=0,n=0}}{\partial\rho} + \iota_{eq}$ is also plotted in Fig.5. The nonlinear effect on the average rotational transform is much weaker than on the pressure. Note that the $n = 1$ mode is dominant in the kinetic energy at $t = 24000\tau_A$, which is linearly stable.

4. Global Pressure Reduction due to Bursting Activity

Next, we examine the nonlinear evolution of the perturbation for $\beta_0 = 1.0\%$. The calculation is carried out in the Fourier space of $0 \leq n \leq 7$ and $0 \leq m \leq 22$. Figure 6 shows the time evolution of the kinetic energy. The $(m,n) = (5,2)$ component is dominant in the linear phase as in the case of $\beta_0 = 0.5\%$. However, a bursting activity appears after the dominant linear mode saturates. In the bursting phase, the multiple modes with different helicity grow and decay rapidly. The kinetic energy of each mode for $n \geq 1$ is in the level of $E_k^n \geq 10^{-7}$. This fluctuation level is almost one-order larger than that in the case of $\beta_0 = 0.5\%$. This implies that the driving force for each mode is enhanced. Figure 7 shows the flow pattern and the pressure contour at $t = 3840\tau_A$ where E_k has a maximum value. The pressure structure is too complicated to identify the mode number although the $n = 2$ mode is dominant in the kinetic energy at this time. The property of the pressure structure indicates the overlaps of many components in the bursting phase. This is due to the enhancement of the mode width by the large driving force.

The profile of the average pressure shows the several flat regions corresponding to $\iota = 2/5$, 4/9, 1/2 and 4/7 at $t = 3840\tau_A$, as shown in Fig.8. Particularly, there exist large flat pressure regions around the $\iota = 2/5$ and the $\iota = 1/2$ surfaces. The regions with strongly steep pressure gradient are

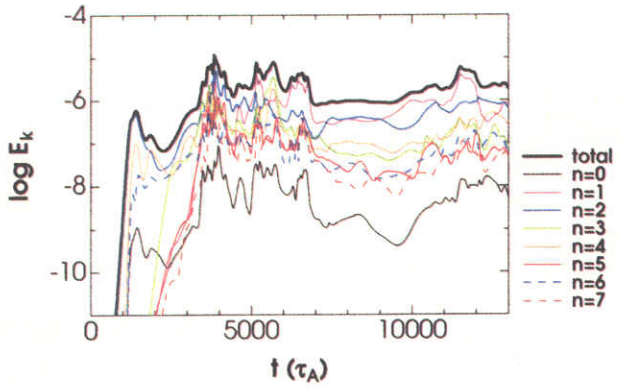

FIG.6. Time evolution of the kinetic energy of the perturbation for the $\beta_0 = 1.0\%$ equilibrium with the pressure of eq.(8). Thick line shows the total energy and thin lines show the $n = 0, 1, 2, 3, 4, 5, 6$ and 7 components.

located just outside the large flat pressure regions. It can be considered that such structure in the average pressure results from the cooperative flow of the overlapped modes. After the bursting phenomena, a large amount of the pressure in the core region is transported to the peripheral region. The central pressure decreases to 90% of the initial value and the whole gradient is also reduced in the region of $\rho \leq 0.5$ at $t = 13000\tau_A$ as shown in Fig.8. Thus, the bursting activity causes the global reduction in the pressure.

5. Stable Path to High Beta Regime

For pressure profile in eq.(8), the results in the previous section indicate that the achievable beta value in LHD may be limited by the bursting activity. On the other hand, as the beta value increases we expect a succession of pressure profiles that vary continuously with the beta. In order to simulate this situation, we utilize the saturated pressure profile at $\beta_0 = 0.5\%$ for the calculation at $\beta_0 = 1.0\%$ here, instead of the profile of eq.(8). The initial profile is determined by taking the average profile at $t = 24000\tau_A$ at $\beta_0 = 0.5\%$ and increasing the beta value up to 1.0%. Then, the three-dimensional equilibrium is calculated with the VMEC code under the free-boundary condition to include the beta dependence of the plasma boundary.

The linear growth rates for this equilibrium are plotted in Fig.2. The dominant mode is the $n = 3$ mode, and the growth rates are reduced for other modes compared with those in the equilibrium with eq.(8). The nonlinear evolution of the kinetic energy is shown in Fig.9. The behavior is similar to that in the $\beta_0 = 0.5\%$ case. The saturation of the $(m,n) = (8,3)$ mode at $t = 1700\tau_A$ slowly excites the $(m,n) = (5,2)$ mode. The saturation of the (5,2) mode occurs at $t = 3000\tau_A$, which excites the $(m,n) = (7,3)$ and (8,3) modes. After the sequence, the variation of the kinetic energy is small and slow. No bursting phenomenon appears in the time range of $t \leq 13000\tau_A$. This is because the driving forces of the $n = 1$, 2 and 4 modes are already reduced by the deformation of the initial pressure profile. New flat regions are generated around $\iota = 2/3$ and 6/11 in the average pressure profile at $t = 13000\tau_A$, as shown in Fig.10. However, they are just the local variations and the reduction of the core pressure is much smaller than that of the bursting case. Thus, the plasma pressure can be self-organized so as to suppress the bursting activity in the increase of the beta value from $\beta_0 = 0.5\%$ to 1.0%.

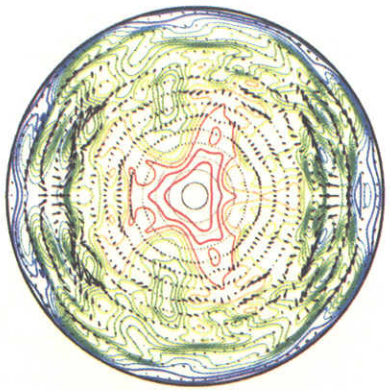

FIG.7. Flow pattern (black arrows) and pressure contour on the (ρ, θ) plane at $\zeta = 0$ cross section at $t = 3840\tau_A$ for the $\beta_0 = 1.0\%$ equilibrium with the pressure eq.(8), plotted only in the region of $\rho \leq 0.6$. Color of the pressure contour varies red to blue as the value decreases. The longest arrow corresponds to the largest velocity in this plane.

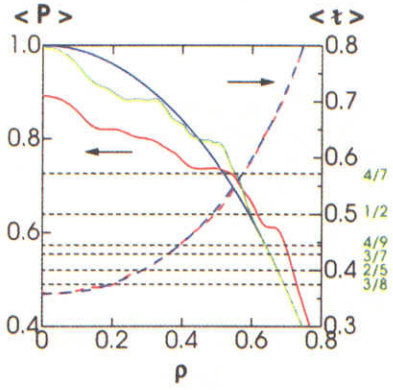

FIG.8. Profiles of average pressure $\langle P \rangle$ (solid lines) at $t = 0$(blue), $3840\tau_A$(green), and $13000\tau_A$(red) and average rotational transform $\langle \iota \rangle$ (dashed lines) at $t = 0$(blue) and $13000\tau_A$(red) in the region of $\rho \leq 0.8$ for the $\beta_0 = 1.0\%$ equilibrium with the pressure eq.(8). Rational surfaces with $\iota = 3/8$, 2/5, 3/7, 4/9, 1/2 and 4/7 are indicated.

6. Conclusions

The nonlinear evolution of the interchange mode with multi-helicity is examined in the inward-shifted low-beta LHD equilibria with almost parabolic pressure profile. The behavior is different depending on the beta value. In the case of the sufficiently low beta value, the perturbations are slowly saturated in the low fluctuation level. The local pressure flattening due to the saturation of a single mode steepens the pressure gradient outside the flat region, and excites other single mode resonant at the steep gradient region. Therefore, the saturation and the excitation of the modes with different helicity are succeeded alternatively in the time evolution. The resultant pressure profile is staircase-like, as is expected by the linear calculation[4]. The occurrence of such mild saturation is attributed to the fact that only a few modes with different helicity are destabilized and the driving force of each mode is weak. In this case, the distance between the resonant surfaces of the unstable modes is wide enough for each mode to generate the flat pressure region needed for the saturation. Thus, the variation in the pressure profile is limited in the local regions.

On the other hand, increasing the beta value with the pressure profile fixed enhances the driving force. Then, the number of the unstable mode increases and the larger width of the flat pressure region is needed for the saturation of each mode. If the distance between the resonant surfaces of the unstable modes is smaller than the width of the necessary flat region for the saturation of the modes, the modes can overlap each other and the bursting activity is observed in the kinetic energy. Because the multiple modes grow and overlap in the core region for $\rho \leq 0.5$ in the present case for $\beta_0 = 1.0\%$, the bursting activity continues until the pressure gradient is decreased all over the region. Thus, the global reduction of the pressure profile is caused.

We simulate the continuous change of the pressure profile in the increase of the beta value by employing the saturated pressure profile at the lower beta value. It is demonstrated that the

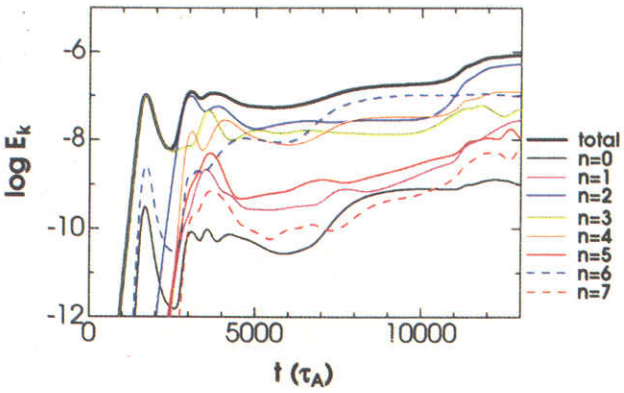

FIG.9. Time evolution of the kinetic energy of the perturbation for the $\beta_0 = 1.0\%$ equilibrium with the saturated pressure profile at $\beta_0 = 0.5\%$. Thick line shows the total energy and thin lines show the $n = 0, 1, 2, 3, 4, 5, 6$ and 7 components.

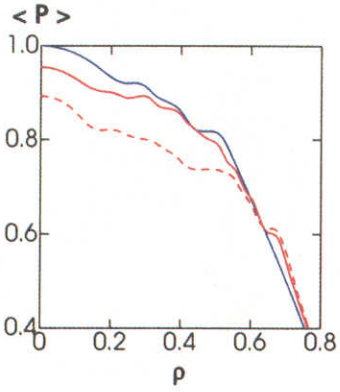

FIG.10. Profiles of average pressure $\langle P \rangle$ (solid lines) at $t = 0$(blue) and $13000\tau_A$(red) in the region of $\rho \leq 0.8$ for the $\beta_0 = 1.0\%$ equilibrium with the saturated pressure profile at $\beta_0 = 0.5\%$. Profile of the average pressure at $t = 13000\tau_A$ in Fig.8 is also shown by dashed red line for the comparison.

modes are nonlinearly saturated slowly as in the lower beta case. The bursting activity, which may limit the achievable beta value, is avoided by the reduction of the driving force due to the local deformation of the initial pressure profile. This result indicates the possibility that the pressure profile is self-organized through the nonlinear evolution of the interchange mode in LHD so that the plasma should attain the high beta regime beyond the linear stability limit for the fixed smooth pressure profiles.

Acknowledgment

This work was partially supported by the Grant-in-Aid for Scientific Research (C) of the Ministry of Education, Culture, Sports, Science and Technology, Japan.

References

[1] MOTOJIMA, O., et al., "Recent Advance in LHD Experiment", this conference, paper OV/1-6.
[2] ICHIGUCHI, K., et al., Nucl. Fusion **29** (1989) 2093.
[3] ICHIGUCHI, K., "Ideal and Resistive Stability of Free-Boundary LHD Equilibria" (Proc. 1999 Intl. Stellarator Workshop, Madison, 1999), CD-ROM file P2-4 (2000).
[4] ICHIGUCHI, K., et al., Nucl. Fusion **41** (2001) 181.
[5] CARRERAS, B.A., et al., Phys. Plasmas **8** (2001) 990.
[6] NAKAMURA, Y., et al., J. Comp. Phys. **128** (1996) 43.
[7] GARCIA, L., et al., J. Comp. Phys. **65** (1986) 253.
[8] HIRSHMAN, S.P., et al., Comp. Phys. Comm. **43** (1986) 143.
[9] ICHIGUCHI, K., et al., Nucl. Fusion **36** (1996) 1157.
[10] LIANG, Y., et al., Plasma Phys. Control. Fusion **44** (2002) 1383.
[11] JOHNSON, J.L., and GREEN, J.M., Plasma. Phys. **9** (1967) 611.
[12] WAKATANI, M. et al., Nucl. Fusion **24** (1984) 1407.

Nonlinear MHD Simulations of Spherical Tokamak and Helical Plasmas

T.Hayashi, N.Mizuguchi, H.Miura, R.Kanno, N.Nakajima, and M.Okamoto

National Institute for Fusion Science, Toki 509-5292, Japan
e-mail contact of main author: hayashi@nifs.ac.jp

Abstract. Nonlinear magnetohydrodynamic (MHD) simulations on relaxation phenomena in a spherical tokamak and a helical plasma, including three-dimensional (3D) equilibrium computations, are executed in full toroidal geometries. For a spherical tokamak, two-step evolution of the medium-n ballooning instabilities and a successive excitation of an internal n=1 crash has been observed. A similar process has been observed in an actual tokamak experiment of TFTR. The process is compared with a previous simulation for another MHD activity that is called the internal reconnection event (IRE). Three dimensional equilibrium code HINT is modified to extend functions, by which an n=1 island structure used for the local island diverter (LID) experiment in the LHD device is analyzed in finite pressure equilibria. Nonlinear simulations are executed for LHD plasma and pressure deformation due to evolution of m=2/n=1 pressure driven mode is observed, which has larger growth rate and saturation level than medium-n ballooning modes.

1. Introduction

We execute MHD simulations to study relaxation phenomena that occur in toroidal plasmas, which are not destructive but spontaneously modify plasma structure such as the pressure profile. In particular, nonlinear dynamics in full toroidal geometries of a spherical tokamak and a helical plasma are studied. The governing equations are a full set of the MHD equations that includes the terms of the resistivity η and the parallel heat conduction κ. The equations are solved by using the fourth-order central-finite-difference scheme and a fourth-order Runge-Kutta scheme.

$$\frac{\partial \rho}{\partial t} = -\nabla \cdot (\rho \boldsymbol{v}), \tag{1}$$

$$\frac{\partial}{\partial t}(\rho \boldsymbol{v}) = -\nabla \cdot (\rho \boldsymbol{v}\boldsymbol{v}) - \nabla p + \boldsymbol{j} \times \boldsymbol{B} + \mu(\nabla^2 \boldsymbol{v} + \frac{1}{3}\nabla(\nabla \cdot \boldsymbol{v})), \tag{2}$$

$$\frac{\partial \boldsymbol{B}}{\partial t} = -\nabla \times \boldsymbol{E}, \tag{3}$$

$$\frac{\partial p}{\partial t} = -\nabla \cdot (p\boldsymbol{v}) - (\gamma - 1)p\nabla \cdot \boldsymbol{v} + (\gamma - 1)(\eta \boldsymbol{j}^2 + \Phi - \nabla \cdot \boldsymbol{q}), \tag{4}$$

$$\boldsymbol{j} = \nabla \times \boldsymbol{B}, \tag{5}$$

$$\boldsymbol{E} = -\boldsymbol{v} \times \boldsymbol{B} + \eta \boldsymbol{j}, \tag{6}$$

$$\Phi = 2\mu(e_{ij}e_{ij} - \frac{1}{3}(\nabla \cdot \boldsymbol{v})^2), \tag{7}$$

$$e_{ij} = \frac{1}{2}(\frac{\partial v_i}{\partial x_j} + \frac{\partial v_j}{\partial x_i}), \tag{8}$$

$$\boldsymbol{q} = -\kappa \nabla_{\parallel}(p/\rho). \tag{9}$$

2. Relaxation Phenomena in Spherical Tokamak

2.1 Simulation Model

The simulation geometry roughly follows the NSTX device. The NSTX device has a conductor shell outside and a rod at the center close to the plasma surface. The computation region covers both the plasma area and the ambient vacuum area which is assumed to be surrounded by perfect conductors. The electron heat conduction is generally large in the direction parallel to the magnetic field in high-temperature plasma. In this paper, we check the effect of such large parallel heat conduction on the dynamics, which is solved with another time intervals, typically several tens of times less than that of the MHD convection terms.

The initial condition is given by an axisymmetric two-dimensional numerical equilibrium which is obtained by the EFIT reconstruction data of the real experiment in NSTX (courtesy of Drs. F. Paoletti, S. Sabbagh, and S. Kaye). The results shown here are derived from the data at 238 msec of the shot #10371, where the central beta is 28%, the central q is 0.89, and the aspect ratio is 1.4. A large scale MHD event was subsequently observed in the experiment. The radial profiles of the pressure, the toroidal current, and the safety factors are shown in Fig.1 (a), and the shape of the plasma is displayed by the contour of the poloidal flux in Fig.1(b). It is noted that the radial profiles are somewhat flat in the core region, compared with the profile for the previous case for the IRE simulation [1].

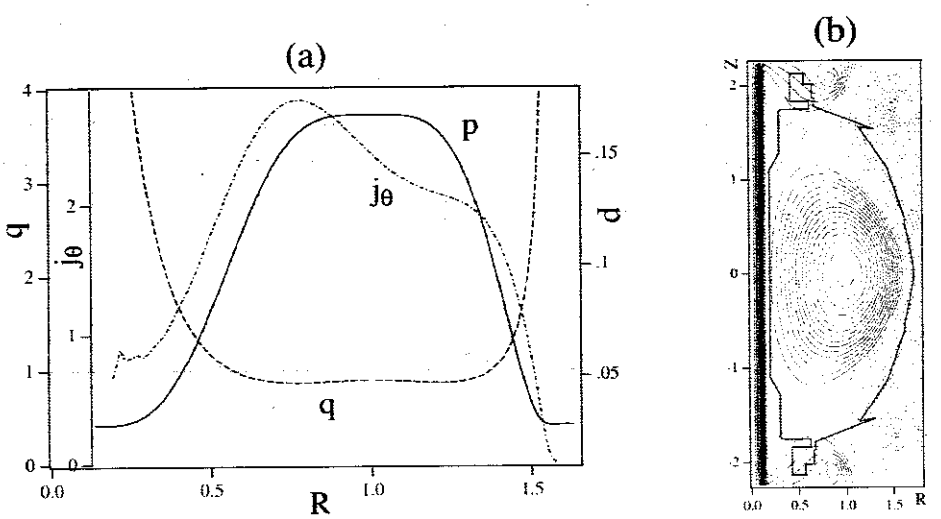

Fig.1 (a)Radial profiles of the pressure, the toroidal current and the safety factor for the initial condition.
(b) Geometry and the magnetic field structure of the initial condition.

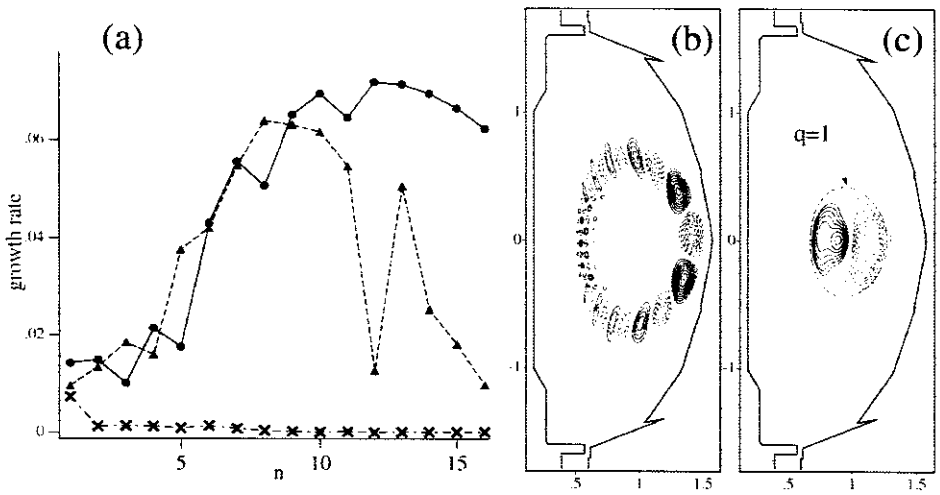

Fig.2 (a) Growth rate of the instabilities for each toroidal modes. The circles, triangles, and the crosses indicate that of the κ=0, κ=4x10^{-0}, and the secondarily induced n=1 mode, respectively. (b)Poloidal mode pattern of the linear n=12 mode for κ=0. The iso-contour of the pressure is plotted. (c)Poloidal mode pattern of the secondarily induced n=1 mode.

2.2 Simulation Results

We calculate the spontaneous time development of the random tiny perturbations given in the initial equilibrium. The initial equilibrium is stable and the perturbations are dumped under the ideal regime, that is, η and κ are substantially small. However, several modes become unstable with larger η. For η=4x10^{-5} (normalized), the most unstable components have medium toroidal mode numbers such as the n=12 and n=13. Shown by the solid circle in Fig.2 (a) is the growth rate for each toroidal mode numbers. The poloidal mode structure is also shown in Fig.2 (b). These resistive modes have the nature of the ballooning modes in that the poloidal mode structures are localized in the bad curvature region. On the other hand, it should be remembered that the lower-n modes is much less unstable in this stage.

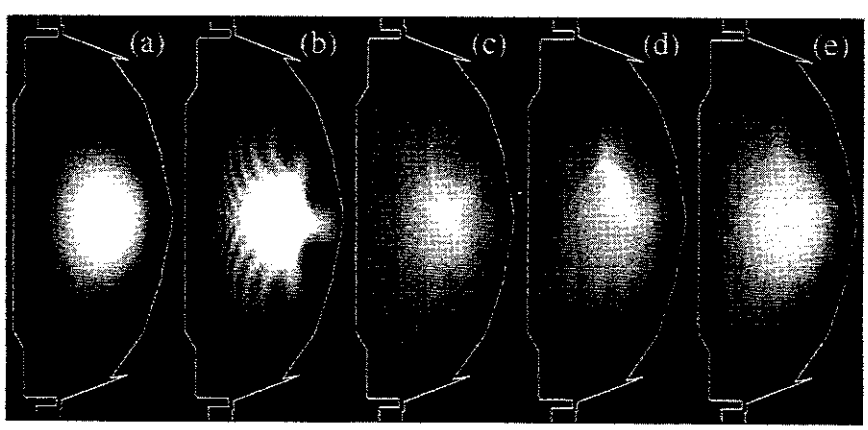

Fig.3 Time development of the poloidal pressure profile for (a)t=0, (b)200, (c)470, (d)550, and (e)760 τ_A.

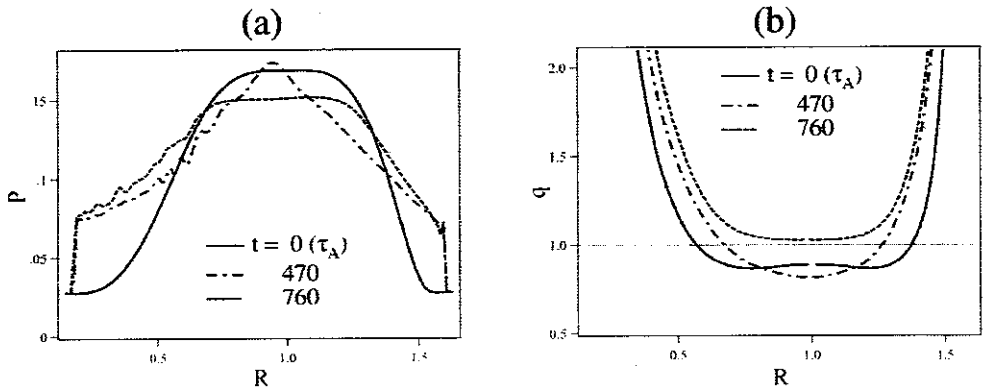

Fig.4 The radial profiles of (a) the pressure and (b) the safety factor for three equilibrium states.

Since the ballooning mode has the parallel component of the wave number to the magnetic field, the growth can be affected by the existence of large heat transport along the magnetic field. We model such heat conduction by adding large parallel thermal conductivity. The symbols with solid triangle in Fig.2(a) indicate the growth rate with normalized $\kappa=2\times10^{+0}$. It can be seen the higher-n ballooning component is suppressed by parallel heat conduction, and the most dominant component is shifted to n=8 in this case.

As the linear unstable modes grow, the amplitude of the perturbation becomes so large that the distortion in global structure becomes visible scale. Shown in Fig.3 is the time evolution of the poloidal pressure profile. The plasma surface wrinkles at the periphery region due to the ballooning modes (Fig.3 (b)). Then the pressure collapses in the periphery, but the high pressure region still remains at the core region (Fig.3(c)). In this state, the total kinetic energy of the plasma decreases to a minimum state, that is, the system is relaxed to a new equilibrium state. The temporal changes in the radial pressure and safety factor profile are shown in Fig.4. The new relaxed state is indicated with dash-dotted line. One can see that the pressure profile becomes more peaked since the peripheral structure collapses by the ballooning modes. The safety factor, on the other hand, also has the region below unity, the system still has instability.

About 200 Alfven transit time later, as is shown in Fig. 3(d), another large-scale instability begins to grow. This mode has the m/n = 1/1 component dominantly. The poloidal mode structure of the n=1 mode is plotted in Fig.2(c). The perturbations consist of a pair of positive and negative pressure fluctuations, and exist widely inside the q=1 rational surface. Another analysis by using the energy principle shows that the source of energy to drive the instability comes from the current-driven term. These observation proves that the secondarily induced instability is an n=1 internal kink mode. The central hot plasma region is largely shifted from the core to the edge, and is split in two fractions in the poloidal cross section near the q=1 rational surface, and the plasma convection motions lead the hot plasma to the core region again. The system relaxes to an axial equilibrium again (Fig. 3(e)). The radial pressure profile in this state becomes a broader one again (Fig. 4(a)), and the region where the safety factor below one vanishes (Fig. 4(b)).

2.3 Discussions on Spherical Tokamak Simulations

The simulation result described above shows some unique features. The sawtooth-like n=1 crash is induced as a result of the spontaneous time development of the middle-n ballooning precursors in our simulation. Such two-step evolution of the medium-n ballooning instabilities and a low-n crash has been observed experimentally in TFTR [2]. In the TFTR case, after the middle-n ($4<n<10$) ballooning activities are observed, an internal beta collapse accompanied by an m/n=1/1 components occurs, and the electron temperature decreased in the core region. This observation is comparable with our simulation results in the mode structures of the related instabilities.

In spherical tokamaks, the n=1 activities are often observed as the Reconnection Events and as the ordinary sawteeth (internal n=1 activities) when the central q goes below one. It is meaningful for us to compare the REs and sawteeth from the point of view of nonlinear simulations. Our previous simulation [1] models the Internal Reconnection Event observed in START. Experimentally, these phenomena have several common features such as a large scale pressure collapse (IRE or RE) and an n=1 fluctuation of the precursors. However, the IRE can be distinguished from the sawtooth in that the plasma global shape is largely distorted and the stored heat energy is lost. The IRE simulation results reproduce the large distortion and related activities on an IRE. These activities are induced by the magnetic reconnection between the internal and external field, which occurs by formation of a large and localized pressure bulge on the torus surface due to the growth of the combination of the m/n=1/1 and 2/2 interchange modes. Significant amount of the plasma pressure energy is lost from the reconnection point, and the overall shape of the torus becomes largely twisted by the strong plasma jet flows excited along the reconnected field lines. Thus, it is shown that the differences on the nonlinear time development between the sawtooth and the IRE case arise from only slight discrepancies in the initial profiles. Though the detailed mechanism is not clear yet, it is revealed by the simulation that the difference between linear instability modes can change the nonlinear time development, i.e., the internal kink induced by ballooning leads the internal n=1 activities, and the interchanges lead the RE.

3. Nonlinear Evolution of Pressure-driven Instabilities in a Helical System

3.1 Extension of the HINT code

The 3D equilibrium code HINT, which does not assume the existence of magnetic surfaces, is modified in a couple of directions to extend the functions [3]. (a) Coil currents can exist in the computation region. (b) The net toroidal current effects (Ohmic and Neoclassical) are consistently treated in the evaluation of the island formation. (c) The full torus configuration is consistently treated [4]. Thus, the usefulness of the code is largely enhanced.

Owing to the modification (c) of the code, behavior of magnetic islands that do not keep the stellarator symmetry can now be treated for a finite beta equilibrium. The m/n=1/1 island structure that is used in the local island divertor (LID) experiment in Large Helical Device (LHD) (ref. [5]) is such an example, as is shown in Fig.5.

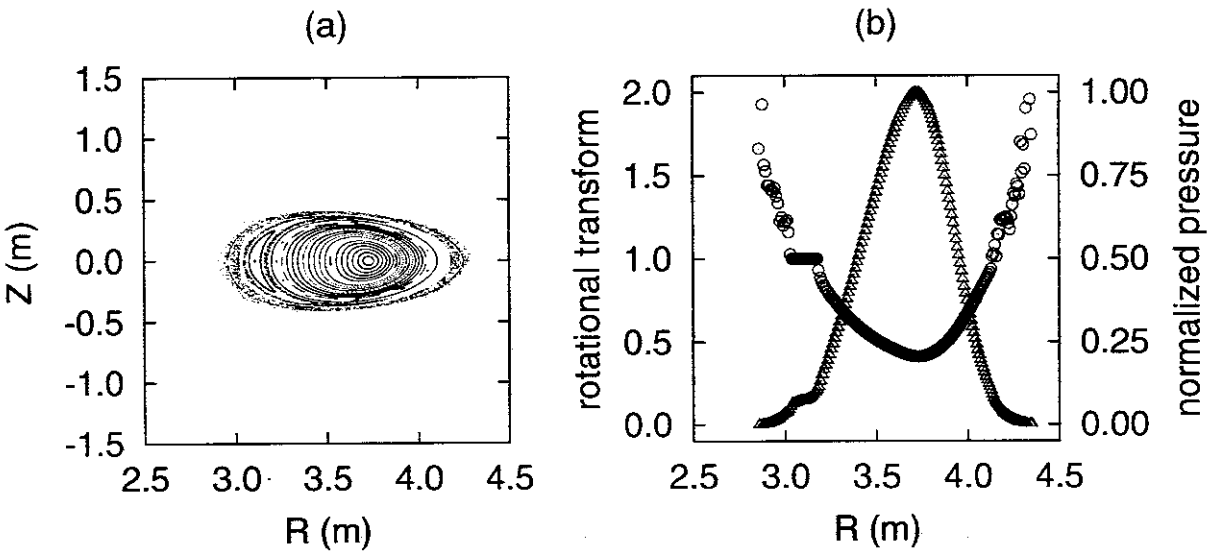

Fig.5 (a) Poincare plots of field lines at the horizontally elongated poloidal cross section and (b) profiles of rotational transform (open circle) and pressure (open triangle) at Z=0 in the horizontally elongated poloidal cross section in a LHD equilibrium with the m/n=1/1 island for beta=2%.

3.2 Simulation Model and Results

Based on a HINT equilibrium, nonlinear evolution of pressure-driven instabilities is studied in a full 3D geometry of LHD (Large Helical Device), which has seldom been attempted. We solve the MHD equations described in the helical-toroidal HINT coordinate system. The number of the grid points is 97x97 on a poloidal section and 640 in the toroidal direction. The kinetic viscosity and the heat diffusion coefficient are fixed as $2.x10^{-2}$ and $1.x10^{-6}$, respectively. Two simulations with the resistivity $1.x10^{-6}$ and $5.16x10^{-6}$ are conducted. We refer to the former (latter) resistivity as the lower (higher) resistivity. We also conduct nonlinear simulations of the half-pitch period system under the stellarator symmetry in order to compare the results with full-torus simulations. The initial equilibrium has the initial position of the vacuum magnetic axis R_{ax}=3.6m for the actual LHD device and the initial central beta $\beta(0)$=4%.

In Fig.6, time evolutions of the kinetic energy per unit volume are shown. The solid lines represent runs with the higher resistivity while the dashed ones represent runs with the lower resistivity. Thick lines are for full-torus runs and thin lines are for half-pitch simulations. We find that the full-torus runs attain higher saturation levels than their half-pitch counterparts. Because of the rapid growth of the kinetic energies in the full-torus simulations than in half-pitch simulations, low toroidal (n) modes are dominant from the initial phase of the growth. However, detailed observations reveal that the smaller poloidal modes (m) are significant in the mid of the energy growth, which are the medium-wave number ballooning instabilities (Miura et al[6]), though the figures are not shown here.

The ballooning instability is saturated due to the nonlinearity of the MHD equation. At the saturation time, a distinct m/n=2/1 structures are observed in the isosurface of the pressure in Fig.7. The mode structures are clearly different from the ridge-like structure formed in the pressure profile that has been

observed in the half-pitch simulations [6].

In order to see how the m/n=2/1 structures are formed, we have observed time-sequence of the pressure on a horizontally- and vertically-elongated poloidal sections. In Fig. 8, color contours of the pressure on a horizontally-elongated poloidal section are shown with the streamlines as a typical example. The black ellipses represent the magnetic surfaces with the rotational transform 1/2 (the inner ellipse) and 2/3 (the outer ellipse).While the initial pressure deformation starts around the outer ellipse, the pressure is exposed to the strong m/n=1/2 flows in the course of time evolution, as is observed in Fig.8. We observed that the poloidal vortices advect and deform the pressure. Consequently, the mushroom-like structure of the pressure is formed on a poloidal section. Note that we have conducted the pressure-budget analysis which had been shown in Ref.[6] for the full-torus simulations and verified that the deformation process is fully dominated by the advection. It makes a clear contrast to the half-pitch simulations in which other processes such as the fluid compression, thermal diffusion and viscous heating work to suppress deformation by the advection. It is also interesting that we observe the mushroom-like structure of the pressure because it is typically observed in inertial-fusion system. Instead of the baroclinic torque which forms mushrooms in the laser-fusion system, strong m/n=2/1 poloidal flow works to form the structure.

In our simulation, the central beta is reduced from 4.0 to 2.0 at the final time. However, the total thermal energy does not decrease so much thanks to the well-confined magnetic surfaces.

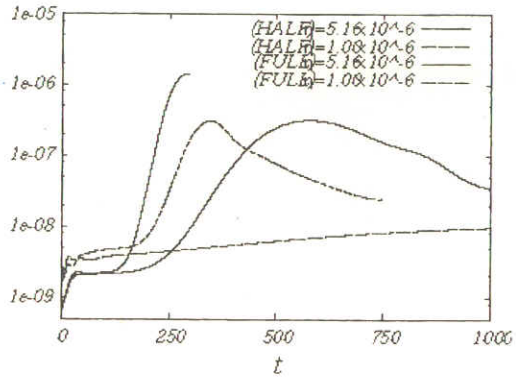

Fig.6 Time evolution of the kinetic energy per unit volume. The solid (dashed) lines represent runs for the higher (lower) resistivy. Thick (thin) lines are for the full-torus (half-pitch) simulations.

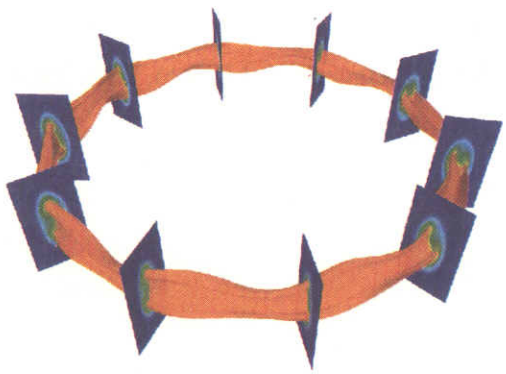

Fig.7 Isosurface of the pressure for full-torus simulation with the lower resistivity. Clear m/n=2/1 deformations are observed.

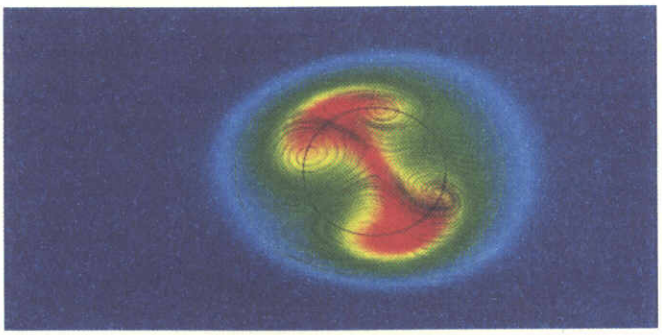

Fig.8 Color contours of the pressure on a horizontally-elongated poloidal section for the full-torus simulation with the lower resistivity at the saturation time of the kinetic energy.
Streamlines are drawn with poloidal components of the velocity field.

Acknowledgements

We acknowledge Drs. F. Paoletti, S. Sabbagh, and S. Kaye for useful discussions and providing us with the reconstructed NSTX equilibrium data.

References

[1] T. Hayashi, et al., Nucl. Fusion 40, 721, (2000); N.Mizuguchi., T.Hayashi., and T.Sato., Phys. Plasmas, 7 (2000) 940.

[2] Y. Nagayama, et al., Phys. Fluids B 5, 2571, (1993).

[3] T. Hayashi, et al., Contrib. Plasma Phys., Vol.42, No.2-4 (2002) 309-320; H. Harafuji, T. Hayashi and T. Sato, J. Comp. Phys. **81** (1989) 169.

[4]R. Kanno, N. Nakajima, T. Hayashi, and M. Okamoto, J. Plasma Fusion Res. SERIES **3** (2000) 584. ; R. Kanno, N. Nakajima, T. Hayashi, and M. Okamoto, Contrib. Plasma Phys. **40** (2000) 260.

[5]A. Komori, N. Ohyabu, et al, Plasma Physics and Controlled Nuclear Fusion Research, (Vienna, 1994), **II** (1995) 773.

[6]H. Miura, T. Hayashi and T. Sato, Phys. Plasmas **8** (2001) 4870.

Profile Relaxation and Tilt Instability in a Field-Reversed Configuration

H.Ohtani 1), R.Horiuchi 1) and T.Sato 2)

1)National Institute for Fusion Science, Toki 509-5292, Japan
2)Japan Marine Science and Technology Center, Yokohama 236-0001, Japan

e-mail contact of main author: ohtani@tcsc.nifs.ac.jp

Abstract. The profile relaxation from a magnetichydrodynamic (MHD) profile to a kinetic equilibrium in field-reversed configurations (FRCs) is investigated by two-dimensional electromagnetic particle simulation. The radial oscillation takes place in order to relax an excess energy in the MHD profile, and the system spontaneously relaxes toward a kinetic equilibrium. In this kinetic equilibrium, the hollow electron current profile is realized as a result of the combined effects of the single particle orbits and the ion finite Larmor radius, and the ion current profile becomes peaked due to the effect of the ion meandering motion. Three-dimensional full electromagnetic particle simulation is also performed to study the stability of these kinetic equilibrium against the tilt mode. The growth rate of the tilt instability is reduced by the kinetic effects. It is found that the stabilization effect of tilt mode becomes much distinct when the current density changes from the peaked profile to the hollow one.

1. Introduction

The tilt instability in the field-reversed configuration (FRC) plasma is predicted by the magnetichydrodynamic (MHD) theory, but it has not been observed in the experiments[1]. It is also reported that most experimental equilibrium states tend to take a hollow current profile[2]. This tilt instability has been studied by the extended MHD models, but they could not give the satisfactory explanation as yet. An MHD equilibrium was used as the initial condition for the three-dimensional (3D) electromagnetic particle simulation[3,4,5]. However, the influence of the kinetic effect on the tilt mode was not clarified, because the MHD equilibrium relaxes to the kinetic one simultaneously with the evolution of the tilt instability. It is important to investigate this problem by the full particle simulation, because most experimental FRC plasmas are so kinetic that the MHD theory can not deal with them.

2. Simulation Method

Taking it into account that the tilt mode is 3D instability, we first perform two-dimensional (2D) electromagnetic particle simulation to get the kinetic equilibrium without exciting the tilt instability, and clarify the property of the kinetic FRC plasma. An initial profile for 2D simulation is given by a one-fluid MHD equilibrium which is controlled by the hollowness parameter D, the plasma beta value β_{sp} at separatrix and the finite Larmor radius (FLR) parameter $\bar{s}$[6]. We choose two-types of initial particle distribution. The first one is the shifted-Maxwellian under the zero $E(0)$ condition, where the average flow velocity is equal to the diamagnetic velocity. The second one is the shifted-Maxwellian under the required $E(0)$ condition, where the electric current is carried only by the electron and the average ion flow velocity is zero. In these distribution, the ion temperature and the electron temperature are the same and spatially constant. Next we examine the feature of the tilt instability by means of 3D full electromagnetic particle simulation in which the kinetic equilibrium obtained from 2D simulation is used as the initial condition.

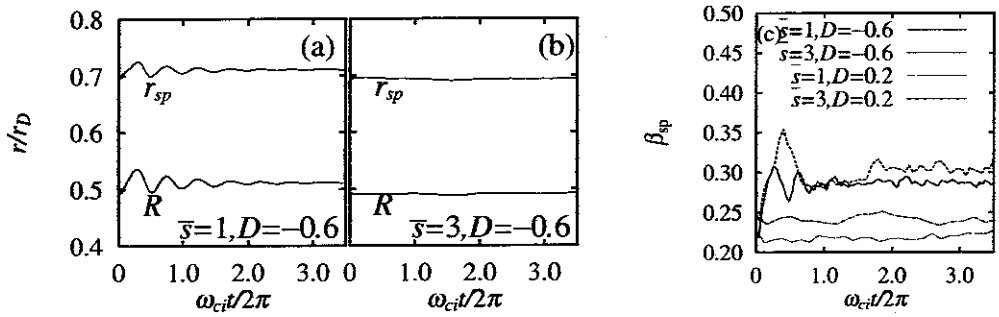

FIG. 1: *Time evolution of the field-null line and separatrix radii (R and r_{sp}) in (a)$\bar{s}=1$, (b)$\bar{s}=3$, and (c)time evolution of the plasma beta value at the separatrix (β_{sp}).*

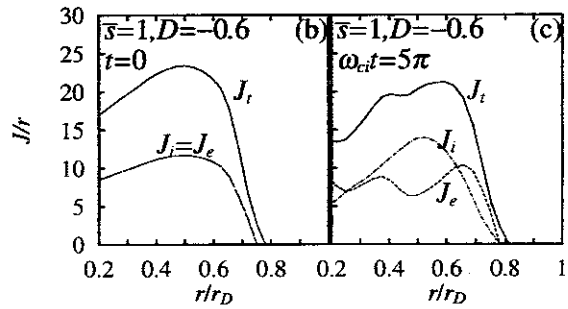

FIG. 2. *The radial profile of toroidal current density in $\bar{s}$=1 at (a)$\omega_{ci}t$=0 and (b)$\omega_{ci}t=5\pi$.*

3. Profile relaxation

Let us examine how the plasma profile changes from an MHD profile to a kinetic equilibrium based on 2D simulation results. Figure 1(a) 1 (b) shows the time evolutions of the field-null line and separatrix radii (R and r_{sp}) on the midplane in (a) $\bar{s}=1$ and (b) $\bar{s}=3$, respectively. In the full kinetic case ($\bar{s}=1$), both R and r_{sp} oscillate with frequency $\omega \sim 2\omega_{ci}$ in the early period and damp gradually until $\omega_{ci}t \sim 5\pi$ shown in Fig. 1(a). The plasma beta value β_{sp} at the separatrix jumps from an initial small value to about 0.3 in an initial moment, and keeps this value after that (Fig. 1(c)). This phenomena indicates that the profile oscillates in the radial direction to relax an excess energy in an MHD profile. In the moderate kinetic case ($\bar{s}=3$), on the other hand, no oscillation appears (Fig. 1(b)) and β_{sp} keeps an initial value (Fig. 1(c)). When a plasma is fully kinetic, the energy difference between an initial MHD profile and an obtained kinetic equilibrium is so large that a relaxation oscillation is excited.

Figure 2 shows the radial profiles of toroidal current density in $\bar{s}=1$ at (a)$\omega_{ci}t=0$ and (b)$\omega_{ci}t=5\pi$, respectively. After the relaxation oscillation, the electron current density J_e increases near the separatrix, and decreases near the field-null line. An initial peaked profile ($D<0$) changes to a hollow profile ($\tilde{D}_e>0$). On the other hand, the ion current density J_i becomes more peaked ($\tilde{D}_i<D<0$). So the total current J_t changes to the hollow profile near the field-null line. Both the decrease of J_e and the increase of J_i near the field-null line can be explained by the character of the single particle orbit (Fig. 3). The dominant electron motion near the field-null line is the gradient-B drift. Because the gradient-B drift has the opposite sign to the electron diamagnetic drift, J_e decreases

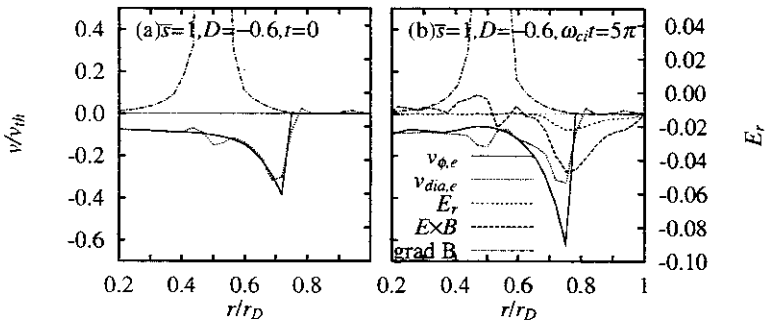

FIG. 3. *The radial profile of toroidal electron flow velocity in $\bar{s}$=1 at (a)$\omega_{ci}t$=0 and (b)$\omega_{ci}t = 5\pi$.*

near the field-null line. On the other hand, when the spatial scale of magnetic field is almost the same as the ion orbit scale, ions execute meandering motions along the field-null line. The average toroidal velocity is so large due to this meandering motion that J_i increases near the field-null line. Next, we consider why J_e increases near the separatrix (Fig. 3). Since the density profile becomes steep locally in the narrow periphery region near the separatrix, the ion FLR effect generates the strong radial electric field E_r there. Because the generated $E \times B$ drift has the same sign as the electron diamagnetic drift, J_e increases in the periphery. On the other hand, E_r acts on ions less effectively since the ion Larmor radius is larger than the spatial size of a strong electric field region. That is, the modification of ion current profile becomes relatively smaller.

In this way, an initial MHD equilibrium with a peaked current profile relaxes to a kinetic equilibrium with a hollow current profile through the effects of the single particle orbit and FLR. We find the tendency for the electron current to become a hollow profile and for the ion current to become a peaked profile independently of the initial condition, such as the initial hollowness parameter D, the FLR effect $\bar{s}$, the initial electric field $E(0)$.

4. Tilt instability

We clarify from 2D simulation that the kinetic equilibrium with the hollow current profile is spontaneously generated in the FRC plasma. In this section, the feature of the tilt mode in the kinetic equilibrium is also investigated based on 3D simulation results. In 3D simulation, the kinetic equilibrium solution obtained after the profile relaxation in 2D simulation is adopted as the initial condition.

There are several parameters which are related to the stabilization of the tilt mode. That is, the plasma beta value β, the Alfvén Mach number M_A, the hollowness parameter D, and the FLR parameter $\bar{s}$. We discuss the relationship between the growth rate of the tilt mode and these parameters. Figure 4 shows the dependence of the tilt growth rate γ_{tilt} on (a) the plasma beta value $\beta_{\rm sp}$ at the separatrix, (b) the Alfvén Mach number M_A, and (c) the electron hollowness parameter $\tilde{D}_e$, where γ_{tilt} is normalized by those obtained from MHD simulation γ_{MHD}, and M_A is the associated with the ion toroidal flow velocity, the plasma density at the field-null line, and the magnetic field at the wall. A glance at Fig. 4 reveals that γ_{tilt} reduces to about 5% to 25% of γ_{MHD} because of the kinetic effect.

Figure 4(a) shows that γ_{tilt} tends to decrease as $\beta_{\rm sp}$ increases. This result means that the separatrix beta value is relevant to the tilt stabilization. Nishimura *et al* suggest from this

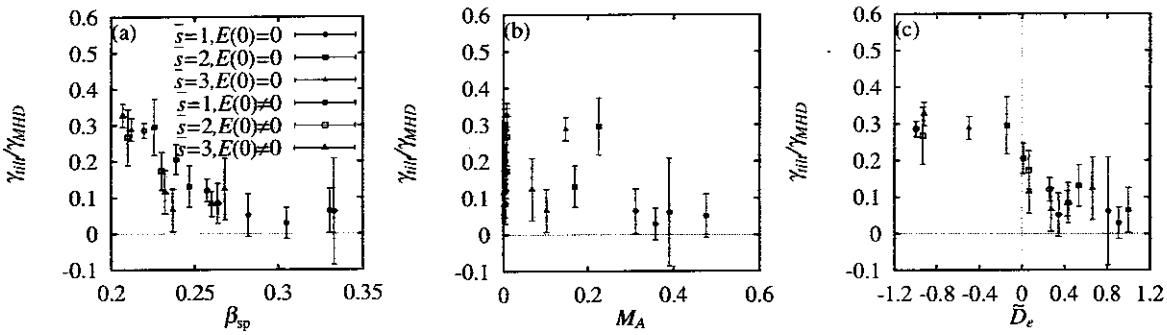

FIG. 4: *Dependence of the tilt growth rate γ_{tilt} on (a)plasma beta value β_{sp} at separatrix, (b)Alfvén Mach number M_A, and (c)electron hollowness parameter $\tilde{D}_e$.*

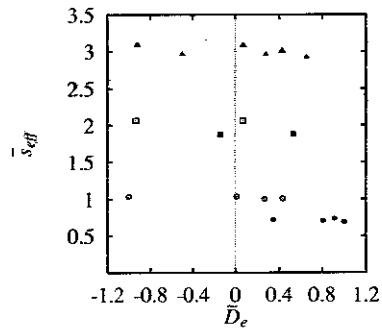

FIG. 5. *Relationship between effective kinetic parameter $\bar{s}_{eff}$ and electron hollowness parameter $\tilde{D}_e$.*

tendency that the anchoring ions may play a role to connect the unstable internal plasmas with stable external plasmas and keep the system stable against the tilt instability[3].

In the MHD simulation[7], the tilt mode is stabilized due to the spin stabilization effect when $M_A > 1$. From Fig. 4(b), on the other hand, the tilt stabilization becomes visible in the region of $M_A \approx 0.5$. Therefore this stabilization is not explained directly by the spin stabilization effect. Because the relationship between γ_{tilt} and M_A is complex, it is suggested that the ion toroidal motion partially contributes to the tilt stabilization.

It is worthly of notice from Fig. 4(c) that the tilt growth rate is remarkably reduced when the electron current profile is hollow ($\tilde{D}_e > 0$). Furthermore, it is important to point out that there is a clear correlation between the growth rate and the electron hollowness parameter, although all sorts of the simulation results obtained from various initial conditions are demonstrated in Fig. 4(c). These results indicate that the electron hollowness parameter has much to do with the tilt stabilization. This tendency coincides with the analysis of the experiments by Steinhauer and Ishida[2].

Let us consider the relationship between the reduction of the tilt growth rate and the electron hollowness parameter by introducing the effective kinetic parameter $\bar{s}_{eff}$ instead of $\bar{s}$, where the effective kinetic parameter $\bar{s}_{eff}$ is given by replacing the thermal velocity in the definition of $\bar{s}$ by the average ion velocity $\sqrt{\langle v_i^2 \rangle}$ as $\bar{s}_{eff} = \frac{m_i c}{r_{sp} q_i} \int_R^{r_{sp}} \frac{\tau dr}{\sqrt{\langle v_i^2 \rangle} B_z(r)}$. The relation between $\bar{s}_{eff}$ and the electron hollowness parameter $\tilde{D}_e$ is presented in Fig. 5. We see from this figure that $\bar{s}_{eff}$ in the initial zero electric field cases (closed symbols) is smaller than $\bar{s}_{eff}$ in the initial finite electric field cases (open symbols). This tendency is clearly seen in $\bar{s} = 1$, where the electron current profile becomes more hollow ($\tilde{D}_e > 0$)

and γ_{tilt} becomes smaller (Fig. 4(c)). From these results, it is indicated that the ions in the vicinity of the field-null line are not magnetized so much by the effect of the electric current shielding since the large electric current flows near the separatrix in the electron hollow current profile. This result suggests that the stabilization of the tilt mode is deeply related to this unmagnetization effect of ions.

The analysis of the results of 3D simulation leads us to the conclusion that the tilt mode tends to be stabilized in the cases of the hollow current profile.

5. Summary

The two-dimensional electromagnetic particle simulation is performed to investigate the profile relaxation from an MHD profile to a kinetic equilibrium and to clarify the property of the kinetic equilibrium of the field-reversed configurations independently of the tilt instability. And then we perform the three-dimensional full electromagnetic particle simulation using the kinetic profile obtained from the two-dimensional simulation as the initial condition to examine the stability of the kinetic equilibrium against the tilt mode.

The relaxation oscillation takes place when the profile relaxes from an MHD profile to a kinetic equilibrium. After this profile relaxation, the electron current profile changes to a hollow profile around the filed-null line as a result of the combined effects of the gradient-B drift near the field-null line and the $E \times B$ drift generated by the ion finite Larmor radius effect near the magnetic separatrix. On the other hand, the ion current profile becomes a peaked profile because of the effect of the ion meandering motion along the field-null line.

The growth rate of the tilt instability in all cases reduces to a small value because of the kinetic effect. In the system where the hollow current profile is realized after the profile relaxation, the growth of the tilt instability is suppressed, while in the system with peaked current profile, the tilt instability grows. From the investigation into the relationship between the tilt growth rate and several parameters, we find that the electron hollowness parameter and the separatrix beta value are important keys to solve the problem of the tilt stabilization.

Acknowledgments

This simulation is performed on the MISSION System (Grand Man-Machine Interactive System for Simulation) at the National Institute for Fusion Science. This work is supported by a Grant-in-Aid from the Ministry of Education, Culture, Sports, Science and Technology in Japan (No. 13640414).

[1]J. T. Slough et al: Phys. Plasmas **2** 2286 (1995).
[2]L. C. Steinhauer et al: Phys. Fluids **B 4**, 645 (1992).
[3]K. Nishimura et al.: Phys. Plasmas **4**, 4035 (1997).
[4]R. Horiuchi et al.: Nucl. Fusion **39**, 2083 (1999).
[5]H. Ohtani et al.: JPRF **5**, in press (2002).
[6]J. W. Cobb et al.: Phys. Fluids **B5**, 3227 (1993).
[7]R. Horiuchi et al.: Phys. Fluids **B1** 581 (1981).

Effect of Electrode Biasing on the Radial Electric Field Structure Bifurcation in Tokamak Plasmas

N. Kasuya 1), K. Itoh 2), Y. Takase 3)

1) Graduate School of Science, University of Tokyo, Tokyo, Japan
2) National Institute for Fusion Science, Toki, Japan
3) Graduate School of Frontier Sciences, University of Tokyo, Tokyo, Japan

e-mail contact of main author: kasuya@plasma.phys.s.u-tokyo.ac.jp

Abstract. The mechanism for formation of a steep structure in the radial electric field is a key issue in plasma confinement. Properties of the radial electric field bifurcation are studied taking into account the effect of electrode biasing. The radial electric field structure is determined by the charge conservation equation. From the nonlinear mechanism associated with local current due to ion bulk viscosity, a transition can take place. Various types of radial electric field structures with multiple peaks are allowed for the same boundary condition. The ion orbit loss term breaks the symmetry of the radial current similarly to the ambipolar radial electric field. A radial current driven by the electrode plays the role of a control parameter in a transition similarly to the pressure gradient. A phase diagram is given in the spontaneous drive vs. external drive space. Differences in the radial shape of solitary electric field structures are demonstrated in the presence of spatial varying components. This study clarifies the mechanisms of nonlinear structure formation in transport barriers.

1. Introduction

Many experiments have shown the importance of the radial electric field in improved confinement states [1,2] and several theories can explain the transition mechanism [3,4]. The mechanism for formation of a steep structure in the radial electric field is a key issue in plasma confinement. In TEXTOR, H-mode was induced by electrode biasing in the plasma edge region, and the spatial profile of the radial electric field changed suddenly from a flat one to a peaked one [5]. In this paper properties of the radial electric field transition between L-mode and H-mode are studied taking into account the effect of electrode biasing. The analysis gives various kinds of solutions, and a possibility to attain wider and stronger transport barriers in fusion devices is discussed.

2. Model Equation

The radial electric field structure is determined by the charge conservation equation [6],

$$\frac{\partial}{\partial t}E_r = -\frac{1}{\varepsilon_0 \varepsilon_\perp}(J_r + J_{visc} - J_{ext} + J_{oth}), \tag{1}$$

where J_r is the local current due to ion bulk viscosity [7], J_{visc} is the current driven by shear viscosity [8], J_{ext} is the current driven into the electrode by the external circuit, J_{oth} represents other contributions, such as orbit losses [3,4] and charge exchange losses with neutrals [9], ε_0 is the vacuum susceptibility, and $\varepsilon_\perp$ is the dielectric constant of a magnetized plasma. In a

stationary state, the normalized form of the model equation can be written as

$$\frac{\partial^2}{\partial x^2}X-(X-X_a)f(X,y)-g(X,y)+I=0, \qquad (2)$$

where $X=E_r/(v_{ti}B_\theta)$, $y=r\nu_{ii}B/(v_{ti}B_\theta)$, $I=J_{ext}/(v_{ti}B_\theta\sigma(0))$, $f(X,y)=\mathrm{Im}\,Z(X,y)$, $x=(r-r_0)/l$, and $l=\sqrt{\mu_i\varepsilon_0\varepsilon_\perp/\sigma(0)}$. Hear X_a is the ambipolar radial electric field, which gives zero radial current, $Z(X,y)$ is the plasma dispersion function, v_{ti} ($\equiv\sqrt{2T_i/m_i}$) is the ion thermal velocity, ν_{ii} is the ion collision frequency, μ_i is the shear viscosity of ions, $\sigma(0)$ is the conductivity for zero radial electric field and B_θ is the poloidal magnetic filed. In the definition above, X is the normalized radial electric field, y is the normalized collision frequency, I is the normalized external current and x is the minor radius normalized by l, which represents the magnitude of the viscosity. The radius r_0 is chosen to be the mid-point between the electrode and the limiter. The function $f(X,y)$ is the conductivity in an axisymmetric confined plasma, given by the neoclassical transport process. The function $g(X,y)$ comes from J_{oth} and in this paper ion orbit losses are considered. The first term of Eq. (2) comes from J_{visc} and acts as a diffusion term due to anomalous shear viscosity. The ambipolar radial electric field depends on the gradient of each plasma parameter. The profiles of plasma parameters, such as the ion density and the ion temperature, contribute to the radial current through this term. We use this term as the control parameter that describes the plasma state.

3. Solutions of the Equation

The nonlinear mechanism associated with J_r is studied first, setting $J_{oth} = 0$ [10]. Various types of radial electric field structure with multiple peaks are allowed for the same boundary condition $\partial X/\partial x=0$. Figure 1 shows examples of the spatial profile of the radial electric field: flat ones (X1 and X2), and peaked ones with single, double and triple peaks (a, b and c), respectively, are illustrated. The solutions with multiple peaks imply states in which the transport barrier has a wider radial extent. This shows the possibility of further confinement improvement. The relationship between the applied voltage V_{ext} and the electrode current I is obtained. The circuit includes a resistance. Figure 2 shows $V-I$ curves for the case with $d=18$, $y=0.1$ and $\hat{r}=4.0$ where d is half the distance between the electrode and the limiter, and $\hat{r}$ is the internal resistance of the external circuit normalized by $\sqrt{\mu_i\varepsilon_0\varepsilon_\perp/\sigma(0)^3}$. Spatially constant solutions exist on branches T1 and T2. S1 and S2 are solutions having solitary structures with one and two peaks, respectively. Both stable and unstable regions exist in stationary solutions and their boundary points are the critical points for transition from one state to another. Point B in Fig. 2 is where a transition takes place. A stability analysis shows that branch S1 is taken after the transition, though there exist two available states with the same applied voltage [11]. For application to realistic cases, the ambipolar radial electric field is included. A phase diagram is given in the spontaneous drive (e.g., pressure gradient) vs. external drive (i.e., external bias voltage) space with various control parameters (e.g., collisionality). The analysis gives a threshold value of 500V for the applied voltage and 80A for the electrode current for plasma parameters of the TEXTOR experiment. These values agree with the experimental results. A change in the radial electric field affects the viscosity [6]. Including this effect is straightforward and does not affect the conclusion.

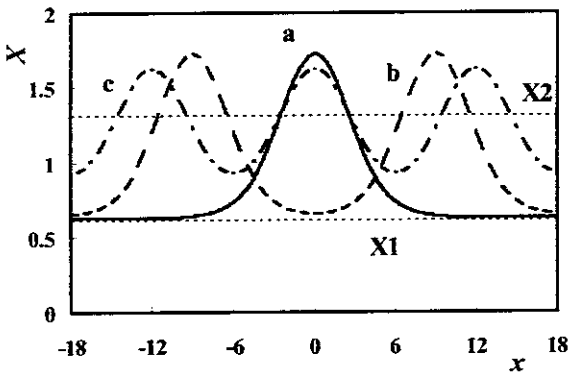

FIG. 1. Solitary structures of the radial electric field for d=18, y=0.1 and I=0.5. x is a spatial coordinate and x=0 corresponds to the mid-point between the electrode and the limiter.

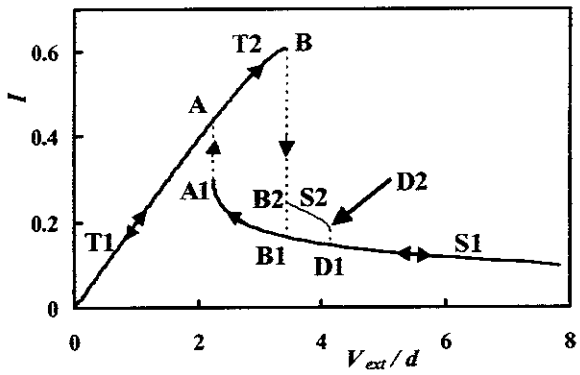

FIG. 2. The relationship between the applied voltage and the current when d=18, y=0.1 and $\hat{r}$ =4.0.

4. Comparison of the Spontaneous and Forced Transitions

We next studied the effect of electrode biasing on spontaneous transition induced by the ion orbit loss [3]. The model of ion orbit loss in Eq. (2) is based on Ref. [4]. Two nonlinear terms affect the radial electric field in this case. The ion orbit loss term breaks the symmetry of the radial current similarly to the ambipolar radial electric field that depends on the pressure gradient. As the pressure gradient increases, a spontaneous hard transition takes place when the collision frequency is small and squeezing of the banana orbit is strong. The radial electric field is negative for the case with $I = 0$. When a current is driven by the electrode, it plays the role of a control parameter in a transition similarly to the pressure gradient. The threshold for transition by electrode biasing changes in accordance with the pressure gradient.

5. Asymmetry in Polarity of the Applied Voltage

There is an asymmetry in polarity of the applied voltage [5]. It comes from the competition between two nonlinear terms. For the positive biasing case, various solitary solutions can exist, and a radial electric field transition can take place even though the profiles of plasma parameters become steeper. On the contrary for the negative biasing case, the two nonlinear terms have opposite signs, so the sum of the nonlinear terms can have more than one maxima or minima and the number of spatially constant solutions increases in such a condition. A radial electric field transition does not take place when the profiles of plasma parameters become steeper. Only a soft transition can take place. Figure 3 shows the phase diagram of the radial electric field structure for $d=20$ in the $X_a - V_{ext}$ space. The threshold voltage for transition is given by the boundaries of the shaded regions. The boundaries neighboring S and T give the forward transition threshold and the backward transition threshold, respectively. In Fig. 3 only solutions that has one peak are considered. When the distance between the electrode and the limiter is large, the competition between the two nonlinear terms can give a larger number of solutions.

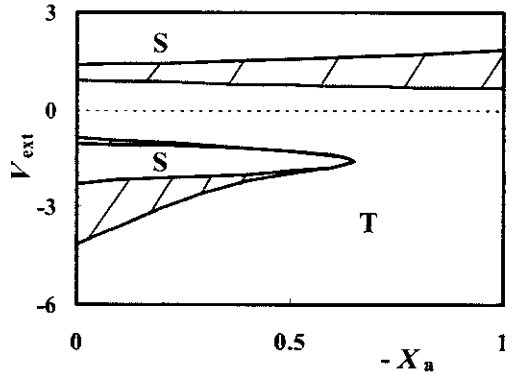

FIG. 3. Phase diagram of the radial electric field structure for d=20. S and T represent regions where a solitary solution and a spatially constant solution exist, respectively. The shaded regions indicate where both solutions can exist and gives hysteresis.

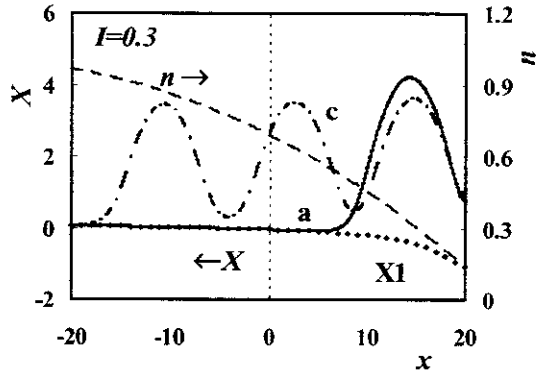

FIG. 4. Effect of a non-uniform background density profile (dashed line) for the case with I=0.3 and d=20.

6. Spatial Asymmetry of the radial electric field structure

We assume the ambipolar radial electric field term to be constant in space, so Eq. (2) has translation invariance in space. In reality there exist spatial variations in plasma parameters, and their non-uniformities affect the structure of the radial electric field through the ambipolar radial electric field. In addition the magnitude of the orbit loss term depends on the spatial position and also affects the shape of the solitary radial electric field. Here we consider these two factors to be possible causes of spatially asymmetric structures. These terms make the nonlinear response terms in Eq. (2) vary in space, and these spatial variations give other scale lengths. Figure 4 shows spatial profiles of the radial electric field with a non-uniform background ion density. A large density gradient has a drawing effect. Peaks of the radial electric field shift to the larger density gradient region for positive biasing. Radial electric field structures with single and triple peaks are shown in Fig. 4. The peaks approach the outermost peak position of the structure that has the largest number of peaks (the triple peaks structure in Fig. 4). The shape of the structure is not sensitive to the asymmetric term but only a small non-uniformity gives a significant change in the peak position. The structures must satisfy the boundary conditions at the electrode and the limiter, and they restrict the change of the structure. The peak settles where the drawing and restricting effects balance. A peak that exists far away from the boundaries can easily gain a large shift, so the first peak of each structure converged to the same position as is shown in Fig. 4. The selection rule for transition [11] shows that the structure with one peak is formed after a transition, but this sensitivity of the peak position to spatial gradients indicates that the peak of the one-peak structure appears at the peak position of the structure with the maximum number of peaks. The maximum number of available peaks is determined by the distance between the electrode and the limiter, so a measurement of the peak position gives information on the scale of the normalizing distance *l*. The spatial variation of the orbit loss term has the same tendency to change the nonlinear response term in Eq. (2), so it also affects the peak position of the radial

electric field in the same way. Peaks of the radial electric field are shifted outward in electrode biasing experiments [5]. These non-uniformity effects are possible causes of spatially asymmetric structures that have been observed in experiments. The non-uniformity makes discontinuity in the relationship between the voltage and the electrode current. This effect appears near the L/H transition points.

7. Conclusions

We have analyzed the radial electric field bifurcation including the effect of electrode biasing in tokamak plasmas. This work is an extension of the previous H-mode theory [3,4], so spontaneous transition is included as a special case when $I=0$. We considered neoclassical bulk viscosity, ion orbit losses, anomalous transport and electrode current to be the dominant contributors to the radial current, and the nonlinear responses of the former two terms to the radial electric field give various structures with multiple peaks for the same boundary condition. The competition between two nonlinear terms gives a unique feature. Their balancing explains the H-mode transition mechanism and an asymmetric bifurcation feature with respect to the electrode current term. Components that give spatial asymmetry are also considered. Only a small spatial variation can cause a large shift of the peak position, so that a measurement of the peak position gives important information on the scale length. The radial electric field contributes to improving plasma confinement. Solitary structures with multiple peaks derived here can give wide large-gradient regions. Such structures are stable, so once they are formed, they can exist stably. A double peak structure can be obtained by inserting one more electrode at the mid-point of the biasing region and improve plasma confinement further. Electrode biasing can thus be used to make wider and stronger transport barriers.

Acknowledgements

It is a pleasure to thank Prof. S.-I. Itoh, Prof. A. Fukuyama and Prof. M. Yagi for useful discussions. This work is partially supported by the LHD Project Research Collaboration Programme and by the Grant-in-Aid for Scientific Research of MEXT Japan.

[1] BURREL, K. H., Phys. Plasmas **4** (1997) 1499.
[2] IDA, K., Plasma Phys. Control. Fusion **40** (1998) 1429.
[3] ITOH, S.-I., ITOH, K., Phys. Rev. Lett. **60** (1988) 2276.
[4] SHAING, K. C., CRUME, E. C., Jr., Phys. Rev. Lett. **63** (1989) 2369.
[5] WEYNANTS, R. R., et al., Nucl. Fusion **32** (1992) 837.
[6] ITOH, K., ITOH, S.-I., YAGI, M., FUKUYAMA, A., Phys. Plasmas **5** (1998) 4121.
[7] STRINGER, T. E., Nucl. Fusion **33** (1993) 1249.
[8] ITOH, K., ITOH, S.-I., FUKUYAMA, A., *Transport and Structural Formation in Plasmas*, IOPP, Bristol (1999).
[9] CARRERAS, B. A., DIAMOND, P. H., VETOULIS, G., Phys. Plasmas **3** (1996) 4106.
[10] KASUYA, N., ITOH, K., TAKASE, Y., Plasma Phys. Control. Fusion **44** (2002) A287.
[11] KASUYA, N., ITOH, K., TAKASE, Y., *Bifurcation Phenomena in Plasmas* (ITOH, S.-I., KAWAI, Y., Ed.), Kyushu University Press, Fukuoka (2002) 341-354.

Simulation Study of Beam Ion Loss due to Alfvén Eigenmode Bursts

Y. Todo 1), H. L. Berk 2), B. N. Breizman 2)
1) Theory and Computer Simulation Center, National Institute for Fusion Science, Toki, Japan
2) Institute for Fusion Studies,University of Texas at Austin, Austin, United States

e-mail contact of main author: todo@nifs.ac.jp

Abstract. Recurrent bursts of toroidicity-induced Alfvén eigenmodes (TAE) are studied using a self-consistent simulation model. Bursts of beam ion losses observed in the neutral beam injection experiment at the Tokamak Fusion Test Reactor are reproduced using experimental parameters. It is found that synchronized TAE bursts take place at regular time intervals of 2.9 ms, which is close to the experimental value of 2.2 ms. The stored beam energy saturates at 40% of that of the classical slowing down distribution. The stored beam energy drop associated with each burst has a modulation depth of 10% which is also close to the inferred experimental value of 7%. Surface of section plots demonstrate that both the resonance overlap of different eigenmodes and the disappearance of KAM surfaces in phase space due to overlap of higher-order islands created by a single eigenmode lead to particle loss. The saturation amplitude is $\delta B/B \sim 2\times10^{-2}$, is larger than would appear to be compatible with experiment, but reasons are given why our other results may be robust. The stored beam is primarily from co-injected particles when there is a limiter leaning on the inner edge.

1. Introduction

The toroidicity-induced Alfvén eigenmode (TAE) [1] can be destabilized by fast ions that have velocities comparable to the Alfvén velocity. A decade ago recurrent bursts of TAEs were observed with drops in neutron emission during neutral beam injection (NBI) in the Tokamak Fusion Test Reactor (TFTR) [2] and DIII-D [3]. The drops in neutron emission have been recognized as a manifestation of TAE-induced beam ion loss. In the experiments cited multiple TAEs were destabilized during TAE bursts that took place at regular time intervals. The modulation depth of the drop in neutron emission in the TFTR plasma was typically ~10% (Fig. 4 of Ref. [2]). The most important result is that the beam confinement time is about one-half to one-third of the collisional slowing-down time [4]. This means that TAE activity expels beam ions before their energy is absorbed by the core plasma. In this paper we report on an investigation, based on a reduced MHD method, for a configuration typical of the TFTR experiment with balanced beam injection [2].

2. Simulation Model

The simulation uses a perturbative approach where the TAE spatial profile is assumed fixed, while amplitudes and phases of the eigenmodes and the fast-ion nonlinear dynamics is followed self-consistently. For simplicity we consider concentric circular magnetic surfaces to describe the equilibrium magnetic field. The magnetic field is given by $\mathbf{B}=B_\varphi\hat{\varphi}+B_\vartheta\hat{\vartheta}$ with $B_\varphi=B_0R_0/R$, $B_\vartheta=-rB_0/q(r)R$, where R is the local major radius, R_0 is the major radius on the magnetic axis, r is the minor radius, $q(r)$ is the safety factor, and ϑ is the poloidal angle with $\nabla\vartheta=\hat{\vartheta}/r$. The electromagnetic field is a superposition of this equilibrium field and the perturbed fields due to the TAE modes. The fast-ion dynamics is followed using the guiding-center approximation with the particle velocity the sum of $\mathbf{E}\times\mathbf{B}/B^2$, grad-B, curvature drifts, and the velocity parallel to the magnetic field lines. A fourth-order Runge-Kutta method is employed to integrate the particle orbit equations. The pitch angle scattering is taken into account at the end of each time step using a Monte Carlo approach [5]. The algorithm to advance the amplitudes and phases of TAE modes are similar to the ones developed in Ref. [6,7].

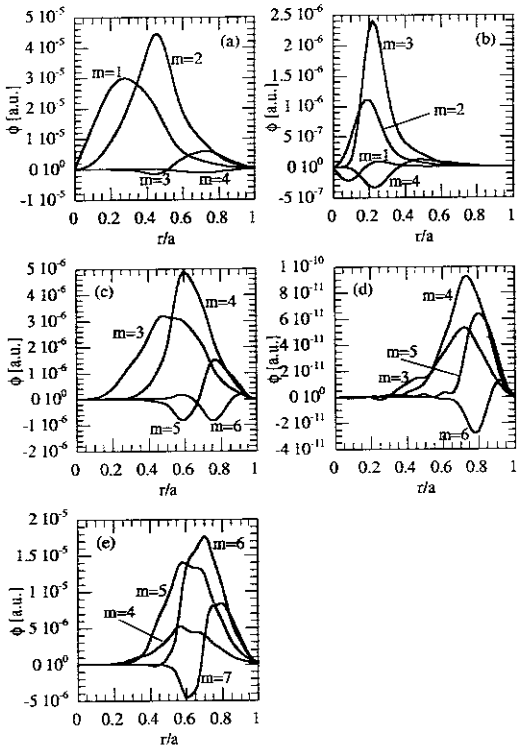

Fig.1 Major four harmonics of the electrostatic potential of Alfvén eigenmodes.

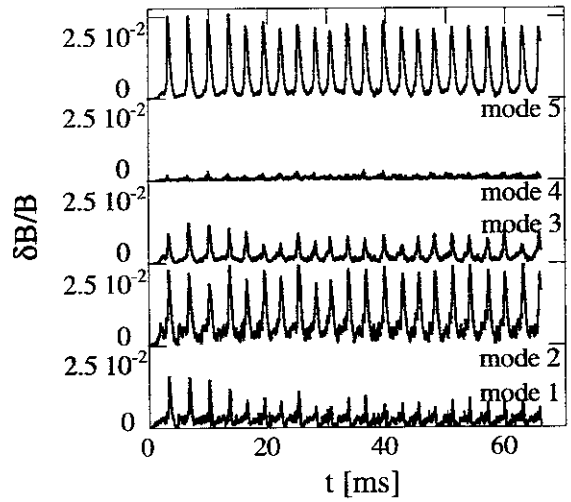

Fig.2 Amplitude evolutions of all the eigenmodes.

3. TAE Bursts

3.1 Simulation Results

For the TAE burst simulation the q-profile is taken to vary quadratically with minor radius from a central value of 1.2 to an edge value of 3.0, $q(r)=1.2+1.8(r/a)^2$. In the "vacuum" region the q-profile is modeled with a simplified form of $q(r)=3(r/a)^2$. The major and minor radii are R_0 =2.4 m and a=0.75 m. The magnetic field is 1.0 T on axis. The spatial structure and the real frequency of the eigenmodes are obtained from a Fokker-Planck-MHD simulation [8]. The plasma density in the simulation is chosen for simplicity to be uniform $2.2\times10^{19}\mathrm{m}^{-3}$. Both the core plasma ions and the beam ions are deuterium. Five eigenmodes are taken into account. Their toroidal mode number and real frequency are, respectively, a) n=1, $\omega=0.283\omega_A$ (mode 1), b) n=2, $\omega=0.404\omega_A$ (mode 2), c) n=2, $\omega=0.278\omega_A$ (mode 3), d) n=2, $\omega=0.257\omega_A$ (mode 4), and e) n=3, $\omega=0.330\omega_A$ (mode 5), where $\omega_A=V_A/R_0=1.35\times10^6\mathrm{s}^{-1}$. The spatial profile of the eigenmodes is shown in Fig. 1. The linear damping rate of each mode is assumed to be constant at $4\times10^3\mathrm{s}^{-1}$. Beam ions have balanced injection with a constant heating power of 10 MW and with a spatial Gaussian profile whose radial scale length is 0.3m. The injection energy is 110 keV which corresponds roughly to the Alfvén velocity parallel to the magnetic field. The injected beam ion has a uniform pitch angle distribution in the range of $0.7\le|V_{\parallel}/V|\le1$ with V the speed of the injected particle. In the TFTR experiment two types of limiters, toroidal belt limiter and three poloidal limiters, were used. In the poloidal cross section the limiters roughly defined a circle of radius 1m. We model these limiters by removing particles if they reach a torus with axis at R=2.65m on the midplane and minor radius 1m. Thus the plasma is leaning on the limiter on the strong field side, while on the weak field side at the midplane there is a 0.5m space between the plasma edge and the limiter. The slowing-down time is assumed to be 100 ms. For the experimental electron temperature of 2 keV the critical energy, above which the collisions with electrons dominate the slowing

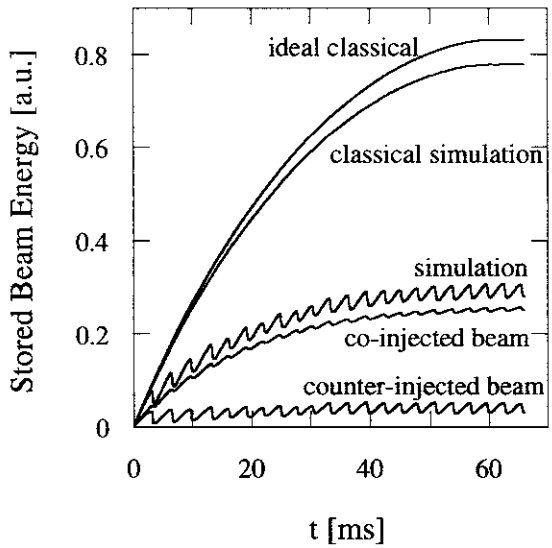

Fig.3 Time evolution of stored beam energy with that of the classical distribution and the classical simulation results.

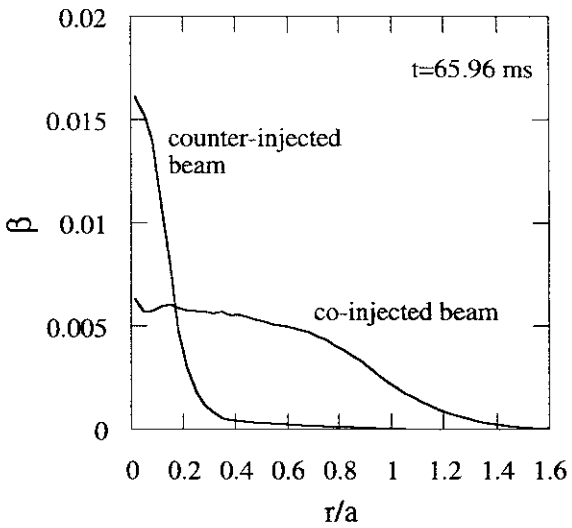

Fig.4 Beta profiles of both co- and counter-injected beams at the end of the simulation.

down process, is 37 keV. In the simulation runs for the TAE bursts described below the number of particles used is 2.1×10^6.

We start the simulation at an initial time taken as t=0 when the beam ions are first injected. As time passes, energetic ions gradually accumulate. The time evolution of the amplitude of each mode is shown in Fig. 2. We see that synchronized bursts take place recurrently at a burst interval that is roughly 2.9 ms which closely matches that of experimental value 2.2 ms in the TFTR experiment that we are comparing with. In Fig. 3 we show the time evolution of the stored beam energy and compare it with that of the "ideal classical" slowing down distribution (without pitch angle scattering) and the "classical simulation" where pitch angle scattering is included but the interaction with the TAEs is switched off. The modulation depth of the drop in the stored beam energy is 10% which is close to the inferred experimental value of 7%. In the relative units of this figure, the classical simulation saturates at relative level of 0.78, whereas that of the simulation saturates at a relative level of 0.31, namely, 40 % of that of the classical simulation The volume average beam ion beta value, which here is 2/3 of stored kinetic energy divided by the magnetic field energy averaged over the volume, is 0.6%. We find a good agreement in simulation and experiment where the beam ion confinement time is about one-half to one-third of their slowing down time and the estimated beam ion beta value is 0.5 % [2,4]. In Fig. 3 we can also see a dramatic difference between the stored beam energy of co- and counter-injected beams whose velocity is parallel and anti-parallel to the plasma current, respectively. The loss in counter-injected beam energy induced by the TAEs' activity is 88%, while that in co-injected beam energy is 37%. Figure 4 shows the spatial beta profiles of both co- and counter-injected beams at the end of the simulation. The beta profile of the co-injected beam ions is broadened and extended beyond the plasma edge (r/a=1), while that of the counter-injected ones sharply peaks at the plasma center. Figure 5 shows the time evolution of the dominant two modes 2 and 5 and the density of the co-injected beam ions. We can see that the mode 2, which is located at the plasma center, has precursory growth before both the modes grow together during each burst. Because the beam injection profile peaks at the plasma center, mode 2 is destabilized before mode 5. We can see a complete flattening of the density at the plasma core (r/a<0.72) while small increase in the density at the plasma edge (r/a>0.72). The beam ions stored at the plasma core during the quiescent phases are transported to the plasma edge and lost during the bursts.

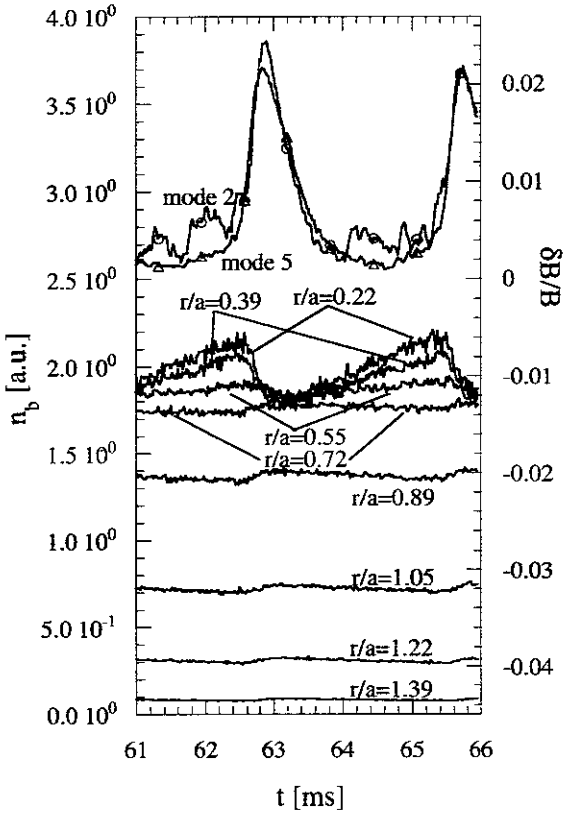

Fig.5 The time evolution of the dominant two modes 2 and 5 and the density of the co-injected beam ions at various minor radius.

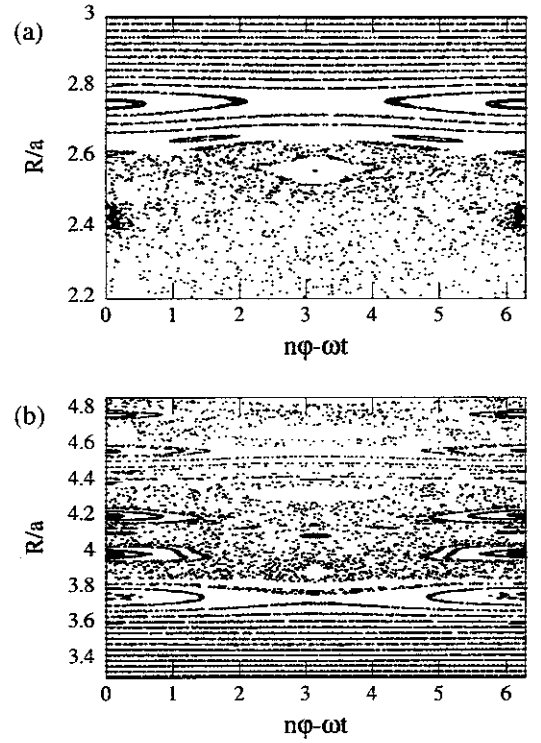

Fig.6 Surface of section plots for a) counter-injected and b) co-injected beam ions where the amplitude of mode 5 is fixed in time at $\delta B/B = 6\times10^{-3}$.

3.2 Particle Loss Mechanism

We now consider how the energetic particle loss mechanism is to be understood. To study this, we study surface of section plots where only one eigenmode is taken into account and the amplitude of the eigenmode is at a constant value. In the surface of section plot we print out the major radius of a counter-passing (co-passing) particle each time the poliodal angle of the particle reaches $\vartheta = 180°$ ($0°$). We examine the field amplitude when the loss stops the increase in the stored beam energy. We show in Fig. 6 surface of section plots for the (a) counter-passing and (b) co-passing particles, respectively, where the field amplitude of mode 5 is fixed in time at $\delta B/B = 6\times10^{-3}$. At this amplitude the stored beam energy takes on relative maximum values during the simulation run. This amplitude is higher than the ambient amplitudes between bursts, but considerably lower than the peak amplitudes the bursts reach. We see in Fig. 6(a) and (b) that the KAM surfaces are destroyed for mode 5 near the plasma edge R/a<2.6 and R/a>4.6, respectively, which then leads particle loss even before the modes reach their peak amplitude. The destruction of KAM surfaces takes place due to overlap of higher-order islands [9]. We should notice that in Fig. 6(b) the KAM surfaces exist at 4.4<R/a<4.6 for co-injected beam ions, which do not allow the particle diffusion from the plasma center to the edge at that field amplitude and lead to substantial delay in particle loss compared with the counter-injected beam ions.

4. Discussion and Summary

In this paper we have made the first numerical demonstration with parameters that are quite similar to that of experiment and closely reproduce many experimental characteristics. These include: a) the synchronization of multiple TAEs takes place at time intervals fairly close to the experimental value, b) the modulation depth of the drop in the stored beam energy that closely matches the experimental value, c) the stored beam energy saturates at about one-half to one-third of the classical slowing down distribution. We have analyzed the particle loss mechanism and found that both the resonance overlap of different eigenmodes and the disappearance of KAM surfaces in phase space due to overlap of higher-order islands created by a single eigenmode lead to particle loss. We have found that counter-injected beam ions are more easily lost than co-injected passing particles when the limiter is such as to preferably scrape-off particles whose equilibrium orbits are shifted to the inside of the toroidal boundary. The co-injected beam ion in plasma that lean on an inner limiter have difficulty being lost, because they can stick out on the outside of the plasma where they interact weakly with the internally generated Alfvén waves. This allows for the support of a relatively high energy density storage of co-injected particles, while there is a low level of counter injected particles supported.

Our simulation of the energetic particle interaction with a selected set of TAE modes predicts saturation levels of $\delta B/B \sim 2\times10^{-2}$. On the other hand, the experimental plasma displacement has been estimated $\xi \sim 5-10$ mm from the density fluctuation [10]. This enables us to estimate the amplitude $\delta B/B \sim V/V_A \sim \omega\xi/\omega_A R \sim 0.6-1.3\times10^{-3}$. What our simulation seems to lack is a mechanism to produce fast diffusion at perturbed field levels that are closer to what experiment would estimate. One possibility is that MHD mode coupling to shorter wavelengths would reduce the saturation level while still allowing the global diffusion of the rate observed in our simulation. Except for the saturation of the field level, our simulations appear to match the TFTR experiment [2,4]. Clearly further experimental studies with TAE experiments with strong particle loss are needed to check our assertion that the stored beam is primarily from co-injected particles (when there is a limiter leaning on the inner edge). In addition more sophisticated MHD calculations are needed to examine how lower level saturation can be achieved.

Acknowledgments
We wish to express our gratitude to Dr. E. D. Fredrickson for helpful suggestions for determining the experimental eigenmode amplitude and for the configuration of limiters. Numerical computations were performed at the Man-Machine Interactive System for Simulation (MISSION) of National Institute for Fusion Science.

References

[1] C. Z. Cheng and M. S. Chance, Phys.Fluids **29**, 3659 (1986).
[2] K. L. Wong *et al.*, Phys. Rev. Lett. **66**, 1874 (1991).
[3] W. W. Heidbrink *et al.*, Nucl. Fusion **31**, 1635 (1991).
[4] K. L. Wong *et al.*, Phys. Fluids B **4**, 2122 (1992).
[5] A. H. Boozer and G. Kuo-Petravic, Phys. Fluids **24**, 851 (1981).
[6] H. L. Berk, B. N. Breizman, and M. S. Pekker, Nucl. Fusion **35**, 1713 (1995).
[7] Y. Chen, R. B. White, G. Y. Fu, and R. Nazikian, Phys. Plasmas **6**, 226 (1999).
[8] Y. Todo, T.-H. Watanabe, Hyoung-Bin Park, T. Sato, Nucl. Fusion **41**, 1153 (2001).
[9] J. Candy, H. L. Berk, B. N. Breizman, and F. Porcelli, Phys. Plasmas **6**, 1822 (1999).
[10] R. D. Durst *et al.*, Phys. Fluids B **4**, 3707 (1992).

Engineering Prospects of Negative-Ion-Based Neutral Beam Injection System from High Power Operation for the Large Helical Device

O. Kaneko, Y. Takeiri, K. Tsumori, Y. Oka, M. Osakabe, K. Ikeda, K. Nagaoka, T. Kawamoto, E. Asano and M. Sato

National Institute for Fusion Science, Oroshi, Toki, 509-5292 Japan

e-mail contact of main author: kosamu@lhd.nifs.ac.jp

Abstract. An overview on four-year operation of the negative-ion-based NBI (N–NBI) system for the Large Helical Device (LHD) is presented, and the prospects of negative-ion technology for applying it to future helical fusion reactors are discussed from theses experiences. The N–NBI system was designed and constructed based on the results of R&D at NIFS. Using three beam lines, the total port-through injection power of 9 MW for 2 s has been achieved. Each beam line attained the same performance: 3.5 MW of the port-through power with the beam energy of 165 keV for hydrogen, which corresponds to the averaged negative ion current density of 25mA/cm^2 from ion sources. Also for long pulse injections, 110 s for 0.1 MW by one ion source, and 80 s for 0.5 MW by two ion sources (one beam line) were carried out. These facts show that the negative ion technology has been established to the same power level of conventional positive ion systems. Several technical improvements needed for getting these successful results are described, and the problems that limit the present performance are clarified. Some R&D programs to solve these problems are proposed for further improvement.

1. Introduction

The neutral beam injectors (NBI) for the Large Helical Device (LHD) is the first negative-ion-based NBI (N–NBI) system that was planned as a main plasma heating facility in helical systems [1]. Differing from JT-60U tokamak which also has introduced an N–NBI facility specified for current drive experiments [2], only N–NBI has been adopted in LHD as a beam injection heating and therefore it is requested high reliability as well as available power. The NBI system has three beam lines, and each beam line was designed to deliver 180 keV, 5 MW, 10 s beam by two high efficient cesium seeded negative ion sources with an external magnetic filter. The ion source had been developed at NIFS [3], and the construction of the system was started in 1996 [4].
Through four-year operation from 1998, NBI heating has revealed an excellent performance in LHD as in other helical devices and tokamaks. What is more, the recent studies in LHD have shown that NBI has other potentials than plasma heating, that is, the plasma initiation [5], and the control of rotational transform by its inducing current. Therefore NBI would be the most useful auxiliary device for the helical fusion reactor to initiate, heat and control plasma. Then the key technical issue is the negative-ion-beam technology, because the beam energy required in helical reactors is around 1 MeV for deuterium, which is the same as that of ITER [6]. A perspective for the future development of N–NBI is given.

2. Present Status of LHD-NBI

The neutral beam injection started in 1998 with 2 MW by two beam lines, and their performances have been improved year by year. The progress of the total injected port-through power and those achieved in each beam line are summarized in Table I. The beam energy increased slowly because the ion sources were reformed in every year for improvement, and the time was insufficient for conditioning. The injection power efficiency (the ratio of the injected port-through power to the input electric power) is around 0.35. The port-through power is evaluated from the heat flux on the armor tile in the LHD vacuum chamber, and therefore it eliminates geometrical and re-

ionization loss in the drift duct tube. The highest averaged negative ion current density is 25 mA/cm^2 over beam extracting area. Pulse length has been extended at low beam power, and the maximum length of 110 s was achieved. In 2001, one more beam line was added and the total port-through power of 9 MW was achieved with a beam energy of 160 keV. It is noted that the new Beam Line 3 (BL-3) revealed the same performance as other two beam lines so quickly after commissioning, which shows that the negative-ion technology of this level has been established.

TABLE I: PROGRESS OF ACHIEVED PORT-THROUGH POWER

	1998	1999	2000	2001
Beam Line 1	2MW / 100keV / 2s	2MW / 133keV / 2s	3MW / 152keV / 2s	3.5MW / 165keV / 2s 1.1MW / 104keV / 10s
Beam Line 2	2MW /100keV / 2s 0.6MW / 66keV / 20s	3.1MW /164keV / 2s 0.5MW / 100keV / 80s	3.6MW /166keV / 2s 0.8MW / 86keV / 64s	⇐ ⇐
Beam Line 3	-	-	-	3.3MW /165keV / 2s 0.1MW* / 81keV / 110s
Total Power	3.7 MW	4.5 MW	5.2 MW	9.0 MW

** one ion source*

3. Improvements Carried Out for Increasing Performance and Reliability

The key component of the N–NBI system is negative ion source. The original design was based on the preceded R&D results by using 1/3-scaled ion source. It has been modified to increase in output power and to improve reliability. These are summarized as below;

Improvement of Arc Efficiency and Stability

Our plasma source uses an external magnetic filter and has no magnetic field-free region. In order to increase in arc efficiency, careful reform of the magnetic field structure was made to prevent local arc discharge. Especially at the long-side end of plasma source, unexpected field lines that connect directly between the plasma and the grid sometimes exit due to a complex magnetic field configuration, and it was carefully avoided. It should also be noted that the position of cathode filaments is important because the induced magnetic field modifies the magnetic configuration [7].

Control of Cesium Effect to Keep Beam Quality

The amount and quality of negative ion beam is very sensitive to the cesium condition. Trial and error have been done to optimize and to keep the cesium effect. So far, the best way is that the cesium is introduced little by little keeping the temperature of plasma grid as high as 250 degree Celsius. Then the cesium effect on negative ion production becomes reproducible and reliable. There is no problem for continuous feed of cesium even during beam pulse. No deteriorate effect on the voltage withstanding of insulators was observed throughout an experimental campaign (experienced about 30,000 pulses including conditioning shots in five months).

Long Pulse Operation

Another technical improvement was needed for a long pulse operation. After the construction of BL-1, BL-2 and BL-3 were redesigned to be able to operate 30 minutes at low power (~1MW injection). As for a negative ion source, the thermal contact of plasma grid to the water-cooled supporting flange is redesigned and the cooling of ground grid was reinforced [8]. Because we do not control the plasma grid temperature actively, its temperature rises during the beam pulse. In some case it was found that the beam divergence changed during pulse even though the acceleration or extraction current did not change. Therefore a steady state condition should be determined more carefully than the case of short pulse considering the balance between the grid

temperature and the amount of cesium supply. It is suggested that the optimum condition of cesium coverage on the plasma grid is determined by the dynamic balance between the supply and the release of cesium from the surface covered by tungsten [9].

Heat Load on the Grids

Reduction of heat load on the grids is a main technical concern. By strengthen the magnetic field on the plasma grid from a magnetic filter and the extracting grid, the amount of extracted electrons associating with negative ions is suppressed sufficiently [10], which is smaller than that of negative ions. However, the heat load on the ground grid still remains (about 10% of the accelerated beam power), which limits the pulse length under high power beam injection. It is considered that both electrons and ions (or neutrals) cause the heat load. The accelerated electron beam is estimated to be several % of the beam power, which is larger than that estimated by stripping of negative ions. The heat load and the X-rays are observed downstream of the ion source, and the protection against their heat load was inevitable for a long pulse operation.

Spatial Non-Uniformity of the Beam

In order to improve the electric efficiency of neutral beam production and to reduce the heat load on the ground grid, the spatial uniformity of the extracted negative ion beam should be improved. The non-uniformity along a long direction of the ion source is usually very large. This is a common problem found in large ion sources [11], and one of the reasons is ascribed to a non-uniform arc discharge. The passive control of arc current distribution was done by inserting series registers in the electric circuit but it was not satisfactory because the current distribution depends on the amount of arc current itself and also on the amount of cesium. In the new BL-3, the filament and arc power supplies have separated twelve outputs (FIG.1) and can control the arc current distribution actively to compensate the non-uniformity. The initial trial showed a favorable result.

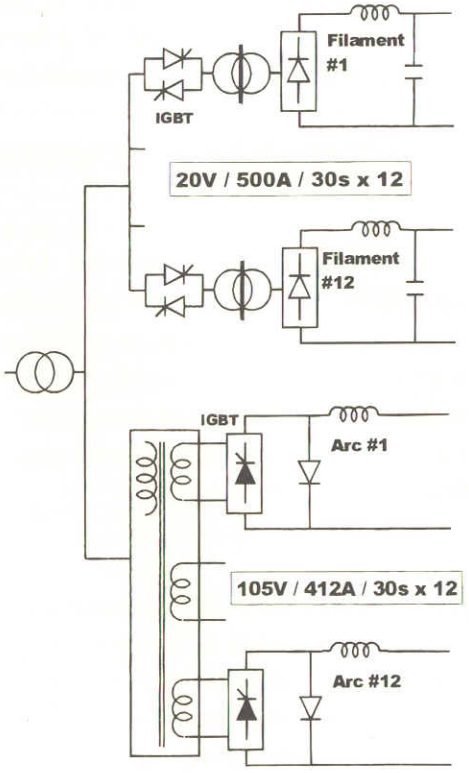

FIG.1. Electric circuit of twelve-output multi filament and arc power supplies.

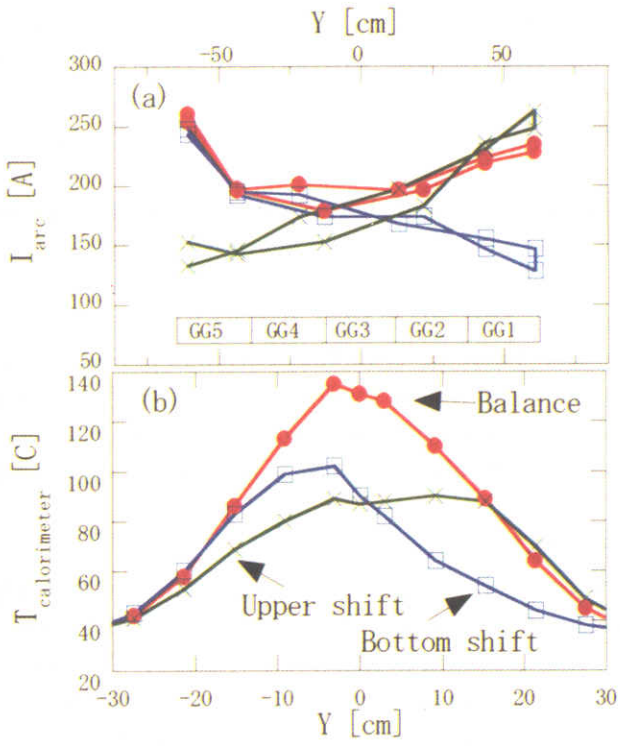

FIG.2. Arc current distribution (a) , and the corresponding beam profile measured at the calorimeter. GG1 to 5 indicate the position of separated ground grids.

Figure 2 shows an example of the control of beam profile by adjusting the distribution of arc currents of each pair of filament cathodes (twenty four filaments are usually used in our ion source).

4. Prospects of negative ion technology

Performance of N–NBI

The neutral beam converted from negative ions shows a great performance and the many fruitful experimental results have been obtained in LHD [12]. From four-year experiences in operating LHD-NBI, the handling of cesium seeded negative ion sources has been established, and the stability or reliability has been improved. As a result, a wide range of operation became possible from high power short pulse to low power long pulse injection. Figure 3 shows the operational results of NBI in the latest LHD experimental campaign. It can be concluded that the negative ion source is acceptable, and as a injection system N–NBI has reached the same level of conventional positive-ion system, that is, a 100 keV, 10 MW injection system becomes available for plasma experiments.

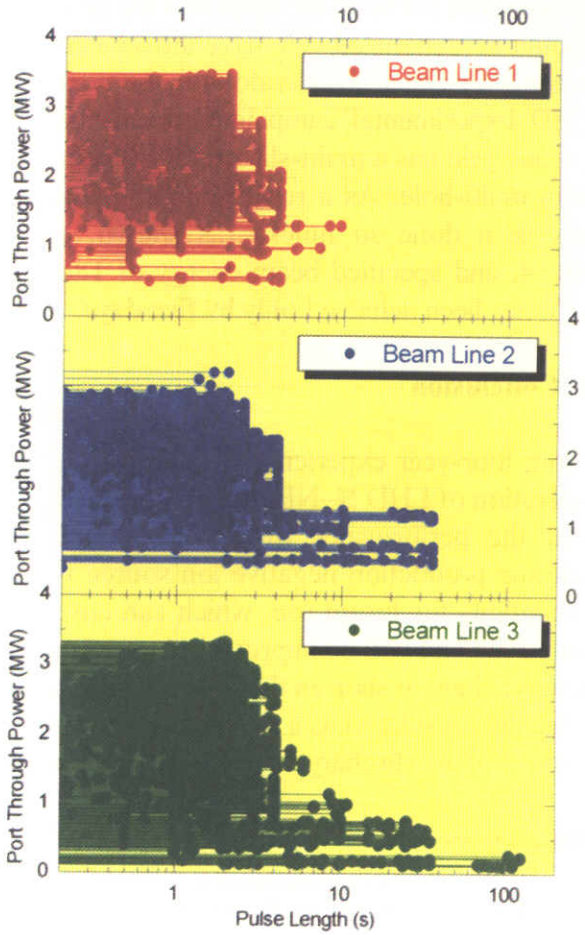

FIG.3. History of all injection shots during the 5th LHD experimental campaign.

Maintainability

So far, we have not succeeded to realize the specified values of each beam line (180 keV, 5 MW). One of the reasons is the short life of cathode. In LHD, plasma is generated in every three minutes, typically. Therefore about 10,000 plasma shots were required during an experimental campaign, and 30,000 shots including conditioning shots were needed. On the other hand, typical lifetime of directly heated tungsten filament cathode, is 10,000 beam shots under the operating condition of producing H^- more than 20 mA/cm^2 (arc discharge time is 10 s in a typical shot). We have to exchange the cathode at least twice during an experimental campaign and it takes weeks for ion sources to recover their best performances after opening them to the air. Although the lifetime of cathode is not determined by the evaporation loss but abnormal arc, it is noted that the measured weight loss of filament is large at the center of plasma source, which corresponds to the beam profile rather than arc current distribution [13]. It should also be noted that the damage of the filament is seen at the position where the back streaming ions hit the cathode directly. From these facts, the development of cathode-less (RF) ion source or other (tough) cathode material should be developed for future stable steady state operation.

Aging of Accelerator

It usually takes a long time to condition the ion source to its specified energy. Breakdowns occurs more frequently when the beam energy is getting close to the maximum value. For the negative ion sources the breakdowns may occur when the electrons, ions or neutrals deposit on the grid locally to outgas. In order to reduce the chance of breakdowns, it is considered that the area of

interference between the beam and the grid should be minimized. We have introduced a newly designed accelerator for the next LHD experimental campaign, where the ground grid has a multi-slit structure other than multi-hole. As a result, conditioning has been done so quickly as shown in FIG.4, and specified beam energy of 180 keV has been achieved only by five days.

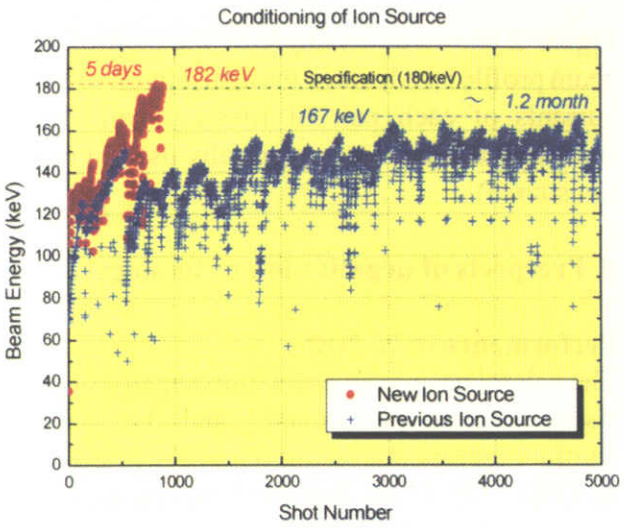

FIG. 4. Comparison of history of conditioning

5. Conclusion

From four-year experience of high power operation of LHD N–NBI, it is prospected that the performance of cesium seeded volume production negative ion source is acceptable for future use, which can cover a wide range of operation. The reliability is being improved and will be improved more when a long lived cathode is developed, and the multi-slit grid will help to shorten the time of aging process. As for the spatial non-uniformity of the beam, which is considered as a main cause of heat load of the accelerating (and ground) grid, an active control of arc discharge current distribution by using separate power supplies works well.

References

[1] Mutoh, T., et al., "HEATING SYSTEMS OF LARGE SUPERCONDUCTING HELICAL DEVICE" Fusion Technology 1988, (1989) 552.
[2] Kuriyama, M., et al., "Development of Negative-Ion Based NBI System for JT-60U" J. of Nucl. Science and Technol., **35** (1998) 739.
[3] Takeiri, Y., et al., "Negative hydrogen ion source development for Large Helical Device neutral beam injector" Rev. Sci. Instrum. **71** (2000) 1225.
[4] Kaneko, O., et al., "Negative-Ion-Based neutral Beam Injector for the large helical Device" Fusion Energy 1996, (1997) 539.
[5] Kaneko, O., et al., "Plasma startup by neutral beam injection in the large Helical Device", Nucl. Fusion **39** (1999) 1087.
[6] Mondino, P., et al., "ITER neutral beam system" Nucl. Fusion **40** (2000) 501.
[7] Asano, S., et al., "Effects of filament positions on the arc discharge characteristics of a negative hydrogen ion source for neutral beam injector " Rev. Sci. Instrum. **70** (1999) 2338.
[8] Takeiri, Y., et al., "Initial long-pulse plasma heating at reduced power with negative-ion-based neutral beam injector in large helical device" Rev. Sci. Instrum. **70** (1999) 4260.
[9] Oka, Y., et al., "Optimization of Cs deposition in the 1/3 scale hydrogen negative ion source for the large helical device-neutral injection system" Rev. Sci. Instrum. **71** (2000) 1379.
[10] Takeiri, Y., et al., "Suppression of accelerated electrons in a high-current large negative ion source" Rev. Sci. Instrum. **68** (1997) 2003.
[11] Grisham, L. R., et al., "Improvement of JT-60U negative ion source performance" Nucl. Fusion, **41** (2001) 597.
[12] Motojima, O., et al., "Recent Advance in LHD Experiment" OV/1-6 in this conference.
[13] Oka, Y., et al., "Performance of LHD-NBI H^- ion Source" Rev. Sci. Instrum. **73** (2002) 1054.

Physics Design of Quasi-Axisymmetric Stellarator CHS-qa

S. Okamura 1), K. Matsuoka 1), S. Nishimura 1), M. Isobe 1), C. Suzuki 1), A. Shimuzu 1), K. Ida 1), A. Fujisawa 1), S. Murakami 1), M. Yokoyama 1), K. Itoh 1), T. Hayashi 1), N. Nakajima 1), H. Sugama 1), M. Wakatani 2), Y. Nakamura 2), W. Anthony Cooper 3)

1) National Institute for Fusion Science, Toki 509-5292, Japan
2) Graduate School of Energy Science, Kyoto University, Uji, 611-0011, Japan
3) Centre de Recherches en Physique des Plasmas, Association Euratom/Confederation Suisse, EPFL, 1015 Lausanne, Switzerland

e-mail contact of main author: okamura@nifs.ac.jp

Abstract. A low aspect ratio stellarator CHS-qa with a quasi-axisymmetric configuration is designed at NIFS with the experimental confinement study as the main objective. The high beta equilibrium was confirmed with the HINT code which does not need the assumption of nested magnetic surfaces. The equilibria with bootstrap current were calculated with the SPBSC code and their global MHD stability was evaluated with the TERPSICHORE code. The boundary structure of the magnetic field was examined to scope divertor options. A new method of calculating the neoclassical transport properties was developed for toroidal configurations with very small nonaxisymmetry. The control knobs of the configuration properties are proposed for the study of improved confinement.

1. Introduction

Plasma confinement study in the stellarator configuration with quasi-symmetry has become a new steady stream in the fusion research. First experiment based on the quasi-helical symmetry has already started with the HSX device [1]. The experiments for two other types of symmetry are also proposed as NCSX [2] (quasi-axisymmetry) and QPS [3] (quasi-poloidal symmetry) projects. In this paper, we discuss the confinement characteristics of CHS-qa which is designed in NIFS, Japan as a quasi-axisymmetric stellarator with a low aspect ratio [4]. For these new generation of devices, most of classical problems of the conventional stellarators have been successfully solved owing to the recent high computing technology, which makes full use of high freedom of configuration design in three dimension. However, as we see in the axisymmetric tokamak experiment, the problem of anomalous transport is the dominant channel for the toroidal plasma confinement. The development of the improved confinement scenarios is still the most important issue for stellarators. In the design of CHS-qa configuration, we took care about such an aspect as well as the optimization in the classical problems.

2. Basic CHS-qa Configuration and Free-boundary Equilibrium

The number of toroidal periods of CHS-qa is two and the average aspect ratio is 3.2 (2b32 configuration). The vacuum rotational transform is designed between 2/6 and 2/5 avoiding low order resonances. The quasi-axisymmetry is evaluated with the Fourier components of the Boozer spectrum and the largest non-axisymmetric component is 3% at the edge and 1.5% at the half radius in the amplitude relative to the toroidal magnetic field. One of the limiting factors for the low aspect ratio design is the availability of the coil design for the practical size of the experimental device. The engineering design of 20 modular coils (for full torus) have been successfully made for the major radius R = 1.5 m and the toroidal magnetic field Bt = 1.5 T. Auxiliary poloidal coils are also designed for the plasma shape and the position control.

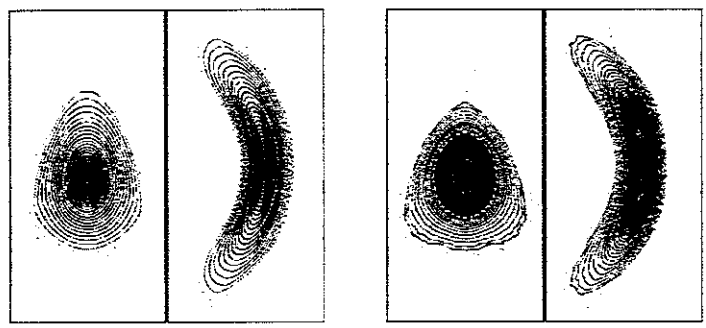

Fig. 1. Puncture plots of magnetic surfaces for vacuum (left) and 3.3% average beta (right) equilibria of CHS-qa calculated by HINT code.

It is necessary to make equilibrium calculations with magnetic coil current so as to confirm whether the obtained configuration is robust against the island formation caused by the equilibrium current of finite beta plasma. For this purpose, free boundary equilibrium calculations were made using HINT code [5]. The vacuum magnetic field created by designed 20 modular coils are used. Figure 1 shows the puncture plots of magnetic surfaces of CHS-qa for the vacuum configuration and the 3.3% average beta equilibrium with zero average toroidal current for each magnetic surface. The vertical field is adjusted to push back the plasma position for high beta equilibrium. It is observed that the magnetic surfaces are robust against the high beta perturbation. In the case of no vertical field control, large part of the closed magnetic surfaces are lost because of the outward shift of the plasma column.

3. Bootstrap Current and Global MHD Stability

The self-consistent bootstrap current (BSC) is calculated using SPBSC code [6] with the connecting formula of the neoclassical theory predictions for different collisionality regime. Calculations are made for several cases taking all Boozer spectra as the information of magnetic configuration. They were compared with the approximate calculation taking only axisymmetric terms of Boozer spectra (pure QA model). The approximate calculations gave generally 20 to 30 % higher current than the full mode calculations. Since the full mode calculation is sometime unstable, we use the approximate calculation for the discussion of pressure profile dependence.

We calculated BSC profiles for two types of high beta plasma: high temperature with low density case and high density and low temperature case. Figure 2(a) shows the rotational transform profiles of high temperature case for two model profiles of the plasma density. The temperature profile is kept constant as parabolic ($T_{e,i} \propto (1-\psi)$: ψ is the toroidal flux, $T_e(0) =$ 5.2 keV, $T_i(0) = 3.9$ keV) and the density profiles are chosen for peaked ($n_e \propto (1-\psi)^{0.5}$) and flat ($n_e \propto (1-\psi^3)$), with the fixed central density $n_e(0) = 2 \times 10^{19}$ m^{-3}. The magnetic field B = 1 T and the major radius R = 1.5 m are assumed. The average beta is 3% for the peaked profile case. For high temperature plasma, the stellarator shear is created with the flat density profile for a wide range of radius. Highest value of the rotational transform rises close to 0.6. Figure 2(b) shows the rotational transform profiles for high density case: the central density $n_e(0) = 1 \times 10^{20}$ m^{-3} and the ion and electron temperatures are 1/5 of the previous case. In this case, the rotational transform at the edge is below 0.5 which is critical value for the external kink stability in CHS-qa.

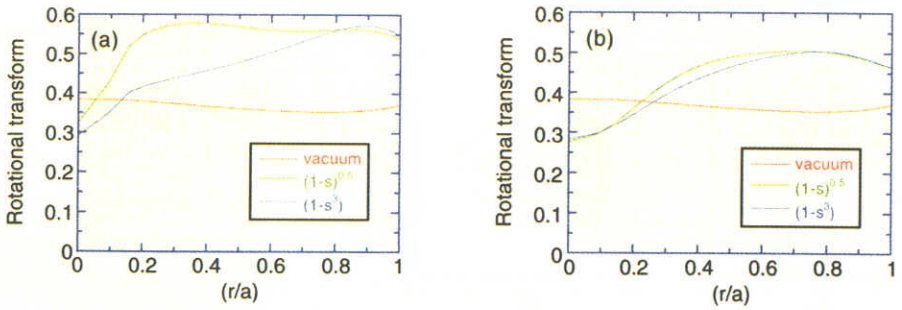

Fig. 2. Rotational transform profiles for different pressure profiles. (a) high temperature and low density case, (b) high density and low temperature case.

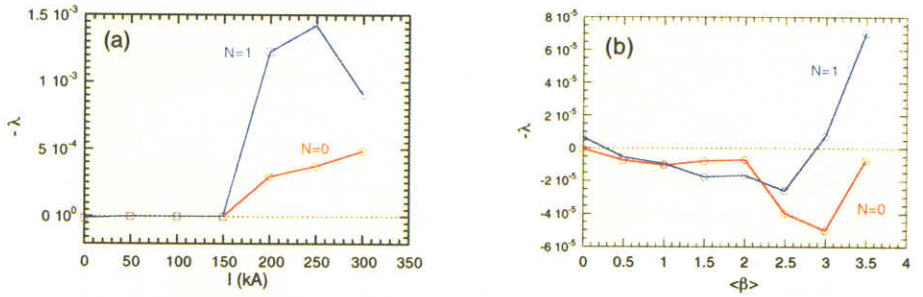

Fig. 3. Global MHD stability analysis. (a) external kink stability with 1% average beta, (b) stability for the pressure driven mode.

The global stability analysis was made using TERPSICHORE code [7] for the plasma pressure profiles described above. The ranges of Fourier modes in the calculation are $m < 36$ and $n < 11$ for the poloidal and toroidal mode, respectively. The shape and the location of the conducting wall in the calculation is designed sufficiently far from the plasma boundary in order to eliminate its effect for the stability. Figure 3(a) shows the growth rate of the external kink mode as a function of the plasma current. In this calculation, the plasma average beta was kept constant at 1% and the current density profile is proportional to the bootstrap current for 1.2% beta. The plasma current, however, is artificially varied which causes the rotational transform to change. The growth rates shown are for the most unstable mode in the two decoupled families (N=0 and N=1 family) of eigen modes. The stability is determined by the rotational transform at the edge, i.e., the iota value higher than 0.5 is unstable. This dependence is insensitive to the plasma beta value. Actually the equlibria shown in Fig. 2(b) for high density plasma are stable for the external kink mode. The stability for the pressure driven mode is also examined with zero plasma current. Figure 3(b) shows the growth rate of two families as a function of the plasma average beta. Full stability is obtained up to 3% average beta.

4. Structure of Boundary Magnetic Field

Although the optimization of the magnetic field configuration is made for the confinement region, namely, for the inside of the last closed magnetic surface (LCMS), the magnetic field structure of the outside of LCMS is very important from the aspect of the plasma surface interaction and the future divertor design. Such problem for CHS-qa was studied by using the conventional way of field line tracing for the vacuum field produced by modular coils starting from the aligned points just outside of LCMS. Figure 4(a) shows the puncture plots

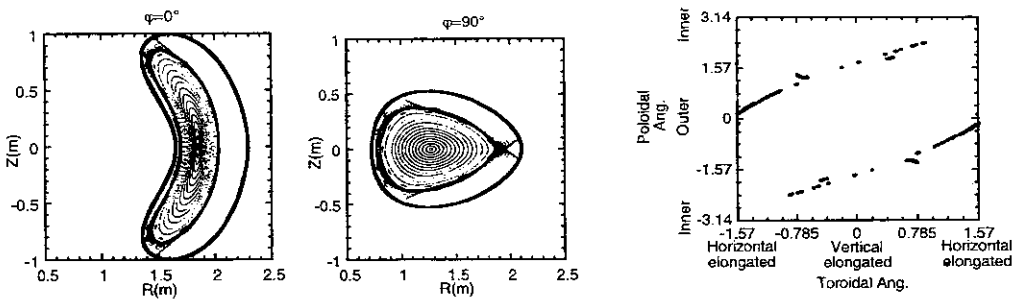

Fig. 4. (a) Puncture plots of magnetic field lines starting from outside of LCMS. (b) Distribution of foot prints of divertor field lines on the model surfac.

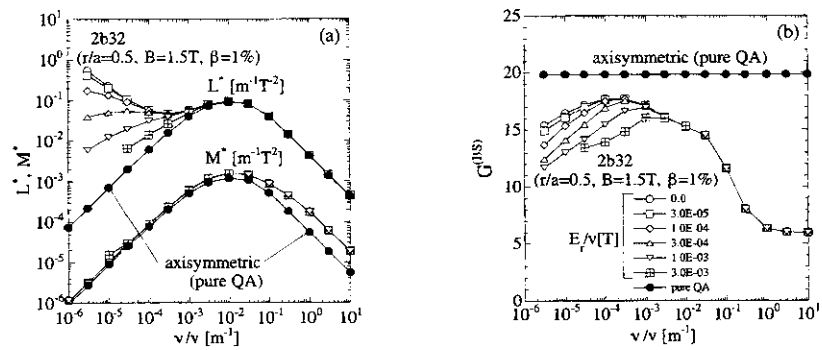

Fig. 5. The mono-energetic viscosity and transport coefficients as a function of collisionality. The open symbols denote 2b32 results and closed circle denotes pure QA model. (a) The ripple and banana-plateau diffusion L and the parallel viscosity M*, and (b) the geometrical factor $G^{(BS)}$.*

of these field lines (starting from 2 mm outside of LCMS. For the purpose of the divertor design, foot points of the field lines on the model surfaces (shape is given for each plot in Fig. 4a) are calculated and the result is shown in Fig. 4(b) on the unfolded. Such aligned foot points are obtained only by the proper design of modular coils and the model surface shape.

5. Neoclassical Transport Calculation

For the transport study of quasi-axisymmetric stellarators, the momentum conservation must be treated properly which was often not the case in the analysis of stellarators. DEKS code [8] is a well known numerical tool for calculating transport matrix but the results does not guarantee the momentum conservation. A new method of calculating the transport matrix was developed in NIFS [9] which incorporates numerical results from DKES code but formulate the transport matrix in a different form. Using this new method, the correct evaluation of transport coefficients becomes possible for quasi-axisymmetric system with a full consideration of friction forces between different species. Figure 5(a) shows the diffusion coefficient L* and the parallel viscosity coefficients M* for a mono-energetic particle as a function of collisionality. It compares CHS-qa and pure QA model. In addition to the parallel viscosity, both poloidal and toroidal viscosity coefficients are calculated by DKES with our new method so that we can identify the direction in which plasma flows are easily generated. Together with the neoclassical geometric factor calculated also by DKES shown in Fig. 5(b), full transport matrix can be evaluated for all species including self-consistent friction forces

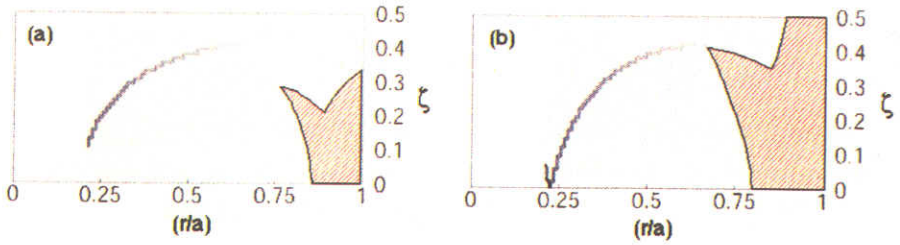

Fig. 6. Contour plot of adiabatic invariant J for (a) standard configuration and (b) outward shifted configuration. Shaded area satisfies maximum-J criterion.

among them.

6. Maximum-J Condition and Its Control

The maximum-J condition (J denotes the second adiabatic invariant) [10], which is favorable for the stabilization of the trapped particle instability, is evaluated. Figure 6 shows an example of the controllability of the maximum-J condition for vacuum configuration. The contour plot of J is shown as a function of minor radius and the toroidal angle. $\zeta = 0$ corresponds to the vertically elongated cross section and $\zeta = 0.5$ to the horizontally elongated cross section. Fig. 6(a) shows a standard configuration without additional vertical field. There is a maximum point of J near the plasma edge for $\zeta < 0.25$ at the normalized radius (r/a) = 0.8. Boundary area outside of that radius satisfies the maximum-J condition. With an additional vertical field, such an area can be expanded and the gradient of J is increased for the outward shifted configuration shown in Fig. 6(b). It is also possible to reduce the area by shifting in the plasma position. For the high beta plasma with bootstrap current, the area for the maximum-J condition expands due the enhanced stellarator shear shown in Fig. 2.

7. Summary

The equilibrium calculation of CHS-qa with the HINT code gave good magnetic surfaces for 3.3% average beta with zero plasma current. The external kink stability is confirmed for the edge rotational transform value below 0.5. The global linear MHD stability for the pressure driven mode was evaluated and stability up to average beta 3.5% was obtained. Good divertor trace of boundary magnetic field lines was found with a proper selection of modular coil design and the divertor plate position. A new method of neoclassical diffusion calculation was applied to obtain reliable physical quantities for quasi-axisymmetric configuration. For the experimental control in the study of anomalous transport, the maximum-J condition was examined for CHS-qa.

[1] TALMADGE, J.N., et al., paper EX/P3-22, this conference
[2] ZARNSTORFF, M., et al., Plasma Phys. Control. Fusion **43**, A237 (2001).
[3] LYON, J., et al., paper IC/P-05, this conference
[4] OKAMURA, S., et al., Nucl. Fusion **41**, 1865 (2001).
[5] HAYASH, T. et al., Contrib. Plasma Phys., **42**, 309 (2002).
[6] WATANABE, K.Y., et al., Nucl. Fusion **35**, 335 (1995).
[7] COOPER, W.A., Plasma Phys. Control. Fusion **34**, 1011 (1992).
[8] RIJ, W.I.VAN and HIRSHMAN, S.P., Phys. Fluids **B1**, 563 (1989).
[9] SUGAMA, H. and NISHIMURA, S., to be published in Phys. Plasmas **9**, No.11 (2002).
[10] YOKOYAMA, et al., paper IC/P-08, this conference
[11] MINAMI, et al., paper EX/C4-3, this conference

Drift Reversal Capability in Helical Systems

M.Yokoyama 1), K.Itoh 1), S.Okamura 1), K.Matsuoka 1), N.Nakajima 1), S.-I.Itoh 2), G. H. Neilson 3), M. C. Zarnstorff 3) and G.Rewoldt 3)

1) National Institute for Fusion Science, 322-6 Oroshi, Toki 509-5292, Japan
2) Research Institute for Applied Mechanics, Kyushu University, Kasuga 816-8580, Japan
3) Princeton Plasma Physics Laboratory, Princeton, NJ 08543, USA

e-mail contact of main author: yokoyama@nifs.ac.jp

Abstract. The maximum-J (J is the second adiabatic invariant) capability, i.e., the drift reversal capability, is examined in quasi-axisymmetric (QAS) stellarators and quasi-poloidally symmetric (QPS) stellarators as a possible mechanism for turbulent transport suppression. Due to the existence of non-axisymmetry of the magnetic field strength in QAS configurations, a local maximum of J is created to cause the drift reversal. The increase of magnetic shear in finite beta equilibria also has favorable effect in realizing the drift reversal. The radial variation of the uniform magnetic field component plays a crucial role for the drift reversal in a QPS configuration. Thus, the drift reversal capability and its external controllability are demonstrated for QAS and QPS stellarators, by which the impact of magnetic configuration on turbulent transport can be studied in experiments.

1. Introduction

Improved plasma confinement has been realized in toroidal plasmas by the turbulent fluctuation suppression. This has been considered to be consistent with theoretical predictions for the stabilization of micro-instabilities [1]. Several kinds of micro-instabilities appear when the directions of the diamagnetic drift and the ∇B drift (B is the magnetic field strength) are the same for trapped particles. The direction of ∇B drift precession can be expressed in terms of the radial derivative of the second adiabatic invariant J. The stability condition for them is derived as $\nabla P \cdot \nabla J > 0$ ($\nabla J < 0$ for $\nabla P < 0$) in terms of J and scalar plasma pressure P, which is called the maximum-J criterion (drift reversal). This condition is realized by q (safety factor) profile control (such as in reversed shear tokamaks) [1], control of the plasma cross-section (such as ellipticity) [2], plasma diamagnetism [3], and strong inhomogeneity of the radial electric field [4]. The experimental demonstration of a significant increase of confinement time in a spherator [5] when trapped particles are localized in a good curvature region is also considered as a remarkable example of this effect.

Innovative helical systems have been widely studied [6-10] based on the quasi-symmetry concept. It is worthwhile to examine the drift reversal capability in such configurations for significant guidance in the configuration design for possible turbulent suppression. Here, we note that the importance of a drift reversal capability for the design of helical systems was already pointed about one decade ago [11]. Its qualitative evaluations are now available as described in this paper.

2. Description of J-calculation

The second adiabatic invariant J for trapped particles is defined as $J \equiv \int v_{||} dl$, where dl denotes the line element along a magnetic field line and the integral is performed over a bounce period. For analytical simplicity, $J^* \equiv \int v_{||} d\zeta$, ($\zeta$ being the toroidal angle) has been frequently utilized, which is based on the assumption that the rotational transform per toroidal field period is sufficiently small that the integral path can be taken in the toroidal direction.

However, in this study, a direct calculation of J is performed by following the guiding center of low energy trapped particles for which the deviation from a magnetic field line is negligibly small. The guiding center equations [12] are expressed by use of the Boozer coordinates (ψ, θ, ζ) [13], with ψ being the normalized toroidal flux, and θ (ζ) the poloidal (toroidal) angle. The motion of the guiding center is defined by five variables ((ψ, θ, ζ) for the real space, velocity and the particle energy, W). Since the direction (sign) of the precession is the key for the stability condition, the W dependence is not important here, so that particles with fixed W(=10eV) are considered. Also, the integral is performed along the particle trajectory so that one out of the θ and ζ dependences is omitted when the launching points of particles are specified. To obtain the radial profile of J, tracer particles which are to be reflected at the same B are launched from the bottom of the dominant magnetic field ripple [e.g., the bottom of the toroidicity induced ripple (θ=0) for QAS configurations, and that of the bumpy (poloidally symmetric) field-induced ripple ($\zeta/(2\pi/M)\equiv\zeta_N$=0.5) for QPS configurations]. Here, M is the number of field periods. The initial velocity of tracer particles, $v_{\|,st}$, is defined as $v_{\|,st}=[2W(1-B_{st}/B_{ref})/m]^{1/2}$, where B_{st} (B_{ref}) is the magnetic field strength at the initial (bounce) point and m is the particle mass. It is noted that the specification of B_{ref} corresponds to treating tracer particles with the same magnetic moment (μ), which is an estimate of how deeply these particles are trapped in a magnetic ripple.

3.1. Drift reversal capability in QAS configurations

Configuration studies based on the QAS concept have been extensively developed in Japan (CHS-qa) [8] and in the USA (NCSX) [9]. In this section, the drift reversal capabilities in candidate configurations for both designs are described.

Firstly, the candidate configuration for CHS-qa (2w39) is examined. This particular configuration (M=2) has an aspect ratio of about 4.3, and the rotational transform lies between 0.37 and 0.4 with a slight increase towards the edge. Several non-axisymmetric components of B appear near the edge with a few percent of the uniform magnetic field strength.

Figure 1 shows contours of J with B_{ref}=1.0 in the (r/a, ζ_N) plane, with $r/a=\psi^{1/2}$, for a vacuum configuration. It shows the existence of a local maximum of J, which gives $dJ/dr<0$ (drift reversal) in the outer radii (hatched region). The local maximum of J is created by the residual non-axisymmetry of B in the edge region due to the larger reduction of the parallel velocity through the conservation of μ [14]. This feature is significantly unique for QAS configurations, and is not realized in axisymmetric tokamaks. The non-axisymmetry of B can be externally controlled through configuration control, such as by shifting the magnetic axis inward/outward. In addition, large positive shear of the rotational transform (negative shear of q) can be realized with the sustenance of the rotational transform through the bootstrap current (in a region of large pressure gradient) and reduction of the central rotational

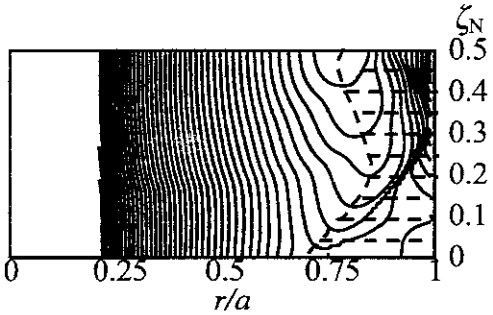

FIG.1. Contours of J (B_{ref}=1.0) on (r/a, ζ_N) plane for the candidate configuration of CHS-qa (2w39). The "Max" denotes the local maximum of J and the hatched region indicates the region where drift reversal is realized.

transform by the Shafranov shift [15]. In such a case, tokamak-like drift reversal (due to the magnetic shear) is also possible in the core region, combined with the non-axisymmetry induced drift reversal in the edge region.

Secondly, a previous candidate configuration for NCSX (li383) is examined. This configuration has been obtained by a numerical optimization study, with a target β value of about 4.1 % with M=3 (with a plasma current of about 125 kA for B=1.2T and a major radius of 1.4 m). Thus, the drift reversal capability is examined at this particular β value. The rotational transform profile is shown in Fig. 2, where relatively large positive shear of the rotational transform (negative shear of q) exists, except very near the edge region. It also has a large radial variation of the uniform magnetic field component (corresponding to a deep magnetic well), which weakens the contribution of the non-axisymmetry of B to the particle trajectories.

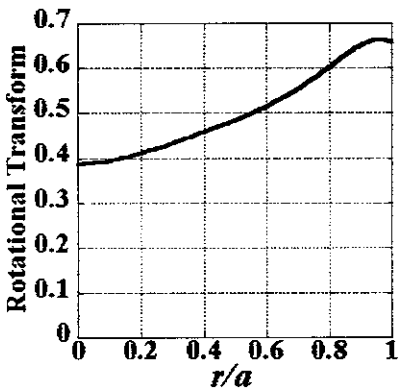

FIG .2. The rotational transform for the li383 configuration at β=4.1%.

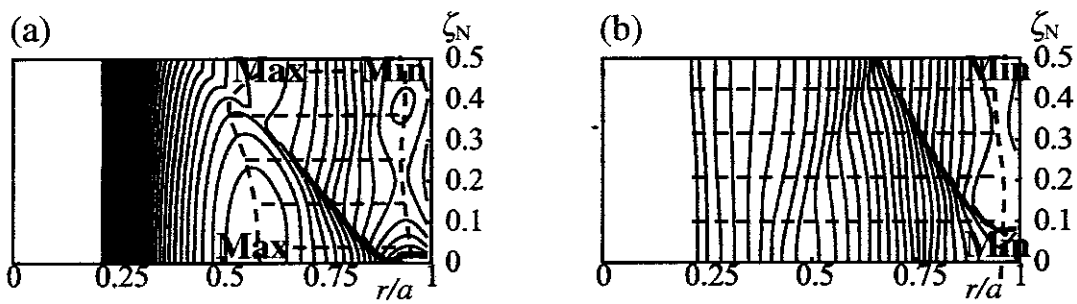

FIG .3. Contours of J ((a) B_{ref}=0.98 and (b) B_{ref}=1.02) in the (r/a, ζ_N) plane for the li383 configuration with β=4.1%. The "Max (Min)" denotes the local maximum (minimum) of J and the hatched region indicates the region where drift reversal is realized.

Figure 3 shows contours of J with (a) B_{ref}=0.98 and (b) B_{ref}=1.02 in the (r/a, ζ_N) plane. For more deeply trapped particles (such as for the B_{ref}=0.98 case), the magnetic shear is not enough to realize drift reversal for the inner region. However, as B_{ref} is increased (that is, as the degree of trapping becomes shallower), the region where drift reversal is possible extends towards the core region. It is recognized from Fig. 4 that the negative shear of the rotational transform (positive shear of q) in the very edge region avoids realizing drift reversal. In this sense, it can be remarked that the drift reversal capability of this configuration strongly depends on the magnetic shear, which is the same mechanism as that in negative shear tokamaks.

The effects of non-axisymmetry of B, magnetic shear (mainly induced by the plasma current) on the drift reversal capability in CHS-qa and NCSX have been described in this section. They provide the "external knob" for the drift reversal capability in QAS configurations.

3.2. Drift reversal capability in a QPS configuration

As for the QPS category, an example configuration (M=4) [16] is investigated. The geometrical aspect ratio is about 10. This configuration has been obtained through plasma boundary shaping. There is a significant variation of area of magnetic surfaces in the toroidal direction. This gives the dominant bumpy component of B through the conservation of toroidal magnetic flux. The bumpy field strength is as much as half of the uniform magnetic field strength. There still remain the symmetry breaking components such as those corresponding to the helicity and toroidicity. However, the amplitudes of these components are less than 1/5 of that of bumpy component, and also it should be noted that the toroidicity is reduced to a level about half of the geometrical inverse aspect ratio.

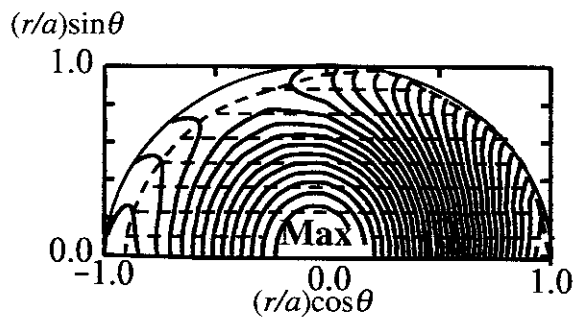

FIG. 4. Contours of J (B_{ref}=0.65) in the (r/a, θ) plane for a QPS finite beta configuration. The "Max" denotes the maximum of J and the hatched region indicates the region where the drift reversal is realized.

Figure 4 shows contours of J (for B_{ref}=0.65, deeply trapped particles) in the (r/a, θ) plane for a finite beta equilibrium (volume averaged β value of about 5 %). J is a maximum at the plasma core and radially decreases, which satisfies the condition $\nabla J<0$. It shows clear drift reversal. It is noted that drift reversal is not realized at vacuum for this particular configuration. It has a large bumpy field component with little radial variation of amplitude. At vacuum case, particles launched from ζ_N=0.5 with constant μ perform similar bounce motion, which gives little radial variation of J profile, since the bumpy field component has little radial variation (cf., Ref. [16]). This is still true even for a finite beta equilibrium. The vacuum magnetic well is much smaller compared to the amplitude of the dominant bumpy component. However, the magnetic well is enhanced up to about half of the bumpy component for the mentioned finite beta equilibrium, which establishes an absolute minimum of B for the core region in the plane where particles are launched. This radial increase of B towards the plasma edge plays an essential role for realizing a radially decreasing J profile (drift reversal) as shown in Fig. 4. This is the unique mechanism for drift reversal in QPS configurations, which is different from that in QAS configurations. This would also be relevant for QPS configurations in the design phase at Oak Ridge National Laboratory [10], which are to be examined from the viewpoint of the drift reversal capability.

4. Conclusions

In conclusion, the drift reversal capability has been analyzed in innovative helical systems to investigate a possible approach towards improved confinement through turbulent transport suppression. The unique external knobs for drift reversal, the residual non-axisymmetry of B for QAS and the magnetic well for QPS, are clarified in addition to the well-known magnetic shear contribution in axisymmetric tokamaks. The external controllability of the drift reversal capability is important in performing a systematic study of the impact of magnetic configuration on turbulent transport. These knobs provide additional approaches towards improved confinement in addition to those (e.g., heating power beyond some threshold value) utilized in previous experiments.

The favorable effect of drift reversal is anticipated to reduce the average bad curvature, so as to reduce the growth rate of instabilities such as trapped particle modes and temperature gradient modes. The relevance of the drift reversal capabilities is currently being examined through quantitative analysis of micro-instabilities by the FULL code [17]. So far, we have found the toroidal drift mode (trapped electron mode) in the collisionless electrostatic limit for the case shown in Fig. 1. The destabilization is dominated by the most deeply trapped particles for which drift reversal is the most difficult to realize due to the non-axisymmetry of B. More extensive and systematic estimate of microinstabilities in QAS and QPS configurations are to be performed to clarify the contribution of drift reversal in helical systems.

Acknowledgements

The authors gratefully acknowledge Dr. Long-Poe Ku (PPPL) for help with the equilibrium calculations required for the FULL code. This work has been supported by grants-in-aid for one of the authors (MY) from The Sumitomo Foundation and The Ministry of Education, Culture, Sports, Science, and Technology, Japan.

References

[1] KADOMTSEV, B.B., and POGUTSE, O.P., Reviews of Plasma Physics, Vol.5 (Consultants Bureau, New York, 1970), p.249.
[2] GLASSER, A.H., FRIEMAN, E.A., and YOSHIKAWA, S., Phys. Fluids **17** (1974) 181.
[3] ROSENBLUTH, M., and SLOAN, M.L., Phys. Fluids **14** (1971) 1725.
[4] ITOH, S.-I., and ITOH, K., J. Phys. Soc. Japan **59** (1990) 3815.
[5] YOSHIKAWA, S., Nucl. Fusion **13** (1973) 433.
[6] NÜHRENBERG, J., et al., Proc. Workshop on Theory of Fusion Plasmas (Varenna, 1994) (Bologna, Editrice Compositori) (1995) p.3.
[7] GARABEDIAN, P.R., Phys. Plasmas **3** (1996) 2483.
[8] OKAMURA, S., et al., Nucl. Fusion **41** (2001) 1865.
[9] NEILSON, G.H., et al., Phys. Plasmas **7** (2000) 1911.
[10] SPONG, D.A., et al., Nucl. Fusion **41** (2001) 711.
[11] ITOH, S.-I., Plasma Phys. Controlled Fusion **12** (1989) 133.
[12] FOWLER, R., er al., Phys. Fluids **28** (1985) 338.
[13] BOOZER, A.H., Phys. Fluids **23** (1980) 904.
[14] YOKOYAMA, M., et al., Phys. Rev. E **64** (2001) R15401.
[15] YOKOYAMA, M., et al., Nucl. Fusion **42** (2002) 1094.
[16] YOKOYAMA, M., et al., Nucl. Fusion **38** (1998) 68.
[17] REWOLDT, G., et al., Phys. Plasmas **6** (1999) 4705.

System Assessment of Helical Reactors in Comparison with Tokamaks

K. Yamazaki, S. Imagawa, T. Muroga, A. Sagara, S. Okamura

National Institute for Fusion Science, 322-6 Oroshi-cho, Toki, 509-5292 Japan

e-mail contact of main author: yamazaki@nifs.ac.jp

Abstract. A comparative assessment of tokamak and helical reactors has been performed using equivalent physics/engineering model and common costing model. Higher-temperature plasma operation is required in tokamak reactors to increase bootstrap current fraction and to reduce current-drive (CD) power. In helical systems, lower-temperature operation is feasible and desirable to reduce helical ripple transport. The capital cost of helical reactor is rather high, however, the cost of electricity (COE) is almost same as that of tokamak reactor because of smaller re-circulation power (no CD power) and less-frequent blanket replacement (lower neutron wall loading). The standard LHD-type helical reactor with 5% beta value is economically equivalent to the standard tokamak with 3% beta. The COE of lower-aspect ratio helical reactor is on the same level of high-β_N tokamak reactors.

1. Introduction

Economically acceptable fusion reactors are anticipated as a future electric power plant, which requires steady-state and good-confinement plasma performances. At present with respect to the plasma confinement property the tokamak system is better than the helical system. However, the inefficient current-drive (CD) re-circulation power and the abrupt plasma current disruption events are worried from the standpoint of reactor economics. In contrast, the helical system is expected as a steady-state reactor [1], but it is supposed to be a rather big and expensive system. The comparative reactor study of tokamak and helical reactors had been carried out in Ref. [2-4] so far. After that period, much progress on physics and engineering databases has been performed [5]. To search for desirable helical reactors, it is worthwhile to carry out the system analysis of helical reactors by comparing with tokamak reactor designs. Moreover, using the common same-graded costing model we can clarify performance differences between helical and tokamak reactors.

2. Model of Helical and Tokamak Reactor Systems

System assessments have been done using newly arranged PEC (Physics, Engineering and Costing) code. The flowchart of this assessment for helical and tokamak reactors is shown in Fig.1. Several items are evaluated and optimized in physics design, engineering design and cost evaluations.

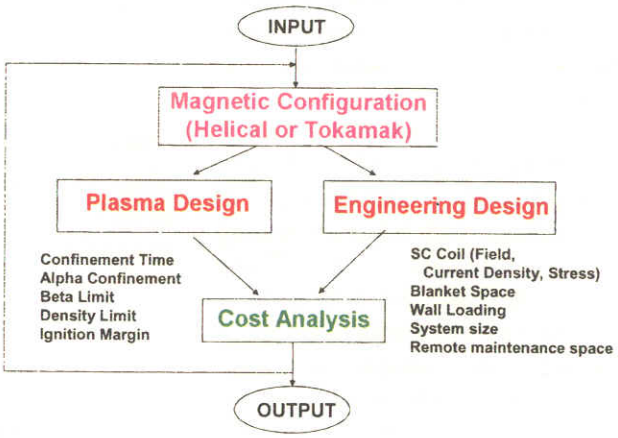

Fig.1 Flowchart of helical and tokamak system analysis

2.1 Magnetic Configurations

As for helical reactors several design concepts are studied here; the LHD (Large Helical Device)-type reactors (LHR) with continuous coil or Modular Heliotron Reactor (MHR) with modularized sector-coil systems [6] and quasi-axisymmetric modular helical reactor (QAR) based on the CHS-qa detailed design [7]. The LHR is characterized by the existence of enough plasma databases and the merits of sufficient spaces of helical

divertor and remote maintenance. The plasma aspect ratio A_p is ~ 6.5 for the standard LHR with m=10 and γ=1.25 (m: helical period, γ: coil pitch parameter). The lower aspect ratio design with m=8 is also evaluated. The MHR was invented to solve the construction difficulties of large continuous superconducting coil systems of LHR. On the other hand, the N=2 QAR (N: toroidal period) with A_p~3-4 is characterized by good confinement properties and compact design concept. In this design we need island divertor scenarios for helium ash exhaust. The tokamak reactors based on standard ITER-like designs (normalized beta: β_N ~3) [8] and higher beta compact designs (β_N ~4-5) [9] are also surveyed for the comparison with helical systems. The reactor models for both systems are shown in Fig.2. The system scale is determined by the radial-build of various system components. The plasma radius a_p and the coil thiskness t_c are deteremined by the plasma and engineering models.

2.2 Physics Model

Reactor plasma performances are determined by beta limits, confinement scaling laws and density limits. We checked several confinement scaling laws [1] including "New LHD" scaling laws. As for tokamak models the ITER Elmy H-mode confinement scaling [8] is used. The alpha-particle confinement fraction is assumed to be 0.9 for helical reactors and 0.95 for tokamaks.

The beta value of 5% is assumed for steady-state helical system without confinement degradation. Recent LHD experiments suggested the good operational regime of inward-shifted quasi-omnigenius configuration that is a target configuration of the LHR operation.

The density limit of the helical system (two times old LHD density scaling) is also considered [1] in comparisons with tokamak scaling laws (Greenwald limit). These plasma databases for both systems are checked comparatively [5]. In addition to simplified zero-dimensional power balance model with profile corrections, the TOTAL code predictive simulation [10] with empirical local transport coefficients has been carried out for the physics projections to the helical and tokamak reactors, which justified the simplified

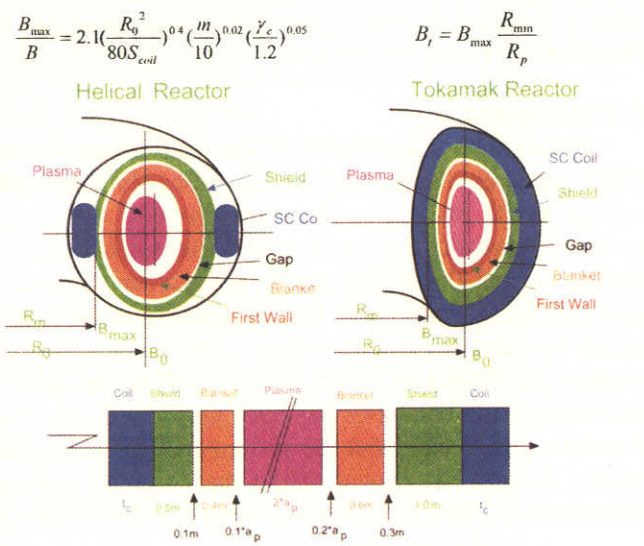

Fig. 2 Model of helical and tokamak reactor systems

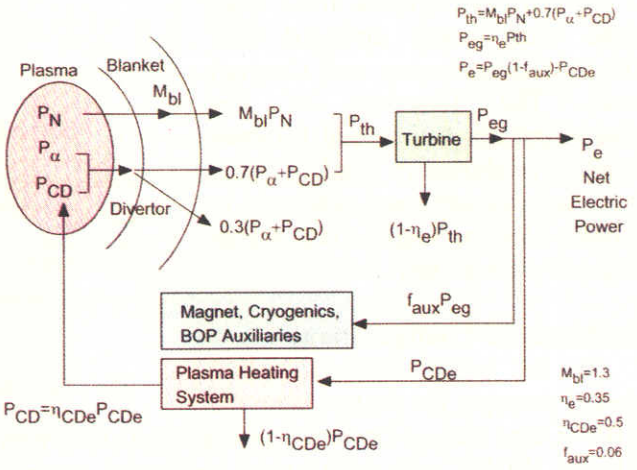

Fig.3 Power flow of fusion reactor

analysis.

2.3 Engineering Models

As for engineering design of helical and tokamak equivalent reactors, we assumed same thickness of blanket (inboard 0.5m, outboard 0.7m), shied (inboard 0.6m, outboard 1.0m) and relevant gaps (inboard 0.1m, outboard 0.3m) as shown in Fig.2. The reference magnet system is assumed made of Nb_3Sn conductor, and its maximum magnetic field strength is 12 Tesla. The superconducting coil engineering scaling for LHR/MHR is described in Ref. [11]. The coil current density, coil stress, wall loading and other engineering items are evaluated. These assumptions and relevant physics/engineering models determine the plasma-coil space and the scale of the reactor system. The thermal and electric power evaluated here is shown in Fig.3.

2.4 Costing Model

The cost analysis is mainly based on the unit costs per weight which values are mainly based on those of Refs. [12-14]. The unit cost of helical coil is assumed 25% higher than those of toroidal and poloidal coils. The main detailed values used here are shown in the Table 1. Here, Y is the normalized unit of cost (roughly 200Y~1US$).

TABLE I Unit Costs of System Components

	Unit Cost (U=100MY)		Thickness(m) inside	outside	Specific Weight (ton/m^3)	Remarks
Capital Cost						
Direct Cost						
Fusion Island						
Blanket	0.2	U/ton	0.45	0.6	4.8	Ferite.Be,Li2O
First Wall	0.1	U/ton	0.05	0.1	3.9	SS/Frite
Shield	0.04	U/ton	0.6	1	7.8	20% additional
TC Magnet	0.12	U/ton			7.9	Nb3Sn
PC Magnet	0.12	U/ton			7.9	25% of TF/HF Volume
HC Magnet	0.15	U/ton			7.9	Nb3Sn
Heating	2	U/MW				ICRF (50% efficiency)
Current Drive	4	U/MW				NNBI (50% efficiency)
Support	0.06	U/ton			6	50% of Coil Volume
Base	0.03	U/ton			6	25% of Coil Volume
Divertor	0.2	U/ton	0.05	0.1	6.9	2x10% of wall
Balance of Plant	2700	U*(Pf/4000)^0.6				6% addiditonal power
Indirect Cost	25% of Direct Cost					
time-related Cost	5% of Direct Cost					
Annual charge	10% of Capital Cost					
Operating Cost	4% of Capital Cost					
Component replacing						
Blanket	until maximum flux					10MW/m^2*year
Divertor	100% of Initial Cost					
Heating & CD	25% of Initial Cost					
Fuel	150	U/yr				
Waste disposal	0.2	Y/kWh				
Decomissioning	0.1	Y/kWh				
Electric conversionnefficiency	35	%				
Availability	75	%				

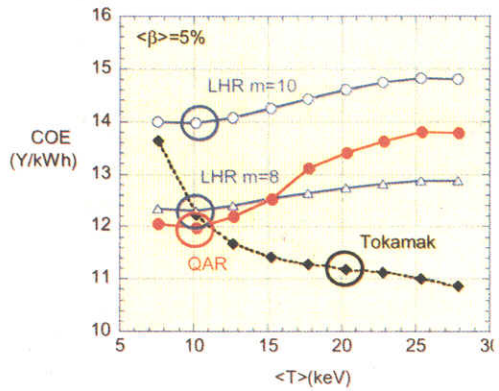

Fig.4 COE vs. averaged temperature.

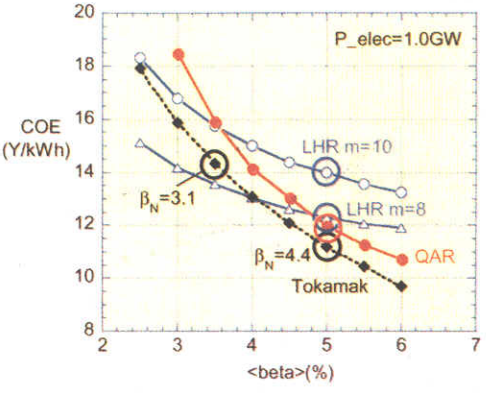

Fig.5 COE as a function of beta value.

3. Assessment Results

Figure 4 shows COE (Cost Of Electricity) as a function of average temperature <T>. High temperature plasma operation (<T>~20keV) is required in tokamak reactors to increase current drive (CD) efficiency and to reduce CD power. In contrast, rather low temperature operation (<T>~10keV) is feasible and desirable in helical system even to reduce helical ripple neo-classical transport. The density limit of helical systems is roughly two times higher than that of tokamaks. The effect of beta value is shown in Fig.5. If the tokamak operation with 5% averaged beta value (normalized beta: β_N =4.4) in the steady-state manner is not achieved, the helical system with 5% beta value will be one of target designs of future economical reactors.

The reference design points for both helical and tokamak systems are also plotted in these figures. The required confinement improvement factor is ~1.2 in these reference cases (see Table II). Figure 5 shows the plasma beta dependence of COE for helical (<T>=10keV) and tokamak (<T>=20keV) systems. In this figure, two tokamak design points are shown. The future reactor economics of tokamak reactors strongly depends on the attainable beta value in the steady-state operation.

The Fusion Island (FI) weight and FI cost of the standard LHD-type helical system are two times higher than those of reference tokamak design with same beta value and same net electric power, as shown in Table 1. However, no need of current drive (CD) power and the less-frequent replacement of blanket/heating equipments within the permissible neutron wall load (10MWyear/m^2) can contribute to the reduction in COE of helical reactor. Typically, for 1 GW plant, the wall load is ~1.5 MW/m^2 for large aspect ratio

Table II Typical Reactor Parameters (:input)*

Type	Helical			Tokamak	
	LHR m=10	LHR m=8	QAR N=2	Reference (β_N=3.1)	Reference (β_N=4.4)
R (m)	15.6	12.5	9.20	7.76	6.36
B (T)	4.5	4.6	4.7	7.0	6.62
Ap_avarage *	6.5	5.0	3.2	3.0	3.0
κ *	--	--	--	2.0	2.0
Vp (m^3)	1,773	1550	1,500	1.025	564
Ip (MA)	--	--	--	14.7	11.4
f_BS (%)	--	--	--	41	65
H_ISS95	2.75	2.54	2.21	--	--
H_NLHD1	1.28	1.15	0.95	--	--
H_ITER	--	--	--	0.908	1.17
<β> (%) *	5.0	5.0	5.0	3.5	5.0
β_N	--	--	--	3.1	4.4
Pwall (MW/m^2)	1.50	1.76	2.10	3.5	4.63
FI weight (ton)	33,870	26,760	23,690	20,814	14,550
FI cost (GY)	199	152	145	182	112
BOP cost (GY)	267	255	250	272	244
Capital (GY)	538	470	456	524	411
f_avail (%) *	75	75	75	75	75
P_thermal (GW)	3.04	3.04	3.06	3.89	3.44
P_elec (GW) *	1.0	1.0	1.0	1.0	1.0
COE (Y/kWh)	14.1	12.4	12.0	14.4	11.3

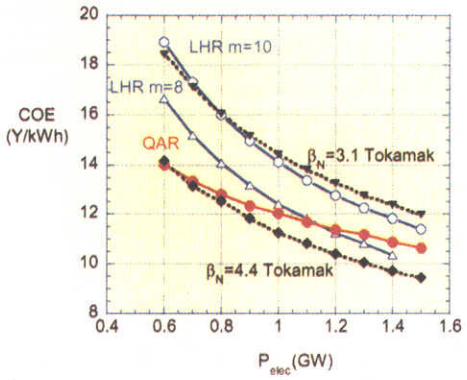

Fig.6 COE vs. electric power output

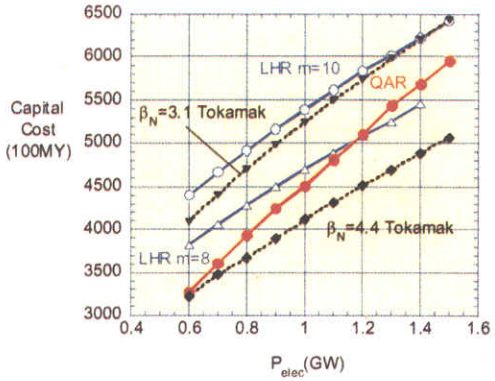

Fig.7Capital cost vs. electric power output

helical reactor and ~4-5 MW/m^2 for reference tokamak reactors. Here the availability is assumed to be 75%. The increase in 10% of availability leads to decrease in 1.5Y/kWh of COE. This availability value should be determined by the easiness of remote maintenance and the probability of plasma disruptions.

The COE and capital costs for five reactor designs are given in Fig. 6 &7. The m=10 LHR with 5 % averaged beta value is economically on the same level of reference (β_N=3.1) tokamak reactors. The more compact helical reactor is more economical, and steady-state operations with higher plasma beta values are required in the future reactors.

The above-mentioned COE values critically depend on the unit cost of relevant equipments and operation scenarios of each reactor, and more detailed and careful assessments are required.

4. Summary

The system assessment of helical and tokamak reactors have been carried out using equivalent physics, engineering and costing models, and came to the following conclusions:
(1) High temperature operation is required in tokamak reactors to increase BS current fraction and to reduce CD power. In contrast, low temperature operation is feasible and desirable in helical system to reduce helical ripple transport.
(2) Capital cost of helical reactors is rather high, however, COE is almost same as that of tokamak reactors, because of smaller re-circulation power (no CD power) and less-frequent blanket replacements (lower neutron wall loading).
(3) The m=10 LHD type helical reactor with 5% beta value is economically equivalent to the standard tokamak with 3% beta value.
(4) The COE of lower-aspect ratio helical reactor (m=8 LHR, N=2 QAR) is on the same level of high-β_N (β_N~4) tokamak reactors.
(5) More compact, higher beta reactors operating in steady-state should be investigated for realization of future attractive fusion reactors.

References

[1]YAMAZAKI, K. et al., 18th Fusion Energy Conference (Sorrento, 2000) IAEA-CN-77/FTP 2/12.
[2] GIBSON,A., et al., in Proceeding of the 4th Inter. Conference on Plasma Physics and Controlled Nuclear Fusion Research (Madison,1971) Vol.3, IAEA, Vienna (1971) p.375.
[3] KRAKOWSKI, R., Fusion Technol. **20** (1991) 121.
[4] LYON, J.F., et al., in Proceeding of the 15th International Conference on Plasma Physics and Controlled Nuclear Fusion Research 1994 (Seville, Spain, 26 September – 1 October 1994) (IAEA-CN-60/F-1-I-4) : LYON, J.F., et al., Fusion Engineering & Design **25** (1994) 85.
[5] YAMAZAKI, K., KIKUCHI, M., 12th International Toki Conference (Toki, 2002) (to be published)
[6] YAMAZAKI, K., WATANABE, K.Y., Nucl.Fusion **35** (1995) 1289 : YAMAZAKI, K., et al., Fusion Engineering and Design 41 (1998) 519.
[7] OKAMURA, S., et al., Nuclear Fusion **41** (2001) 1865
[8] ITER Physics Basis Editors et al., Nucl. Fusion **39** (1999) 2137.
[9] OKANO, K., et al., Nucl. Fusion 40 (2000) 635.
[10] YAMAZAKI, K., et al., 27th EPS Conf. (2000) P4.016.: YAMAZAKI, K., AMANO, T., Nucl. Fusion **32**, 633 (1992).
[11] YAMAZAKI, K., et al., Fusion Technol. **21** (1992) 147.
[12] TOKIMATSU, K., et al., Nucl. Fusion **38** (1998) 885.
[13] SHEFFIELD, J., et al., Fusion Technol. **9** (1986) 199.
[14] KRAKOWSKI, R., and DELENE, J.G., J. Fusion Energy 7 (1988) 49.

Development of a Fishbone Travelling Wave Antenna for LHD*

Y. Takase, A. Ejiri, S. Shiraiwa, N. Kasuya, H. Wada, H. Kasahara, T. Taniguchi, K. Yamagishi
University of Tokyo, Hongo 7-3-1, Bunkyo-ku, Tokyo 113-0033 Japan
E-mail: takase@k.u-tokyo.ac.jp

N. Takeuchi, T. Seki, R. Kumazawa, T. Mutoh, T. Watari, K. Saito, H. Torii, T. Yamamoto,
National Institute for Fusion Science, Oroshi 322-6, Toki 509-5292 Japan

M. Saigusa,
Ibraki University
Japan

C.P. Moeller, R.A. Olstad, H. Ikezi, R. Callis
General Atomics, P.O. Box 85608, San Diego, CA 92186 U.S.A.

A travelling wave antenna in the ion cyclotron range of frequencies (ICRF) is being developed for LHD, motivated by the need to provide a capability for rotational transform profile control by noninductively driven current. Stability calculations suggest that it is possible to increase the beta limit and obtain access to the second stability regime by controlling the rotational transform profile [1,2]. Current drive by the ICRF fast wave (magnetosonic wave) can be used for such a purpose.

A simple combline antenna [3] has been used successfully on JFT-2M [4]. The antenna being built for LHD is equivalent to two combline antennas stacked vertically, but has only one input and one output. Such a design enables high power operation even with limited port space. This antenna will be placed on the large major radius side of the torus where the plasma is elongated in the vertical direction (Fig. 1). The antenna is divided into 10 nearly identical modules, each consisting of a stainless steel half-wavelength resonant structure approximately 1 meter long, grounded at the midplane (T-bar current strap), a water-cooled stainless steel backplate, and a U-shaped molybdenum Faraday shield, shown in Fig. 2. These modules are placed side by side in the toroidal direction, following the helical shape of the plasma surface (Fig. 1). The whole assembly is surrounded by carbon protection tiles arranged in a "picture frame" configuration to reduce the plasma density at the Faraday shield. The

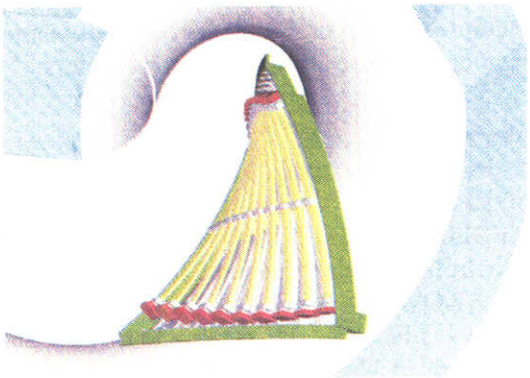

Fig. 1. A drawing of the fishbone antenna inside the LHD vacuum vessel. The Faraday shield elements and the side protection tiles are removed for ease of viewing.

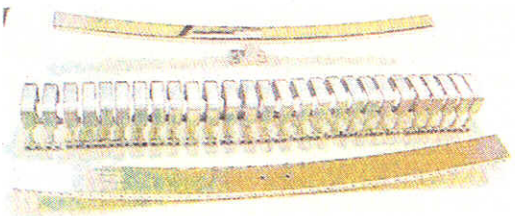

Fig. 2. The T-bar current strap, the Faraday shield elements, and the backplate.

spacing between adjacent straps (center to center) is 0.11 m, which corresponds to a wavenumber of 14 m^{-1} when the phase difference between adjacent current straps is 90°. The frequency of operation is chosen to be in the neighborhood of 75 MHz, with a bandwidth of about 20 MHz. Electron Landau damping of the fast wave will be used to heat electrons and to drive current in the plasma. In addition, second harmonic heating of hydrogen ions is also possible at a magnetic field of around 2.5 T. A schematic configuration of the fishbone antenna and an equivalent circuit are shown in Figs. 3 and 4, respectively. Here L, C, R are the self inductance, capacitance, and resistance (including the radiation resistance) of the top or the bottom half of the antenna, L_c is the inductance of the support leg of the T-bar current strap. The mutual inductance between neighboring current straps are different for even and odd modes, and are denoted M_{ee} and M_{oo}. The even mode is defined as the mode with current in the same direction in the top half and the bottom half of the current strap, whereas the odd mode has current in opposite directions in the top and bottom halves. It is assumed that there is no coupling from the even mode to the odd mode, and only the nearest neighbor coupling is considered. The resonant frequencies are given by

$$\omega_{\text{even}} = \frac{1}{\sqrt{CL}}$$

for the even mode (which has no net current in the support leg) and

$$\omega_{\text{odd}} = \frac{1}{\sqrt{C(L+2L_c)}}$$

for the odd mode (which has twice the current in the support leg).

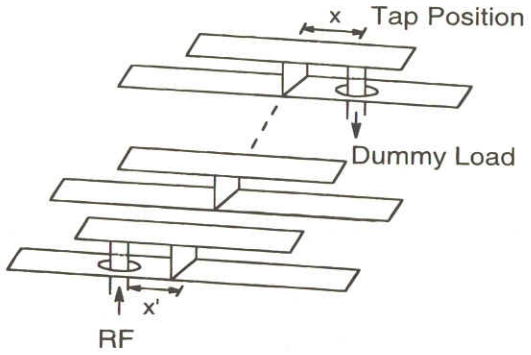

Fig. 3. A schematic of the fishbone antenna configuration.

Several mockup antennas were built to optimize the electrical properties of the antenna. The effects of geometry (strap length, strap to Faraday shield distance, Faraday shield geometry, strap to backplate distance, and strap spacing) on the pass-band characteristics were examined. The radiation resistance due to power radiated into the plasma was simulated by placing a resistive film in front of the antenna. The RF magnetic field in front of the Faraday shield was measured using a single-turn loop probe, approximately 1 cm in diameter. As expected, the phase varied monotonically in a step-wise fashion for a simple combline antenna, confirming that a traveling wave was excited. In the simple combline configuration, it is possible to select the phase shift between adjacent current straps arbitrarily in the range from 0 to π by choosing an appropriate frequency within the passband of the antenna. This gives a great flexibility in selecting the wavenumber of the excited wave. In

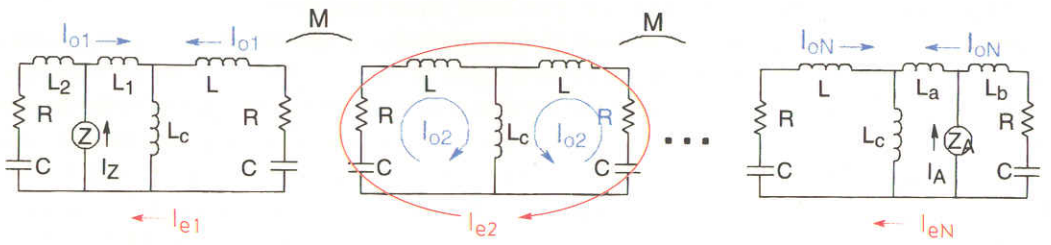

Fig. 4. An equivalent circuit diagram of the fishbone antenna.

the fishbone configuration, this flexibility is compromised because of the presence of even and odd modes as discussed in the next paragraph.

A 2 × 2 array was built to test the fishbone configuration. Two types of coupled resonances (symmetric and antisymmetric current modes), corresponding to the top-to-bottom pair (even and odd mode) and the side-to-side pair (0 and π mode), were observed. The even mode is the desired mode because it realizes the lowest poloidal mode number. Controlled excitation of the even mode is a major issue in the development of the fishbone antenna. The four resonances are shown in Fig. 5(a). The resonant frequencies for the 0 and π modes are given by

$$\omega_{\text{even}} = \frac{1}{\sqrt{C(L \pm M_{\text{ee}})}}$$

for the even mode and

$$\omega_{\text{odd}} = \frac{1}{\sqrt{C(L + 2L_{\text{c}} \pm M_{\text{oo}})}}$$

for the odd mode [5]. Relative magnitudes of inductances can be determined from these resonances as follows: L_c/L = 0.13, M_{ee}/L = 0.27, M_{oo}/L = 0.12. If the capacitance is assumed to be C = 50 pF, the self inductance is L = 100 nH. The data shown in Fig. 5(b) indicates that it is possible to separate the even and odd modes in frequency by installing a loop which links the top and bottom halves of the current strap. This has the effect of reducing L and M for the even mode but not affecting them much for the odd mode. This would make it easier to excite only the even mode, and is an option in case it proves difficult to not excite the odd mode.

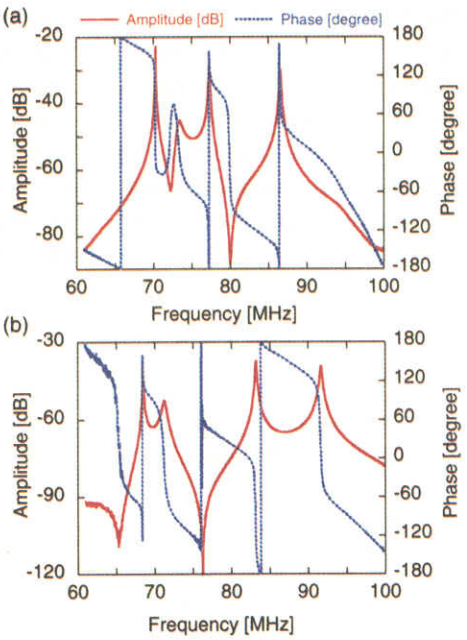

Fig. 5. Resonances of the four modes of the 2 x 2 array, (a) without the coupling loop 70.36MHz (odd-0), 73.13MHz (odd-π), 77.38MHz (even-0), 86.62MHz (even-π), and (b) with the coupling loop 68.72MHz (odd-0), 71.53MHz (odd-π), 83.23MHz (even-0), 91.93MHz (even-π).

A 4-module LHD prototype antenna was assembled. Since the first and the last elements have only one neighboring element, they are different from other elements. Therefore, adjustments must be made to ensure a clean bandpass characteristic. Extender elements were added to either the end elements or the middle elements to adjust the length of the straps (and therefore their inductance and capacitance). Matching from the feeder to the antenna was improved (the reflection within the passband decreased from –5 dB to –15 dB) by adopting a direct feeding method instead of the originally proposed loop coupling method. The top row and the bottom row can be excited either in phase or out of phase (or their linear combination). Coupling loops linking the top row and the bottom row (added to the first and last elements) have enabled approximately in-phase excitation of the top and bottom rows. A clean bandpass characteristic of the antenna with a 10 dB bandwidth of over 10 MHz centered around 74 MHz was obtained by adjusting the feeder position. Additional measurements using a 10-element mockup antenna (same dimensions as the LHD elements, but arranged on a flat plane) indicated that the coupling loop is not necessary provided the operating frequency is selected high enough to suppress excitation of the odd mode.

The LHD fishbone antenna has been assembled (Fig. 6) and final testing is being performed. Measurements of the excited fields suggest that because of the helical twist of the assembly, there is finite coupling between the even mode and the odd mode between adjacent current straps. Presently the carbon protection tiles (corresponding to the wooden parts in Fig. 6) are being designed to intersect the field lines of the LHD plasma. In addition, final adjustment of the antenna feeder position will be made before installation of the antenna in LHD.

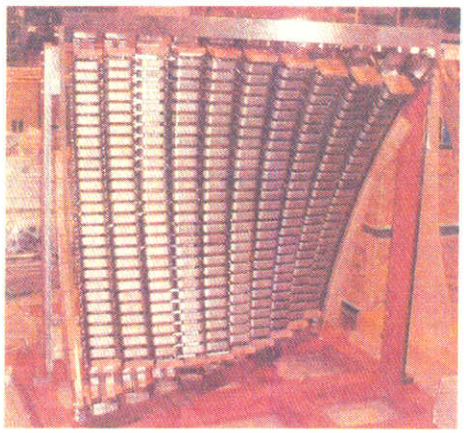

Fig. 6. The LHD "fishbone" antenna assembled for final testing.

A test with plasma load was performed on the TST-2 spherical tokamak at the University of Tokyo using a 6-strap combline antenna with a passband (defined as the frequency range where the transmission is greater than –10dB) of 22–28 MHz. A low-power (1 kW level) high-harmonic fast wave (HHFW) was excited. At 25 MHz (approximately $8\Omega_H$) the excited toroidal wavenumber is 13 m^{-1} at R = 0.57 m, which corresponds to a toroidal refractive index of 25 and a toroidal mode number of 7.4. The loading resistance was so high that RF currents induced in the second strap became much smaller than that in the first strap. It is necessary to reduce the radiation resistance low enough to allow excitation of a travelling wave with high directivity. This was accomplished by reducing the density at the antenna by inserting a movable limiter beyond the antenna radius. In LHD, the antenna will be installed sufficiently far away from the plasma. This is an advantage compared to conventional loop antennas. We note that this type of antenna is equally applicable to next generation tokamaks such as ITER, as a simple high power in-port travelling wave antenna.

*Work performed as LHD Project Research Collaboration. The US collaboration was supported by US DOE.

[1] K. Ichiguchi, et al., Nucl. Fusion **33**, 481 (1993).
[2] T. Matsumoto, et al., Nucl. Fusion **36**, 1571 (1996).
[3] Moeller, C.P., et al., in Radio Frequency Power in Plasmas (Proc. 10th Top. Conf., Boston, 1993), AIP Conference Proceedings 289 (AIP Press, Woodbury, NY), p. 323.
[4] T. Ogawa, et al., Nucl. Fusion **41**, 1767 (2001).
[5] N. Takeuchi, et al., to be published in J. Plasma Fusion Res. (2002).